Quantum Fields in Curved Spacetimes: From Detector Entanglement to Black Hole Thermodynamics

by

Dyuman Bhattacharya

A thesis
presented to the University of Waterloo
in fulfillment of the
thesis requirement for the degree of
Doctor of Philosophy
in
Physics

Waterloo, Ontario, Canada, 2025

© Dyuman Bhattacharya 2025

Examining Committee Membership

The following served on the Examining Committee for this thesis. The decision of the Examining Committee is by majority vote.

External Examiner:	Viqar Husain Professor, Dept. of Mathematics and Statistics, University of New Brunswick
Supervisor(s):	Robert B. Mann Professor, Dept. of Physics and Astronomy, University of Waterloo
Internal Member:	Niayesh Afshordi Professor, Dept. of Physics and Astronomy, University of Waterloo
Internal-External Member:	Eduardo Martin-Martinez Professor, Dept. of Applied Mathematics, University of Waterloo
Other Member(s):	Lucien Hardy Research Faculty, Perimeter Institute for Theoretical Physics, Adjunct Professor, Dept. of Physics and Astronomy, University of Waterloo

Author's Declaration

This thesis consists of material all of which I authored or co-authored: see Statement of Contributions included in the thesis. This is a true copy of the thesis, including any required final revisions, as accepted by my examiners.

I understand that my thesis may be made electronically available to the public.

Statement of Contributions

This thesis is based on the following publications and forthcoming articles.

Chapter 3 is based on:

Dyuman Bhattacharya, Kensuke Gallock-Yoshimura, Laura J. Henderson, and Robert B. Mann *Extraction of entanglement from quantum fields with entangled particle detectors*, Physical Review D 107, 105008, (2023) [46] DOI: 10.1103/PhysRevD.107.105008

Chapter 4 is based on:

Dyuman Bhattacharya, Jorma Louko, and Robert B. Mann *Probing hidden topology with quantum detectors*, Physical Review D 111, 045005 (2025) [48] DOI: 10.1103/PhysRevD.111.045005

Chapter 5 is based on:

Dyuman Bhattacharya, Jiayue Yang, Ming Zhang, and Robert B. Mann *Analytical Results for Entanglement Harvesting in Curved Spacetimes*, Forthcoming

Chapters 7 through 11 are based on:

Dyuman Bhattacharya, Robie A. Hennigar, Robert B. Mann, Ming Zhang *Charged rotating quantum black holes*, Forthcoming [47]

Contributions not included in this thesis:

Jiayue Yang, **Dyuman Bhattacharya**, Ming Zhang, Robert B. Mann *Analytic Tools for Harvesting Magic Resource in Curved Spacetime*, Forthcoming [456]

Ming Zhang, Wen-Di Tan, Mengqi Lu, **Dyuman Bhattacharya**, Jiayue Yang, Robert B. Mann *Finite-cutoff Holographic Thermodynamics*, Forthcoming [459]

Abstract

This thesis presents two independent investigations into quantum field theory in curved spacetime. The first concerns relativistic quantum information, with a focus on entanglement harvesting and detector-based probes of quantum fields in curved spacetimes. The second addresses semiclassical aspects of black hole thermodynamics in AdS braneworld settings, incorporating the backreaction of quantum fields to all orders of perturbation theory, and extending previous studies of quantum black holes to include both charge and spin.

In Part I, we study the entanglement of quantum fields in curved spacetime, using localized particle detectors interacting with a scalar field. We analyze scenarios involving both flat and curved backgrounds, including gravitational shock waves, the BTZ black hole, and general dimensional anti–de Sitter and de Sitter spacetimes. For the case of initially entangled detectors, we find that interactions with the field can lead to either degradation or amplification of entanglement, depending on the initial state and spacetime geometry. We further derive exact expressions for density matrix elements, at the lowest perturbative order, in the form of infinite analytical series, for detectors on static worldlines in various spacetimes. The transition rate of an in-falling detector in the BTZ black hole spacetime is also derived as an infinite series. These analytic results allow for exact evaluation of quantities, namely the entanglement measures of concurrence and negativity, which are typically computed numerically. In addition, we provide a new example of the ability of detectors to distinguish topologically distinct spacetimes which are locally identical outside of horizons, focusing on the $\mathbb{RP}^2$ and Swedish geons built from the BTZ spacetime. Our results show that localized measurements are sensitive not only to curvature but also to topological features of the underlying geometry.

Part II is concerned with the construction and thermodynamic analysis of quantum-corrected black holes in a doubly holographic braneworld model. We obtain a charged and rotating solution localized on an AdS_3 brane embedded in an AdS_4 bulk, incorporating the full backreaction from conformal fields to all orders of perturbation theory. We compute the thermodynamic properties of these black holes, and examine their behavior in extended thermodynamic phase space where the cosmological constant is a variable. We find that the inclusion of charge or spin removes re-entrant phase transitions present in the neutral-static case, and that the critical exponents of these objects match those predicted by classical mean-field theory. The re-entrant phase transitions of the neutral-static quantum black hole has critical exponents which differ from the mean-field values.

Acknowledgements

I am deeply grateful to my supervisor, Robert Mann for his guidance, patience, and readiness to engage with my ideas throughout my time at Waterloo. His support was indispensable and made it possible for me to pursue independent directions while keeping the broader vision in focus. I am proud to have been his student.

I owe special thanks to my collaborators: Kensuke Gallock-Yoshimura, Laura J Henderson, Robie A Hennigar, Jorma Louko, Mengqi Lu, Wen-Di Tan, Jiayue Yang, and Ming Zhang. Working with them has been instructive and rewarding. I also benefited from the broader research environment fostered at the University of Waterloo, where the seminars and academic community created a productive backdrop for research.

I thank my friend and teacher Sayeh Rajabi for being my first guide to quantum field theory.

Finally, I am indebted to my parents for their support, and the interest they showed in my work. This thesis is dedicated to them.

Dedication

To my parents, with gratitude for their patience and support.

Table of Contents

Examining Committee ii

Author's Declaration iii

Statement of Contributions iv

Abstract v

Acknowledgements vi

Dedication vii

List of Figures xiv

1 Introduction 1

2 Quantum Field Theory in Curved Spacetime and Particle Detectors 5

2.1 Quantum field theory in curved spacetime 5

2.1.1 The ambiguity of the notion of a particle in curved spacetime . . . 6

2.1.2 The Wightman function 10

2.2 Relativistic quantum information 11

2.2.1 Unruh-DeWitt detectors 11

2.2.2 Single detectors, excitation probabilities and transition Rates 13

2.2.3 Multiple detectors and entanglement harvesting . . . 17
2.2.4 Entanglement in Quantum Field Theory: Traditional Approaches and Their Limitations . . . 20
2.2.5 Entanglement measures . . . 21
2.2.6 Generating magic . . . 24

3 Entanglement Dynamics in Minkowski and Shock Wave Spacetimes 29
3.1 Initially entangled detectors . . . 29
3.1.1 Approximating the concurrence . . . 32
3.2 Smeared detectors in Minkowski spacetime . . . 34
3.3 The fate of entanglement between inertial detectors . . . 39
3.4 Entanglement in the presence of a shockwave . . . 42
3.4.1 Shockwave spacetime . . . 43
3.4.2 Results . . . 44
3.5 Conclusion . . . 47

4 Probing Hidden Topology with UDW Detectors 50
4.1 Introduction . . . 50
4.2 Physical Setup . . . 52
4.3 Quotients of AdS_3 . . . 53
4.3.1 AdS_3 . . . 53
4.3.2 BTZ black hole . . . 55
4.3.3 $\mathbb{R}P^2$ geon . . . 56
4.3.4 Swedish geon . . . 56
4.4 Transition rate comparisons . . . 57
4.4.1 Preamble: choice of the state . . . 57
4.4.2 Image sum in the state induced from the AdS_3 global vacuum . . . 59
4.4.3 BTZ . . . 60

4.4.4 $\mathbb{R}P^2$ geon . . . 60
4.4.5 Swedish geon . . . 61
4.5 Results . . . 62
4.6 Conclusions and discussion . . . 65

5 Analytic Methods for Harvesting Entanglement in AdS, dS, BTZ, and Minkowski spacetimes 67
5.1 Solutions for AdS_{d+1} . . . 68
5.1.1 Wightman function . . . 68
5.1.2 Excitation probability . . . 70
5.1.3 Correlation term: X . . . 72
5.1.4 Correlation term: C . . . 78
5.1.5 Comparison . . . 79
5.2 Solutions for dS_{d+1} . . . 79
5.2.1 Wightman function . . . 79
5.2.2 Excitation probability . . . 83
5.2.3 Correlation term: X . . . 85
5.3 Solutions for the BTZ black hole . . . 88
5.3.1 Wightman function . . . 88
5.4 Solutions for Minkowski Spacetime . . . 90
5.4.1 Wightman function . . . 90
5.4.2 Excitation Probability . . . 91
5.4.3 Correlation term: X . . . 93
5.5 Concluding remarks . . . 93

6 Braneworld Holography and Quantum Black Holes 94
6.1 Holographic preliminaries . . . 95
6.1.1 the AdS/CFT correspondence . . . 95

6.1.2 Holographic Renormalization . . . 97
6.1.3 Braneworld Holography . . . 98
6.1.4 Double Holography . . . 100
6.2 Quantum black holes . . . 101
6.2.1 The AdS C-metric . . . 102
6.3 Black hole thermodynamics . . . 106
6.3.1 Classical Black Holes and the Laws of Mechanics . . . 106
6.3.2 Hawking radiation . . . 107
6.4 Black hole chemistry . . . 108
6.4.1 Pressure–Volume Thermodynamics . . . 108
6.4.2 Smarr Relation . . . 108
6.4.3 Phase Structure and Critical Phenomena . . . 109
6.4.4 Holographic Interpretation . . . 109

7 Charged and Rotating Quantum Black Holes **111**
7.1 Solution and braneworld embedding . . . 111
7.2 Thermodynamic quantities . . . 116
7.2.1 Brane expressions . . . 118
7.2.2 Bulk expressions . . . 123
7.2.3 Boundary expressions . . . 127

8 Phase Transitions and Criticality **132**
8.1 Brane perspective . . . 132
8.2 Bulk perspective . . . 138
8.3 Boundary perspective . . . 139
8.4 Elimination of re-entrant phase transitions . . . 139

9 Validity of the Semiclassical Approximation **142**

9.1 Static charged quantum black holes 143

9.2 Neutral rotating quantum black holes 143

9.3 Charged and rotating quantum black holes 149

9.4 Connection with weak cosmic censorship 150

10 Quantum Inequalities **154**

10.1 Quantum Penrose inequality 154

10.2 Penrose inequality with angular momentum 156

10.3 Quantum reverse isoperimetric inequality 158

11 The Gyromagnetic Ratio of the Charged and Rotating Quantum Black Hole **160**

11.1 The renormalized gyromagnetic ratio 160

11.2 Discussion 163

12 Conclusion **166**

References **170**

APPENDICES **206**

A Explicit construction of the Swedish geon **207**

A.1 Swedish geon generators 207

A.1.1 Fundamental domain on the Poincaré disk 207

A.1.2 Generators in the spacetime 210

A.2 Fundamental domain deformation 212

A.3 Topology 213

B Explicit Expressions for the Charged Rotating Quantum Black Hole 219
B.1 Explicit expressions 219
B.1.1 Brane volume and chemical potential 219
B.1.2 Boundary pressure 223
B.2 Tensionless limit: Kerr-Newman-AdS 227

List of Figures

3.1 Real and imaginary parts of $J_{kk}^{(-+)} + J_{kk}^{(+-)*}$ with $\sigma/T = 1$ and $\lambda = 1/10$. The real part converges quickly to 0 with large $|\Omega T|$ while the imaginary part is nonzero for a wide range of ΩT. 37

3.2 (a) Finite-sized detectors in Minkowski spacetime. The center of mass of detector B is located at $(t_{B,0}, \boldsymbol{x}_B)$; each detector has the respective spatial and temporal Gaussian widths σ and T. The diagonal orange-shaded strip represents the null trajectories from detector A; detector A can directly signal to B by exchanging field quanta once the support of detector B crosses this region. (b) A plot of the positive part of the difference $\mathcal{C}_{AB} - \mathcal{C}_{AB,0}$ between the concurrence before and after the interaction, with $\beta = 10^{-15}, \lambda = 1/10, \Omega T = 5, \sigma/T = 0$, and $\theta = 0$. The green dots represent $\mathcal{C}_{AB} - \mathcal{C}_{AB,0} \leq 0$, which means the initial entanglement is degraded, and the dashed lines indicate the null trajectory corresponding to the one in (a). . . 38

3.3 (a) The positive part of $\mathcal{C}_{AB} - \mathcal{C}_{AB,0}$ as a function of ΩT and $\log_{10}\beta$ when $\lambda = 1/10, L/T = 7, \Delta t/T = 0, \sigma/T = 0$, and $\theta = 0$. The green dots represent degradation. The detectors can gain entanglement when β is small enough. The range of ΩT that enables the detectors to gain entanglement enlarges as $\beta \to 0$. (b) $\max[0, \mathcal{C}_{AB} - \mathcal{C}_{AB,0}]$ as a function of $\log_{10}\beta$ for $\lambda = 1/10, L/T = 7, \Delta t/T = 0, \sigma/T = 0$, and $\Omega T = 7$. The blue curve shows a slice in (a) at $\Omega T = 7$, whereas the orange dashed curve represents the case when $\theta = \pi$. (c) Each component $\mathcal{C}_{AB}$ and $\mathcal{C}_{AB,0}$ in (b) with the same parameters. 41

3.4 The positive part of difference $\mathcal{C}_{AB} - \mathcal{C}_{AB,0}$ as a function of L/T and ΩT. Here, $\Delta t/T = 0, \beta = 10^{-15}$, and $\theta = 0$. Entanglement degradation occurs in the region with green dots. 42

3.5 (a-i) Initial and final concurrences when $\Omega T = 2, \beta = 10^{-5}, \lambda = 1/10$, and $\theta = 0$. The location of detector B is fixed at $z_B/T = 7$. detector A encounters the shockwave near $z_A/T = 0$. (a-ii) The concurrences when $\Omega T = 2, z_A/T = -0.5$ and $z_B/T = 7$ with varying initial amount of entanglement. Two curves will cross and degradation takes place after $\log_{10}\beta > -3$. (b) Final concurrence $\mathcal{C}_{AB}$ for initially maximally entangled detectors ($\mathcal{C}_{AB,0} = 1$) with $\Omega T = 2$ and $\theta = 0$. The green dotted curve corresponds to detectors in Minkowski spacetime. In this case, the shockwave can either reduce or amplify the degradation effect. 45

3.6 Diagram for two pointlike inertial detectors in a shockwave spacetime. Detectors A and B are static at $z = z_A$ and z_B, respectively, and the shockwave travels along $u = 0$ (the green wiggling line). The red and blue bars indicate the effective interaction duration of the detectors. 46

4.1 The transition rate of a gapless detector, switched on in the asymptotic past, as a function of the switch-off moment, for AdS_3, the BTZ black hole, the $\mathbb{R}P^2$ geon, and the Swedish geon. The parameters are $r_h/\ell = \sqrt{7}$ and $R^2/r_h^2 = \frac{25}{7}$. Panels (a), (b) and (c) are for the Neumann ($\zeta = -1$), Dirichlet ($\zeta = 1$), and transparent ($\zeta = 0$) boundary condition, respectively. The transition rates on AdS_3 and the BTZ black hole so close that they are indistinguishable by the naked eye. 63

4.2 As in Fig. 4.1(a) but with $\ell\beta\Omega = 5$, giving the excitation rate of a detector with a nonzero gap. The transition rates on AdS_3 and the BTZ black hole are again so close that they are indistinguishable by the naked eye. 64

4.3 As in Figures 4.1(a) (Panel (a)) and 4.2 (Panel (b)) but with a smaller black hole, $r_h/\ell = \sqrt{3}$, with detector position still such that $R^2/r_h^2 = \frac{25}{7}$. 66

5.1 The concurrence of the final reduced density matrix of two static detectors with a given fixed proper distance between them, that reach peak interaction simultaneously in the field's frame (i.e., in the global time coordinate the global AdS vacuum is defined with), plotted as a function of their energy gap. All possible AdS boundary conditions are displayed. The AdS length scale ℓ is chosen to be equal to the switching width σ, and one detector is placed at the origin. Panel (a) shows the plots generated by the analytical formulas for the density matrix elements. Panel (b) is from the corresponding numerical plot in [203]. 80

5.2 The final concurrence of the two detectors as a function of the the relative time delay in their switching functions t_0, where the AdS length scale is $\ell/\sigma = 1$, a proper distance of $5\sigma/2$ and where we impose Neumann boundary conditions ($\zeta = 1$) and an energy gap of $\Omega\sigma = 2$ and $\Omega\sigma = -2$. Panel (a) shows the plots generated by the analytical formulas. Panel (b) is from the corresponding numerical plot in [203]. Note the difference in the number of points, and that the analytical result took a few seconds to generate. . . . 81

8.1 Free energy-temperature curves for neutral-static systems in the canonical ensemble with different pressures. The central charge for each curve is kept at $c_3 = 10$. The cusps on each curve are highlighted in red. From left to right are curves at $P < P_C$, $P = P_c$, and $P > P_c$. 134

8.2 An isobar that corrects the presence of metastable states in the isotherm. The area above and below the isobar are equal. The smaller volume is marked in red while the larger volume is marked in blue. These are points on the coexistence curve. For the sake of visibility, this is far away from the critical point, and the curve corresponds to $\tilde{t} = -1/10$. When calculating the critical exponents, we take these points to be very close. 136

8.3 (Left) Free energy-temperature curves for the charged-static quantum black hole, with central charge $c_3 = 10$ and pressure $G_3^3 P_3 = 1.81 \times 10^{-4}$, for three different charges: (blue) $\sqrt{G_3}Q = 0$, (purple) $\sqrt{G_3}Q = \frac{1}{10}$, (orange) $\sqrt{G_3}Q = \frac{1}{3}$. The last of these has an electric charge that exceeds the critical electric charge value Q_c, and the cusp does not reappear, signifying a non-re-entrant phase transition. (Right) The same curves separated by vertical offsets for the sake of visibility. Note how the neutral curve extends to $T \to \infty$, but the charged curves have a maximum possible temperature. Note also how increasing the electric charge of the system pulls the new turning point/cusp towards another, until (at criticality) they merge and disappear. 137

9.1 Left: A plot of the temperature as a function of α for the neutral rotating quantum black hole. Here the red dots indicate the extremal solutions with $\alpha = \alpha_{\rm I}$ while the green squares are the extremal solutions with $\alpha = \alpha_{\rm II}$. The blue curve corresponds to $(z, \nu) = (1, 1/2)$ while the green curve corresponds to $(z, \nu) = (1.5, 0.125)$. The dashed portions of the curves have $\bar{a}^2 > 1$ and are therefore unphysical. Right: The (z, ν, α) parameter space color-coded according to the type of extremal solutons. For those parameters in the green region (leftmost side of the plot) the $\alpha_{\rm II}$ extremal solution is reached first. For those parameters in the blue region (rightmost side of the plot) the $\alpha_{\rm I}$ extremal solution is reached first, while the $\alpha_{\rm II}$ solution is unphysical with $\bar{a}^2 > 1$. 145

9.2 We show the (ν, z) parameter space for the neutral rotating quantum black hole characterizing the regions where $M^{\rm I}_{\rm gap}$ is negative (red) and positive (blue). The black cross-hatched portion of the parameter space shows where $\alpha_{\rm I} < \alpha_{\rm II}$. 147

9.3 Left: $M^{\rm I}_{\rm gap}$ as a function of the angular momentum for difference choices of backreaction parameter ν. Right: $M^{\rm II}_{\rm gap}$ as a function of the angular momentum for difference choices of backreaction parameter ν. In each case, the darker the shade of blue, the larger the value of ν for that curve. The thin red lines in each plot show the value of $M^{\rm BTZ}_{\rm gap} = 16 G_3/\ell_3^2$ for the classical rotating BTZ black hole. On the right plot, the black line is $z = \nu^{-1/3}$ which marks the boundary of the physical parameter space. In both cases, $M_{\rm gap} \to 0$ when the angular momentum takes its largest value for a given ν. 148

9.4 We extend Fig. 9.2 to show how the regions in (ν, z) parameter space where $M^{\rm I}_{\rm gap}$ is negative evolves as χ increases. From the top left across and down, we have shown the regions for $\chi = 0, 1/4, 1/2, 3/4, 1, 5/4$. Just as before, the red-shaded portion of the parameter space corresponds to $M^{\rm I}_{\rm gap} < 0$ and the black cross-hatched portion of the parameter space shows where $\alpha_{\rm I} < \alpha_{\rm II}$. Note that increasing χ increases the portion of parameter space where there exist solutions satisfying physicality conditions, and shrinks the portion where $M^{\rm I}_{\rm gap}$ is negative. The apparent dashed curve is a thin section of meshed area. 151

11.1 The renormalized gyromagnetic ratio of the quantum black hole on the brane as a function of the backreaction parameter ν for the displayed values of the Casimir subtracted mass ΔM, charge Q and spin J. The structure of this curve is insensitive to the fixed physical values that an observer would measure, of the black hole on the brane. The gauge coupling g_3 has been set to unity. 162

A.1 Two fundamental domains on the Poincaré disk. **(a)** In panel (a), the fundamental domain is between the four symmetrically-arranged geodesic circle segments, and the identifications of the segments use the generators $\tilde{A}$ and $\tilde{B}$ (A.5) as shown. The fundamental domain reaches the boundary of the disk in four segments, and the identifications join these segments into a circle. **(b)** In panel (b), the fundamental domain is between the seven geodesic circle segments, and the identifications of the segments use the generators A and B (A.6) as shown. The fundamental domain is adapted to the infinity, where it reaches the boundary of the disk in a single segment, and the identification by $BAB^{-1}A^{-1} = -D_V(\psi_h)$, with ψ_h given by (A.10), joins this segment into a circle. The horizon is on the axis of $D_V(\psi_h)$ as shown. . . . 209

A.2 **(a)** The upper half-plane fundamental domain D_1 to which the fundamental domain in Figure A.1(a) is mapped by the fractional linear transformation (A.15). $\hat{A}$ maps the left single-arrowed semicircle to the right one, and $\hat{B}$ maps the quadruple-arrowed semicircle to the positive imaginary axis. **(b)** D_1 together with its image under $\hat{A}$, shown shaded. 214

A.3 **(a)** As in Figure A.2 (b), but showing also a geodesic arc (in red) that cuts D_1 in two symmetric halves, and the image of this arc in the shaded image of D_1. **(b)** A new fundamental domain D_2, combining half of D_1 and half of the shaded image of D_1. The upper triple-arrowed boundary is mapped to the lower triple-arrowed boundary by $\hat{A}$. The left single-arrowed boundary is mapped to the right single-arrowed boundary by $\hat{A}\hat{B}\hat{A}^{-1}$. 215

A.4 **(a)** D_2 together with its image under $\hat{B}$, shown shaded. Also shown is a geodesic arc (in green) that cuts D_2 in two symmetric halves, and the image of this arc in the shaded image of D_2. **(b)** A new fundamental domain D_3, combining half of D_2 and half of the shaded image of D_2. The left quadruple-arrowed boundary is mapped to the right quadruple-arrowed boundary by $\hat{B}$. The left single-arrowed boundary is mapped to the right single-arrowed boundary by $\hat{B}\hat{A}\hat{B}^{-1}\hat{A}^{-1}$, whose fixed points are $w = \pm 1$. The dashed curve is the geodesic circle joining $w = \pm 1$ and forming the horizon. 216

A.5 **(a)** Fundamental domain of a punctured torus, realised as a rectangle with a hole in the middle. The arrows show the pairwise identifications of the sides. All the four corner points, labelled q, are identified. **(b)** A pair of identified points labelled p on the boundary are chosen. The double-arrowed boundary segments are identified, and the triple-arrowed boundary segments are identified. 217

A.6 **(a)** A cut is introduced from one of the points p to the puncture. **(b)** The surface is continuously deformed around the new cut. 217

A.7 **(a)** The straight boundary segments of Figure A.6 (b) are deformed to curved boundary segments that match those in the upper half-plane fundamental domain in Figure A.4 (b). **(b)** A perspective picture in which the fundamental domain of panel (a) has been embedded in $\mathbb{R}^3$ and glued across the identified boundaries. The top side of the surface in panel (a) has become the inner side in panel (b). 218

Chapter 1

Introduction

Quantum field theory in curved spacetime (QFTCS) provides a setting in which both gravitational and quantum effects can be studied without quantizing the gravitational field itself. This regime is semiclassical—the spacetime geometry is fixed and only the matter fields are quantized. Despite its conceptual simplicity, QFTCS has revealed fundamental phenomena such as Hawking radiation, the Unruh effect, and cosmological particle creation and continues to serve as an essential theoretical laboratory for exploring the subtle interplay between quantum phenomena and gravitational fields [195, 428, 354]. Moreover, it is the foundation of relativistic quantum information (RQI), an interdisciplinary field that extends traditional quantum information theory to relativistic settings, based on localized probes known as Unruh-DeWitt (UDW) detectors interacting with quantum fields, which are used to investigate the structure of spacetime and the nature of field correlations.

This thesis is divided into two largely independent parts. The first is composed of various problems in the context of RQI: the extraction, degradation, and operational characterization of the quantum entanglement of selected vacuum states in a variety of curved spacetimes using UDW detectors. We investigate how spacetime curvature, causal structure, and global topology influence entanglement dynamics between two detectors, and focus on the use of the transition rate of a single detector as a means of identifying spacetimes that are locally identical but differ in terms of global topological identifications. The second part details the construction and thermodynamic analysis of charged and rotating quantum black holes in a doubly holographic AdS braneworld model, alongside tests of the validity of the semiclassical approximation. The two programs differ in both method and motivation, but are united by a common theme: quantum fields propagating on curved spacetimes. Thus, both address the broader conceptual question of how spacetime geometry imprints itself on observable quantities.

The rest of this thesis has the following structure. Part I consists of the following chapters

- **Chapter 2:** *Quantum Field Theory in Curved Spacetimes and Particle Detectors*
  We provide a brief introduction to the principles of both QFTCS and RQI, with special attention paid to the fundamental conceptual shift in moving from flat to curved spacetimes as the arena for quantum field theory, namely the loss of a natural or preferred vacuum state and Fock space and the resultant ambiguity in the notion of a particle. This motivates the operational framework of RQI. A similarly brief overview is given of entanglement measures in quantum information and computation, as well as the magic resource. The chapter concludes by reviewing the concept of entanglement harvesting as a probe of the entanglement structure of the field, and lays out the general steps of calculation for its quantification.

- **Chapter 3:** *Entanglement Dynamics in Minkowski and Shock wave Spacetimes*
  We consider the case of two initially entangled UDW detectors in flat spacetime and examine how the entanglement evolves after interacting with a quantum scalar field. We find that these initially entangled detectors can gain more entanglement, as measured by the concurrence, so long as they are weakly correlated in the initial state. Initial states with strongly entangled UDW detectors only experience entanglement degradation. This analysis is then applied to a gravitational shock wave spacetime, and it is shown that the presence of a shock wave can enhance the initial entanglement of weakly entangled detectors. We find that the enhancement of entanglement in the shock wave spacetime can occur for greater detector separations than in Minkowski spacetime.

- **Chapter 4:** *Probing Hidden Topology With Quantum Detectors*
  We study the impact of global topology on the response of a single detector. By comparing the behavior of individual detectors in locally identical but globally distinct geometries, such as the $\mathbb{RP}^2$ geon and the Swedish geon—both constructed as quotient spaces of the BTZ geometry—we demonstrate that detector transition rates encode global topological identifications hidden behind the black hole horizon. These results indicate that localized measurements may be capable of detecting global geometric structure, an inherently nonlocal effect.

- **Chapter 5:** *Analytic Methods for Harvesting Entanglement in AdS, dS, BTZ, and Minkowski spacetimes*
  We derive analytic expressions for the reduced density matrix elements of two detectors, at leading order in the field-detector coupling, in various curved backgrounds,

namely the AdS_{d+1}, dS_{d+1}, and BTZ black hole spacetimes. These results allow for exact analytic evaluations of entanglement measures that previously required numerical methods. The fields considered are massless conformally coupled scalar fields, and the worldlines of the detectors are static. These analytical results are used to calculate entanglement harvesting and found to agree with prior, numerical, calculations.

The chapters that compose Part II may be read independently of Part I, listed above. Unlike Part I, where chapters 3 to 5 can be read in any order and function independently of one another, each chapter in Part II builds on the other, so that a full understanding requires the part to be read in its entirety.

- **Chapter 6:***Braneworld Holography and Quantum Black Holes*
  We present a rapid-fire survey of AdS/CFT correspondence and its extension, the doubly-holographic braneworld formulation. Black hole solutions in the bulk localized on the brane are singled out, as are their duals of codimension-one. The latter are exact solutions to a semiclassical effective theory on the brane with a higher derivative gravitational action, and are interpreted as including the backreaction of conformal matter fields on the spacetime, to all orders of perturbation theory, and are therefore referred to as "quantum black holes." We consider charged and rotating quantum black holes, generalizing previous investigations which dealt with charged and rotating solutions separately.

- **Chapter 7:** *Charged and Rotating Quantum Black Holes*
  Working directly from the AdS C-metric solution restricted to the brane, we carefully construct solutions describing black holes that carry both angular momentum and electric charge. The physical parameters of the system are then gleaned from the metric. From this, the thermodynamic properties of the system are calculated from the bulk, brane, and boundary perspectives.

- **Chapter 8:** *Phase Transitions and Criticality*
  The phase structure of the thermodynamic space of the system is investigated from the bulk, brane, and boundary perspectives, using numerical methods that rely on the equality of free-energy between two coexisting phases, as well as on the Maxwell equal-area construction. We find that the neutral-static quantum black hole can undergo re-entrant phase transitions, associated with critical exponents that differ from those predicted by mean-field theory. An important result arising from an algebraic analysis of the functions for the thermodynamic parameters of the system

is that introducing charge or rotation in any quantity drastically modifies the thermodynamics observed in the neutral-static solutions. In particular, we find that the re-entrant phase transitions are entirely removed. Interestingly, our analysis reveals that these charged or spinning solutions exhibit critical behavior in accordance with classical mean-field theory. The presence of unorthodox critical exponents is the first instance of non-mean-field theory critical exponents in a theory of Einstein gravity.

- **Chapter 9:** *Validity of the Semiclassical Approximation*
  We use a definition of a mass-gap energy scale (M_{gap}) from a near-extremal expansion of the black hole entropy to quantify the domain of validity of the semiclassical approximation, identifying conditions under which quantum gravitational fluctuations become significant. An analysis of this mass gap and the corresponding types of extremal quantum black holes is then carried out. Finally, we present a connection between the above analysis and the weak cosmic censorship conjecture.

- **Chapter 10:** *Quantum Inequalities*
  We explore geometric inequalities fundamental to black hole physics, extending and generalizing the quantum Penrose and reverse isoperimetric inequalities to explicitly account for charge and angular momentum. A numerical sweep indicates that this inequality is obeyed for the charged and rotating quantum black hole.

- **Chapter 11:** *The Gyromagnetic Ratio of the Charged and Rotating Quantum Black Hole*
  We introduce and motivate a formula for a renormalized gyromagnetic ratio g. We demonstrate that significant quantum backreaction pushes the value away from the classical Kerr–Newman benchmark of $g = 2$, underscoring the role of quantum corrections in black hole geometries.

The organizing aim of this thesis is to make specific aspects of spacetime geometry accessible to calculable diagnostics. Part I does this operationally: detector observables built from the Wightman function (transition rates and entanglement measures) are used to isolate how curvature, causal structure, and global identifications affect weak-coupling measurements. Part II does this semiclassically: in a concrete doubly holographic braneworld constructed from the AdS C-metric, quantum backreaction of conformal matter is encoded in a higher-derivative effective theory on the brane, whose black-hole thermodynamics and phase structure can be computed. The two programs use different frameworks, but in both cases geometry enters as explicit input and its consequences are derived within clearly stated assumptions. The resulting statements are diagnostic about how curvature, topology, and backreaction control the computed quantities.

Chapter 2

Quantum Field Theory in Curved Spacetime and Particle Detectors

Quantum field theory in curved spacetime (QFTCS) is a natural extension of ordinary (flat-spacetime) quantum field theory, which is relevant when gravitational effects on the system under consideration are weak but not entirely negligible. Here, gravitational effects being weak is taken to mean that the quantum nature of the gravitational field can safely be neglected. We consider quantum fields propagating on a fixed Lorentzian manifold $(\mathcal{M}, g_{\mu\nu})$, without attempting to quantize the spacetime geometry itself. As stated in the previous chapter, while this is an approximation, it has proved to be remarkably fruitful, and provided the theoretical basis for the discovery of fundamental phenomena from Hawking radiation, to cosmological particle creation. More recently, it has provided a foundation for relativistic quantum information (RQI). A successful theory of quantum gravity may be expected to reproduce the results of QFTCS in a suitable limit. In this thesis, we will consider the quantum field in question to be a real scalar field. The presentation of the fundamentals of QFTCS follows [50] while the presentation of the fundamentals of RQI follows [399].

2.1 Quantum field theory in curved spacetime

The most immediate difference between flat and curved spacetimes is the absence of global Poincaré symmetry. In Minkowski spacetime, time translation symmetry means that there exists a globally defined timelike Killing vector field, through which we can define positive

frequency modes universally. The unique decomposition of field modes into positive and negative frequency components leads to the notion of a canonical vacuum, via annihilation operators. In curved spacetime, this symmetry is typically absent—there is no preferred global timelike Killing vector, so the mode decomposition of the field by globally defined inertial observers is no longer possible. Without a global notion of positive frequency, quantities like particle number become ambiguous. Indeed, in curved backgrounds, the concept of a "particle" is often ill-defined. A state considered to be the vacuum by one observer may be filled with particles in the frame of another. We expand on these points in the subsection below.

2.1.1 The ambiguity of the notion of a particle in curved spacetime

The notion of a particle in ordinary relativistic quantum field theory is fundamentally tied to the symmetries of (n-dimensional) Minkowski spacetime $(\mathbb{R}^{1,n-1}, \eta_{\mu\nu})$, given by the *Poincaré group* $\mathrm{ISO}(1, n-1)$. This group is composed of Lorentz transformations (rotations and boosts) and spacetime translations, and reflects the invariance of physical laws under those symmetries. Particles are then defined as those states that transform as irreducible unitary representations of the Poincaré group [388]. Famously, there are no finite-dimensional unitary representations of the Poincaré group. Unitary irreducible representations of the Poincaré group, classified by Wigner, are infinite-dimensional and described by fields [445].

We therefore consider the set of states describing a particle to be tied to fields transforming under specific representations of the Lorentz group—scalar, vector, spinor, or tensor fields. For example, spin-0 particles are represented by scalar fields, spin-1/2 particles by spinor fields, and spin-1 particles by vector fields. The mass and spin of a particle are directly determined by how the states describing them, which are constructed by the action of the creation operators of their associated quantum field on the vacuum state, transform under action by the Poincaré group. Given that the rigorous notion of a particle is fundamentally tied to the Poincaré group, one might expect that making the transition to curved spacetime, where the Poincaré group is not a symmetry group, will muddy the waters and introduce ambiguities, and this is in fact the case.

Consider the action of a real scalar field propagating on an n-dimensional curved spacetime manifold with metric $g_{\mu\nu}$[50],

$$S = \int \mathrm{d}x^n \mathcal{L}(x) = \frac{1}{2} \int \mathrm{d}x^n \sqrt{-g} \left[\partial_\mu \phi(x) \partial^\mu \phi(x) - (m^2 + \zeta R(x)) \phi(x)^2 \right], \tag{2.1}$$

where g is the determinant of the metric $g_{\mu\nu}$, $R(x)$ is the Ricci scalar and ζ is a dimensionless coupling constant between the scalar and gravitational fields. The associated equation of motion satisfied by the field is

$$[\Box + m^2 + \zeta R(x)]\phi(x) = 0, \tag{2.2}$$

where $\Box\phi(x) = \nabla^\mu\nabla_\mu\phi(x) = (-g)^{-1/2}\partial_\mu[(-g)^{-1/2}g^{\mu\nu}\partial_\nu\phi(x)]$. We assume that the spacetime in question is globally hyperbolic, meaning that it can be foliated by Cauchy spacelike hypersurfaces. This allows us to define the scalar product between two fields

$$(\phi_1, \phi_2) = -i\int_\Sigma \mathrm{d}\Sigma^\mu\sqrt{-g_\Sigma}\phi_1(x)\overleftrightarrow{\partial}_\mu\phi_2^*(x), \tag{2.3}$$

where Σ is a spacelike hypersurface with volume element $\mathrm{d}\sigma$ and a future-directed unit vector orthogonal to it n^μ, and $\mathrm{d}\sigma^\mu = n^\mu\mathrm{d}\sigma$. It may be shown using Gauss' theorem [194], that the value of (ϕ_1, ϕ_2) is independent of the choice of the Cauchy surface Σ. The Fock quantization of our real Klein-Gordon field relies on decomposing the space of solutions to the equation of motion into a positive Klein-Gordon norm subspace and a negative Klein-Gordon norm subspace, where the norm is defined above. In Minkowski spacetime, we choose the positive norm subspace to be the positive frequency subspace with respect to Minkowski time translations. This results in the standard Minkowski Fock vacuum being the ground state of the theory, which is physically interpreted as the state without any particles, as measured by all inertial observers [50, 48].

In our curved spacetime, the field operator $\hat{\phi}(x)$ can still be quantized using a mode expansion. Let $\{u_k(x)\}$ be a complete, orthonormal set of complex solutions to (2.2). Following [50] and [399] we "place the theory in a box," so to speak. That is, we will confine the solutions to an $(n-1)$-torus with length scale L, though the expansion below can easily be generalized to the continuum case by replacing the discrete sum with an integral and the Kronecker delta with a Dirac delta. We can expand the field operator $\hat{\phi}(x)$ as

$$\hat{\phi}(x) = \sum_k \left[\hat{a}_k u_k(x) + \hat{a}_k^\dagger u_k^*(x)\right]. \tag{2.4}$$

The set of solutions being orthonormal means

$$(u_i, u_j) = \delta_{ij}, \quad (u_i^*, u_j^*) = -\delta_{ij}, \quad (u_i, u_j^*) = 0. \tag{2.5}$$

The field is quantized by promoting $\hat{a}_k$ and $\hat{a}_k^\dagger$ to operators that obey the canonical commutation relations,

$$[a_i, a_j^\dagger] = \delta_{ij}. \tag{2.6}$$

Following this, we can construct a vacuum state and Fock space using the ladder operators defined above, just as in Minkowski space. However, unlike the case in Minkowski spacetime, the choice of mode expansion is generally not privileged or in any sense canonical. The Minkowski metric

$$ds^2 = dt^2 - \left(\sum_i dx_i^2\right) \tag{2.7}$$

is defined by its invariance with respect to action by the Poincaré symmetry group. The time translation element of the symmetry group is generated by the Killing vector $\partial/\partial t$. There exists a natural set of mode solutions, which are eigenfunctions of this Killing vector with eigenvalue $-i\omega$, where $\omega > 0$ [50]. The vacuum state $|0\rangle$ associated with this set of modes, i.e., the state annihilated by the annihilation operators coupled to these eigenfunctions in a mode expansion of the field operator

$$\hat{a}_k |0\rangle = 0, \tag{2.8}$$

is invariant under the Poincaré group.

In a generic curved spacetime we will not have the luxury of Killing vectors with which to define privileged positive frequency modes. Consider a different set of orthonormal modes $\{v_j\}$ that we can expand $\hat{\phi}(x)$ in,

$$\hat{\phi}(x) = \sum_j \left[\hat{b}_j v_j(x) + \hat{b}_j^\dagger v_j^*(x)\right]. \tag{2.9}$$

Upon quantization, the annihilation operator $\hat{b}_j$ associated with the new set of modes defines a different vacuum $|\overline{0}\rangle$

$$\hat{b}_j |\overline{0}\rangle = 0 \tag{2.10}$$

and therefore gives us a different Fock space. Importantly, the two Fock spaces we have selected are generally not unitarily equivalent. Since both sets of solutions provide a complete orthonormal basis, the solution of any given set can be rewritten in terms of a linear combination of the other. We use the notation such that the new basis $\{v_j\}$ may be expanded as

$$v_j = \sum_i (\alpha_{ji} u_i + \beta_{ji} u_i^*). \tag{2.11}$$

The components of the matrices, known as Bogoliubov coefficients, can be read off by using (2.5). They are

$$\alpha_{ij} = (v_i, u_j), \quad \beta_{ij} = -(v_i, u_j^*). \tag{2.12}$$

We can also write $\{u_k\}$ in terms of $\{v_j\}$,

$$u_i = \sum_j (\alpha^*_{ji} v_j - \beta_{ji} v^*_j). \tag{2.13}$$

The transformation between the differing ladder operators is obtained similarly, by equating the two different mode expansions (2.4), (2.9) and using (2.5) again,

$$\begin{aligned} \hat{a}_i &= \sum_j (\alpha_{ji} \hat{b}_j + \beta^*_{ji} \hat{b}^\dagger_j), \\ \hat{b}_j &= \sum_j (\alpha^*_{ji} \hat{a}_i - \beta^*_{ji} \hat{a}^\dagger_i). \end{aligned} \tag{2.14}$$

We can see that the presence of non-zero β_{ji} means that the new positive frequency modes are made of a mixture of old positive frequency and negative frequency modes. As a result, the two Fock spaces built out of the respective sets of modes are inequivalent. This means that the vacuum state $|\overline{0}\rangle$ is not destroyed by $\hat{a}_i$,

$$\hat{a}_i \, |\overline{0}\rangle = \sum_j \beta^*_{ji} \hat{b}_j \, |0\rangle \, . \tag{2.15}$$

Using (2.14), we can see that the expectation value of the number operator $\hat{N}_i = \hat{a}^\dagger_i \hat{a}_i$, associated with the measurement of the number of particles in the u_i-mode, for the vacuum state $|\overline{0}\rangle$ is

$$\langle \overline{0} | \hat{N}_i | \overline{0} \rangle = \sum_j |\beta_{ji}|^2. \tag{2.16}$$

The notion of a particle and of a vacuum state is inextricably tied to the set of mode functions used to decompose the field. This set of mode functions is in turn tied to the coordinate system adapted to the worldline of an observer. Particles are therefore fundamentally an observer-dependent concept. The ambiguity discussed above is therefore not merely technical, but reflects a fundamental conceptual shift in our understanding of particles. Because particle number operators are constructed directly from the chosen mode decomposition, observers associated with different mode sets will, in general, measure different numbers of particles even in what is ostensibly the same quantum state. This ambiguity referring to the worldlines of observers holds even in flat space. As we have stated repeatedly throughout this section, Minkowski spacetime contains a global family of inertial observers, owing to the Poincaré symmetry group of the metric, and all these observers will share a common notion of particle number for the same given state, due to

global time translation symmetry. However, a non-inertial worldline, such as that of an observer undergoing constant acceleration in the same Minkowski inertial vacuum perceives a thermal bath of particles. This is an example of what is known as the Unruh effect [50]. Indeed, what distinguishes Minkowski spacetime from generic curved spacetime is not some unique vacuum (which does not exist, since there can be multiple mode decompositions even in Minkowski space), but the presence of a global timelike Killing vector and a global family of inertial observers invariant under the Poincaré symmetry group. In an arbitrary spacetime where global symmetry and a preferred mode decomposition are absent, freely falling observers will not agree on a vacuum state (i.e., the same state which they would all observe to be free of particles) [397].

This motivates the operational approach to the definition of particles summed up in the maxim that "a particle is what a particle detector measures." We therefore turn to a specific local measurement scheme, known as the Unruh–DeWitt (UDW) particle detector model. This approach will be foundational for the study of RQI presented throughout the remainder of Part I of this thesis. However, to fully characterize the response of any local measurement scheme, we require a precise mathematical tool that captures the field correlations across spacetime. This tool is the two-point correlation function, known as the Wightman function, which encapsulates the vacuum structure and the subtle observer-dependent features of quantum fields in curved backgrounds. Before delving into the specifics of detector models and their implications for relativistic quantum information, we first outline the properties, structure, and significance of Wightman functions.

2.1.2 The Wightman function

The Wightman function for a particular vacuum state $|0\rangle$, is given by

$$W(x,x') = \langle 0|\hat{\phi}(x)\hat{\phi}(x')|0\rangle. \tag{2.17}$$

It satisfies the same equation of motion as the field operator

$$[\Box_x + m^2 + \zeta R(x)]W(x,x') = 0, \tag{2.18}$$

and is a distribution on smooth functions. The principal value prescription is followed when evaluating the action of this distribution on specific functions in the context of detector-based physics, which is discussed in the proceeding section. The Wightman function satisfies

$$W(x,x')^* = W(x',x). \tag{2.19}$$

For a free field, the commutator can be written in terms of the Wightman function as

$$[\hat{\phi}(x), \hat{\phi}(x')] = W(x, x') - W(x', x). \tag{2.20}$$

Taken with (2.19), (2.20) means that it is the imaginary part of the Wightman function that encodes the causal structure of the field theory. Indeed, (2.20) is the Pauli-Jordan function, which vanishes for spacelike separated points, ensuring microcausality. In other words, when $\mathrm{Im}\,[W(x, x')] = 0$, the field cannot propagate influence between the two points x and x'.

The distributional nature of the Wightman function is made apparent by the presence of a small positive constant ϵ, which regulates the singularities. The location of this regulator must be chosen with care to ensure that the spectral condition (that only positive frequency modes are propagated forward in time) is obeyed. The Wightman function sidesteps the ambiguity in the notion of a particle in curved spacetime by providing a direct characterization of field correlations for a given vacuum state.

2.2 Relativistic quantum information

RQI refers to the study of quantum information–theoretic phenomena in the context of quantum field theory on curved backgrounds. It accounts for observer dependence, causal structure, and accommodates the absence of a preferred vacuum state. This framework allows one to ask operationally meaningful questions, such as how localized detectors perceive entanglement, how acceleration or curvature affects quantum correlations, and how information is encoded and transferred in a relativistic setting. Building on the formalism developed in the previous sections, we now turn to a brief introduction to the theoretical and operational tools of RQI, beginning with detector models that couple locally to quantum fields. Especially important to the remainder of this thesis are the notions of entanglement harvesting and magic generation.

2.2.1 Unruh-DeWitt detectors

The fundamentally ambiguous nature of a particles motivates us to adopt an operational definition. This requires the specification of the detector model used to quantify the presence of particles in QFTCS. The UDW [428, 119] detector model is arguably the simplest model of a particle detector. It consists of a two-level localized atom (a qubit) linearly coupled to the real scalar field. The detector's energy eigenbasis consists of two states

we label $|g\rangle$ (the ground state), and $|e\rangle$ (the excited state). The two states are separated by an energy gap Ω. The Hilbert space associated with the UDW detector is identical to that of an ordinary qubit in quantum information and computation, $\mathcal{H} \simeq \mathbb{C}^2$. We define the ground state $|g\rangle$ as having an energy of 0, which means that the free evolution of the detector is governed by the Hamiltonian

$$\hat{H}_D = \Omega \, |e\rangle \langle e| \, . \tag{2.21}$$

The detector is coupled to the real scalar field in a simplified analogy of quantum electrodynamics, namely, the light-dipole moment interaction [399]. Indeed, the UDW detector-scalar field interaction Hamiltonian presented below is known to capture the essence of light-matter interactions when no angular momentum is exchanged [318, 9, 363]. Let λ characterize the strength of the coupling between the detector and the field, which we take to be in the perturbative regime, and let the worldline of the detector, parameterized by its proper time, be denoted by $x_D(\tau)$. Furthermore, in order to prevent divergences, we introduce a smooth switching function $\chi_D(\tau)$ which adiabatically (i.e., smoothly) turns on and off and determines the window of interaction between the detector and field. Then the interaction Hamiltonian (in the interaction picture) is given by [399]

$$\hat{H}_I(\tau) = \lambda \chi_D(\tau)[\hat{\sigma}^+(\tau) + \hat{\sigma}^-(\tau)] \otimes \hat{\phi}(x_D[\tau]), \tag{2.22}$$

where $\hat{\sigma}^+(\tau)$, and $\hat{\sigma}^-(\tau)$ are defined to be the ladder operators,

$$\hat{\sigma}^+(\tau) := e^{i\Omega\tau} \, |e\rangle \langle g| \, , \quad \hat{\sigma}^-(\tau) := e^{-i\Omega\tau} \, |g\rangle \langle e| \, . \tag{2.23}$$

Since we work in the interaction picture, the evolution of the field-detector joint system from the asymptotic past ($\tau \to -\infty$), to the asymptotic future ($\tau \to \infty$), when the state of the detector is measured, is given by the Dyson time-evolution operator

$$\begin{aligned} \hat{U} :=& \mathcal{T}\left[-i \int_{-\infty}^{\infty} \mathrm{d}\tau \hat{H}_I(\tau)\right] \\ =& 1 + (-i) \int_{-\infty}^{\infty} \mathrm{d}\tau \hat{H}_I(\tau) + \frac{(-i)^2}{2!} \int_{-\infty}^{\infty} \mathrm{d}\tau \int_{-\infty}^{\infty} \mathrm{d}\tau' \mathcal{T} \hat{H}_I(\tau) \hat{H}_I(\tau') + \mathcal{O}(\lambda^3), \end{aligned} \tag{2.24}$$

where $\mathcal{T}$ is the time ordering operator defined by

$$\mathcal{T} \hat{H}_I(\tau) \hat{H}_I(\tau') = \begin{cases} \hat{H}_I(\tau) \hat{H}_I(\tau') & \tau > \tau', \\ \hat{H}_I(\tau') \hat{H}_I(\tau) & \tau < \tau'. \end{cases} \tag{2.25}$$

2.2.2 Single detectors, excitation probabilities and transition Rates

If we prepare the field-detector system in the initial state $|\Psi_i\rangle = |g\rangle \otimes |0\rangle$ in the asymptotic past ($\tau \to -\infty$), we may perturbatively calculate its evolution in time to the moment of measurement in the asymptotic future ($\tau \to \infty$) using the Dyson operator (2.24),

$$\begin{aligned} |\Psi_f\rangle =& \hat{U} |\Psi_i\rangle \\ =& |\Psi_i\rangle - i \int_{-\infty}^{\infty} \mathrm{d}\tau \hat{H}_I(\tau) |\Psi_i\rangle - \frac{1}{2} \int_{-\infty}^{\infty} \mathrm{d}\tau \int_{-\infty}^{\infty} \mathrm{d}\tau' \mathcal{T} \hat{H}_I(\tau) \hat{H}_I(\tau') |\Psi_i\rangle + \mathcal{O}(\lambda^3). \end{aligned} \tag{2.26}$$

But the final state of the detector alone is measured by taking the evolved joint-state density matrix $\hat{\rho}_f$ and tracing out the field degrees of freedom. The evolved density matrix is given by

$$\begin{aligned} \hat{\rho}_f =& |\Psi_f\rangle \langle \Psi_f| \\ =& \hat{U} \hat{\rho}_i \hat{U}^\dagger, \end{aligned} \tag{2.27}$$

where $\hat{\rho}_i = |\Psi_i\rangle \langle \Psi_i| = |g\rangle \langle g| \otimes |0\rangle \langle 0|$. In what follows, it is helpful to introduce shorthand notation for the perturbative terms in the Dyson series [176]

$$\hat{U} = 1 + \hat{U}^{(1)} + \hat{U}^{(2)} + \mathcal{O}(\lambda^3), \tag{2.28}$$

where

$$\hat{U}^{(1)} = -i \int_{-\infty}^{\infty} \mathrm{d}\tau \hat{H}_I(\tau), \tag{2.29}$$

and

$$\begin{aligned} \hat{U}^{(2)} =& -\frac{1}{2} \int_{-\infty}^{\infty} \mathrm{d}\tau \int_{-\infty}^{\infty} \mathrm{d}\tau' \mathcal{T} \hat{H}_I(\tau) \hat{H}_I(\tau') \\ =& -\frac{1}{2} \int_{-\infty}^{\infty} \mathrm{d}\tau \int_{-\infty}^{\infty} \mathrm{d}\tau' \left[\theta(\tau - \tau') \hat{H}_I(\tau) \hat{H}_I(\tau') + \theta(\tau' - \tau) \hat{H}_I(\tau') \hat{H}_I(\tau) \right] \\ =& -\int_{-\infty}^{\infty} \mathrm{d}\tau \int_{-\infty}^{\infty} \mathrm{d}\tau' \theta(\tau - \tau') \hat{H}_I(\tau) \hat{H}_I(\tau'). \end{aligned} \tag{2.30}$$

The last line of the above equation was achieved by relabeling the variables in the second term. Tracing out the field degrees of freedom gives the reduced density matrix of the UDW detector

$$\begin{aligned} \hat{\rho}_D =& \mathrm{tr}_\phi \left(\hat{\rho}_f \right) \\ =& \mathrm{tr}_\phi \left(\hat{U} \hat{\rho}_i \hat{U}^\dagger \right) \\ =& |g\rangle \langle g| + \hat{\rho}_D^{(1)} + \hat{\rho}_D^{(2)} + \mathcal{O}(\lambda^3), \end{aligned} \tag{2.31}$$

where $\hat{\rho}_D^{(k)}$ is the correction to the detector's reduced density matrix proportional to λ^k. Grouping the terms together, we see that, up to the quadratic order in λ, these corrections are

$$\begin{aligned}\hat{\rho}_D^{(1)} =& \mathrm{tr}_\phi[\hat{U}^{(1)}\hat{\rho}_i] + \mathrm{tr}_\phi[\hat{\rho}_i\hat{U}^{(1)\dagger}],\\ \hat{\rho}_D^{(2)} =& \mathrm{tr}_\phi[\hat{U}^{(2)}\hat{\rho}_i] + \mathrm{tr}_\phi[\hat{\rho}_i\hat{U}^{(2)\dagger}] + \mathrm{tr}_\phi[\hat{U}^{(1)}\hat{\rho}_i\hat{U}^{(1)\dagger}].\end{aligned} \tag{2.32}$$

Recall that tracing out the field degrees of freedom for a generic operator $\hat{\rho}$ amounts to summing over the expectation values of that operator in a complete basis of the field's Hilbert space

$$\mathrm{tr}_\phi(\hat{\rho}) = \sum_n \langle n|\,\hat{\rho}\,|n\rangle\,. \tag{2.33}$$

Using the definition of the interaction Hamiltonian (2.22), and the trace (2.33), as well as the fact that the vacuum expectation value of the field is zero, $\langle 0|\,\hat{\phi}(x)\,|0\rangle$, it may be shown that $\hat{\rho}^{(1)} = 0$. Indeed, all odd-order corrections vanish $\hat{\rho}^{(2k+1)} = 0$. The three terms that make up $\rho_D^{(2)}$ can be calculated straightforwardly. First,

$$\begin{aligned}\hat{U}^{(2)}\hat{\rho}_i = -\lambda^2 \int_{-\infty}^{\infty}\mathrm{d}\tau \int_{-\infty}^{\infty}\mathrm{d}\tau' \theta(\tau-\tau')\chi(\tau)\chi(\tau')e^{-i\Omega(\tau-\tau')}\\ \times |g\rangle\langle g| \otimes \hat{\phi}(x_D[\tau])\hat{\phi}(x_D[\tau'])\,|0\rangle\langle 0|\,.\end{aligned} \tag{2.34}$$

Now take the trace

$$\begin{aligned}\mathrm{tr}_\phi[\hat{U}^{(2)}\hat{\rho}_i] = -\lambda^2 \int_{-\infty}^{\infty}\mathrm{d}\tau \int_{-\infty}^{\infty}\mathrm{d}\tau' \theta(\tau-\tau')\chi(\tau)\chi(\tau')e^{-i\Omega(\tau-\tau')}\\ \times |g\rangle\langle g| \sum_n \langle n|\,\hat{\phi}(x_D[\tau])\hat{\phi}(x_D[\tau'])\,|0\rangle\langle 0|n\rangle\,.\end{aligned} \tag{2.35}$$

Evaluating the trace sum gives

$$\begin{aligned}\mathrm{tr}_\phi[\hat{U}^{(2)}\hat{\rho}_i] = -\lambda^2 \int_{-\infty}^{\infty}\mathrm{d}\tau \int_{-\infty}^{\infty}\mathrm{d}\tau' \theta(\tau-\tau')\chi(\tau)\chi(\tau')e^{-i\Omega(\tau-\tau')}\\ \times W(x_D[\tau],x_D[\tau'])\,|g\rangle\langle g|\,,\end{aligned} \tag{2.36}$$

where $W(x_D[\tau],x_D[\tau']) = \langle 0|\,\hat{\phi}[x_D(\tau)]\hat{\phi}[x_D(\tau')]\,|0\rangle$ is the Wightman function pulled back onto the worldline of the detector. We can similarly calculate $\mathrm{tr}_\phi[\hat{\rho}_i\hat{U}^{(2)\dagger}]$,

$$\begin{aligned}\mathrm{tr}_\phi[\hat{\rho}_i\hat{U}^{(2)\dagger}] = -\lambda^2 \int_{-\infty}^{\infty}\mathrm{d}\tau \int_{-\infty}^{\infty}\mathrm{d}\tau' \theta(\tau'-\tau)\chi(\tau)\chi(\tau')e^{-i\Omega(\tau-\tau')}\\ \times W(x_D[\tau],x_D[\tau'])\,|g\rangle\langle g|\,.\end{aligned} \tag{2.37}$$

The sum of the two terms we have calculated so far is

$$\begin{aligned}\mathrm{tr}_\phi[\hat{U}^{(2)}\hat{\rho}_i] + \mathrm{tr}_\phi[\hat{\rho}_i\hat{U}^{(2)\dagger}] = -\lambda^2 \int_{-\infty}^{\infty} \mathrm{d}\tau \int_{-\infty}^{\infty} \mathrm{d}\tau' \chi(\tau)\chi(\tau') e^{-i\Omega(\tau-\tau')} \\ \times W(x_D[\tau], x_D[\tau']) \left|g\right\rangle \left\langle g\right| .\end{aligned} \tag{2.38}$$

To calculate the remaining term, we start with the operator that is being traced over

$$\begin{aligned}\hat{U}^{(1)}\hat{\rho}_i\hat{U}^{(1)\dagger} = \lambda^2 \int_{-\infty}^{\infty} \mathrm{d}\tau \int_{-\infty}^{\infty} \mathrm{d}\tau' \chi(\tau)\chi(\tau') e^{-i\Omega(\tau-\tau')} \\ \times \left|e\right\rangle \left\langle e\right| \otimes \hat{\phi}(x_D[\tau']) \left|0\right\rangle \left\langle 0\right| \hat{\phi}(x_D[\tau]).\end{aligned} \tag{2.39}$$

Then the trace is

$$\begin{aligned}\mathrm{tr}_\phi[\hat{U}^{(1)}\hat{\rho}_i\hat{U}^{(1)\dagger}] = \lambda^2 \int_{-\infty}^{\infty} \mathrm{d}\tau \int_{-\infty}^{\infty} \mathrm{d}\tau' \chi(\tau)\chi(\tau') e^{-i\Omega(\tau-\tau')} \\ \times \left|e\right\rangle \left\langle e\right| \sum_n \left\langle n\right| \hat{\phi}(x_D[\tau']) \left|0\right\rangle \left\langle 0\right| \hat{\phi}(x_D[\tau]) \left|n\right\rangle .\end{aligned} \tag{2.40}$$

It may be shown that the final term in the product that makes up the integrand is the Wightman function,

$$\begin{aligned}\sum_n \left\langle n\right| \hat{\phi}(x_D[\tau']) \left|0\right\rangle \left\langle 0\right| \hat{\phi}(x_D[\tau]) \left|n\right\rangle &= \sum_n \left\langle 0\right| \hat{\phi}(x_D[\tau]) \left|n\right\rangle \left\langle n\right| \hat{\phi}(x_D[\tau']) \left|0\right\rangle \\ &= \left\langle 0\right| \hat{\phi}(x_D[\tau])\hat{\phi}(x_D[\tau']) \left|0\right\rangle \\ &= W(x_D[\tau], x_D[\tau']),\end{aligned} \tag{2.41}$$

so

$$\mathrm{tr}_\phi[\hat{U}^{(1)}\hat{\rho}_i\hat{U}^{(1)\dagger}] = \lambda^2 \int_{-\infty}^{\infty} \mathrm{d}\tau \int_{-\infty}^{\infty} \mathrm{d}\tau' \chi(\tau)\chi(\tau') e^{-i\Omega(\tau-\tau')} W(x_D[\tau], x_D[\tau']) \left|e\right\rangle \left\langle e\right| . \tag{2.42}$$

This means, that up to quadratic order in λ, the final reduced density matrix is given by

$$\hat{\rho}_D = (1-P) \left|g\right\rangle \left\langle g\right| + P \left|e\right\rangle \left\langle e\right| + \mathcal{O}(\lambda^4), \tag{2.43}$$

where P is the excitation probability of the detector, given by

$$P_D := \lambda^2 \int_{-\infty}^{\infty} \mathrm{d}\tau \int_{-\infty}^{\infty} \mathrm{d}\tau' \chi(\tau)\chi(\tau') e^{-i\Omega(\tau-\tau')} W(x_D[\tau], x_D[\tau']). \tag{2.44}$$

We may write the reduced density matrix in an explicit form as

$$\hat{\rho}_D = \begin{pmatrix} 1-P_D & 0 \\ 0 & P_D \end{pmatrix} + \mathcal{O}(\lambda^4), \tag{2.45}$$

in the basis $\{|g\rangle, |e\rangle\}$. Recall that the Wightman function is a distribution on smooth functions. When evaluating the excitation probability, like any other density matrix element in what follows, the principal value prescription must be followed.

We may define a time-dependent quantity for the single detector as well, in the form of the transition rate. The probability of the detector being excited when measured at its proper time τ is given by

$$P_D(\tau) = \lambda^2 \int_{-\infty}^{\tau} \mathrm{d}t \int_{-\infty}^{\tau} \mathrm{d}t' \chi(t)\chi(t') e^{-i\Omega(t-t')} W(x_D[t], x_D[t']). \tag{2.46}$$

Then, the transition rate of the detector is defined to be the derivative of this probability with respect to the detector's proper time

$$\dot{P}_D(\tau) := \frac{\mathrm{d}}{\mathrm{d}\tau} P_D(\tau). \tag{2.47}$$

Schlicht [386] reformulates (2.46) in terms of the variables $u = t$ and $s = t - t'$ for $t > t'$ and $u = t'$ and $s = t' - t$ for $t < t'$. After this change of variables, the time dependent excitation probability may be written as

$$\begin{aligned} P_D(\tau) = \lambda^2 \int_{-\infty}^{\tau} \mathrm{d}u \int_0^{\infty} \mathrm{d}s \chi(u)\chi(u-s) \Big[& e^{-i\Omega s} W(x_D[u], x_D[u-s]) \\ & + e^{i\Omega s} W(x_D[u-s], x_D[u]) \Big]. \end{aligned} \tag{2.48}$$

The sum in the brackets is that of complex conjugates, which means we may rewrite (2.48) as

$$P_D(\tau) = 2\lambda^2 \int_{-\infty}^{\tau} \mathrm{d}u \int_0^{\infty} \mathrm{d}s \chi(u)\chi(u-s) \mathrm{Re}\Big[e^{-i\Omega s} W(x_D[u], x_D[u-s]) \Big]. \tag{2.49}$$

The transition rate (2.47) may then be written in terms of a single integral

$$\dot{P}_D(\tau) = 2\lambda^2 \int_0^{\infty} \mathrm{d}s \chi(\tau)\chi(\tau-s) \mathrm{Re}\Big[e^{-i\Omega s} W(x_D[\tau], x_D[\tau-s]) \Big]. \tag{2.50}$$

Although the switching function $\chi(\tau)$ is generally smooth, when evaluating transition rates (as in chapter 4), it is convenient to consider the limit where it approaches a sharp characteristic function (the sharp switching limit), which is non-zero only over an interval

$$\chi(t) = \begin{cases} 1 & t \in [\tau_0, \tau], \\ 0 & t \notin [\tau_0, \tau]. \end{cases} \tag{2.51}$$

Physically, the sharp switching limit corresponds to the coupling being abruptly "switched off" at proper time τ, and the state of the detector being measured. Louko and Satz [294] evaluated the transition rate (2.50) in this limit, and found that the result was nontrivial. The Wightman function, being a distribution, is represented by an $i\epsilon$ regularized function. Crucially, the $\epsilon \to 0^+$ limit does not commute with the sharp switching limit. The ϵ limit must be evaluated first, while the sharp switching limit comes second. The sharp switching limit itself is implemented by evaluating the integral with a switching function that approaches the characteristic function in some limit. The result is

$$\dot{P}_D(\tau) = \lambda^2 \left(\frac{1}{4} + 2 \int_0^{\Delta\tau} \mathrm{d}s \, \mathrm{Re}\Big[e^{-i\Omega s} W(x_D[\tau], x_D[\tau - s]) \Big] \right). \tag{2.52}$$

Note the presence of the additive constant $\frac{1}{4}$.

2.2.3 Multiple detectors and entanglement harvesting

A central insight of algebraic quantum field theory, made by Summers and Werner [410, 411], is that the vacuum state of a free is an entangled state, and that the correlations of vacuum fluctuations at different spacetime points violate Bell-like inequalities, even when those points are spacelike separated. Operationally speaking, RQI provides a framework for measuring the entanglement structure of fields in arbitrary spacetimes, by probing the correlations of these vacuum fluctuations with multiple UDW detectors. In the simplest version of this setup, two UDW detectors on two distinct worldlines are each locally coupled to the field by the interaction Hamiltonian (2.22). The detectors and field are generally taken to be initially separable (i.e., not entangled) and in some suitable vacuum state respectively. At some suitably late time when the interaction is over (as dictated by the switching functions), the final reduced density matrix of the two UDW detectors may show that the two detectors have become entangled. This may be the case even when the worldlines of the two detectors are causally disconnected (i.e., they were never in causal contact throughout their entire histories).

This phenomenon is known as entanglement harvesting [399]. The entanglement between the detectors emerges through their local coupling to the field, and (provided the detectors were causally disconnected throughout their entire history) is a direct reflection of the entanglement of the field's vacuum state between the spacetime regions along the respective wordlines of the detectors. If the detectors were in causal contact during their history, then the entanglement measured in the final reduced state may be due to an interaction between the two detectors through the field [425].

The entanglement may be quantified using measures taken from ordinary quantum information theory. These measures in turn, depend on the elements of the final reduced density matrix representing the joint state of the two UDW detectors after the field degrees of freedom have been traced out. This density matrix may be calculated by means of a (conceptually) simple extension of the case of a single detector. Labeling each detector, we begin with the initial state of the detectors-field system

$$|\Psi_i\rangle = |g_A\rangle \otimes |g_B\rangle \otimes |0\rangle \,. \tag{2.53}$$

Since there are two detectors that are each locally coupled to the field, the evolved state is given by

$$|\Psi_f\rangle = \hat{U} \, |\Psi_i\rangle \,, \tag{2.54}$$

where the Dyson time evolution operator is

$$\hat{U} = \mathcal{T} \exp\left[-i \int_{-\infty}^{\infty} \mathrm{d}t \hat{H}_I(t)\right], \tag{2.55}$$

and the interaction Hamiltonian is now given by

$$\hat{H}_I(t) = \sum_{D\in\{A,B\}} \frac{\mathrm{d}\tau_D}{\mathrm{d}t} \hat{H}_D(\tau_D(t)), \tag{2.56}$$

where $\hat{H}_D(\tau_D(t))$ is given by (2.22). We are evolving the state forward in some appropriate coordinate time t, associated with the timelike Killing vector field with respect to which the positive frequency modes (and therefore the vacuum state of the field $|0\rangle$) are defined. The time ordering is being done with respect to this time coordinate. The reduced density matrix of the detectors may be calculated along the same lines as for the single detector, with contributions being grouped perturbatively. Before proceeding with the calculation, it is helpful to perform a quick analysis that yields the form of the reduced density matrix. The Dyson time evolution operator may be expanded perturbatively as

$$\hat{U} = \sum_n \hat{U}^{(n)}, \tag{2.57}$$

where

$$\hat{U}^{(n)} = \frac{(-i)^n}{n!} \int_{-\infty}^{\infty} \mathrm{d}t_1 \cdots \int_{-\infty}^{\infty} \mathrm{d}t_n \mathcal{T} \hat{H}(t_1) \cdots \hat{H}(t_n). \tag{2.58}$$

The reduced density matrix we have after tracing out the field degrees of freedom may then be written as

$$\hat{\rho}_{AB} = \mathrm{tr}_\phi(|\Psi_f\rangle\langle\Psi_f|) = \sum_{m,n} \mathrm{tr}_\phi(\hat{U}^{(m)}|\Psi_i\rangle\langle\Psi_i|\hat{U}^{(n)\dagger}). \tag{2.59}$$

The term $\hat{U}^{(n)}|\Psi_i\rangle$ applies the field operator $\hat{\phi}$ onto the vacuum n times. The partial trace of $\hat{U}^{(m)}|\Psi_i\rangle\langle\Psi_i|\hat{U}^{(n)\dagger}$ over the field will then involve an integral over the $(n+m)$-point Wightman function. Since odd n-point correlations functions vanish, this means that the only terms that contribute after the partial trace are those where m and n have the same parity [198]. Furthermore, for odd n, the state $\hat{U}^{(n)}|\Psi_i\rangle$ has one detector excited while the other remains in its ground state, while for even n, both detectors are either excited or in the ground state. In conjunction these two observations mean that, to all orders in perturbation theory, ρ_{AB} takes the form

$$\begin{aligned}\hat{\rho}_{AB} =& \mathrm{tr}_\phi(|\Psi_f\rangle\langle\Psi_f|) \\ =& \begin{pmatrix} \rho_{11} & 0 & 0 & \rho_{14} \\ 0 & \rho_{22} & \rho_{23} & 0 \\ 0 & \rho_{23}^* & \rho_{33} & 0 \\ \rho_{14}^* & 0 & 0 & \rho_{44} \end{pmatrix},\end{aligned} \tag{2.60}$$

where the matrix is expressed in the basis $\{|g_A\rangle\otimes|g_B\rangle, |g_A\rangle\otimes|e_B\rangle, |e_A\rangle\otimes|g_B\rangle, |e_A\rangle\otimes|e_B\rangle\}$. Upon calculation to the lowest contributing order, we find

$$\begin{aligned}\hat{\rho}_{AB} =& \mathrm{tr}_\phi(|\Psi_f\rangle\langle\Psi_f|) \\ =& \begin{pmatrix} 1-P_A-P_B & 0 & 0 & X \\ 0 & P_B & C & 0 \\ 0 & C^* & P_A & 0 \\ X^* & 0 & 0 & 0 \end{pmatrix} + \mathcal{O}(\lambda^4).\end{aligned} \tag{2.61}$$

The excitation probabilities of each individual detector are independent, and given by (2.44), while

$$C := \lambda^2 \int_{-\infty}^{\infty} \mathrm{d}\tau_A \int_{-\infty}^{\infty} \mathrm{d}\tau_B \chi_A(\tau_A)\chi_B(\tau_B) e^{-i(\Omega_A\tau_A - \Omega_B\tau_B)} W(x_A[\tau_A], x_B[\tau_B]), \tag{2.62}$$

and

$$\begin{aligned}X := -\lambda^2 \int_{-\infty}^{\infty} \mathrm{d}\tau_A \int_{-\infty}^{\infty} \mathrm{d}\tau_B \chi_A(\tau_A)\chi_B(\tau_B) e^{-i(\Omega_A\tau_A + \Omega_B\tau_B)} \\ \times \Big[\theta(t(\tau_A) - t(\tau_B)) W(x_A[\tau_A], x_B[\tau_B]) \\ + \theta(t(\tau_B) - t(\tau_A)) W(x_B[\tau_B], x_A[\tau_A])\Big].\end{aligned} \tag{2.63}$$

We have written the integrals such that they are over the detectors' proper times, and not with respect to the coordinate time used to define the vacuum. Higher order terms would involve integrals over n-point correlation functions. Note that the density matrix element ρ_{44} is non-zero at higher perturbative order. It is given by [399]

$$\rho_{44} = |X|^2 + |C|^2 + P_A P_B + \mathcal{O}(\lambda^6). \tag{2.64}$$

2.2.4 Entanglement in Quantum Field Theory: Traditional Approaches and Their Limitations

In quantum field theory (QFT), entanglement between degrees of freedom in different spacetime regions is most commonly quantified using entanglement entropy. Given a quantum field in a global pure state, typically the vacuum, and a spatial subregion A on a Cauchy surface, one formally defines a reduced density matrix ρ_A by tracing out the field degrees of freedom in the complement $\bar{A}$. The entanglement entropy is then given by the von Neumann entropy $S_A = -\mathrm{tr}(\rho_A \log \rho_A)$. However, this construction relies on several assumptions that are problematic in a continuum QFT. First, the total Hilbert space does not rigorously decompose into a tensor product $\mathcal{H}_A \otimes \mathcal{H}_{\bar{A}}$ due to the field's infinite number of degrees of freedom and the presence of correlations at arbitrarily short distances across the boundary ∂A. As a result, the entanglement entropy is divergent, with a leading divergence proportional to the area of the boundary and dependent on an arbitrary ultraviolet cutoff [406]. While practical calculations are possible in flat or highly symmetric spacetimes, the methods involved in such successful calculations quickly become intractable in generic backgrounds.

More formal approaches based on algebraic QFT define entanglement by working with the algebra of observables directly, and treating states as positive linear functionals over operator algebras. Entanglement is quantified through structures like modular operators and relative entropy between local algebras [447]. These constructions avoid ultraviolet divergences and do not rely on a Hilbert space factorization, but they are abstract, computationally inaccessible, and often require knowledge of the so-called modular Hamiltonian, which is only known in very special cases (e.g., Rindler wedges). Furthermore, these definitions are generally non-operational, and do not correspond to physical observables that can be extracted from localized measurements. In curved spacetime, these difficulties are exacerbated by the lack of a preferred vacuum state or global time slicing, making traditional entropy-based notions of entanglement ambiguous and practically unusable.

2.2.5 Entanglement measures

The key advantage of the RQI approach lies in its formulation in terms of qubits (or more generally, discrete-level systems), which enables a direct extraction of entanglement using standard qubit measures, without recourse to abstract regulator-sensitive constructions like the field-theoretic entropy or modular operators. Two such measures used in this thesis are negativity and concurrence. Before introducing these measures, we include a short discussion on entanglement below.

The state of the two detectors, which is an element of the joint Hilbert space, a tensor product of the individual detector Hilbert spaces, $\mathcal{H}_{AB} = \mathcal{H}_A \otimes \mathcal{H}_B$, is said to be entangled if it cannot be written as a tensor product of individual states $|\psi\rangle_A \in \mathcal{H}_A$ and $|\phi\rangle_B \in \mathcal{H}_B$. In general, after tracing out the field degrees of freedom, the reduced state of the two detectors $\hat{\rho}_{AB}$ will be a mixed state, which must be expressed in the language of density matrices. The state $\hat{\rho}_{AB} \in \mathcal{S}(\mathcal{H}_A \otimes \mathcal{H}_B)$ (where $\mathcal{S}(\mathcal{H})$ is the space of states on a Hilbert space $\mathcal{H}$) is factorized if it is a tensor product $\hat{\rho}_{AB} = \rho_A \otimes \hat{\rho}_B$. Then $\hat{\rho}_{AB}$ is said to be separable (i.e., not entangled) if it may be written as a convex combination of factorized states [399]. This means that $\hat{\rho}_{AB}$ is not entangled if it is possible to write it as

$$\hat{\rho}_{AB} = \sum_i p_i \hat{\rho}_A^i \otimes \hat{\rho}_B^i, \tag{2.65}$$

where $p_i > 0$ and $\sum_i p_i = 1$. An entanglement measure $E(\hat{\rho}_{AB})$ of a given state $\hat{\rho}_{AB} \in \mathcal{S}(\mathcal{U}_A \otimes \mathcal{H}_B)$ is defined to be a map

$$E : \mathcal{S}(\mathcal{H}_A \otimes \mathcal{H}_B) \to \mathbb{R}^+, \tag{2.66}$$

with the properties that $E(\hat{\rho}_{AB}) = 0$ if $\hat{\rho}_{AB}$ is separable, and that $E(\rho_{AB})$ does not increase on average under local operations on $\mathcal{H}_A$ and $\mathcal{H}_B$, or classical communication between the observers associated with those respective Hilbert spaces [71].

The partial transpose of $\hat{\rho}_{AB}$ with respect to $\mathcal{H}_A$ is defined as

$$\hat{\rho}_{AB}^{\Gamma_A} := [T_A \otimes \mathcal{I}_B](\rho_{AB}), \tag{2.67}$$

where $t_A : \mathcal{S}(\mathcal{H}_A) \to \mathcal{S}(\mathcal{H}_A)$ is the transposition map. The negativity of $\hat{\rho}_{AB}$ [431] is then defined to be

$$\mathcal{N}(\hat{\rho}_{AB}) := \frac{\|\rho_{AB}^{\Gamma_A}\| - 1}{2} = \sum_{\lambda_i < 0} |\lambda_i|. \tag{2.68}$$

Here $\|\cdot\|$ is the trace norm (defined such that $\|A\| = \mathrm{tr}(\sqrt{A^*A})$, and λ_i are the eigenvalues of $\hat{\rho}_{AB}^{\Gamma_A}$ (the sum being over those which are negative). This is an effective measure of entanglement, because of the Peres-Horodecki criterion, which states that $\hat{\rho}_{AB}$ is entangled if it does not remain positive under partial transpositions with respect to either $\mathcal{H}_A$ or $\mathcal{H}_B$[399]. This is a necessary and sufficient condition for entanglement provided that $\mathcal{H}_A \simeq \mathbb{C}^2$ and $\mathcal{H}_B \in \{\mathbb{C}^2, \mathbb{C}^3\}$ [215, 357]. For our density matrix, of the form (2.60), $\hat{\rho}_{AB}^{\Gamma_A}$ is given by

$$\hat{\rho}_{AB}^{\Gamma_A} = \begin{pmatrix} \rho_{11} & 0 & 0 & \rho_{23}^* \\ 0 & \rho_{22} & \rho_{14}^* & 0 \\ 0 & \rho_{14} & \rho_{33} & 0 \\ \rho_{23} & 0 & 0 & \rho_{44} \end{pmatrix}, \tag{2.69}$$

which has the eigenvalues

$$\begin{aligned}
\lambda_1 =& \frac{\rho_{22}+\rho_{33}}{2} - \sqrt{\left(\frac{\rho_{22}-\rho_{33}}{2}\right)^2 + |\rho_{14}|^2} \\
=& \frac{P_A+P_B}{2} - \sqrt{\left(\frac{P_A-P_B}{2}\right)^2 + |X|^2} + \mathcal{O}(\lambda^4), \\
\lambda_2 =& \frac{\rho_{22}+\rho_{33}}{2} + \sqrt{\left(\frac{\rho_{22}-\rho_{33}}{2}\right)^2 + |\rho_{14}|^2} \\
=& \frac{P_A+P_B}{2} + \sqrt{\left(\frac{P_A-P_B}{2}\right)^2 + |X|^2} + \mathcal{O}(\lambda^4), \\
\lambda_3 =& \frac{\rho_{11}+\rho_{44}}{2} - \sqrt{\left(\frac{\rho_{11}-\rho_{44}}{2}\right)^2 + |\rho_{23}|^2} \\
=& |X|^2 + P_A P_B + \mathcal{O}(\lambda^6), \\
\lambda_4 =& \frac{\rho_{11}+\rho_{44}}{2} + \sqrt{\left(\frac{\rho_{11}-\rho_{44}}{2}\right)^2 + |\rho_{23}|^2} \\
=& 1 - P_A - P_B + \mathcal{O}(\lambda^4).
\end{aligned} \tag{2.70}$$

Of these eigenvalues, only λ_1 can be negative, which means that the negativity of ρ_{AB} is given by

$$\mathcal{N}(\rho_{AB}) = \max\left[0, \sqrt{\left(\frac{P_A-P_B}{2}\right)^2 + |X|^2} - \frac{P_A+P_B}{2}\right]. \tag{2.71}$$

The Peres-Horodecki criterion for entanglement for our specific system maps on to the statement that we must have $|X|^2 > P_A P_B$. While the negativity is straightforward to

compute, and an entanglement monotone, since it does not increase under local operations and classical communication, it does not have an operational interpretation [399]. This motivates us to use the concurrence, which is related to the entanglement of formation.

If we consider a global pure state represented by the state vector $|\psi\rangle \in \mathcal{H}_A \otimes \mathcal{H}_B$, then the entanglement entropy of subsystem A is defined to be the von Neumann entropy of the reduced density matrix $\hat{\rho}_A = \mathrm{tr}_B(|\psi\rangle \langle\psi|)$,

$$S_A = -\mathrm{tr}\ \hat{\rho}_A \log_2 \hat{\rho}_A. \tag{2.72}$$

Since the global state is pure, the entanglement entropy is a good measure of entanglement between the subsystems A, and B. Note that (again, for the bipartite pure state), $S_A = S_B$. For global mixed states however, the entanglement entropy is no longer a suitable entanglement measure, since it may be nonzero for separable states [71]. A suitable generalization to mixed states is the entanglement of formation. This is defined as the minimum (over all possible decompositions) of the weighted sum of the entanglement entropies of those pure states that may be combined to form a given mixed state $\hat{\rho}_{AB}$ [43]. We may write this as

$$E_f(\hat{\rho}_{AB}) := \min \sum_i p_i E(\psi_i), \tag{2.73}$$

where the minimization is over all possible pure state decompositions of ρ_{AB}, and $E(\psi_i)$ is the von Neumann entropy of either of the two subsystems A, and B of the global pure state $|\psi_i\rangle \langle\psi_i|$ in the decomposition (i.e., the entanglement entropy of each of the pure states in the sum). The operational interpretation of the entanglement of formation is that it is the number of Bell states required to prepare the state $\hat{\rho}_{AB}$ via local operations and classical communication [43]. For two qubits, the solution to the minimization (2.73) is given by [448]

$$E_f(\hat{\rho}_{AB}) = h\left(\frac{1+\sqrt{1-\mathcal{C}(\hat{\rho}_{AB})^2}}{2}\right), \tag{2.74}$$

where $h(x) := -x\log_2(x) - (1-x)\log_2(1-x)$, and $\mathcal{C}(\hat{\rho}_{AB})$ is the concurrence,

$$\mathcal{C}(\hat{\rho}_{AB}) := \max[0, w_1 - w_2 - w_3 - w_4], \tag{2.75}$$

where w_i are the square roots of the ordered eigenvalues ($w_1 \geq w_2 \geq w_3 \geq w_4$) of the matrix

$$\hat{\rho}_{AB}\left[(\hat{\sigma}_y \otimes \hat{\sigma}_y)\hat{\rho}^*(\hat{\sigma}_y \otimes \hat{\sigma}_y)\right], \tag{2.76}$$

where $\hat{\sigma}_y$ is the Pauli y-matrix. The entanglement of formation is a monotonically increasing function of the concurrence, and ranges from 0 to 1 as the concurrence itself goes from 0 to 1. This means that the concurrence is a genuine entanglement measure [448]. For our density matrix (2.60), the (unordered) square roots of the eigenvalues of (2.76) are given by

$$\begin{aligned} w_1 =& \sqrt{\rho_{11}\rho_{44}} + |\rho_{14}| \\ =& \sqrt{|X|^2 + |C|^2 + P_A P_B} + |X| + \mathcal{O}(\lambda^4), \\ w_2 =& \sqrt{\rho_{22}\rho_{33}} + |\rho_{23}| \\ =& \sqrt{P_A P_B} + |C| + \mathcal{O}(\lambda^4), \\ w_3 =& \sqrt{\rho_{11}\rho_{44}} - |\rho_{14}| \\ =& \sqrt{|X|^2 + |C|^2 + P_A P_B} - |X| + \mathcal{O}(\lambda^4), \\ w_4 =& \sqrt{\rho_{22}\rho_{33}} - |\rho_{23}| \\ =& \sqrt{P_A P_B} - |C| + \mathcal{O}(\lambda^4). \end{aligned} \tag{2.77}$$

Recall that, owing to the Peres-Horodecki criterion for entanglement, for $\hat{\rho}_{AB}$ to be entangled we must have $|X| > \sqrt{P_A P_B}$. This means that the largest eigenvalue in (2.77) is w_1. Using (2.75), the concurrence of our specific reduced density matrix is given by

$$\mathcal{C}(\hat{\rho}_{AB}) = 2\max[0, |X| - \sqrt{P_A P_B}] + \mathcal{O}(\lambda^4). \tag{2.78}$$

In the special case where the two detectors have equal excitation probabilities $P_A = P_B = P$, the concurrence of $\hat{\rho}_{AB}$ is given by twice its negativity

$$\begin{aligned} \mathcal{C}(\hat{\rho}_{AB}) =& 2\mathcal{N}(\hat{\rho}_{AB}) \\ =& 2\max[0, |X| - P] + \mathcal{O}(\lambda^4). \end{aligned} \tag{2.79}$$

The form (2.78) makes it clear that the detectors are entangled if the coherence term $|X|$ dominates the local noise terms $\sqrt{P_A P_B}$ [198].

2.2.6 Generating magic

The main obstacle to practical quantum computers is the presence of random noise in the real world. Fault-tolerant schemes of quantum computation work around this presence by encoding logical qubits into highly entangled states of multiple physical qubits, and

then using quantum error correction algorithms, which work without directly measuring or disturbing the encoded information. The fault tolerance here means that each computational step (including the error correction) is performed in such a way as to prevent errors from cascading. Given an error rate for the physical computation, the logical encodings may be applied to create arbitrarily small effective error rates for the logically encoded computation. Fault tolerant quantum computation relies heavily on transversal unitary gates, defined to be those gates that can be encoded in a bitwise fashion so that error probabilities do not grow out of control of the error-correcting code [337, 430].

Many fault-tolerant schemes rely on the stabilizer formalism. The stabilizer codes privilege certain states, operators, and measurements that have fault tolerant implementations [430]. The stabilizer formalism for qubits is defined more precisely as follows. Consider the Pauli group G_n on n-qubits, defined to be the group consisting of all n-fold tensor products of Pauli matrices, together with multiplicative factors of $\pm 1, \pm i$ [337]. A stabilizer S, is a subgroup of G_n associated with a vector space V_S, that is the set of n-qubit states that are fixed (i.e., unchanged) by every element of S. In order for V_S to be non-trivial (i.e., contain more than just $|\psi\rangle = 0$), S must not contain the operator $-\mathcal{I}$. A non-stabilizer/magic state is defined to be a state that lies outside the convex hull of the stabilizer states, i.e., a state that cannot be constructed as a probabilistic mixture of stabilizer states [430].

The Clifford group is defined as the group of unitary operators that map the Pauli group to itself under conjugation [61]. The set of operations in the stabilizer formalism are: the preparation of a qubit in the ground state $|g\rangle$, the application of unitary operators from the Clifford group, and the measurement of an eigenvalue of a Pauli operator on a single qubit. These operations are not sufficient for universal quantum computation (the ability of a quantum computational model to approximate any unitary transformation on a state to arbitrary accuracy using a finite set of gates and operations). The fault tolerant operations of the stabilizer formalism not only fail to be universal, but may be efficiently simulated by a classical probabilistic computer, according to the Gottesman-Knill theorem [337, 430]. Therefore, in order to achieve universal quantum computation and quantum advantage, the stabilizer operations must be supplemented with some other fault-tolerant resource.

The magic state model of quantum computation overcomes this through the use of an ancillary system in some non-stabilizer state. Non-stabilizer/magic resource states are consumed using stabilizer operations, in order to implement non-stabilizer unitary gates. This promotes ordinary staibilizer computation to a universal quantum computation [430]. These raw resource states are necessarily created by a process outside of the stabilizer formalism, which makes them subject to physical error rates, and are therefore usually highly mixed, and not useful for the implementation of non-stabilizer gates. This problem

is solved by distilling a large number of such raw, mixed resource states via stabilizer operations into a small number of pure resource states, in a process called 'magic state distillation' [430]. Magic may be referred to as the resource that describes the ability of a quantum system to perform tasks that cannot be efficiently simulated classically [338]. A generalization of the magic state model to higher-level qudit systems (e.g., three-level qutrits instead of two-level qubits) is possible, via the use of generalized Pauli (Heisenberg-Weyl) matrices [430]. This generalization is covered briefly below.

We may define the generalized Pauli operators for prime dimension as follows. Let d be some prime number. Then, the shift and clock operators are defined as

$$\begin{aligned} \hat{X}\left|j\right\rangle =& \left|j+1 \mod d\right\rangle, \\ \hat{Z}\left|j\right\rangle =& \omega^{j}\left|j\right\rangle, \quad \omega = \exp\left(\frac{2\pi i}{d}\right). \end{aligned} \tag{2.80}$$

These generate the Heisenberg-Weyl matrices, in prime dimensions

$$\hat{T}_{(a_1,a_2)} = \begin{cases} i^{a_1 a_2}\hat{Z}^{a_1}\hat{X}^{a_2} & (a_1,a_2)\in\mathbb{Z}_2\times\mathbb{Z}_2, \quad d=2, \\ \omega^{-\frac{a_1 a_2}{2}}\hat{Z}^{a_1}\hat{X}^{a_2} & (a_1,a_2)\in\mathbb{Z}_d\times\mathbb{Z}_d, \quad d>2, \end{cases} \tag{2.81}$$

where $\mathbb{Z}_d$ are the integers modulo d [430]. A composite system with the tensor product Hilbert space $\mathcal{H}_a\otimes\mathcal{H}_b\otimes\cdots\otimes\mathcal{H}_u$, the Heisenberg-Weyl operators are defined as

$$\hat{T}_{(a_1,a_2)\oplus(b_1,b_2)\oplus\cdots\oplus(u_1,u_2)} = \hat{T}_{(a_1,a_2)}\otimes\hat{T}_{(b_1,b_2)}\otimes\cdots\otimes\hat{T}_{(u_1,u_2)}. \tag{2.82}$$

The Clifford group for dimension d is the set of all Clifford operators $\mathcal{C}_d$, which are defined as the unitary operators that, up to a phase, map the Heisenberg-Weyl operators to themselves under conjugation. Then the pure stabilizer states of dimension d are defined to be those states that can be constructed out of the ground state $\left|0_D\right\rangle$ by the action of a Clifford operator,

$$\{S_i\} = \{\hat{U}\left|0_D\right\rangle : \hat{U}\in\mathcal{C}_d\}, \tag{2.83}$$

while the full set of stabilizer states is the convex hull of these pure stabilizer states (i.e., the set of mixed states that can be constructed out of the pure stabilizer states). Stabilizer operations are defined as any combination of computational basis preparation, computational basis measurement, and action by Clifford operators [430].

To quantify magic, we must first review discrete Wigner functions. These are defined as the discrete analogues to the usual infinite-dimensional Wigner functions, which

are themselves quasi-probability distributions used to represent quantum states in phase space. In any representation, some quantum states and measurements will be mapped to distributions with negative values, hence the Wigner functions being quasi-probability distributions [430, 338]. The discrete Wigner representation, which is defined for quantum systems with an odd-dimensional Hilbert space has the property that stabilizer operations can be represented non-negatively, which means that it may be interpreted as a classical probability model for the stabilizer sub-theory. Magic states will then be associated with negativity of the discrete Wigner function.

The discrete Wigner representation of a state described by the density matrix $\hat{\rho} \in L(\mathbb{C}^{d^n})$ is a quasi-probability distribution over $(\mathbb{Z}_d \times \mathbb{Z}_d)^n$, which may be seen as a $d^n \times d^n$ grid. The quantum state $\hat{\rho}$ is mapped on to the discrete Wigner function $\mathcal{W}_{\hat{\rho}}(\mathbf{u})$, defined to be

$$\mathcal{W}_{\hat{\rho}}(\mathbf{u}) = \frac{1}{d^n} \mathrm{tr}(\hat{A}_{\mathbf{u}} \hat{\rho}), \tag{2.84}$$

where $\{\hat{A}_{\mathbf{u}}\}$ are the phase space point operators, which are in turn defined in terms of the Heisenberg-Weyl operators as

$$\begin{aligned} \hat{A}_{\mathbf{0}} &= \frac{1}{d^n} \sum_{\mathbf{u}} \hat{T}_{\mathbf{u}}, \\ \hat{A}_{\mathbf{u}} &= \hat{T}_{\mathbf{u}} \hat{A}_{\mathbf{0}} \hat{T}_{\mathbf{u}}^{\dagger}. \end{aligned} \tag{2.85}$$

In this thesis, we will quantify the magic resource with mana, which is defined to be

$$M(\hat{\rho}) := \ln \left[\sum_{\mathbf{u}} \mathcal{W}_{\hat{\rho}}(\mathbf{u}) \right], \tag{2.86}$$

where $\mathbf{u} = (u, u') \in \mathbb{Z}_d^n \times \mathbb{Z}_d^n$ label the points of the discrete phase space [430, 338].

It is possible to generate magic from a quantum field, just as it is possible to harvest entanglement, in the context of RQI [338]. Consider a single three-level UDW detector, (the lowest dimensional quantum system that admits a discrete Wigner function) with first and second energy gaps Ω_1 and Ω_2 respectively, whose free evolution is governed by the Hamiltonian

$$\hat{H}_D = \mathrm{diag}(0, \Omega_1, \Omega_1 + \Omega_2) \tag{2.87}$$

in the computational basis of energy levels $\{|0_D\rangle, |1_D\rangle, |2_D\rangle\}$, coupled to a real scalar field via an interaction Hamiltonian which is a simple modification of (2.22),

$$\hat{H}_I(\tau) = \lambda \chi_D(\tau) \hat{\mu}(\tau) \otimes \hat{\phi}(x_D[\tau]), \tag{2.88}$$

where $\hat{\mu}$ is the monopole moment operator of the qutrit, given by

$$\hat{\mu}(\tau) = \frac{1}{\sqrt{2}}\left(|1_D\rangle\langle 0_D| e^{i\Omega_1\tau} + |2_D\rangle\langle 1_D| e^{i\Omega_2\tau}\right) + \text{h.c.}. \tag{2.89}$$

Taking the initial state of the detector-field system to be $|\Psi_i\rangle = |0_D\rangle \otimes |0\rangle$, where $|0\rangle$ is some suitably chosen vacuum state, the final reduced state of the detector is given by [338]

$$\hat{\rho}_D = \begin{pmatrix} p & 0 & \beta^* \\ 0 & q & 0 \\ \beta & 0 & 1-p-q \end{pmatrix}, \tag{2.90}$$

where p is the probability that the detector is found in its ground state, q is the probability that it is found in its first excited state, and β is the coherence between the ground state and the second excited state. The mana of this reduced state is given by the elements q and β of (2.90),

$$\begin{aligned} M(\hat{\rho}_D) = \ln\Big[1 - q \\ + \frac{1}{3}\Big(|q - \text{Re}[\beta] - \sqrt{3}\text{Im}[\beta]| + |q + 2\text{Re}[\beta]| \\ + |q - \text{Re}[\beta] + \sqrt{3}\text{Im}[\beta]|\Big)\Big]. \end{aligned} \tag{2.91}$$

Assuming, as was the case in entanglement harvesting, that the coupling λ is sufficiently small for perturbation theory, the element q may be written as [338]

$$\begin{aligned} q &=_D \langle 1|\hat{\rho}_{\mathcal{D}}|1\rangle_D \\ &= \frac{\lambda^2}{2}\int_{-\infty}^{\infty} d\tau \int_{-\infty}^{\infty} d\tau' \chi_D(\tau)\chi_D(\tau') e^{-i\Omega_1(\tau-\tau')} W(x_D[\tau], x_D[\tau']) + \mathcal{O}(\lambda^4), \end{aligned} \tag{2.92}$$

and β as

$$\begin{aligned} \beta &=_D \langle 2|\hat{\rho}_{\mathcal{D}}|0_D\rangle \\ &= -\frac{\lambda^2}{4}\int_{-\infty}^{\infty} d\tau \int_{-\infty}^{\infty} d\tau' \chi_D(\tau)\chi_D(\tau') \\ &\qquad \times \Big[\theta(\tau-\tau') e^{i(\Omega_1\tau' + \Omega_2\tau)} W(x_D[\tau], x_D[\tau']) \\ &\qquad\quad + \theta(\tau'-\tau) e^{i(\Omega_1\tau + \Omega_2\tau')} W(x_D[\tau'], x_D[\tau])\Big] + \mathcal{O}(\lambda^4). \end{aligned} \tag{2.93}$$

Having provided the necessary background and definitions, we proceed to the results of Part I.

Chapter 3

Entanglement Dynamics in Minkowski and Shock Wave Spacetimes

While the harvesting of entanglement from the field vacuum has received considerable attention, much less is known about how pre-existing entanglement between detectors evolves under field interaction. This is a physically distinct question from that of standard harvesting: here, the detectors are already entangled prior to their interaction with the field, and we ask whether the field amplifies or degrades that entanglement. It is clear that when detectors begin to entangle in a maximally entanglement state, the entanglement can only degrade. However, it is not immediately obvious whether the field interaction will suppress or enhance the quantum correlations between the detectors when the initial entanglement is weak. This chapter explores this question in detail. We analyze the evolution of entanglement between two initially entangled UDW detectors coupled to a massless scalar field, working within the framework of perturbation theory. Our treatment accounts for both pointlike and spatially extended detectors.

3.1 Initially entangled detectors

We consider two UDW detectors labelled A and B, linearly coupled to a real massless quantum scalar field. Let τ_j ($j \in \{A, B\}$) be the proper time of detector j and t be a common time, with an associated timelike Killing vector used to define the vacuum. The

interaction Hamiltonian is given by

$$\hat{H}_I(t) = \frac{\mathrm{d}\tau_A}{\mathrm{d}t}\hat{H}_A\Big(\tau_A(t)\Big) + \frac{\mathrm{d}\tau_B}{\mathrm{d}t}\hat{H}_B\Big(\tau_B(t)\Big)\,, \tag{3.1}$$

where $\hat{H}_j(\tau_j)$ is

$$\hat{H}_j(\tau_j) = \lambda_j \chi_j(\tau_j)\hat{\mu}_j(\tau_j) \otimes \int \mathrm{d}^3x\, F_j(\boldsymbol{x}-\boldsymbol{x}_j)\hat{\phi}(x_j(\tau_j))\,. \tag{3.2}$$

We have modified (2.22) through the inclusion of $F_j(\boldsymbol{x}-\boldsymbol{x}_j)$, a smearing function which specifies the spatial profile and the position of the center of mass $\boldsymbol{x}_j$ of detector j. To recover the usual pointlike case, we can take the limit of F_j to be the Dirac delta distribution.

We assume that the field is in the vacuum state $|0\rangle$, and that the detectors A and B start out entangled so that the joint system has the initial state

$$|\Psi_i\rangle = \Big(\alpha\,|g_A\rangle \otimes |g_B\rangle + \beta e^{i\theta}\,|e_A\rangle \otimes |e_B\rangle\Big) \otimes |0\rangle\,, \tag{3.3}$$

where α, $\beta \in [0,1]$, with the constraint that $\alpha^2+\beta^2=1$, and $\theta \in [0,2\pi)$ is the relative phase. For example, $\alpha = 0$, 1 correspond to separable states while $\alpha = 1/\sqrt{2}$ gives a Bell state. We will refer to $\alpha = 1$ as the entanglement harvesting scenario. Note that we could also consider initial states of the form

$$|\Psi_i\rangle = \Big(\alpha\,|g_A\rangle \otimes |e_B\rangle + \beta e^{i\theta}\,|g_B\rangle \otimes |e_A\rangle\Big) \otimes |0\rangle\,, \tag{3.4}$$

by applying a bit-flip gate $\mathcal{I}_A \otimes \hat{\sigma}_x$ and setting $\Omega_B \to -\Omega_B$; the resultant behavior in this case is qualitatively similar to what we present below, as was the case for an earlier non-perturbative analysis of harvesting of mutual information [164].

As usual, we obtain the reduced state of the detectors $\hat{\rho}_{AB}$ after the interaction by tracing out the field degree of freedom. Writing $\hat{\rho}_i \coloneqq |\Psi_i\rangle\langle\Psi_i|$, we obtain

$$\begin{aligned}\hat{\rho}_{AB} &= \mathrm{Tr}_\phi(\hat{U}\hat{\rho}_i\hat{U}^\dagger)\\ &= \mathrm{Tr}_\phi(\hat{\rho}_i) + \mathrm{Tr}_\phi(\hat{U}_1^{(1)}\hat{\rho}_i\hat{U}_1^{(1)\dagger}) + \mathrm{Tr}_\phi(\hat{U}_I^{(2)}\rho_0) + \mathrm{Tr}_\phi(\hat{\rho}_i\hat{U}^{(2)\dagger}) + \mathcal{O}(\lambda^4)\,.\end{aligned} \tag{3.5}$$

In the basis $\{|g_A\rangle\otimes|g_B\rangle\,, |g_A\rangle\otimes|e_B\rangle\,, |e_A\rangle\otimes|g_B\rangle\,, |e_A\rangle\otimes|e_B\rangle\}$, the density matrix $\hat{\rho}_{AB}$ can be obtained as follows [317].

$$\begin{aligned}\hat{\rho}_{AB} =& \mathrm{tr}_\phi(|\Psi_f\rangle\langle\Psi_f|)\\ =& \begin{pmatrix}\rho_{11} & 0 & 0 & \rho_{14}\\ 0 & \rho_{22} & \rho_{23} & 0\\ 0 & \rho_{23}^* & \rho_{33} & 0\\ \rho_{14}^* & 0 & 0 & \rho_{44}\end{pmatrix} + \mathcal{O}(\lambda^4),\end{aligned} \tag{3.6}$$

where the elements are given by

$$\rho_{11} = \alpha^2 + 2\alpha^2 \mathrm{Re}[J_{AA}^{(-+)} + J_{BB}^{(-+)}] + 2\alpha\sqrt{1-\alpha^2}\mathrm{Re}[e^{i\theta}(J_{AB}^{(--)} + J_{BA}^{(--)})] \tag{3.7a}$$

$$\rho_{14} = \alpha\sqrt{1-\alpha^2}e^{-i\theta}(1 + J_{AA}^{(-+)} + J_{AA}^{(+-)*} + J_{BB}^{(-+)} + J_{BB}^{(+-)*}) + \alpha^2(J_{AB}^{(++)*} + J_{BA}^{(++)*}) \tag{3.7b}$$

$$+ (1-\alpha^2)(J_{AB}^{(--)} + J_{BA}^{(--)}) \tag{3.7c}$$

$$\rho_{22} = (1-\alpha^2)I_{AA}^{(+-)} + 2\alpha\sqrt{1-\alpha^2}\mathrm{Re}[e^{-i\theta}I_{AB}^{(++)}] + \alpha^2 I_{BB}^{(-+)} \tag{3.7d}$$

$$\rho_{23} = \alpha\sqrt{1-\alpha^2}e^{i\theta}I_{AA}^{(--)} + (1-\alpha^2)I_{BA}^{(+-)} + \alpha^2 I_{AB}^{(-+)} + \alpha\sqrt{1-\alpha^2}e^{-i\theta}I_{BB}^{(++)} \tag{3.7e}$$

$$\rho_{33} = \alpha^2 I_{AA}^{(-+)} + 2\alpha\sqrt{1-\alpha^2}\mathrm{Re}[e^{i\theta}I_{AB}^{(--)}] + (1-\alpha^2)I_{BB}^{(+-)} \tag{3.7f}$$

$$\rho_{44} = (1-\alpha^2) + 2(1-\alpha^2)\mathrm{Re}[J_{AA}^{(+-)} + J_{BB}^{(+-)}] + 2\alpha\sqrt{1-\alpha^2}\mathrm{Re}[e^{-i\theta}(J_{AB}^{(++)} + J_{BA}^{(++)})] \tag{3.7g}$$

where

$$I_{jk}^{(pq)} \coloneqq \lambda_j\lambda_k \int_{-\infty}^{\infty} \mathrm{d}\tau_j \int_{-\infty}^{\infty} \mathrm{d}\tau_k\, \chi_j(\tau_j)\chi_k(\tau_k) e^{i(p\Omega_j\tau_j + q\Omega_k\tau_k)} \mathcal{W}\Big(x_j(\tau_j), y_k(\tau_k)\Big)\,, \tag{3.8}$$

$$J_{jk}^{(pq)} \coloneqq -\lambda_j\lambda_k \int_{-\infty}^{\infty} \mathrm{d}\tau_j \int_{-\infty}^{t_1(\tau_j)} \mathrm{d}\tau_k\, \chi_j(\tau_j)\chi_k(\tau_k) e^{i(p\Omega_j\tau_j + q\Omega_k\tau_k)} \mathcal{W}\Big(x_j(\tau_j), y_k(\tau_k)\Big)\,, \tag{3.9}$$

and we have used the fact that $I_{AB}^{(\pm\pm)} = I_{BA}^{(\mp\mp)*} \in \mathbb{C}$ in ρ_{22} and ρ_{33}, respectively. The elements $I_{AB}^{(\pm\pm)}$ and $J_{kk}^{(\pm\mp)}$ only appear in the density matrix (3.6) in the case of initially entangled detectors. The quantity

$$\mathcal{W}(x_j, y_k) \coloneqq \int \mathrm{d}^3x \int \mathrm{d}^3y\, F_j(\boldsymbol{x} - \boldsymbol{x}_j) F_k(\boldsymbol{y} - \boldsymbol{y}_j) W(x, y), \tag{3.10}$$

is simply the smeared Wightman function. In what follows, we will consider the case where the energy gaps and couplings of the detectors are equal ($\Omega_A = \Omega_B = \Omega$, and $\lambda_A = \lambda_B = \lambda$).

We use the concurrence, $\mathcal{C}_{AB} = \mathcal{C}(\hat{\rho}_{AB}) = 2\max[0, |\rho_{14}| - \sqrt{\rho_{22}\rho_{33}}]$ to quantify the entanglement between the detectors. One can easily verify that the initial entanglement in (3.3) is

$$\mathcal{C}_{AB,0} = 2\alpha\sqrt{1-\alpha^2}$$

Although evaluating the concurrence (2.78) may seem straightforward, inspection of (3.7c), (3.7d), and (3.7f) indicates that care must be taken in its perturbative calculation. This is because both ρ_{22} and ρ_{33} are of order λ^2 (and so their geometric mean $\sqrt{\rho_{22}\rho_{33}}$ is of order λ^2), whereas a perturbative expansion of ρ_{14}

$$\rho_{14} = \rho_{14}^{(0)} + \lambda^2\rho_{14}^{(2)} + \lambda^4\rho_{14}^{(4)} + \mathcal{O}(\lambda^6)\,, \tag{3.11}$$

yields

$$|\rho_{14}|^2 = |\rho_{14}^{(0)}|^2 + 2\lambda^2 \mathrm{Re}[\rho_{14}^{(0)}\rho_{14}^{(2)*}] + \lambda^4(|\rho_{14}^{(2)}|^2 + 2\mathrm{Re}[\rho_{14}^{(0)}\rho_{14}^{(4)*}]) + \mathcal{O}(\lambda^6)\,. \tag{3.12}$$

For initially separable states, (i.e., the standard harvesting protocol) $\rho_{14}^{(0)} = 0$, and so $|\rho_{14}|^2 = \lambda^4|\rho_{14}^{(2)}|^2 + \mathcal{O}(\lambda^6)$, indicating that there are values of α, close to 0 and 1, for which λ^4 terms must make a significant contribution to $|\rho_{14}|$. In order to keep the perturbative expansion of $|\rho_{14}|$ consistent, we will separately consider cases where the detectors are nearly separable and the case where the detectors are sufficiently entangled.

Another issue has to do with the structure of ρ_{14}. Starting from (3.7c), we may rewrite the density matrix element as

$$\rho_{14}^{(0)} = \alpha\sqrt{1-\alpha^2}e^{-i\theta}\,, \tag{3.13}$$
$$\lambda^2\rho_{14}^{(2)} = \lambda^2\Big[\alpha\sqrt{1-\alpha^2}e^{-i\theta}(Y_A+Y_B) + \alpha^2 X_{AB}^*(-\Omega) + (1-\alpha^2)X_{AB}(\Omega)\Big]\,,$$

where

$$\lambda^2 Y_k \equiv J_{kk}^{(-+)} + J_{kk}^{(+-)*}\,, \tag{3.14a}$$
$$\lambda^2 X_{AB}(\Omega) \equiv J_{AB}^{(--)} + J_{BA}^{(--)}\,, \tag{3.14b}$$
$$\lambda^2 X_{AB}^*(-\Omega) \equiv J_{AB}^{(++)*} + J_{BA}^{(++)*}\,. \tag{3.14c}$$

The imaginary part of Y_k is divergent in the pointlike limit [317]. Although this divergence is regularized by the smearing functions, we shall demonstrate that it does not appear in the concurrence under the approximations we consider, when working with pointlike detectors.

3.1.1 Approximating the concurrence

We consider three scenarios: (i) initial weak entanglement with $\alpha \approx 0$, (ii) initial weak entanglement with $\alpha \approx 1$, and (iii) initially sufficient entanglement.

Initial weak entanglement: $\alpha \approx 0$

Let us assume that $\alpha \ll 1$ and perform a series expansion of Eq. (3.12) in terms of $\lambda^n\alpha^m$:

$$|\rho_{14}|^2 = \underbrace{\alpha^2(1-\alpha^2)}_{\text{initial}} + \underbrace{2\lambda^2\alpha\mathrm{Re}[X_{AB}(\Omega)e^{i\theta}]}_{\text{neutral}}$$

$$+\underbrace{\lambda^4|X_{AB}(\Omega)|^2}_{\text{harvesting}}+\underbrace{2\lambda^2\alpha^2\mathrm{Re}[Y_A+Y_B]}_{\text{degradation}}$$
$$+\mathcal{O}(\lambda^n\alpha^m)\qquad(n+m>4). \tag{3.15}$$

Note that $\rho_{14}^{(4)}$ and the divergent element $\mathrm{Im}[Y_k]$ do not exist in lower-order terms.

Initial weak entanglement: $\alpha \approx 1$

In the same manner, one can obtain a similar expression for $\alpha \approx 1$. For simplicity, let us use $\beta = \sqrt{1-\alpha^2}$ and expand Eq. (3.12) around $\beta = 0$:

$$|\rho_{14}|^2 = \underbrace{\beta^2(1-\beta^2)}_{\text{initial}}+\underbrace{2\lambda^2\beta\mathrm{Re}[X_{AB}^*(-\Omega)e^{i\theta}]}_{\text{neutral}}$$
$$+\underbrace{\lambda^4|X_{AB}(-\Omega)|^2}_{\text{harvesting}}+\underbrace{2\lambda^2\beta^2\mathrm{Re}[Y_A+Y_B]}_{\text{degradation}}$$
$$+\mathcal{O}(\lambda^n\beta^m)\,.\qquad(n+m>4) \tag{3.16}$$

As before, the elements $\rho_{14}^{(4)}$ and $\mathrm{Im}[Y_k]$ are absent. Note that $\beta = 0$ reduces to the entanglement harvesting scenario: $|\rho_{14}| = \lambda^2|X_{AB}(-\Omega)|$.

In both cases $\alpha \approx 0$ and 1, the approximated $|\rho_{14}|^2$ consists of four parts. The initial entanglement contribution in (3.15) is $\alpha^2(1-\alpha^2)$ (and $\beta^2(1-\beta^2)$ in (3.16)). The third term containing $X_{AB}(\Omega)$ is the part contributing to entanglement harvesting. The last term, $\mathrm{Re}[Y_A+Y_B]$, depends only on each individual detector and not on their correlations. This term corresponds to an outcome of local operations and can never enhance entanglement. Indeed, one can show that $\lambda^2\mathrm{Re}[Y_j] = -(I_{jj}^{(-+)}+I_{jj}^{(+-)})/2 \leq 0$ and so degrades entanglement. The second term, which we denote as the neutral contribution, can be positive or negative. By choosing the relative phase θ appropriately, we can ensure that $\mathrm{Re}[e^{i\theta}X_{AB}] > 0$, which enhances entanglement.

If the harvesting part does not exceed *both* the initial and degradation contributions to $|\rho_{14}|$, then entanglement degradation is inevitable, regardless of the value of $\sqrt{\rho_{22}\rho_{33}}$ since this term *always* contributes to entanglement degradation as it is positive and is subtracted from $|\rho_{14}|$. The converse case does not entail inevitable enhancement of entanglement: even if the harvesting contribution is greater than initial and degradation contributions in $|\rho_{14}|$, entanglement enhancement will not necessarily take place, because this depends on $\sqrt{\rho_{22}\rho_{33}}$.

Initial sufficient entanglement

In this approximation we assume $|\rho_{14}^{(0)}|^2 \gg \mathcal{O}(\lambda^4)$ and write Eq. (3.12) explicitly as [95]

$$|\rho_{14}^{(0)}|^2 = \alpha^2(1-\alpha^2)\,, \tag{3.17a}$$

$$\begin{aligned}\mathrm{Re}[\rho_{14}^{(0)}\rho_{14}^{(2)*}] =& \alpha\sqrt{1-\alpha^2}\Big[\alpha\sqrt{1-\alpha^2}\mathrm{Re}[Y_A+Y_B] \\ &+\Big(\alpha^2\mathrm{Re}[X_{AB}^*(-\Omega)e^{i\theta}]+(1-\alpha^2)\mathrm{Re}[X_{AB}(\Omega)e^{i\theta}]\Big)\Big]\,,\end{aligned} \tag{3.17b}$$

$$\begin{aligned}|\rho_{14}^{(2)}|^2 =& \Big|\alpha^2 X_{AB}^*(-\Omega)+(1-\alpha^2)X_{AB}(\Omega)\Big|^2+\alpha^2(1-\alpha^2)|Y_A+Y_B|^2 \\ &+2\alpha\sqrt{1-\alpha^2}\Big(\alpha^2\mathrm{Re}[X_{AB}^*(-\Omega)(Y_A+Y_B)^*e^{i\theta}] \\ &+(1-\alpha^2)\mathrm{Re}[X_{AB}(\Omega)(Y_A+Y_B)^*e^{i\theta}]\Big)\,.\end{aligned} \tag{3.17c}$$

Omitting the $\mathcal{O}(\lambda^4)$ terms, we obtain

$$|\rho_{14}|^2 \approx |\rho_{14}^{(0)}|^2 + 2\lambda^2\mathrm{Re}[\rho_{14}^{(0)}\rho_{14}^{(2)*}] \tag{3.18}$$

which is also independent of $\rho_{14}^{(4)}$ and $\mathrm{Im}[Y_k]$. Obviously this approximation does not work for $\alpha \approx 0$ and $\alpha \approx 1$ since it cannot recover the entanglement harvesting results in those limits. As in the previous approximations, (3.18) consists of three components: the initial entanglement, the harvesting contribution, and the degradation contribution. However, in this case, the harvesting contribution does not contain $|X_{AB}(\Omega)|^2$ or $|X_{AB}^*(-\Omega)|^2$. Note that for $\alpha \ll 1$ the leading term in (3.17c) yields the harvesting contribution in (3.15) (and likewise for $\beta \ll 1$ the harvesting contribution in (3.16) is recovered). Henceforth, we shall use these approximations (which are applicable even to pointlike detectors) in evaluating the concurrence in the scenarios we consider.

3.2 Smeared detectors in Minkowski spacetime

We now compute the elements in the density matrix (3.6) in (3+1)-dimensional Minkowski spacetime. We assume that the detectors are identical (have the same shape and internal structure) and are both at rest in a single frame of reference. We choose the switching function $\chi_j(\tau_j)$, and smearing function $F_j(\boldsymbol{x}-\boldsymbol{x}_j)$, to be Gaussian functions:

$$\chi_j(\tau_j) = e^{-(\tau_j-\tau_{j,0})^2/T^2}\,, \tag{3.19}$$

$$F_j(\boldsymbol{x}-\boldsymbol{x}_j) = \frac{1}{(\sqrt{\pi}\sigma)^3} e^{-(\boldsymbol{x}-\boldsymbol{x}_j)^2/\sigma^2}\,, \tag{3.20}$$

where T and σ are their temporal and spatial widths, respectively.

The imaginary part of $\lambda^2 Y_k \equiv J_{kk}^{(-+)} + J_{kk}^{(+-)*}$ in ρ_{14} for pointlike detectors is known to be divergent. We will show that this term can be regularized by introducing finite-sized UDW detectors as suggested in [317]. In particular, we consider initially entangled smeared detectors at rest in $(3+1)$-dimensional Minkowski spacetime. Assuming a massless scalar field, the mode decomposition of $\hat{\phi}(x(t))$ is known to be

$$\hat{\phi}(t,\boldsymbol{x}) = \int \frac{\mathrm{d}^3k}{\sqrt{(2\pi)^3 2|\boldsymbol{k}|}} \left(\hat{a}_{\boldsymbol{k}} e^{-i|\boldsymbol{k}|t+i\boldsymbol{k}\cdot\boldsymbol{x}} + \hat{a}_{\boldsymbol{k}}^\dagger e^{i|\boldsymbol{k}|t-i\boldsymbol{k}\cdot\boldsymbol{x}}\right), \tag{3.21}$$

and so the Wightman function becomes

$$W(x_j(t_1), y_k(t_2)) = \int \frac{\mathrm{d}^3k}{(2\pi)^3 2|\boldsymbol{k}|} e^{-i|\boldsymbol{k}|(t_1-t_2)+i\boldsymbol{k}\cdot(\boldsymbol{x}-\boldsymbol{y})}. \tag{3.22}$$

Let us first consider $\lambda^2 Y_A \equiv J_{AA}^{(-+)} + J_{AA}^{(+-)*}$ for detector A in ρ_{14}. We find

$$\begin{aligned} J_{AA}^{(-+)} + J_{AA}^{(+-)*} &= -2\lambda_A^2 \int_{-\infty}^{\infty} \mathrm{d}t_1 \int_{-\infty}^{t_1} \mathrm{d}t_2\, \chi_A(t_1)\chi_A(t_2) e^{-i\Omega_A(t_1-t_2)} \\ &\quad \times \int \mathrm{d}^3x\, F_A(\boldsymbol{x}-\boldsymbol{x}_A) \int \mathrm{d}^3y\, F_A(\boldsymbol{y}-\boldsymbol{x}_A) \mathrm{Re}[W(x_A(t_1), y_A(t_2))] \\ &= -2\lambda_A^2 \int \frac{\mathrm{d}^3k}{2|\boldsymbol{k}|} \tilde{F}_A(\boldsymbol{k})\tilde{F}_A(-\boldsymbol{k}) \\ &\quad \times \int_{-\infty}^{\infty} \mathrm{d}t_1 \int_{-\infty}^{t_1} \mathrm{d}t_2\, \chi_A(t_1)\chi_A(t_2) e^{-i\Omega_A(t_1-t_2)} \cos[|\boldsymbol{k}|(t_1-t_2)]\,, \end{aligned} \tag{3.23}$$

where we have performed the Fourier transform:

$$\tilde{F}_j(\boldsymbol{k}) = \int \frac{\mathrm{d}^3x}{\sqrt{(2\pi)^3}} F_j(\boldsymbol{x}) e^{i\boldsymbol{k}\cdot\boldsymbol{x}}\,. \tag{3.24}$$

Note that we must have $\tilde{F}_j(-\boldsymbol{k}) = \tilde{F}_j(\boldsymbol{k})$ if $F_j(\boldsymbol{x}) \in \mathbb{R}$. With a Gaussian switching function centered at $t = t_{A,0}$, the double integral over time in (3.23) is

$$\int_{-\infty}^{\infty} \mathrm{d}t_1 \int_{-\infty}^{t_1} \mathrm{d}t_2\, e^{-(t_1-t_{A,0})^2/T^2} e^{-(t_2-t_{A,0})^2/T^2} e^{-i\Omega_A(t_1-t_2)} \cos[|\boldsymbol{k}|(t_1-t_2)]$$

$$= \frac{T\sqrt{2\pi}}{2}\int_0^\infty \mathrm{d}u\, e^{-u^2/2T^2} e^{-i\Omega u}\cos(|\boldsymbol{k}|u) \tag{3.25}$$

$$= \frac{\pi T^2}{4} e^{-T^2(|\boldsymbol{k}|+\Omega)^2/2}\left[1 + e^{2|\boldsymbol{k}|T^2\Omega}\left(1 + i\mathrm{erfi}\frac{T(|\boldsymbol{k}|-\Omega)}{\sqrt{2}}\right) - i\mathrm{erfi}\frac{T(|\boldsymbol{k}|+\Omega)}{\sqrt{2}}\right], \tag{3.26}$$

and (3.23) is therefore (after substituting in the smearing function (3.20) and its Fourier transform (3.24)),

$$\begin{aligned}
&J_{AA}^{(-+)} + J_{AA}^{(+-)*} \\
&= -\frac{\lambda_A^2\pi T^2}{2}\int \frac{\mathrm{d}^3k}{2|\boldsymbol{k}|}\tilde{F}_A^2(\boldsymbol{k}) e^{-T^2(|\boldsymbol{k}|+\Omega)^2/2} \\
&\qquad\qquad \times\left[1 + e^{2|\boldsymbol{k}|T^2\Omega}\left(1 + i\mathrm{erfi}\frac{T(|\boldsymbol{k}|-\Omega)}{\sqrt{2}}\right) - i\mathrm{erfi}\frac{T(|\boldsymbol{k}|+\Omega)}{\sqrt{2}}\right] \\
&= -\frac{\lambda_A^2 e^{-T^2\Omega^2/2}}{8\pi(1+\sigma^2/T^2)^{3/2}}\left[2\sqrt{1+\sigma^2/T^2} + e^{T^2\Omega^2/2(1+\sigma^2/T^2)}\sqrt{2\pi}T\Omega\mathrm{erf}\frac{T\Omega}{\sqrt{2(1+\sigma^2/T^2)}}\right] \\
&\quad - i\frac{\lambda_A^2 T^2}{8\pi}\int_0^\infty \mathrm{d}|\boldsymbol{k}|\,|\boldsymbol{k}| e^{-|\boldsymbol{k}|^2\sigma^2/2} \\
&\qquad\qquad \times\left[e^{-T^2(|\boldsymbol{k}|-\Omega)^2/2}\mathrm{erfi}\frac{T(|\boldsymbol{k}|-\Omega)}{\sqrt{2}} - e^{-T^2(|\boldsymbol{k}|+\Omega)^2/2}\mathrm{erfi}\frac{T(|\boldsymbol{k}|+\Omega)}{\sqrt{2}}\right],
\end{aligned} \tag{3.27a}$$

where we have used $\mathrm{d}^3k = |\boldsymbol{k}|^2\sin\theta\mathrm{d}|\boldsymbol{k}|\mathrm{d}\theta\mathrm{d}\varphi$ with $|\boldsymbol{k}| \in [0,\infty), \theta \in [0,\pi]$, and $\varphi \in [0, 2\pi)$. The regularized real and imaginary parts of $J_{kk}^{(-+)} + J_{kk}^{(+-)*}$ are plotted as functions of the energy gap in Fig.(3.1).

Similar calculations yield the remaining terms in ρ_{14}, ρ_{22}, and ρ_{33}. In particular, the expressions for $I_{kk}^{(-+)}$ in ρ_{22} and ρ_{33} in (3.28c) and for $J_{AB}^{(++)}$ (and its counterparts) in (3.28b) that contribute to $\lambda^2 X_{AB}^*(-\Omega) \equiv J_{AB}^{(++)*} + J_{BA}^{(++)*}$ in ρ_{14} can be found in Ref. [362]. The quantities $J_{AB}^{(++)*}$, and $J_{AB}^{(--)}$ in ρ_{14}, and $I_{jk}^{(\pm\pm)}$ in ρ_{22} and ρ_{33} are then given by

$$J_{AB}^{(--)} = -\frac{\lambda_A\lambda_B T^2}{8\pi L} e^{-i\Omega(t_{A,0}+t_{B,0})} e^{-T^2\Omega^2/2} \tag{3.28a}$$

$$\times \int_0^\infty \mathrm{d}|\boldsymbol{k}|\, e^{-|\boldsymbol{k}|^2(\sigma^2+T^2)/2} e^{i\Delta t|\boldsymbol{k}|}\mathrm{erfc}\left(\frac{\Delta t + iT^2|\boldsymbol{k}|}{\sqrt{2}T}\right)\sin(|\boldsymbol{k}|L), \tag{3.28b}$$

$$\begin{aligned}
I_{kk}^{(-+)} &= \frac{\lambda_k^2 e^{-T^2\Omega^2/2}}{8\pi(1+\sigma^2/T^2)^{3/2}} \\
&\quad\times\left[2\sqrt{1+\sigma^2/T^2} - \sqrt{2\pi}T\Omega e^{T^2\Omega^2/2(1+\sigma^2/T^2)}\mathrm{erfc}\left(\frac{T\Omega}{\sqrt{2(1+\sigma^2/T^2)}}\right)\right],
\end{aligned} \tag{3.28c}$$

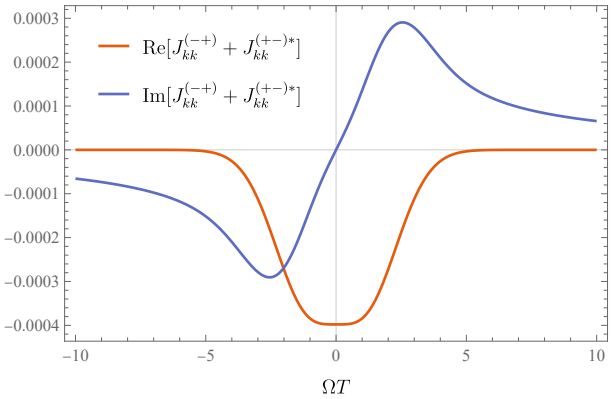


Figure 3.1: Real and imaginary parts of $J_{kk}^{(-+)} + J_{kk}^{(+-)*}$ with $\sigma/T = 1$ and $\lambda = 1/10$. The real part converges quickly to 0 with large $|\Omega T|$ while the imaginary part is nonzero for a wide range of ΩT.

$$I_{AB}^{(++)} = \frac{i\lambda_A\lambda_B T e^{i\Omega(t_{A,0}+t_{B,0})}e^{-T^2\Omega^2/2}}{8\pi L\sqrt{1+\sigma^2/T^2}}\sqrt{\frac{\pi}{2}}\left[e^{-\Gamma_-^2}\mathrm{erfc}(i\Gamma_-) - e^{-\Gamma_+^2}\mathrm{erfc}(-i\Gamma_+)\right] \tag{3.28d}$$

where $L \coloneqq |\boldsymbol{x}_B - \boldsymbol{x}_A|$ and $\Delta t \coloneqq t_{B,0} - t_{A,0}$ are the spatial and temporal separation of the detectors' Gaussian peaks, and

$$\Gamma_\pm \coloneqq \frac{L \pm \Delta t}{T\sqrt{2(1+\sigma^2/T^2)}}\,. \tag{3.29}$$

This physical setup is illustrated in Fig. 3.2 (a). Note that that $J_{AB}^{(++)*}$ may be obtained from $J_{AB}^{(--)}$ by $\Omega \to -\Omega$ and then conjugating the result. In the same manner, one finds that $I_{BA}^{(--)} = I_{AB}^{(++)*}$. The real part of (3.27a) is always non-positive, which means that $\mathrm{Re}[Y_A + Y_B]$ in $|\rho_{14}|$ acts as noise that inhibits the detectors from gaining entanglement. In fact, one can verify from (3.27a) that $\mathrm{Re}[Y_k] \sim -T\Omega$ when $T\Omega \gg 1$ for $\sigma \geq 0$. This suggests that the longer the interaction, the greater the leakage of entanglement, and therefore entanglement extraction becomes more difficult as the effective duration of interaction increases.

Thanks to the smearing function, all the elements in the density matrix are finite and well-defined. One may then perform the approximations in Sec. 3.1.1 and take the limit $\sigma \to 0$ if one wants to work with pointlike detectors. We will work with initially entangled pointlike detectors in the following sections. The qualitative behavior for smeared detectors is not so different from the pointlike ones. Note that if we had first taken the limit of $\sigma \to 0$

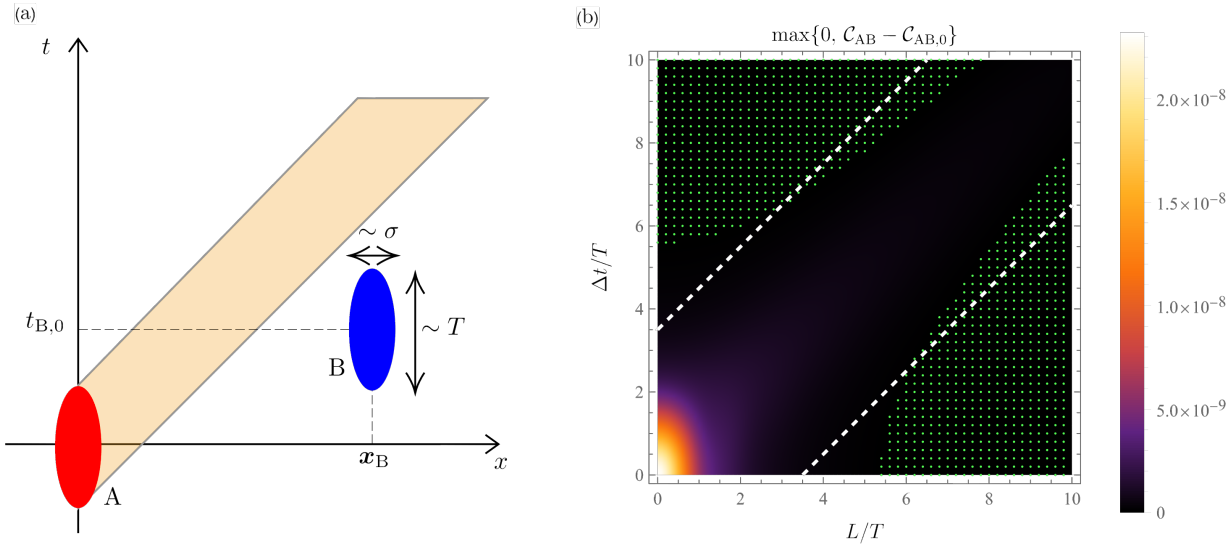


Figure 3.2: (a) Finite-sized detectors in Minkowski spacetime. The center of mass of detector B is located at $(t_{B,0}, \boldsymbol{x}_B)$; each detector has the respective spatial and temporal Gaussian widths σ and T. The diagonal orange-shaded strip represents the null trajectories from detector A; detector A can directly signal to B by exchanging field quanta once the support of detector B crosses this region. (b) A plot of the positive part of the difference $\mathcal{C}_{AB} - \mathcal{C}_{AB,0}$ between the concurrence before and after the interaction, with $\beta = 10^{-15}, \lambda = 1/10, \Omega T = 5, \sigma/T = 0$, and $\theta = 0$. The green dots represent $\mathcal{C}_{AB} - \mathcal{C}_{AB,0} \leq 0$, which means the initial entanglement is degraded, and the dashed lines indicate the null trajectory corresponding to the one in (a).

and then performed the perturbative approximations employed in Sec. 3.1.1 the density matrix would be ill-defined due to the presence of divergent matrix elements. Realistically, all UDW detectors will have some finite spatial extension. In what follows, we can consider σ to be smaller than all other relevant length scales in the system, justifying the procedure described above.

3.3 The fate of entanglement between inertial detectors

In this section, we consider pointlike ($\sigma \to 0$) detectors in $(3+1)$-dimensional Minkowski spacetime and see how the initial entanglement changes after the interaction. As shown in Fig. 3.2 (a), we work in a setup where the center of mass of detector A is located at the origin and the peak of Gaussian switching is at $t = 0$. Detector B is fixed at the spatial coordinate $\boldsymbol{x}_B$, and experiences peak switching at $t_{B,0}$. Since the detectors are in $(3+1)$-dimensional Minkowski spacetime, and interacting with a massless field, the detectors may only communicate with each other when they are lightlike separated. This is depicted as an orange strip in the figure; detector A can send quanta to detector B once the support of detector B has overlap with this region. It is natural to ask whether initially entangled detectors can gain more entanglement after interacting with their local fields. The answer is *yes*, though we find that the condition is very limited: only initially weakly entangled detectors can gain entanglement.

Consider weakly entangled detectors with $\beta \approx 0$ (i.e., $\alpha \approx 1$). Using (3.16) to calculate the concurrence $\mathcal{C}_{AB}$ after the interaction we may plot the difference between the initial and final concurrences of the detectors for $\beta = 10^{-15},\ \lambda = 1/10,\ \Omega T = 5,\ \sigma/T = 0$, and $\theta = 0$. This is illustrated in Fig. 3.2 (b). We plot $\max[0, \mathcal{C}_{AB}\mathcal{C}_{AB,0}]$ so that we can see the region of entanglement enhancement, and highlight values of the final concurrence that are less than the initial value $\mathcal{C}_{AB,0}$ with green dots. We first note that communication between the detectors greatly assists in the extraction of entanglement, since one can see from Fig. 3.2 (b) that two detectors gain entanglement when they are in causal contact (within the dashed lines). This phenomenon can be explained from the entanglement harvesting viewpoint: communication increases the value of the harvesting term $|X_{AB}(-\Omega)|$ of $|\rho_{14}|$ in (3.16), in the entanglement harvesting scenario ($\beta = 0$) [424]. Nevertheless, as described in the previous section, the degradation term $\mathrm{Re}[Y_A + Y_B]$ will suppress this communication assistance if the duration of interaction is too long.

One can also ask whether detectors that are not communicating can gain entanglement from the field. The answer is also *yes*. To see this, we plot concurrence for pointlike detectors when they are *effectively*[1] causally disconnected ($L/T = 7,\ \Delta t/T = 0$) in Fig. 3.3. Figure 3.3 (a) shows the values of ΩT and $\log_{10}\beta$ that enhance entanglement without

[1]Since we are using Gaussian switching, the interaction is not compactly supported in the spacetime. In other words, the detectors are always communicating. However, due to a Gaussian function's exponential suppression, it can be thought of as an effectively compactly supported interaction in $\tau \in [-3.5T + \tau_{j,0}, 3.5T + \tau_{j,0}]$, where τ is a proper time and $\tau_{j,0}$ is the center of Gaussian of detector j [424].

communication. The parameters are set to be $\lambda = 1/10$, $L/T = 7$, $\Delta t/T = 0$, $\sigma/T = 0$, and $\theta = 0$. We emphasize that the detectors experience entanglement degradation when the parameters $(\Omega T,\ \log_{10}\beta)$ are chosen such that they are represented in the region colored by green dots in Fig. 3.3 (a). We find that a pair of causally disconnected detectors can enhance their initial entanglement as long as they are weakly entangled at the beginning. In addition, one must choose ΩT from a suitable range: if the initial entanglement is, for example, $\log_{10}\beta = -30$ with the given parameters, then the energy gap must be $\Omega T \in [6.8, 11]$ to gain more correlation. This range of energy gaps conducive to entanglement enhancement increases as $\beta \to 0$. Specifically, the upper bound on Ω for entanglement harvesting gets pushed to infinity in the limit $\beta \to 0$. We also note that there is a maximum value of β for a fixed L/T, beyond which entanglement cannot be extracted for any ΩT.

The blue curve in Fig. 3.3 (b) represents a slice at $\Omega T = 7$ in (a), and each factor $\mathcal{C}_{AB}$ and $\mathcal{C}_{AB,0}$ in $\max[0, \mathcal{C}_{AB} - \mathcal{C}_{AB,0}]$ is shown in Fig. 3.3 (c) as blue and green curves, respectively. It is interesting to note from Fig. 3.3 (c) that for sufficiently large β, entanglement is completely extinguished after the interaction. There is also a dependence on the relative initial phase θ; for $\theta = \pi$ (the orange curve in 3.3 (b) and 3.3 (c)), the positive difference $\mathcal{C}_{AB} - \mathcal{C}_{AB,0}$ persists for larger values of β, allowing for a wider range of entanglement extraction. This dependence on the relative phase θ arises from the term $\mathrm{Re}[X^*_{AB}(-\Omega)e^{-i\theta}]$ in (3.16) and elements in $\rho_{22}\rho_{33}$.

For the case of initially sufficiently entangled detectors, no entanglement extraction can occur—only degradation takes place. One of the reasons comes from the fact that the degradation part $\mathrm{Re}[Y_A + Y_B]$ is no longer suppressed in (3.16) as β grows. Extracting entanglement with $\alpha \approx 0$ is also difficult since $I^{(+-)}_{kk}$ in $\sqrt{\rho_{22}\rho_{33}}$ dominates with large Ω.

One notable difference from pure entanglement harvesting ($\beta = 0$) is the dependence on the energy gap. In the harvesting scenario, detectors with Gaussian switching[2] can extract entanglement even when they are far apart ($L/T \gg 1$) if Ω is large enough [362]. That is, once the detector separation L is fixed, there exists a minimum energy gap $\Omega_{\min}$ such that the detectors can harvest entanglement for all $\Omega \geq \Omega_{\min}$. In our case however, this is no longer true. Figure 3.4 shows $\max[0, \mathcal{C}_{AB} - \mathcal{C}_{AB,0}]$ as a function of L/T and ΩT for pointlike detectors with $\Delta t = 0$, $\beta = 10^{-15}$, and $\theta = 0$. That is, we are exploring the region of entanglement extraction in the $(L/T,\ \Omega T)$ plane when the centers of Gaussian switching in Fig. 3.2 (a) are on the same time slice. We see that there exist minimum and maximum values of Ω for some L that allow detectors to extract entanglement; once Ω gets large enough, only degradation takes place. This is due to a competition between the harvesting

[2]This is not the case for sudden/sharp switching functions [362].

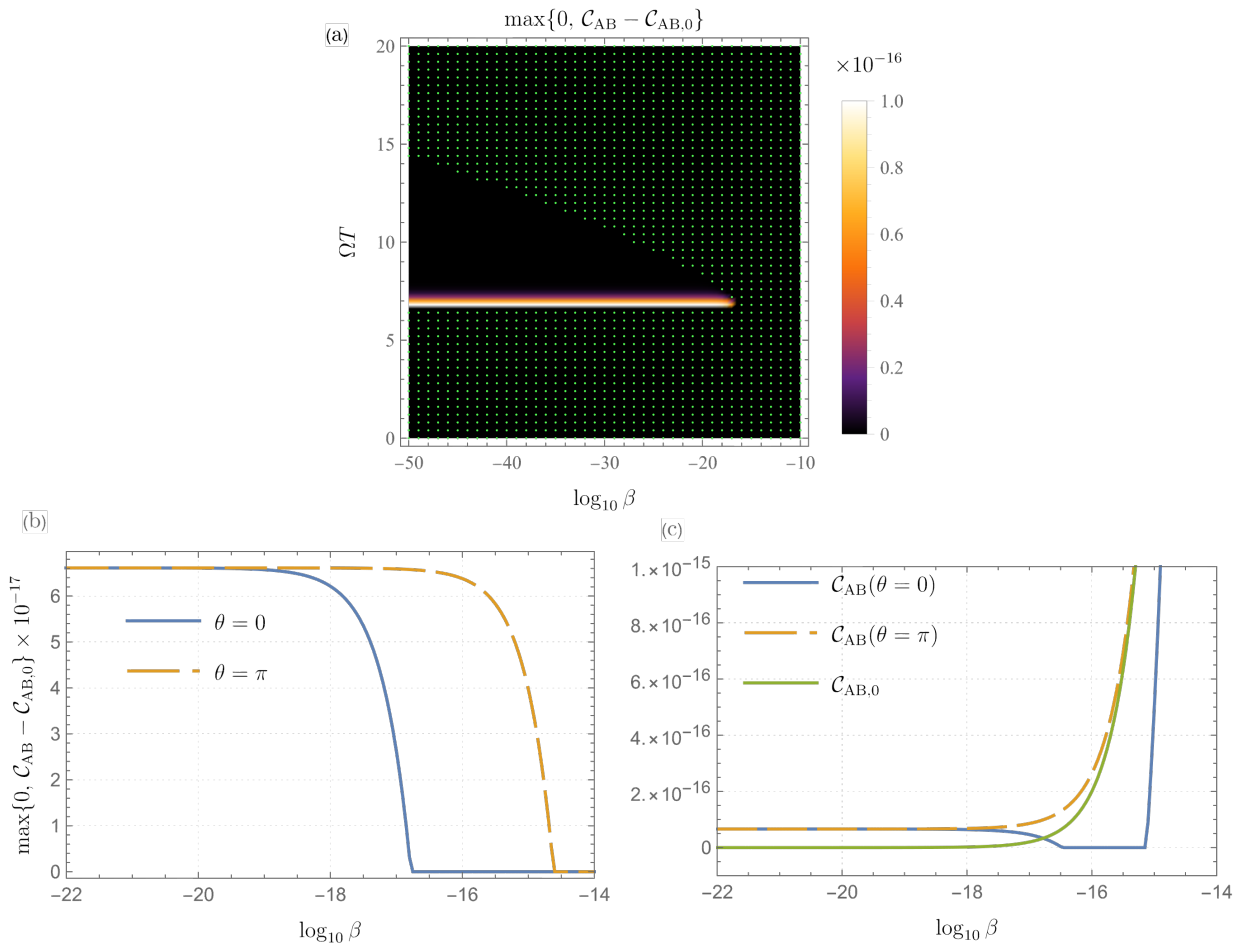


Figure 3.3: (a) The positive part of $\mathcal{C}_{AB} - \mathcal{C}_{AB,0}$ as a function of ΩT and $\log_{10}\beta$ when $\lambda = 1/10, L/T = 7, \Delta t/T = 0, \sigma/T = 0$, and $\theta = 0$. The green dots represent degradation. The detectors can gain entanglement when β is small enough. The range of ΩT that enables the detectors to gain entanglement enlarges as $\beta \to 0$. (b) $\max[0, \mathcal{C}_{AB} - \mathcal{C}_{AB,0}]$ as a function of $\log_{10}\beta$ for $\lambda = 1/10, L/T = 7, \Delta t/T = 0, \sigma/T = 0$, and $\Omega T = 7$. The blue curve shows a slice in (a) at $\Omega T = 7$, whereas the orange dashed curve represents the case when $\theta = \pi$. (c) Each component $\mathcal{C}_{AB}$ and $\mathcal{C}_{AB,0}$ in (b) with the same parameters.

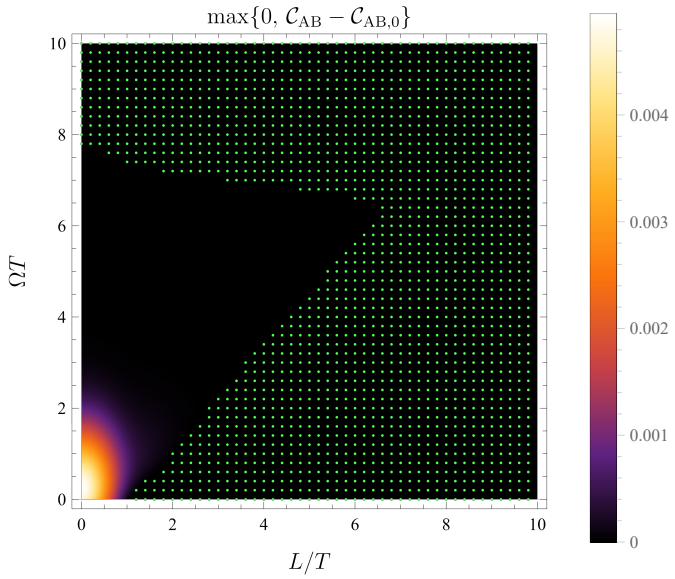


Figure 3.4: The positive part of difference $\mathcal{C}_{AB} - \mathcal{C}_{AB,0}$ as a function of L/T and ΩT. Here, $\Delta t/T = 0, \beta = 10^{-15}$, and $\theta = 0$. Entanglement degradation occurs in the region with green dots.

part and the degradation part of $|\rho_{14}|$. When Ω is sufficiently large, the latter quantity is larger than the former, ensuring entanglement degradation. This leads to a maximal value of Ω for which entanglement harvesting is possible. There is also a minimum value of Ω below which harvesting is not possible due to "detector noise"—the positive $\sqrt{\rho_{22}\rho_{33}}$ term will be larger than the $|\rho_{14}|$ term since excitation probabilities increase as the energy gap decreases. The maximum energy gap $\Omega_{\rm max}$ allowing harvesting is pushed to infinity as $\beta \to 0$, recovering the usual harvesting scenario [362].

3.4 Entanglement in the presence of a shockwave

We now extend our results in Minkowski spacetime to a nontrivial spacetime. We consider in particular a gravitational shockwave spacetime, since it has been shown that a weak gravitational field can enhance entanglement harvesting from the vacuum [98]. Furthermore, for the type of gravitational shockwave that we consider in this chapter, the Wightman function for a massless scalar field has a nontrivial, but closed form expression [176].

This latter study considered initially separable detectors in their ground states; we extend this to consider initially entangled detectors with the aim of understanding if the shockwave mitigates or enhances entanglement degradation. We find that a shockwave admits greater entanglement harvesting relative to the flat space setting, and extends the region in Fig. 3.3 (a) dramatically.

3.4.1 Shockwave spacetime

As in [176] we shall be working with the Dray and 't Hooft generalization [128] of the Aichelburg-Sexl shockwave spacetime [7]. Consider a planar shockwave propagating in the z direction in D-dimensional Minkowski spacetime. The metric describing such a spacetime in the so-called Brinkmann coordinates [64] is

$$\mathrm{d}s^2 = -\mathrm{d}u\mathrm{d}v + f(\vec{x})\delta(u-u_0)\mathrm{d}u^2 + \delta_{ij}\mathrm{d}x^i\mathrm{d}x^j\,, \tag{3.30}$$

where $u = t - z$ and $v = t + z$ are null coordinates, and $\vec{x}$ or x^i, $i \in \{1, ..., D-2\}$ are the transverse coordinates (i.e., the remaining spatial coordinates). The wavefront of the shockwave is located at $u = u_0$. We consider an idealized scenario in which the spacetime is exactly Minkowski on either side of u_0.

The term $f(\vec{x})$ is the shockwave profile, which is directly related to the energy density $\varrho(\vec{x})$ through the Einstein field equations:

$$\Delta f(\vec{x}) = -16\pi G_N \varrho(\vec{x})\,, \tag{3.31}$$

where $\Delta = \delta^{ij}\partial_i\partial_j$ is the flat Laplacian in the transverse direction. We use a quadratic profile given by

$$f(\vec{x}) = -\vec{x}\cdot A\cdot\vec{x} = -\sum_{i=1}^{D-2} a_i (x^i)^2, \tag{3.32}$$

where A is a symmetric constant matrix, whose eigenvalues are a_i. Such a profile represents an ultrarelativistic domain wall in the transverse plane [298], as one can see from (3.31) that the energy density is constant everywhere: $\varrho(\vec{x}) = \mathrm{Tr}[A]/8\pi G_N$.

Using the notation $x = (u, v, \vec{x})$ and $y = (U, V, \vec{X})$ the exact form of the Wightman

function is [176]

$$W(x,y) = \frac{(-i)^{D-2}\Gamma(D/2-1)}{4\pi^{D/2}} \prod_{i=1}^{D-2} \left(1 + a_i \Delta\theta \frac{(u-u_0-i\epsilon)(U-u_0+i\epsilon)}{\Delta u - i\epsilon}\right)^{-1/2} \times \left((\Delta v - i\epsilon)(\Delta u - i\epsilon) - \Delta\vec{x}^2 + \sum_{i=1}^{D-2} \frac{a_i \Delta\theta \Big([U-u_0+i\epsilon]x^i - [u-u_0-i\epsilon]X^i\Big)^2}{\Delta u - i\epsilon + a_i \Delta\theta (u-u_0-i\epsilon)(U-u_0+i\epsilon)} \right)^{(2-D)/2}, \tag{3.33}$$

where $\Delta v \equiv v - V$, $\Delta u \equiv u - U$, $\theta_u \equiv \theta(u-u_0)$, and $\Delta\theta = \theta_u - \theta_U$ with the Heaviside step function $\theta(u)$. $\Gamma(x)$ is the gamma function and by choosing $D = 4$ it gives $\Gamma(1) = 1$. The Wightman function reduces to the standard Minkowski space form if $f(\vec{x}) = 0$ (in which case there is no shockwave at all) or $\Delta\theta = 0$ (so the events u and U are localized at the same side of the shockwave).

3.4.2 Results

We restrict to $D = 4$ and consider two inertial UDW detectors

$$\begin{aligned} x_A(\tau_A) &= (t(\tau_A), x(\tau_A), y(\tau_A), z(\tau_A)) = (\tau_A, 0, 0, z_A)\,, \\ x_B(\tau_B) &= (t(\tau_B), x(\tau_B), y(\tau_B), z(\tau_B)) = (\tau_B, 0, 0, z_B)\,. \end{aligned} \tag{3.34}$$

We further assume that $a_x = a_y \equiv a(>0)$ and $u_0 = 0$ as in Fig. 3.6 and $\vec{x} = \vec{X} = \vec{0}$. The Wightman function then reduces to

$$W(x,y) = -\frac{1}{4\pi^2} \frac{1}{1 + a\Delta\theta \dfrac{(u-i\epsilon)(U+i\epsilon)}{\Delta u - i\epsilon}} \frac{1}{(\Delta v - i\epsilon)(\Delta u - i\epsilon)}\,. \tag{3.35}$$

It is worth noting that in this setup, the proper spatial distance between the two detectors, $L = |z_A - z_B|$, is the same as in Minkowski space, and that the two detectors are placed in the longitudinal direction of the shockwave.

In Fig. 3.5 (a), we plot the initial ($\mathcal{C}_{AB,0}$) and final ($\mathcal{C}_{AB}$) concurrences in the shockwave spacetime with $aT = 1$. In all figures, detector B is fixed at the position $z_B/T = 7$ which is located on the $u < u_0$ part of shockwave spacetime (see Fig. 3.6) and the energy gap is $\Omega T = 2$. Note that in Minkowski space, the non-communicating detectors cannot extract entanglement with $\Omega T = 2$, as shown in Figs. 3.3 (a) and 3.4.

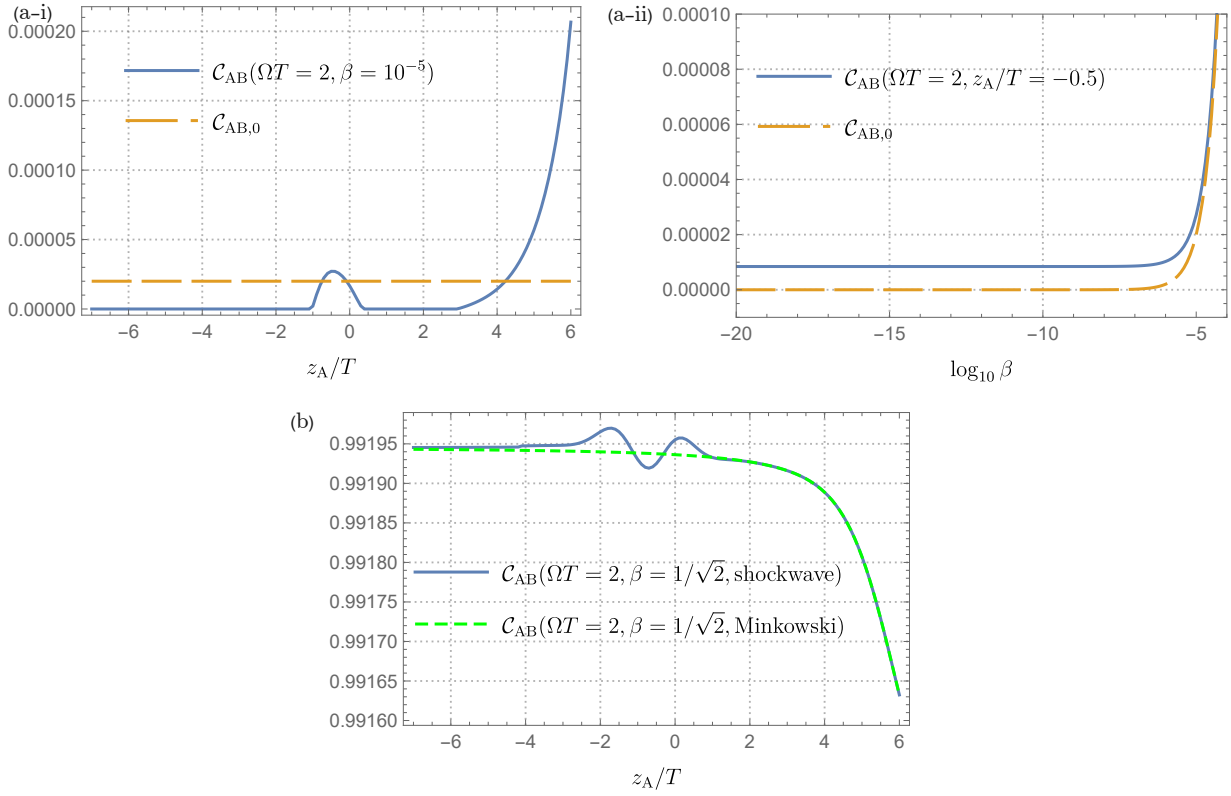


Figure 3.5: (a-i) Initial and final concurrences when $\Omega T = 2, \beta = 10^{-5}, \lambda = 1/10$, and $\theta = 0$. The location of detector B is fixed at $z_B/T = 7$. detector A encounters the shockwave near $z_A/T = 0$. (a-ii) The concurrences when $\Omega T = 2, z_A/T = -0.5$ and $z_B/T = 7$ with varying initial amount of entanglement. Two curves will cross and degradation takes place after $\log_{10}\beta > -3$. (b) Final concurrence $\mathcal{C}_{AB}$ for initially maximally entangled detectors ($\mathcal{C}_{AB,0} = 1$) with $\Omega T = 2$ and $\theta = 0$. The green dotted curve corresponds to detectors in Minkowski spacetime. In this case, the shockwave can either reduce or amplify the degradation effect.

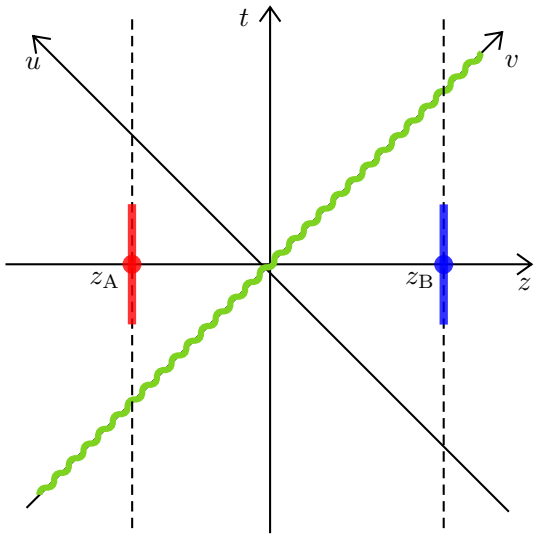


Figure 3.6: Diagram for two pointlike inertial detectors in a shockwave spacetime. Detectors A and B are static at $z = z_A$ and z_B, respectively, and the shockwave travels along $u = 0$ (the green wiggling line). The red and blue bars indicate the effective interaction duration of the detectors.

Figure 3.5 (a-i) depicts the concurrences as functions of detector A's static position z_A/T when $\beta = 10^{-5}$. As shown in Fig. 3.6, detector A encounters the shockwave around $z_A/T = 0$. For $z_A/T \lesssim -1$ the plot indicates that full entanglement degradation from the initial value of $\mathcal{C}_{AB,0}$ occurs, due to the fact that the geometry is Minkowski except along the shockwave trajectory. In other words, the behavior in $z_A/T \lesssim -1$ follows from the results in Minkowski spacetime given in Figs. 3.3 and 3.4. This is also true for $z_A/T \gtrsim 0.5$. The growth of $\mathcal{C}_{AB}$ in $z_A/T > 3$ comes from the communication effect in $|X_{AB}(-\Omega)|$ between the two detectors, which corresponds to the bottom left corner in Fig. 3.2 (b). The effect of the shockwave can be seen in the region $z_A/T \in [-1, 0.5]$; not only is the degradation effect reduced, but we find $\mathcal{C}_{AB} > \mathcal{C}_{AB,0}$—the initial entanglement is enhanced. Somewhat surprisingly, the shockwave allows causally disconnected detectors to gain more entanglement even when it is impossible to do this in Minkowski spacetime.

Figure 3.5 (a-ii) shows the β dependence of the concurrences when $z_A/T = -0.5$ (i.e., $L/T = 7.5$), where maximal entanglement enhancement occurs, with $\Omega T = 2, \lambda = 1/10$, and $\theta = 0$. We find that entanglement enhancement by the shockwave is possible so long as $\beta \lesssim 10^{-3}$. Recall that for any β, only degradation occurs for these parameters in Minkowski spacetime. Furthermore, even when $\Omega T = 7$ as in Figs. 3.3 (b) and 3.3 (c), the

initial amount of entanglement needs to be $\beta \lesssim 10^{-17}$ in order to extract entanglement. In this sense, a shockwave drastically assists extraction of entanglement.

However, the shockwave does not always enhance entanglement. In Fig. 3.5 (b), we plot the final concurrence when the detectors are initially maximally entangled, $\mathcal{C}_{AB,0} = 1$. In both Minkowski (dotted curve) and shockwave (solid) spacetimes, degradation takes place as expected. Notice that the shockwave could either reduce or assist degradation. This is due to the fact that the concurrence is now determined by (3.18); the degradation part $\mathrm{Re}[Y_A + Y_B]$ is no longer suppressed by small β^2 and the harvesting part $|X_{AB}(-\Omega)|$ is negligible.

3.5 Conclusion

We considered two initially entangled UDW detectors interacting with a quantum scalar field and examined how their initial entanglement behaves after the interaction. The entanglement harvesting protocol allows initially uncorrelated detectors to extract entanglement from the field in its vacuum state without signaling, whereas entanglement degradation is the process in which initial entanglement decreases due to the detectors becoming entangled with the field. We have investigated which phenomenon is dominant when the detectors are neither uncorrelated nor maximally entangled.

Such an analysis is known to be difficult when a perturbative method is employed since there is a UV-divergent element in the density matrix for the pointlike detectors (and hence in entanglement measures). One can circumvent this issue by introducing a smearing function and performing an approximation to an entanglement measure such as concurrence and negativity. We have dealt with this by introducing an approximation for weakly entangled detectors, supplementing the method used for initially sufficiently entangled detectors [95]. Under any of these approximations, the divergent element is absent in the entanglement measure.

With these approximations, we examined the fate of entanglement in detectors at rest in $(3 + 1)$-dimensional Minkowski spacetime. We found that initially weakly entangled detectors can gain entanglement even when they are causally disconnected. This can be understood by looking at the distinct contributions to the concurrence: one part is from the initial entanglement, another yields entanglement harvesting, and a third causes entanglement degradation. The detectors extract entanglement if the entanglement harvesting contribution to the concurrence exceeds the other two. Otherwise, entanglement degradation takes place and the initial amount of entanglement will be reduced after the interaction.

The fact that only weakly entangled detectors can gain entanglement is consistent with previous results (Ref. [164]) demonstrating that, non-perturbatively, quantum mutual information (i.e., total correlations including classical ones) between entangled detectors can be enhanced only when their initial entanglement is weak.[3] It is important to note, however, that the detectors can gain mutual information even when they are causally disconnected. Our results provide an interesting contrast insofar as we employ a perturbative analysis with a Gaussian switching function and near-pointlike detectors.

We have also analyzed the energy gap Ω dependence for entanglement extraction. In the entanglement harvesting scenario [362], detectors with Gaussian switching can extract entanglement so long as their energy gap is above the minimum value: $\Omega \geq \Omega_{\text{min}}$. This feature allows one to harvest entanglement with detectors arbitrarily far away from each other once a sufficiently large energy gap is chosen. This is not the case for entangled detectors. Instead there is a range $\Omega \in [\Omega_{\text{min}}, \Omega_{\text{max}}]$ within which the detectors can extract entanglement. This range tends to zero as the distance between the detectors increases. This suggests that entanglement extraction is not allowed for detectors arbitrarily far away from each other. Nevertheless, the maximum value Ω_{max} will increase as the initial state approaches a separable state, recovering the results of the standard entanglement harvesting protocol.

We found that the presence of a gravitational shockwave, in which the metric is identical to that of Minkowski spacetime except along a single null trajectory, significantly modifies these effects. Detectors far from the shockwave exhibit the same behavior as in Minkowski spacetime. However as they come closer to the shockwave their behavior markedly changes. The shockwave enhances entanglement as compared to Minkowski spacetime. The range $\Omega \in [\Omega_{\text{min}}, \Omega_{\text{max}}]$ of energy gap that enables entanglement extraction becomes wider, which in turn allows the detectors to gain entanglement for smaller values of Ω.

Although the shockwave enhances entanglement, its extraction is still limited to weakly entangled detectors. If the initial state of the detectors is sufficiently entangled, the shockwave weakens the effect of degradation rather than enhancing extraction of correlations. Nevertheless, our results show that spacetime geometry can enhance initial entanglement harvesting, indicating that the quantum vacuum is indeed a resource (at least in principle) for carrying out quantum information tasks. We close by commenting on a recent similar investigation of the negativity [40] of two initially entangled detectors in Minkowski spacetime with constant switching. Using an approximation corresponding to our sufficiently entangled case, the detectors were found to only experience entanglement degradation,

[3] The nonperturbative method employed in [164] uses a delta-switching function, which cannot harvest entanglement at all if each detector switches only once [393, 392].

consistent with our results for sufficiently entangled detectors with an infinitely long interaction.

Chapter 4

Probing Hidden Topology with UDW Detectors

We consider the transition rate of a static Unruh-DeWitt detector in two (2+1)-dimensional black hole spacetimes that are isometric to the static Bañados-Teitelboim-Zanelli (BTZ) black hole outside the horizon but have no asymptotically locally anti-de Sitter exterior behind the horizon. The spacetimes are the $\mathbb{R}\mathrm{P}^2$ geon, with spatial topology $\mathbb{R}\mathrm{P}^2 \setminus \{\text{point at infinity}\}$, and the Swedish geon of Åminneborg *et al*, with spatial topology $T^2 \setminus \{\text{point at infinity}\}$. For a conformal scalar field, prepared in the Hartle-Hawking-type state that is induced from the global vacuum on the anti-de Sitter covering space, we show numerically that the detector's transition rate distinguishes the two spacetimes, particularly at late exterior times, and we trace this phenomenon to the differences in the isometries that are broken by the quotient construction from the universal covering space. Our results provide an example in which information about the interior topology of a black hole is accessible to a quantum observer outside the black hole.

4.1 Introduction

Black holes are amongst the most fascinating objects in nature, in large part because they cloak certain regions of space and time from all distant observers. While black holes created in a gravitational collapse are not time symmetric, their eternal counterparts contain both a future horizon and past horizon, and continuing the spacetime analytically past these horizons reveals new structure, a prime example of which is the second asymptotically

flat region in the Kruskal(-Szekeres-Fronsdal) [258, 414, 160] extension of positive mass Schwarzschild spacetime. The structure past the horizon has a pivotal role in recognising Hawking temperature as the distinguished temperature for quantum fields in thermal equilibrium with the black hole [190, 230], and it provides the cornerstone to the view of black hole entropy as a fundamentally quantum-gravitational concept [171].

What lies beyond the black hole horizon is, by definition, inaccessible to classical observers outside the horizon. However, in an eternal black hole spacetime, with both a future horizon and a past horizon, states of quantum fields that are regular on the extended spacetime are constrained by the spacetime structure behind the horizons. For such states, it is therefore possible for a local quantum observer to distinguish what lies behind the horizon by probing the state of a quantum field outside the horizon [288, 290, 291, 70, 285, 397]. In this chapter we address this phenomenon for a class of black hole spacetimes known as topological geons [404], in which there is no second asymptotic region behind the horizon [285, 287, 256].

The geon black hole spacetimes that we consider are $(2+1)$-dimensional eternal black holes, which are solutions to Einstein's equations with a negative cosmological constant, and have an exterior region that is isometric to that of the spinless non-extremal Bañados-Teitelboim-Zanelli (BTZ) black hole [36, 34].We consider two families, both obtained as a quotient of an open set in $(2+1)$-dimensional anti-de Sitter spacetime (AdS_3) by a discrete group of isometries. One family is the $\mathbb{R}\mathrm{P}^2$ geon [290], which is a $\mathbb{Z}_2$ quotient of the BTZ black hole and has spatial topology $\mathbb{R}\mathrm{P}^2 \setminus \{\text{point at infinity}\}$. The other is the "Swedish geon" of Åminneborg *et al* [24], which has spatial topology $T^2 \setminus \{\text{point at infinity}\}$. In both of these spacetimes, the exterior Killing vector that generates exterior BTZ time translations does not extend to a Killing vector on the full spacetime. The state that a quantum field inherits from the global vacuum on AdS_3 is hence not static in the exterior region [290, 291], in contrast to the Hartle-Hawking-type state inherited by the BTZ spacetime [273, 77], and this nonstaticity bears an imprint of the spacetime structure behind the horizon. We shall analyse how a local quantum observer outside the horizon can access this imprint.

We consider a massless conformal scalar field and model a local quantum observer by a UDW detector, working to linear order in the field-detector coupling. We compute the detector's transition rate on a trajectory that is static in the exterior geometry: the time dependence in this transition rate is then precisely due to the geon-like spacetime structure behind the horizon. For both the $\mathbb{R}\mathrm{P}^2$ geon and the Swedish geon, our numerical results show that the transition rate in the asymptotic past reduces to that on the BTZ hole. Assuming the detector to be switched on in the asymptotic past, the late time behaviour, however, differs for the two spacetimes. The late time transition rate in the Swedish geon

asymptotes to that in the BTZ hole. The late time transition rate in the $\mathbb{R}\mathrm{P}^2$ geon, by contrast, asymptotes to a different constant for a gapless detector, and it displays persisting oscillations for a detector with a nonvanishing gap; the latter property is consistent with what was previously found for the $\mathbb{R}\mathrm{P}^2$ geon [397], and with what happens for uniformly accelerated detectors in flat spacetimes with a similar structure behind the Rindler horizon [270, 268]. This difference between the late time transition rates is a dramatic demonstration of how the detector in the exterior can distinguish different spacetime topologies behind the horizon.

As a side product, we give explicit formulas for the isometries by which the Swedish geon is quotiented from AdS_3, in a representation in which the exterior region takes a standard form, and we display a fundamental domain for the spacelike hypersurface of time symmetry. This representation of the isometries can be employed to investigate other properties of the quantum state that the Swedish geon inherits from the global vacuum on AdS_3, such as the stress-energy tensor.

This chapter is organized as follows. Section 4.2 gives a brief review of an UDW detector coupled to a scalar field, writing down the transition rate of a detector that is switched on and off sharply. Section 4.3 presents the static BTZ black hole, the $\mathbb{R}\mathrm{P}^2$ geon and the Swedish geon as quotients of subsets of AdS_3, deferring technicalities to appendix A. Section 4.4 gives the image sum constructions for the static detector's transition rate on these spacetimes, for a conformal scalar field in the state induced from the global vacuum on AdS_3. Numerical results for the detector's transition rate are presented in Section 4.5. Section 4.6 gives the conclusions and a brief discussion.

4.2 Physical Setup

Before the interaction is turned on, we prepare the detector in the state $|0_D\rangle$ and the field ϕ in the state that we denote here by $|0\rangle$ and specify individually in the applications in the later sections. Working in first-order perturbation theory, the probability of finding the detector in the state $|1_D\rangle$ after the interaction has ceased, regardless the final state of the field, is [242, 294]

$$P(\Omega) = \lambda^2 \mathcal{F}(\Omega), \tag{4.1}$$

where the response function $\mathcal{F}(\Omega)$ is given by

$$\mathcal{F}(\Omega) = \int_{-\infty}^{\infty} d\tau \int_{-\infty}^{\infty} d\tau' \chi(\tau)\chi(\tau')\, e^{-i\Omega(\tau-\tau')} W(\tau,\tau'). \tag{4.2}$$

We take χ to be the characteristic function of an interval of time, as the response function remains well defined in this limit in $2+1$ spacetime dimensions despite the discontinuities at the switch-on and switch-off moments. We further consider not the response function itself, but its derivative with respect to the switch-off moment, denoted by $\dot{\mathcal{F}}$, which has an interpretation as (a multiple of) the detector's transition rate, operationally measurable using ensembles of detectors [268, 385, 294]. For a detector switched on at time τ_0 and off at time τ, the transition rate is given by [211]

$$\dot{\mathcal{F}}(\Omega) = \frac{1}{4} + 2\int_0^{\Delta\tau} ds\ \mathrm{Re}\left[e^{-i\Omega s} W(\tau, \tau - s)\right], \tag{4.3}$$

where $\Delta\tau = \tau - \tau_0$. If the detector is switched on in the asymptotic past, $\tau_0 \to -\infty$, the transition rate (4.3) becomes

$$\dot{\mathcal{F}}(\Omega) = \frac{1}{4} + 2\int_0^{\infty} ds\ \mathrm{Re}\left[e^{-i\Omega s} W(\tau, \tau - s)\right]. \tag{4.4}$$

Note that while $W(\tau, \tau')$ has a distributional singularity at $\tau = \tau'$, the integrals in (4.3) and (4.4) do not have distributional contributions from $s = 0$. This is because the singularity in $W(\tau, \tau')$ is that of

$$\frac{-i}{4\pi(\tau - \tau' - i\epsilon)} \xrightarrow[\epsilon \to 0_+]{} \frac{-i}{4\pi} P\left(\frac{1}{\tau - \tau'}\right) + \frac{1}{4}\delta(\tau - \tau'), \tag{4.5}$$

where P stands for the Cauchy principal value: the term $\frac{1}{4}$ in (4.3) and (4.4) has come from the Dirac delta in (4.5), and the integrals in (4.3) and (4.4) are nonsingular at $s = 0$ on taking the real part.

4.3 Quotients of AdS_3

In this section we describe three black hole spacetimes that are quotients of an open subset in AdS_3.

4.3.1 AdS_3

Recall that AdS_3 may be defined as the hyperboloid

$$X_1^2 + X_2^2 - T_1^2 - T_2^2 = -\ell^2 \tag{4.6}$$

in $\mathbb{R}^{2,2}$ with the metric

$$ds^2 = dX_1^2 + dX_2^2 - dT_1^2 - dT_2^2, \tag{4.7}$$

where ℓ is a positive constant of dimension length. This spacetime is a solution to Einstein's equations with the cosmological constant $\Lambda = -\ell^2$ [77].

It is useful to introduce two local coordinate systems on open subsets of AdS_3 as follows. First, in the subset B_1, defined as $T_1 > |X_1|$, we introduce the coordinates (U, V, ϕ) by

$$\begin{aligned} T_1 &= \ell \left(\frac{1-UV}{1+UV}\right) \cosh(\sqrt{M}\,\phi), \\ X_1 &= \ell \left(\frac{1-UV}{1+UV}\right) \sinh(\sqrt{M}\,\phi), \\ T_2 &= \ell \left(\frac{V+U}{1+UV}\right), \\ X_2 &= \ell \left(\frac{V-U}{1+UV}\right), \end{aligned} \tag{4.8}$$

where $-1 < UV < 1$, $-\infty < \phi < \infty$, and M is a positive parameter. The metric takes the form

$$ds^2 = -\frac{4\ell^2}{(1+UV)^2} dU dV + r_h^2 \left(\frac{1-UV}{1+UV}\right)^2 d\phi^2. \tag{4.9}$$

Second, in the subset of B_1 where $U < 0$ and $V > 0$, we introduce the coordinates (t, r, ϕ), where

$$\begin{aligned} \frac{r}{r_h} &= \frac{1-UV}{1+UV}, \\ \frac{r_h t}{\ell^2} &= \frac{1}{2} \ln\left(-\frac{V}{U}\right), \end{aligned} \tag{4.10}$$

where $r_h = \ell\sqrt{M}$, so that $r_h < r < \infty$ and $-\infty < \phi < \infty$. In terms of the embedding

space coordinates, this means

$$\begin{aligned} X_1 &= \ell \frac{r}{r_h} \sinh\left(\frac{r_h}{\ell}\phi\right), \\ X_2 &= \ell \sqrt{\frac{r^2}{r_h^2} - 1} \cosh\left(\frac{r_h}{\ell^2}t\right), \\ T_1 &= \ell \frac{r}{r_h} \cosh\left(\frac{r_h}{\ell}\phi\right), \\ T_2 &= \ell \sqrt{\frac{r^2}{r_h^2} - 1} \sinh\left(\frac{r_h}{\ell^2}t\right), \end{aligned} \tag{4.11}$$

and the metric reads

$$ds^2 = -\left(\frac{r^2 - r_h^2}{l^2}\right)dt^2 + \left(\frac{r^2 - r_h^2}{l^2}\right)^{-1} dr^2 + r^2 d\phi^2. \tag{4.12}$$

We refer to (4.12) as the AdS-Rindler metric [399].

4.3.2 BTZ black hole

The spinless BTZ spacetime is obtained from B_1 with the metric (4.9) by the identification $(U, V, \phi) \sim (U, V, \phi + 2\pi)$. This spacetime is an eternal black-and-white-hole spacetime, with a bifurcate Killing horizon at $|U| = |V|$, and (U, V, ϕ) are Kruskal-type coordinates [36, 34, 77]. The mass of the black hole is M. We may write the spacetime as the quotient space

$$\mathcal{M}_{\mathrm{BTZ}} = \mathsf{B}_1/\mathbb{Z}, \tag{4.13}$$

where $\mathbb{Z} \simeq \{\Gamma^n : n \in \mathbb{Z}\}$ with

$$\Gamma : \ (U, V, \phi) \mapsto (U, V, \phi + 2\pi). \tag{4.14}$$

The quadrant where $U < 0$ and $V > 0$, covered by the coordinates (t, r, ϕ) with the identification $(t, r, \phi) \sim (t, r, \phi + 2\pi)$, is an exterior region. The metric is given by (4.12), and the horizon is at $r \to r_h$.

4.3.3 $\mathbb{R}\mathrm{P}^2$ geon

The $\mathbb{R}\mathrm{P}^2$ geon [290] is the quotient of the BTZ spacetime by the isometry group $\{e, J\} \simeq \mathbb{Z}_2$, where e is the identity and

$$J : (U, V, \phi) \mapsto (V, U, \phi + \pi). \tag{4.15}$$

We may write

$$\mathcal{M}_{\mathbb{R}\mathrm{P}^2} = \mathcal{M}_{\mathrm{BTZ}}/\mathbb{Z}_2. \tag{4.16}$$

This spacetime is an eternal black and white hole spacetime with just a single exterior region, in which the metric is as in (4.12). While the exterior is static, with the timelike Killing vector ∂_t, this Killing vector does not extend to all of the geon spacetime, and the geometry behind the horizons hence makes the $t = 0$ hypersurface a distinguished hypersurface of time symmetry [290, 397, 399].

4.3.4 Swedish geon

The Swedish geon [24] is a single-exterior black-and-white hole quotient of an open region in AdS_3, with the exterior metric given by the BTZ exterior (4.12), but with behind-the-horizon identifications that give the spacetime the spatial topology of a punctured torus, the puncture being at the AdS infinity, $r \to \infty$ in (4.12). We review the construction of this spacetime in the three appendices, showing that the spacetime is a quotient of a subset of AdS_3 by the free group generated by the $O(2,2)$ matrices A and B given by

$$A = \begin{pmatrix} 1 & 0 & 0 & 0 \\ 0 & \dfrac{\cosh(6z) + 2\cosh(4z) + \cosh(2z)}{4\sinh^2(z)} & \dfrac{\sqrt{\cosh(2z)}\cosh(4z)}{\sinh^2(z)} & \sinh(4z) \\ 0 & -\dfrac{\sqrt{\cosh(2z)}}{\sinh^2(z)} & -\coth^2(z) & 0 \\ 0 & -\dfrac{\cosh(5z) + 3\cosh(3z) + 4\cosh(z)}{2\sinh(z)} & -4[\cosh(2z)]^{3/2}\coth(z) & -\cosh(4z) \end{pmatrix}, \tag{4.17a}$$

$$B = \begin{pmatrix} 1 & 0 & 0 & 0 \\ 0 & \dfrac{\cosh(4z)+\cosh(2z)}{2\sinh^2(z)} & \dfrac{[\cosh(2z)]^{3/2}}{\sinh^2(z)} & \dfrac{\cosh(3z)+\cosh(z)}{\sinh(z)} \\ 0 & -\dfrac{[\cosh(2z)]^{3/2}}{\sinh^2(z)} & -\coth^2(z) & -2\sqrt{\cosh(2z)}\coth(z) \\ 0 & \dfrac{\cosh(3z)+\cosh(z)}{\sinh(z)} & 2\sqrt{\cosh(2z)}\coth(z) & 2\cosh(2z)+1 \end{pmatrix}, \tag{4.17b}$$

acting by matrix multiplication on the column vectors

$$\begin{pmatrix} T_2 \\ T_1 \\ X_2 \\ X_1 \end{pmatrix}, \tag{4.18}$$

where $z = \frac{1}{4}\pi\sqrt{M}$. (We have dropped in (4.17) the undertildes by which these matrices are denoted in (A.14) in A.1.) The exterior region is again covered by the coordinates (t, r, ϕ) (4.11), so that M is the black hole mass. The isometry $(t, r, \phi) \mapsto (t, r, \phi + 2\pi)$ is generated by the matrix $BAB^{-1}A^{-1}$.

4.4 Transition rate comparisons

In this section we present the image sum expressions for the detector's transition rate on the BTZ black hole, the $\mathbb{R}\mathrm{P}^2$ geon and the Swedish geon, in the state induced from the AdS_3 global vacuum.

4.4.1 Preamble: choice of the state

An example close to the spacetimes considered in the present chapter is the Schwarzschild black hole spacetime. In the exterior region, Schwarzschild time translations single out the state known as the Boulware state [55], which is close to the Minkowski vacuum at asymptotically flat infinity, but is singular on approaching the black and white hole horizons. On the Kruskal extension of Schwarzschild, translations along the horizon generator affine parameters single out the state known as the Hartle-Hawking or Hartle-Hawking-Israel state [190, 230], which physically describes a Hawking-radiating black hole in thermal

equilibrium with a heat bath at infinity, and is the unique regular state that is invariant under all the continuous isometries [248]. A third state of interest is the Unruh state [428], defined on the union of an exterior region, the black hole region, and the black hole horizon joining the two: this state is defined in terms of positive frequency with respect to Minkowski time translations at the past infinity and with respect to the future horizon generator on the future horizon, and it physically describes a Hawking-radiating black hole with no infalling radiation from the past infinity, but it is singular on the past horizon.

On the spinless BTZ black hole spacetime, a new feature compared with Schwarzschild is that the asymptotically AdS infinity requires a boundary condition to make the theory unitary [33]. Physically, the effect of asymptotically AdS infinity on wave propagation is similar to that of a boundary at a finite distance, and the boundary condition means specifying the phase shift for waves that are reflected back from infinity. The boundary condition therefore does not allow the field to be decomposed into "incoming" and "outgoing" parts near infinity, and this prevents the construction of a time-asymmetric state similar to the Unruh state on Schwarzschild. A Boulware-type state in the BTZ black hole exterior can be readily defined, using the boundary condition at infinity and the notion of positive frequency with respect to the exterior Killing time translations, but this state is singular on the future and past horizons, like the Boulware state on exterior Schwarzschild.

The state we consider on the spinless BTZ black hole spacetime is the state induced from the AdS_3 global vacuum by the $\mathbb{Z}$ quotient described in Section 4.3.2 [409]. We may refer to this state as a Hartle-Hawking type state: it is regular over all of the BTZ spacetime, it is invariant under the continuous isometries of the spacetime, and it physically describes a Hawking-radiating black hole in thermal equilibrium with a heat bath at asymptotic infinity. We emphasize that this state knows not just about the geometry in a single exterior region: it knows about the full global structure that the spacetime has behind the black and white hole horizons. Detectors interacting with this state have been considered in [211, 365].

On the $\mathbb{R}P^2$ geon and the Swedish geon, we follow the example of the BTZ spacetime and consider the state induced from the AdS_3 global vacuum by the quotients described in Sections 4.3.3 and 4.3.4. In each case, the state is regular on all of the spacetime, including the horizons, and the state knows about the full global spacetime structure, including that behind the horizons. What is new is that the restriction of the state to the exterior region is not invariant under the exterior Killing time translations, because the quotienting group contains elements that do not commute with these translations. Detectors interacting with this state on the $\mathbb{R}P^2$ geon have been considered in [397, 399, 405]. We shall consider a detector interacting with this state on the Swedish geon, and compare with detectors on the BTZ spacetime and on the $\mathbb{R}P^2$ geon.

4.4.2 Image sum in the state induced from the AdS_3 global vacuum

On each of the three quotients of an open region in AdS_3, we now consider the state induced from the AdS_3 global vacuum, as described above.

We denote by G the discrete group by which the quotient is taken. The Wightman function on the quotient spacetime is then given by the method-of-images sum

$$W_{\mathrm{AdS}_3/G}(x,x') = \sum_{g\in G} W_{\mathrm{AdS}_3}(x,gx'), \tag{4.19}$$

where W_{AdS_3} is the Wightman function on AdS_3.

The global vacuum Wightman function for a massless conformally-coupled scalar field in AdS_3 takes the form [77, 399]

$$W_{\mathrm{AdS}_3}(x,x') = \frac{1}{4\pi\sqrt{2}\ell}\left(\frac{1}{\sqrt{\sigma(x,x')}} - \frac{\zeta}{\sqrt{\sigma(x,x')+2}}\right), \tag{4.20}$$

where $\sigma(x,x')$ is $1/(2\ell^2)$ times the square of the geodesic distance between the spacetime points x and x' in the embedding space $\mathbb{R}^{2,2}$,

$$\sigma(x,x') = \frac{1}{2\ell^2}\Big[(X_1-X_1')^2 - (T_1-T_1')^2 + (X_2-X_2')^2 - (T_2-T_2')^2\Big], \tag{4.21}$$

and the parameter $\zeta \in \{-1,0,1\}$ specifies the boundary condition at the asymptotically AdS infinity. $\zeta = 1$ and $\zeta = -1$ are respectively the Dirichlet and Neumann boundary conditions, each of which determines a quantum theory with unitary evolution. $\zeta = 0$ is the transparent boundary condition, with no reflection from the infinity, and a less clear physical interpretation [33].

In all three spacetimes, we consider a UDW detector on the static exterior worldline that is given in the BTZ exterior coordinates (4.12) by

$$(t,r,\phi) = \left(\frac{\ell}{\sqrt{R^2-r_h^2}}\tau,\ R,\ 0\right), \tag{4.22}$$

where $R > r_h$ is the detector's radial coordinate and τ is the detector's proper time. Taking the detector to be switched on in the asymptotic past, the detector's transition rate may then be obtained by inserting the trajectory (4.22) in (4.4) with (4.19) and (4.20).

We consider the three spacetimes in turn.

4.4.3 BTZ

On the BTZ spacetime, we have

$$W_{\mathrm{BTZ}}(x,x') = \sum_{n=-\infty}^{\infty} W_{\mathrm{AdS}_3}(x,\Gamma^n x'), \tag{4.23}$$

where Γ is given in (4.14). In the exterior, in the coordinates (4.11), the action of Γ reads

$$\Gamma: \ (t,r,\phi) \mapsto (t,r,\phi+2\pi). \tag{4.24}$$

It follows that [211]

$$\dot{\mathcal{F}}_{\mathrm{BTZ}}(\Omega) = \frac{e^{-\ell\beta\Omega/2}}{2\pi} \sum_{n=-\infty}^{\infty} \int_0^\infty dy \cos(y\ell\beta\Omega/2) \left(\frac{1}{\sqrt{K_n+\cosh^2 y}} - \frac{\zeta}{\sqrt{Q_n+\cosh^2 y}} \right), \tag{4.25}$$

where

$$\begin{aligned} K_n &:= \frac{R^2}{R^2-r_h^2} \sinh^2\left(n\pi \frac{r_h}{\ell}\right), \\ Q_n &:= K_n + \frac{r_h^2}{R^2-r_h^2}, \\ \beta &:= 2\pi \frac{\sqrt{R^2-r_h^2}}{r_h}. \end{aligned} \tag{4.26}$$

Note that the transition rate has no dependence on the switch-off moment τ. This is because the isometry Γ (4.14) commutes with translations along the trajectory (4.22).

4.4.4 $\mathbb{R}\mathrm{P}^2$ geon

On the $\mathbb{R}\mathrm{P}^2$ geon, we have

$$W_{\mathbb{R}\mathrm{P}^2}(x,x') = W_{\mathrm{BTZ}}(x,x') + W_{\mathrm{BTZ}}(x,Jx'), \tag{4.27}$$

where J is given in (4.15). It follows that

$$\dot{\mathcal{F}}_{\mathbb{R}\mathrm{P}^2}(\Omega) = \dot{\mathcal{F}}_{\mathrm{BTZ}}(\Omega) + \Delta\dot{\mathcal{F}}_{\mathbb{R}\mathrm{P}^2}(\Omega,\tau), \tag{4.28}$$

where the additional contribution due to the geon identification may be written as [397]

$$\Delta\dot{\mathcal{F}}_{\mathbb{R}\mathrm{P}^2}(\Omega,\tau)=\frac{1}{2\pi}\sum_{n=-\infty}^{\infty}\int_0^\infty dy\cos(y\ell\beta\Omega/2)\\ \times\left[\frac{1}{\sqrt{\bar{K}_n+\cosh^2\left(y-\frac{\pi\tau}{\beta\ell}\right)}}-\frac{\zeta}{\sqrt{\bar{Q}_n+\cosh^2\left(y-\frac{\pi\tau}{\beta\ell}\right)}}\right] \tag{4.29}$$

where

$$\bar{K}_n:=\frac{R^2}{R^2-r_h^2}\sinh^2\left[\left(n+\frac{1}{2}\right)\pi\frac{r_h}{\ell}\right],\\ \bar{Q}_n:=K_n+\frac{r_h^2}{R^2-r_h^2}. \tag{4.30}$$

Note that the transition rate now depends on the switch-off moment τ. If the detector is switched off in the distant past, $\tau\to-\infty$, the geon correction term $\Delta\dot{\mathcal{F}}_{\mathbb{R}\mathrm{P}^2}$ (4.29) is small, and the response is nearly identical to that in BTZ spacetime. However, $\Delta\dot{\mathcal{F}}_{\mathbb{R}\mathrm{P}^2}$ becomes significant near $\tau=0$, and it stays significant as $\tau\to\infty$. This is because the isometry J (4.15) does not commute with translations along the trajectory (4.22): among all constant t surfaces in the geon's exterior, the surface $t=0$ is the only one that extends to a smooth geodesically complete surface in the geon spacetime [290].

4.4.5 Swedish geon

Since the matrices A and B (4.17) are a pair of free generators for the fundamental group of the Swedish geon, the Swedish geon Wightman function takes the form (4.19), where each g is a unique string in A and B and their inverses, such that A and A^{-1} may not appear next to each other and B and B^{-1} may not appear next to each other, but subject to no other conditions. For g with exactly $N\geq 1$ generators in the string, there are $4\cdot 3^{N-1}$ terms in the sum, in addition to the pure AdS_3 term $W_{\mathrm{AdS}_3}(x,x')$; for g with up to $K\geq 1$ generators in the string, there are

$$\sum_{N=1}^{K}4\cdot 3^{N-1}=2(3^K-1) \tag{4.31}$$

terms in addition to the pure AdS_3 term. The detector's transition rate is now obtained from (4.4) with (4.22), (4.19) and (4.20).

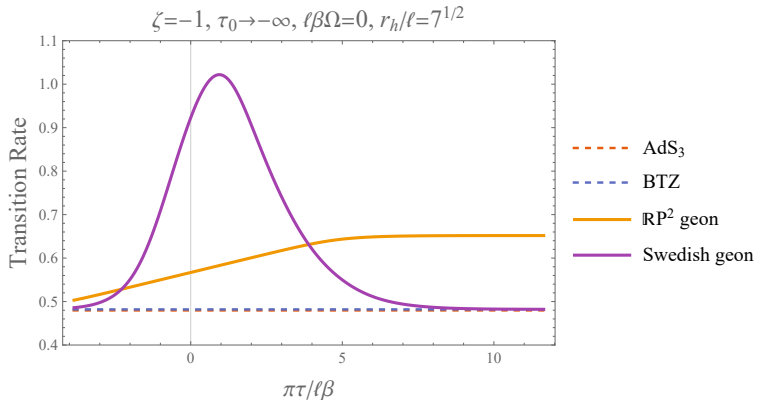
In numerical evaluation, we group the terms in the sum by the number of generators in the string, and we truncate the sum at a finite number K of generators, monitoring the accuracy of the truncation by increasing K. As terms with a large number of generators are suppressed by successive factors that are negative exponentials in $\sqrt{M}$, accurate evaluation requires fewer terms for larger values of M.

4.5 Results

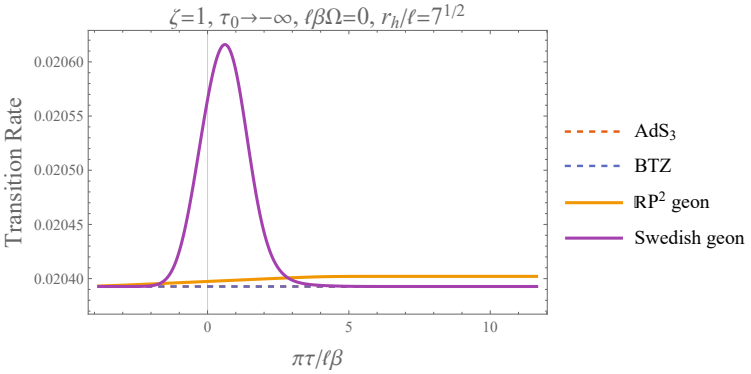
Fig. 4.1 shows numerical results for the detector's transition rate as a function of the switch-off moment on AdS_3, the BTZ black hole, the $\mathbb{R}P^2$ geon, and the Swedish geon. The detector is switched on in the asymptotic past and the detector's gap is set to zero. We have set $M = 7$, so that $r_h = \sqrt{7}\ell$, and the detector is placed at $R = \frac{5}{\sqrt{7}} r_h$. The three panels show the boundary condition at infinity being respectively Neumann, Dirichlet, and transparent.

On AdS_3 and on the BTZ hole, the transition rate is independent of the switch-off moment, by the time translation symmetry of the global vacuum on AdS, and by the corresponding time translation symmetry inherited by the Hartle-Hawking state on the BTZ black hole. This independence is clear in all three panels in Fig. 4.1. With the parameters chosen, the transition rates on AdS_3 and the BTZ hole are so close that they are indistinguishable by the naked eye. On the $\mathbb{R}P^2$ geon, the transition rate in the asymptotic past agrees with that for the BTZ black hole, but in the asymptotic future it differs: this phenomenon was previously noticed in [397], and traced to the fact that the Hartle-Hawking-type state on the $\mathbb{R}P^2$ geon exterior is not invariant under the exterior Killing time translations, and to the way in which the late time additional contributions arise from the detector having operated in the distant past. Related observations in flat spacetimes with similar isometries were made in [270, 268].

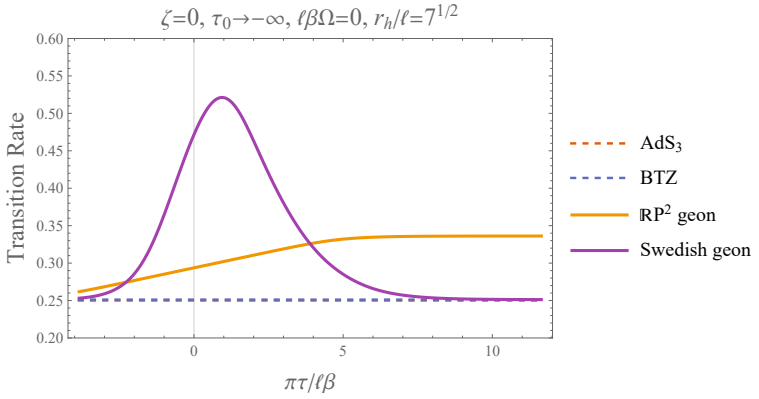
Now, for the Swedish geon, Fig. 4.1 shows that the transition rate agrees with that for the BTZ black hole both in the asymptotic past and in the asymptotic future, but it displays a distinct bump at intermediate times. The behaviour seen in the asymptotic past is as expected, stemming from the lack of exterior time translation symmetry of the Hartle-Hawking type state induced from the global vacuum. The behaviour seen in the asymptotic future is numerical evidence that the Swedish geon correlations between the asymptotic future and asymptotic past are significantly more involved than those on the $\mathbb{R}P^2$ geon. An analytic explanation of this phenomenon and the underlying correlations would require a deeper geometric study of the discrete group action by which the Swedish geon is quotiented from AdS_3.



(a)



(b)



(c)

Figure 4.1: The transition rate of a gapless detector, switched on in the asymptotic past, as a function of the switch-off moment, for AdS_3, the BTZ black hole, the $\mathbb{RP}^2$ geon, and the Swedish geon. The parameters are $r_h/\ell = \sqrt{7}$ and $R^2/r_h^2 = \frac{25}{7}$. Panels (a), (b) and (c) are for the Neumann ($\zeta = -1$), Dirichlet ($\zeta = 1$), and transparent ($\zeta = 0$) boundary condition, respectively. The transition rates on AdS_3 and the BTZ black hole so close that they are indistinguishable by the naked eye.

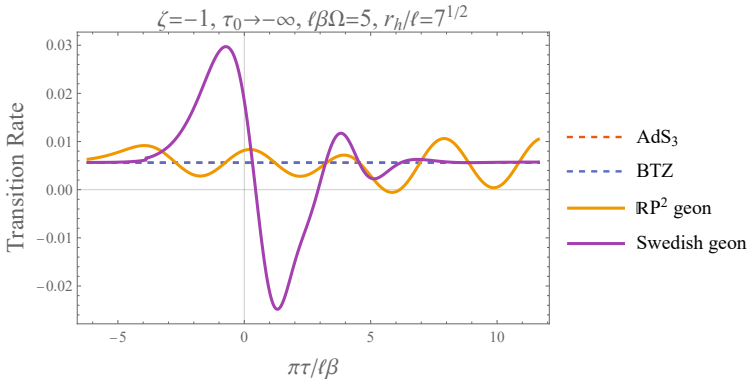


Figure 4.2: As in Fig. 4.1(a) but with $\ell\beta\Omega = 5$, giving the excitation rate of a detector with a nonzero gap. The transition rates on AdS_3 and the BTZ black hole are again so close that they are indistinguishable by the naked eye.

For a detector with a nonzero gap, a plot for $\ell\beta\Omega = 5$ and the Neumann boundary condition is shown in Fig. 4.2. The graph shows that the transition rate on the $\mathbb{R}P^2$ geon and the Swedish geon display more oscillations as a function of the switch-off moment. For the $\mathbb{R}P^2$ geon these oscillations continue to asymptotically late times, as noted in [397], but on the Swedish geon we see the late time transition rate again asymptotically approaches the stationary BTZ value.

Fig. 4.3 is as in Figures 4.1(a) and 4.2 but with a smaller black hole. The qualitative features are similar, but the bumps in the Swedish geon transition rate are now noticeably larger. The AdS_3 transition rate and the BTZ black hole transition rate are now distinguishable by eye in Fig. 4.3.

Regarding numerical accuracy, the more massive Swedish geon plots include contributions from image terms with up to $K = 5$ generators in the strings that define the group elements. We checked that the results did not change visibly on taking $K = 6$. We also made additional spot checks at late times with $K = 8$, involving a total of $13,120$ image terms. While we found this to be sufficient for the more massive black hole mass $M = 7$ used in the plots, numerical accuracy for smaller values of M would require more image terms. The less massive ($M = 3$) Swedish geon plots include contributions from image terms with up to $K = 8$ generators, for sufficient accuracy.

4.6 Conclusions and discussion

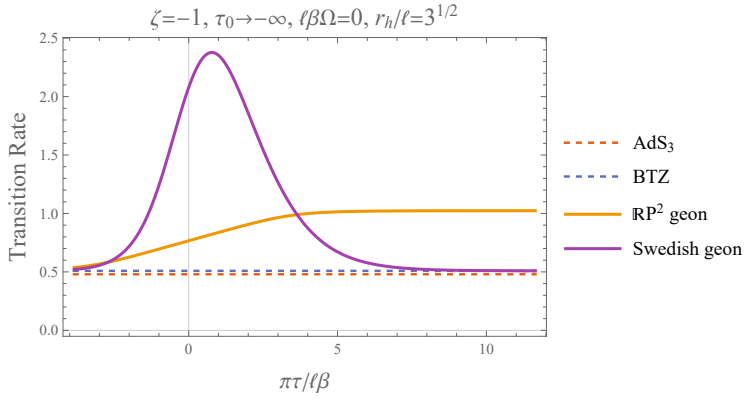
We have considered the transition rate of a static UDW detector in two $(2+1)$-dimensional black hole spacetimes that are isometric to the static BTZ black hole outside the horizon but have the spatial topology of a topological geon, with no second exterior region behind the black-and-white-hole horizons. The detector was coupled linearly to a conformal scalar field, prepared in the Hartle-Hawking-type state that is induced from the global vacuum on AdS_3, with Dirichlet, Neumann or transparent boundary conditions at the infinity. The detector was treated in first-order perturbation theory and assumed switched on in the asymptotic past.

The spacetimes were the $\mathbb{R}\mathrm{P}^2$ geon [290] and the Swedish geon of Åminneborg *et al* [24], each obtained as a quotient of an open subset in AdS_3 under a discrete isometry group. For both of these topological geon spacetimes, we found that the detector's response differs from that for the BTZ black hole, and the responses for the two spacetimes differ from each other. In particular, the detector's late time transition rate in the $\mathbb{R}\mathrm{P}^2$ geon differs from that in the BTZ black hole, as previously found in [397], and the geometric reasons for this were identified in a related context in [270, 268]; by contrast, our numerical results show that the late time response in the Swedish geon approaches that on the BTZ black hole. An analytic explanation of this late time phenomenon would require a deeper geometric study of the discrete group action by which the Swedish geon is quotiented from AdS_3.

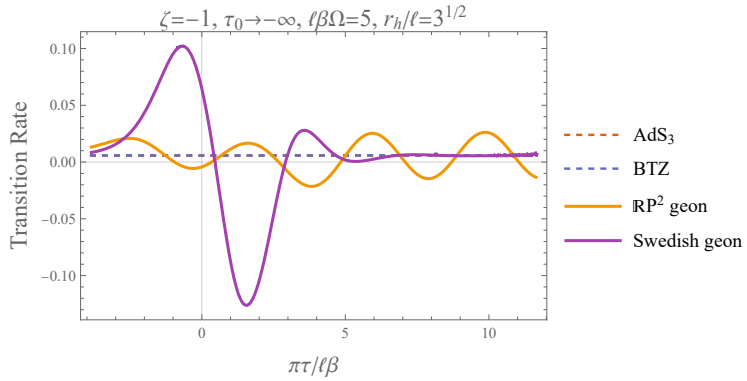
Our numerical results also show that, for the Swedish geon, at intermediate times the transition rate is much larger than for the $\mathbb{R}\mathrm{P}^2$ geon with the same mass. This is perhaps not unexpected, as the image sum for the field's Wightman function on the $\mathbb{R}\mathrm{P}^2$ geon consists of a strict subset of the terms in the image sum on the Swedish geon, but a more quantitative explanation would again require a deeper study of the discrete group action by which the Swedish geon is constructed from AdS_3.

The salient lesson from our results is that specific information about the interior topology of a black hole is accessible to an observer outside the black hole by allowing them to probe a quantum state that has been prepared with knowledge of the global topology of the spacetime.

A limitation of our results is the restriction to static observers. The response rate of infalling detectors for the spinless [365] and spinning [441] BTZ black holes has been recently investigated, as well as for the $\mathbb{R}\mathrm{P}^2$ geon [405]. These results suggest that the Swedish geon case will exhibit more detailed differences as compared to its $\mathbb{R}\mathrm{P}^2$ geon counterpart. This remains an interesting subject for future work.



(a)



(b)

Figure 4.3: As in Figures 4.1(a) (Panel (a)) and 4.2 (Panel (b)) but with a smaller black hole, $r_h/\ell = \sqrt{3}$, with detector position still such that $R^2/r_h^2 = \frac{25}{7}$.

Chapter 5

Analytic Methods for Harvesting Entanglement in AdS, dS, BTZ, and Minkowski spacetimes

In this chapter, we present analytic results for entanglement harvesting from conformally coupled massless scalar fields by UDW detectors on static worldlines in three key geometries: anti–de Sitter (AdS_{d+1}), de Sitter (dS_{d+1}), and BTZ black hole spacetimes. We obtain formulas for reduced density matrices valid for arbitrary detector gap, separation, and spatial dimension $d \geq 2$. These results demonstrate the advantages of analytic control in RQI: they expose how curvature and topology shape entanglement harvesting, provide benchmarks for numerical calculations, and reveal systematic trends across spacetime dimensions. In practical terms, they also allow for investigations to proceed in a very small fraction of the time it would have taken to carry out numerically.

Since the detectors are on static worldlines, their proper times are proportional to the coordinate time, with the constant of proportionality η being dependent on their respective spatial positions. Following [203], we consider the detectors to have Gaussian switching functions, with the same proper switching width, and the same proper energy gap

$$\begin{aligned} \chi_A(\tau_A) &= \exp\left(-\frac{(\tau_A + \eta_A t_0/2)^2}{2\sigma^2}\right), \\ \chi_B(\tau_B) &= \exp\left(-\frac{(\tau_B - \eta_B t_0/2)^2}{2\sigma^2}\right). \end{aligned} \tag{5.1}$$

When $t_0 > 0$, detector A reaches peak interaction with the field before detector B, in coordinate time, with the reverse being true when $t_0 < 0$. In what follows, it is helpful

to introduce the notational shorthand $p = (d-1)/2$, where d is the number of spatial dimensions in AdS_{d+1} and dS_{d+1}.

5.1 Solutions for $\mathbf{AdS}_{d+1}$

5.1.1 Wightman function

The Wightman function for a conformally coupled real scalar field in AdS_{d+1}, with the AdS length scale ℓ, in the global AdS vacuum state takes the form [203, 231]

$$W(x,x') = \frac{A_d}{\ell^{d-1}}\left[[\sigma(x,x')]^{-p} - \zeta[\sigma(x,x')+2]^{-p}\right], \tag{5.2}$$

where $\sigma(x,x')$ is the geodesic distance squared between two points in the embedding space $\mathbb{R}^{2,d}$, and $\zeta \in \{-1,0,1\}$ specifies Neumann ($\zeta=-1$), transparent ($\zeta=0$), or Dirichlet ($\zeta=1$), boundary conditions satisfied by the field at spatial infinity. The factor A_d is given by

$$A_d = \frac{\Gamma(d-1)}{2^{(d-1)/2}(4\pi)^{d/2}\Gamma(\frac{d}{2})}. \tag{5.3}$$

The geodesic distance squared takes the form

$$\sigma(x,x') = \frac{1}{2\ell^2}\Big[-\Delta T_1^2 - \Delta T_2^2 + \sum_{i=1}^{d}\Delta X_i^2\Big], \tag{5.4}$$

where (T_1, T_2, X_i) are the coordinates of the embedding space (see 4.3 for further details). Global AdS_{d+1} coordinates are obtained via the coordinate transformation $T_1 = \ell\cosh\rho\cos\bar{\tau}$, $T_2 = \ell\cosh\rho\sin\bar{\tau}$, and $X_i = \ell\sinh\rho\ \hat{n}_i$, where $\hat{n}_i$ are the unit vectors parameterizing a hypersphere. Substituting this in to the geodesic distance squared gives us

$$\sigma(x,x') = -1 + \cos(\bar{\tau}-\bar{\tau}')\cosh\rho\cosh\rho' - \cos\theta\sinh\rho\sinh\rho', \tag{5.5}$$

where $\cos\theta = \hat{n}\cdot\hat{n}'$ so that θ is the angular distance between the two detectors on the hypersphere. Now let $t = \ell\bar{\tau}$ and $r = \ell\sinh\rho$, to get

$$\sigma(x,x') = -1 + \sqrt{1+\frac{r^2}{\ell^2}}\sqrt{1+\frac{r'^2}{\ell^2}}\cos\left(\frac{t-t'}{\ell}\right) - \frac{rr'}{\ell^2}\cos\theta. \tag{5.6}$$

The geodesic squared distance between two detectors A and B on static worldlines is given by

$$\begin{aligned}\sigma(x_A, x_B) =& -1 + \sqrt{1+\frac{R_A^2}{\ell^2}}\sqrt{1+\frac{R_B^2}{\ell^2}}\cos\left(\frac{t_A - t_B}{\ell}\right) - \frac{R_A R_B}{\ell^2}\cos\theta \\ =& -1 + \frac{\gamma_A\gamma_B}{\ell^2}\cos\left(\frac{t_A - t_B}{\ell}\right) - \frac{R_A R_B}{\ell^2}\cos\theta\end{aligned} \tag{5.7}$$

where we have introduced $\gamma_D \equiv \sqrt{\ell^2 + R_D^2}$. Parameterizing the worldlines by the proper times of the detectors τ_A and τ_B, where $t_D = \tau_D \ell/\gamma_D$, we have

$$\sigma(x_A[\tau_A], x_B[\tau_B]) = -1 + \frac{\gamma_A\gamma_B}{\ell^2}\cos\left(\frac{\tau_A}{\gamma_A} - \frac{\tau_B}{\gamma_B}\right) - \frac{R_A R_B}{\ell^2}\cos\theta, \tag{5.8}$$

where $\gamma_D = \sqrt{\ell^2 + R_D^2}$. Substituting this into the Wightman function, we get

$$\begin{aligned}W(x_A[\tau_A], x_B[\tau_B]) =& A_d\Bigg[\left[-\ell^2 + \gamma_A\gamma_B\cos\left(\frac{\tau_A}{\gamma_A} - \frac{\tau_B}{\gamma_B}\right) - R_A R_B\cos\theta\right]^{-p} \\ &- \zeta\left[\ell^2 + \gamma_A\gamma_B\cos\left(\frac{\tau_A}{\gamma_A} - \frac{\tau_B}{\gamma_B}\right) - R_A R_B\cos\theta\right]^{-p}\Bigg].\end{aligned} \tag{5.9}$$

The pullback of the Wightman function onto a single detector's static worldline is given by taking the limit of $R_A = R_B = R$ and $\theta = 0$. This gives

$$W(x[\tau], x[\tau']) = A_d\gamma^{1-d}\left[\left[\cos\left(\frac{\tau - \tau'}{\gamma}\right) - 1\right]^{-p} - \zeta\left[\cos\left(\frac{\tau - \tau'}{\gamma}\right) + \mu\right]^{-p}\right], \tag{5.10}$$

where $\mu = (\ell^2 - R^2)/\gamma^2$. Similarly introducing notational shorthand for the Wightman function pulled back to two static worldlines gives

$$\begin{aligned}W(x_A[\tau_A], x_B[\tau_B]) =& \frac{A_d}{(\gamma_A\gamma_B)^p}\Bigg[\left[\cos\left(\frac{\tau_A}{\gamma_A} - \frac{\tau_B}{\gamma_B}\right) - \alpha_+\right]^{-p} \\ &- \zeta\left[\cos\left(\frac{\tau_A}{\gamma_A} - \frac{\tau_B}{\gamma_B}\right) + \alpha_-\right]^{-p}\Bigg].\end{aligned} \tag{5.11}$$

where $\alpha_\pm = \frac{\ell^2 \pm R_A R_B\cos\theta}{\gamma_A\gamma_B}$. The regulator is introduced by inserting $-i\epsilon$ into the argument of the cosine functions.

5.1.2 Excitation probability

The excitation probability is given by

$$P = \lambda^2 \int \mathrm{d}\tau \, \mathrm{d}\tau' \chi(\tau)\chi(\tau') e^{-i\Omega(\tau-\tau')} W(\tau,\tau'). \tag{5.12}$$

Unless otherwise specified, all integrals are over the real line, and double integrals are represented with one integral sign and two measures. We will use a Gaussian switching function $\chi(\tau) = e^{-\tau^2/2\sigma^2}$. Let $s = \tau - \tau'$, and $u = \tau + \tau'$. We may then carry out the integral over u, leaving a single integral over s,

$$\begin{aligned} P =& \frac{\lambda^2}{2} \int \mathrm{d}u \, \mathrm{d}s \, e^{-(u^2+s^2)/4\sigma^2} e^{-i\Omega s} W(s) \\ =& \sqrt{\pi}\sigma\lambda^2 \int \mathrm{d}s \, e^{-s^2/4\sigma^2} e^{-i\Omega s} W(s) \\ =& \sqrt{\pi}\sigma \frac{A_d}{\gamma^{d-2}} \lambda^2 \int \mathrm{d}s \, e^{-s^2\gamma^2/4\sigma^2} e^{-i\Omega\gamma s} \left[[\cos(s-i\epsilon)-1]^{-p} - \zeta \left[\cos(s-i\epsilon)+\mu\right]^{-p} \right]. \end{aligned} \tag{5.13}$$

We may use the identity $\cos(s) = 1 - 2\sin^2\left(\frac{s}{2}\right)$ to get

$$\begin{aligned} P = \sqrt{\pi}\sigma A_d \gamma^{2-d} \lambda^2 \int \mathrm{d}s \, e^{-s^2\gamma^2/4\sigma^2} e^{-i\Omega\gamma s} \Bigg[& 2^{-p} \left[i \sin\left(\frac{s}{2} - i\epsilon\right) \right]^{-2p} \\ & - \zeta \left[\cos(s-i\epsilon)+\mu\right]^{-p} \Bigg]. \end{aligned} \tag{5.14}$$

The integral may be split into two parts, $P = P_0 - \zeta P_b$, where

$$P_0 = \sqrt{\pi}\sigma 2^{\frac{1-d}{2}} \gamma^{2-d} A_d \lambda^2 \int \mathrm{d}s \, e^{-s^2\gamma^2/4\sigma^2} e^{-i\Omega\gamma s} \left[i \sin\left(\frac{s}{2} - i\epsilon\right) \right]^{-p}, \tag{5.15}$$

and

$$P_b = \sqrt{\pi}\sigma A_d \gamma^{2-d} \lambda^2 \int \mathrm{d}s \, e^{-s^2\gamma^2/4\sigma^2} e^{-i\Omega\gamma s} \left[\cos(s-i\epsilon)+\mu\right]^{-p}. \tag{5.16}$$

Let's focus on P_0 first. The integrand may be rewritten as

$$\begin{aligned} P_0 =& 2^{\frac{d-1}{2}} \sqrt{\pi}\sigma\gamma^{2-d} A_d \lambda^2 \int \mathrm{d}s \, e^{-s^2\gamma^2/4\sigma^2} e^{-i\Omega\gamma s} \left[\exp\left(\frac{is}{2} + \epsilon\right) - \exp\left(-\frac{is}{2} - \epsilon\right) \right]^{-2p} \\ =& 2^{\frac{d+1}{2}} \sqrt{\pi}\sigma\gamma^{2-d} A_d \lambda^2 \int \mathrm{d}s \, e^{-s^2\gamma^2/\sigma^2} e^{-2i\Omega\gamma s} \left(e^{is+\epsilon} - e^{-is-\epsilon} \right)^{-2p} \\ =& 2^{\frac{d+1}{2}} \sqrt{\pi}\sigma\gamma^{2-d} A_d \lambda^2 \int \mathrm{d}s \, e^{-s^2\gamma^2/\sigma^2} e^{-2i\Omega\gamma s} e^{-2p(is+\epsilon)} \left[1 - e^{-2(is+\epsilon)} \right]^{-2p}. \end{aligned} \tag{5.17}$$

Remember that for $|x| < 1$

$$(1-x)^{-m} = \sum_{n=0}^{\infty} \binom{n+m-1}{n} x^n, \tag{5.18}$$

which means

$$\begin{aligned} P_0 =& 2^{\frac{d+1}{2}} \sqrt{\pi} \sigma \gamma^{2-d} A_d \lambda^2 \int \mathrm{d}s \; e^{-s^2\gamma^2/\sigma^2} e^{-2i\Omega\gamma s} e^{-2p(is+\epsilon)} \sum_{n=0}^{\infty} \binom{n+2p-1}{n} e^{-2n(is+\epsilon)} & (5.19) \\ =& 2^{\frac{d+1}{2}} \pi \sigma^2 \gamma^{1-d} A_d \lambda^2 \sum_{n=0}^{\infty} \binom{n+d-2}{n} e^{-\frac{\sigma^2(2\gamma\Omega+d+2n-1)^2}{4\gamma^2}}, & (5.20) \end{aligned}$$

where we let $\epsilon \to 0^+$ after performing the integration, and substituted in $p = (d-1)/2$. Substituting in the form of A_d, and writing the binomial coefficients in terms of the Gamma function, we get

$$P_0 = \frac{2^{-d} \lambda^2 d \pi^{1-\frac{d}{2}} \sigma^2 \gamma^{1-d}}{\Gamma\left(\frac{d}{2}+1\right)} \sum_{n=0}^{\infty} \frac{\Gamma(d+n-1)}{\Gamma(n+1)} e^{-\sigma^2(\Omega+\frac{d+2n-1}{2\gamma})^2}. \tag{5.21}$$

We now move on to P_b. The Gegenbauer polynomials are defined by a generating function in the following way

$$\frac{1}{(1-2xt+t^2)^{\alpha}} = \sum_{n=0}^{\infty} C_n^{\alpha}(x) t^n. \tag{5.22}$$

Let's examine the kernel. Note that if we let $t = e^{-i(s-i\epsilon)}$, then $\cos(s-i\epsilon) = \frac{t+t^{-1}}{2}$. Further manipulation shows

$$\begin{aligned} [\cos(s-i\epsilon)+\mu]^{-p} =& \left(\frac{t+t^{-1}}{2}+\mu\right)^{-p} \\ =& (2t)^p (t^2+2\mu t+1)^{-p} \\ =& (2t)^p \sum_{n=0}^{\infty} C_n^p(-\mu) t^n \\ =& 2^p \sum_{n=0}^{\infty} C_n^p(-\mu) t^{n+p} \\ =& 2^p \sum_{n=0}^{\infty} C_n^p(-\mu) e^{-i(n+p)(s-i\epsilon)}. \end{aligned} \tag{5.23}$$

Substitute this in to (5.16) get

$$P_\zeta = \sqrt{\pi}\sigma A_d \gamma^{2-d}\lambda^2 2^p \sum_{n=0}^{\infty} C_n^p(-\mu)\int \mathrm{d}s\; e^{-s^2\gamma^2/4\sigma^2} e^{-i\Omega\gamma s} e^{-i(n+p)(s-i\epsilon)}. \tag{5.24}$$

Evaluating the integral and then letting $\epsilon \to 0^+$ gives us

$$P_\zeta = -\frac{1}{2}\pi^{\frac{1}{2}-\frac{d}{2}}\zeta\sigma^2\gamma^{1-d}\Gamma\left(\frac{d-1}{2}\right)\sum_{n=0}^{\infty} C_n^p(-\mu) e^{-\sigma^2(\Omega+\frac{d+2n-1}{2\gamma})^2} \tag{5.25}$$

With this, we can write down the total excitation probability of a static detector in AdS_{d+1} as

$$\boxed{P = \frac{2^{-d}\lambda^2 d\pi^{1-\frac{d}{2}}\sigma^2\gamma^{1-d}}{\Gamma\left(\frac{d}{2}+1\right)}\sum_{n=0}^{\infty}\left[\frac{\Gamma(d+n-1)}{\Gamma(n+1)} - \zeta\Gamma(d-1)C_n^p(-\mu)\right] e^{-\sigma^2\left(\Omega+\frac{d+2n-1}{2\gamma}\right)^2}} \tag{5.26}$$

where $\mu = \frac{\ell^2 - R^2}{\gamma^2}$.

5.1.3 Correlation term: X

The pullback of the Wightman function onto the two static worldlines (5.116) parameterized by their global time coordinates is given by,

$$\begin{aligned} W(t_A, t_B) = &\frac{A_d}{(\gamma_A\gamma_B)^p}\Bigg[\left[\cos\left(\frac{t_A - t_B}{\ell} - i\epsilon\right) - \alpha_+\right]^{-p} \\ &- \zeta\left[\cos\left(\frac{t_A - t_B}{\ell} - i\epsilon\right) + \alpha_-\right]^{-p}\Bigg]. \end{aligned} \tag{5.27}$$

The correlation term in the reduced density matrix is given by

$$\begin{aligned} X = -\lambda^2 \int \mathrm{d}\tau_A \mathrm{d}\tau_B \chi_A(\tau_A)\chi_B(\tau_B) e^{-i\Omega(\tau_A+\tau_B)} \\ \times \Big[\theta(t_A(\tau_A) - t_B(\tau_B))W(t_A(\tau_A), t_B(\tau_B)) \\ + \theta(t(\tau_B) - t(\tau_A))W(t_B(\tau_B), t_A(\tau_A))\Big]. \end{aligned} \tag{5.28}$$

Let's change the variables of integration to be the global times. For the static worldlines, the proper time differs from the global time by a simple scaling relationship, $\tau_D = t_D\gamma_D/\ell$, where $\gamma_D = \sqrt{R_D^2 + \ell^2}$.

$$\begin{aligned} X = -\frac{\lambda^2\gamma_A\gamma_B}{\ell^2}\int dt_A dt_B \chi_A\left(\frac{\gamma_A t_A}{\ell}\right)\chi_B\left(\frac{\gamma_B t_B}{\ell}\right) e^{-i\Omega(\gamma_A t_A+\gamma_B t_B)/\ell} \\ \times\left[\theta(t_A-t_B)W(t_A,t_B)+\theta(t_B-t_A)W(t_B,t_A)\right]. \end{aligned} \tag{5.29}$$

The Wightman function is a function of the difference in global time coordinates,

$$\begin{aligned} X = -\frac{\lambda^2\gamma_A\gamma_B}{\ell^2}\int dt_A dt_B\ \chi_A\left(\frac{\gamma_A t_A}{\ell}\right)\chi_B\left(\frac{\gamma_B t_B}{\ell}\right) e^{-i\Omega(\gamma_A t_A+\gamma_B t_B)/\ell} \\ \times\left[\theta(t_A-t_B)W(t_A-t_B)+\theta(t_B-t_A)W(t_B-t_A)\right]. \end{aligned} \tag{5.30}$$

Let's change the variables of integration to t_B and $s = t_A - t_B$.

$$\begin{aligned} X = -\frac{\lambda^2\gamma_A\gamma_B}{\ell^2}\int \mathrm{d}s\ dt_B\ \chi_A\left(\frac{\gamma_A(s+t_B)}{\ell}\right)\chi_B\left(\frac{\gamma_B t_B}{\ell}\right) e^{-i\Omega(\gamma_A s+(\gamma_A+\gamma_B)t_B)/\ell} \\ \times\left[\theta(s)W(s)+\theta(-s)W(-s)\right]. \end{aligned} \tag{5.31}$$

Carrying out the integral over t_B then gives

$$X = a_1\int_{-\infty}^{\infty}\mathrm{d}s\ e^{-a_2 s^2+ia_3 s}\left[\theta(s)W(s)+\theta(-s)W(-s)\right], \tag{5.32}$$

where

$$\begin{aligned} a_1 =& -\frac{\sqrt{2\pi}\sigma\gamma_A\gamma_B}{\ell\sqrt{\gamma_A^2+\gamma_B^2}} \\ & \times\exp\left(-\frac{t_0^2\gamma_A^2\gamma_B^2 - i\sigma^2 t_0\Omega\ell^2\left(\gamma_A-\gamma_B\right)\left(\gamma_A+\gamma_B\right)^2+\sigma^4\Omega^2\ell^4\left(\gamma_A+\gamma_B\right)^2}{2\sigma^2\ell^2\left(\gamma_A^2+\gamma_B^2\right)}\right) \\ a_2 =& \frac{\gamma_A^2\gamma_B^2}{2\sigma^2\ell^2\left(\gamma_A^2+\gamma_B^2\right)} \\ a_3 =& \frac{\gamma_A\gamma_B\left(\sigma^2\Omega\ell^2\left(\gamma_A-\gamma_B\right)+it_0\gamma_A\gamma_B\right)}{\sigma^2\ell^2\left(\gamma_A^2+\gamma_B^2\right)}. \end{aligned} \tag{5.33}$$

We can split this up

$$X = X_1 + X_2, \tag{5.34}$$

where

$$X_1 = a_1 \int_0^\infty \mathrm{d}s\; e^{-a_2 s^2 + i a_3 s} W(s) \tag{5.35}$$

$$X_2 = a_1 \int_{-\infty}^0 \mathrm{d}s\; e^{-a_2 s^2 + i a_3 s} W(-s). \tag{5.36}$$

Let's take a look at our Wightman function as a function of s. It is

$$W(s) = A_d (\gamma_A \gamma_B)^{-p} \left[\left[\cos\left(\frac{s}{\ell} - i\epsilon \right) - \alpha_+ \right]^{-p} - \zeta \left[\cos\left(\frac{s}{\ell} - i\epsilon \right) + \alpha_- \right]^{-p} \right]. \tag{5.37}$$

We can exploit the even nature of the cosine function, and write X_1 and X_2 down explicitly as

$$\begin{aligned} X_1 &= \frac{a_1 A_d}{(\gamma_A \gamma_B)^p} \int_0^\infty \mathrm{d}s\; e^{-a_2 s^2 + i a_3 s} \left[\left[\cos\left(\frac{s}{\ell} - i\epsilon \right) - \alpha_+ \right]^{-p} - \zeta \left[\cos\left(\frac{s}{\ell} - i\epsilon \right) + \alpha_- \right]^{-p} \right] \\ X_2 &= \frac{a_1 A_d}{(\gamma_A \gamma_B)^p} \int_{-\infty}^0 \mathrm{d}s\; e^{-a_2 s^2 + i a_3 s} \left[\left[\cos\left(\frac{s}{\ell} + i\epsilon \right) - \alpha_+ \right]^{-p} - \zeta \left[\cos\left(\frac{s}{\ell} + i\epsilon \right) + \alpha_- \right]^{-p} \right]. \end{aligned} \tag{5.38}$$

We can absorb the prefactor into the definition of a_1, and transform s to $-s$ in X_2. Exploiting the symmetry properties of the cosine function gives us

$$X_2 = a_1 \int_0^\infty \mathrm{d}s\; e^{-a_2 s^2 - i a_3 s} \left[\left[\cos\left(\frac{s}{\ell} - i\epsilon \right) - \alpha_+ \right]^{-p} - \zeta \left[\cos\left(\frac{s}{\ell} - i\epsilon \right) + \alpha_- \right]^{-p} \right]. \tag{5.39}$$

We can rescale s and add the two contributions together to get X, which is (after absorbing changes into the definitions of the constants)

$$X = a_1 \int_0^\infty \mathrm{d}s\; e^{-a_2 s^2} \cos(a_3 s) \left[\left[\cos\left(s - i\epsilon \right) - \alpha_+ \right]^{-p} - \zeta \left[\cos\left(s - i\epsilon \right) + \alpha_- \right]^{-p} \right] \tag{5.40}$$

Note that since we've rescaled s by $1/\ell$, it is now dimensionless. Remember that

$$\alpha_\pm = \frac{\ell^2 \pm R_A R_B \cos\theta}{\gamma_A \gamma_B}, \tag{5.41}$$

which means both are bounded $-1 < \alpha_\pm < 1$. The constants a_i have the definitions:

$$\begin{aligned} a_1 =& -\frac{(2\pi)^{-p-\frac{1}{2}}\sigma\gamma_A\gamma_B\Gamma(p)\left(\gamma_A\gamma_B\right)^{-p}}{\sqrt{\gamma_A^2+\gamma_B^2}} \\ & \times \exp\left(-\frac{\sigma^2\Omega^2\left(\gamma_A+\gamma_B\right)^2+\frac{t_0^2\gamma_A^2\gamma_B^2}{\sigma^2\ell^2}+\frac{it_0\Omega(\gamma_B-\gamma_A)(\gamma_A+\gamma_B)^2}{\ell}}{2\left(\gamma_A^2+\gamma_B^2\right)}\right) \\ a_2 =& \frac{\gamma_A^2\gamma_B^2}{2\sigma^2\left(\gamma_A^2+\gamma_B^2\right)} \\ a_3 =& \frac{\gamma_A\gamma_B\left(\sigma^2\Omega\ell\left(\gamma_A-\gamma_B\right)+it_0\gamma_A\gamma_B\right)}{\sigma^2\ell\left(\gamma_A^2+\gamma_B^2\right)} \end{aligned} \tag{5.42}$$

Just as before, we can split X into a transparent contribution, and a boundary contribution, $X = X_0 - \zeta X_b$, where

$$\begin{aligned} X_0 =& a_1\int_0^\infty \mathrm{d}s\, e^{-a_2s^2}\cos(a_3s)\left[\cos\left(s-i\epsilon\right)-\alpha_+\right]^{-p}, \\ X_b =& a_1\int_0^\infty \mathrm{d}s\, e^{-a_2s^2}\cos(a_3s)\left[\cos\left(s-i\epsilon\right)+\alpha_-\right]^{-p}. \end{aligned} \tag{5.43}$$

Since the forms of both integrals are identical, we can focus on X_0. Using the Gegenbauer expansion of the kernel, we may write this as

$$X_0 = 2^p a_1\sum_{n=0}^\infty C_n^p(\alpha_+)J_n, \tag{5.44}$$

where

$$\begin{aligned} J_n =& \int_0^\infty \mathrm{d}s\, e^{-a_2s^2-i(n+p)(s-i\epsilon)}\cos(a_3s) \\ =& \frac{1}{4}\sqrt{\frac{\pi}{a_2}}\sum_{x\in\{-1,1\}} e^{-(n+p)\epsilon}\left[e^{-\frac{(xa_3+n+p)^2}{4a_2}}\left(1-i\mathrm{erfi}\left(\frac{xa_3+n+p}{2\sqrt{a_2}}\right)\right)\right]. \end{aligned} \tag{5.45}$$

It is worth noting that in the limit of $n\to\infty$, this falls off as $\sim 1/n$. The Gegenbauer polynomial grows like $\mathcal{O}(n^{p-1})$ as $n\to\infty$. For $p = 1/2$, the naive sum converges, and for $p = 1$, the sum oscillates and avoids harmonic divergence. However, for $p > 1$, (5.44) diverges. This divergence can be dealt with via a subtraction and re-summation technique.

We may find the coefficients of an asymptotic expansion of J_n in inverse powers of $n+p$ as follows. Let $f(s) = e^{-a_2s^2}\cos(a_3s)$. Integrating by parts gives us

$$e^{(n+p)\epsilon}J_n = \frac{1}{-i(n+p)}\left[f(s)\,e^{-i(n+p)s}\right]\Big|_0^\infty + \frac{1}{i(n+p)}\int_0^\infty f'(s)\,e^{-i(n+p)s}\,ds. \tag{5.46}$$

Because $f(s)$ decays rapidly at infinity, the boundary term at $s = \infty$ vanishes. At $s = 0$ we obtain $f(0)/(i(n+p))$. Repeating the integration by parts on the remaining integral yields

$$e^{(n+p)\epsilon} J_n = \frac{f(0)}{i(n+p)} + \frac{f'(0)}{(i(n+p))^2} + \frac{1}{(i(n+p))^2} \int_0^\infty f''(s)\, e^{-i(n+p)s}\, ds. \tag{5.47}$$

Iterating this procedure M times gives the general expansion

$$e^{(n+p)\epsilon} J_n = \sum_{m=0}^{M} \frac{f^{(m)}(0)}{(i(n+p))^{m+1}} + \frac{1}{(i(n+p))^{M+1}} \int_0^\infty f^{(M+1)}(s)\, e^{-i(n+p)s}\, ds. \tag{5.48}$$

The large–n behaviour of J_n is therefore given by

$$e^{(n+p)\epsilon} J_n \sim \sum_{m=0}^{\infty} \frac{f^{(m)}(0)}{(i(n+p))^{m+1}}, \tag{5.49}$$

which is valid as an asymptotic expansion as $n \to \infty$. The function $f(s)$ is even, so all odd derivatives vanish at the origin. We therefore have

$$e^{(n+p)\epsilon} J_n \sim \sum_{j=0}^{\infty} \frac{f^{(2j)}(0)}{(i(n+p))^{2j+1}}. \tag{5.50}$$

We may split the asymptotic expansion as follows,

$$e^{(n+p)\epsilon} J_n \sim \sum_{j=0}^{\lceil p \rceil} \frac{f^{(2j)}(0)}{(i(n+p))^{2j+1}} + \sum_{j=\lceil p \rceil}^{\infty} \frac{f^{(2j)}(0)}{(i(n+p))^{2j+1}}. \tag{5.51}$$

It is the first part of (5.51) which is responsible for the divergence of the naive series for $p > 1$. We may write (5.44) as

$$\begin{aligned} X_0 =& 2^p a_1 \sum_{n=0}^{\infty} C_n^p(\alpha_+) \left(J_n - \sum_{j=0}^{\lceil p \rceil} \frac{f^{(2j)}(0)}{(i(n+p))^{2j+1}} \right) \\ &+ 2^p a_1 \sum_{j=0}^{\lceil p \rceil} f^{(2j)}(0) \sum_{n=0}^{\infty} \frac{C_n^p(\alpha_+)}{(i(n+p))^{2j+1}} e^{-(n+p)\epsilon}, \end{aligned} \tag{5.52}$$

where we have let the regulator go to zero in the first term (which is finite), and interchanged the order of summation in the second term, which is naively divergent when $\epsilon \to 0^+$. To fix this, we must us analytic continuation. Let's give the inner sum a label:

$$S_{2j+1} = e^{-ij\pi/2} \sum_{n=0}^{\infty} \frac{C_n^p(\alpha_+)}{(n+p)^{2j+1}} e^{-(n+p)\epsilon}. \tag{5.53}$$

The Mellin transform allows us to write,

$$\frac{1}{(n+p)^y} = \frac{1}{\Gamma(y)} \int_0^\infty \mathrm{d}t\; t^{y-1} e^{-(n+p)t}. \tag{5.54}$$

This means the terms we are interested in may be written as

$$\begin{aligned} S_j =& e^{-ij\pi/2} \sum_{n=0}^{\infty} \frac{C_n^p(\alpha_+)}{(n+p)^j} e^{-(n+p)\epsilon} \\ =& \frac{e^{-ij\pi/2}}{\Gamma(j)} \sum_{n=0}^{\infty} C_n^p(\alpha_+) e^{-(n+p)\epsilon} \int_0^\infty \mathrm{d}t\; t^{j-1} e^{-(n+p)t} \\ =& \frac{e^{-ij\pi/2}}{\Gamma(j)} \int_0^\infty \mathrm{d}t\; e^{-p(t+\epsilon)} t^{j-1} \sum_{n=0}^{\infty} C_n^p(\alpha_+) e^{-n(t+\epsilon)}. \end{aligned} \tag{5.55}$$

The interchange of integration and summation is justified since we have not yet analytically continued to $j < 2p$, or set the regulator to zero. Using (5.22), we can rewrite S_j as

$$S_j = \frac{e^{-ij\pi/2}}{\Gamma(j)} \int_0^\infty \mathrm{d}t\; e^{-p(t+\epsilon)} t^{j-1} \left[1 - 2\alpha_+ e^{-(t+\epsilon)} + e^{2(t+\epsilon)}\right]^{-p}. \tag{5.56}$$

We may now set the regulator to zero without any trouble, and analytically continue the integral to $j < 2p$. The transparent contribution is therefore given by

$$X_0 = 2^p a_1 \sum_{n=0}^{\infty} C_n^p(\alpha_+) \left(J_n - \sum_{j=0}^{\lceil p \rceil} \frac{f^{(2j)}(0)}{(i(n+p))^{2j+1}} \right) + 2^p a_1 \sum_{j=0}^{\lceil p \rceil} f^{(2j)}(0) S_{2j+1}, \tag{5.57}$$

where

$$S_{2j+1} = \frac{e^{-i(2j+1)\pi/2}}{(2j)!} \int_0^\infty \mathrm{d}t\; e^{-pt} t^{2j} \left(1 - 2\alpha_+ e^{-t} + e^{-2t}\right)^{-p}. \tag{5.58}$$

We may rewrite this as

$$S_{2j+1} = \frac{e^{-i(2j+1)\pi/2}}{(2j)!} 2^{-p} \int_0^\infty \mathrm{d}t\; t^{2j} \left(\cosh t - \alpha_+\right)^{-p}. \tag{5.59}$$

Using the Mellin transform again, we may write (5.59) as

$$S_{2j+1} = \frac{e^{-i(2j+1)\pi/2}}{(2j)!\Gamma(p)} 2^{-p} \int_0^\infty \mathrm{d}t\; t^{2j} \int_0^\infty \mathrm{d}u\; u^{p-1} e^{u\alpha_+} e^{-u\cosh t}. \tag{5.60}$$

Let's focus on the integral over t. Note that the modified Bessel function of the second kind may be defined as

$$K_\nu(u) = \int_0^\infty \mathrm{d}t\; e^{-u\cosh t}\cosh(\nu t). \tag{5.61}$$

Differentiating both sides with respect to ν repeatedly gives

$$\frac{\partial^{2j}}{\partial\nu^{2j}}K_\nu(u) = \int_0^\infty \mathrm{d}t\; t^{2j}e^{-u\cosh t}\cosh(\nu t). \tag{5.62}$$

We recover the integral we're interested in by evaluating this at $\nu = 0$,

$$\int_0^\infty \mathrm{d}t\; t^{2j}e^{-u\cosh t} = \left(\frac{\partial^{2j}}{\partial\nu^{2j}}K_\nu(u)\right)\Bigg|_{\nu=0}. \tag{5.63}$$

This means

$$S_{2j+1} = \frac{e^{-i(2j+1)\pi/2}}{(2j)!\Gamma(p)}2^{-p}\left(\frac{\partial^{2j}}{\partial\nu^{2j}}\int_0^\infty \mathrm{d}u\; u^{p-1}e^{u\alpha_+}K_\nu(u)\right)\Bigg|_{\nu=0}. \tag{5.64}$$

It is possible to evaluate the remaining integral in closed form, but this is less than ideal, since the remaining expression may only be evaluated at $\nu = 0$ via a careful limit. Instead, it is helpful to Taylor expand the exponential, and evaluate a series of integrals that do not require limits to evaluate at $\nu = 0$. We are left with

$$S_{2j+1} = -\frac{ie^{-i\pi j}}{(2j)!\Gamma(p)}\sum_{m=0}^{\infty}\frac{2^{m-2}\alpha^m}{m!}g_m^{(2j)}(0). \tag{5.65}$$

where $g_m(\nu)$ is given by

$$g_m(\nu) = \Gamma\left(\frac{1}{2}(m+p-\nu)\right)\Gamma\left(\frac{1}{2}(m+p+\nu)\right). \tag{5.66}$$

We may insert (5.65) into (5.57) to get our final expression for the transparent contribution to the correlation term X_0. To get the boundary contribution X_b, we may use the same formula, and merely substitute $-\alpha_-$ for α_+.

5.1.4 Correlation term: C

The C-term of the reduced density matrix (ρ_{23}) is given by

$$C := \lambda^2\int_{-\infty}^{\infty}\mathrm{d}\tau_A\int_{-\infty}^{\infty}\mathrm{d}\tau_B\chi_A(\tau_A)\chi_B(\tau_B)e^{-i\Omega(\tau_A-\tau_B)}W(x_A[\tau_A],x_B[\tau_B]), \tag{5.67}$$

Its calculation proceeds along the same lines as that of P_D and X. Unlike our calculation of X, we may rely on a universal Gegenbauer-based formula, since the relevant single-variable integral is over the real line. Using (5.116), converting the integral to be over global time coordinates, changing the variables of integration to be over t_B and s, and then integrating over t_B gives us

$$\begin{aligned} C_0 =& \frac{1}{2} a_1 \int \mathrm{d}s \; e^{-a_2 s^2 - i a_3 s} \left[\cos\left(s - i\epsilon\right) - \alpha_+\right]^{-p}, \\ C_b =& \frac{1}{2} a_1 \int \mathrm{d}s \; e^{-a_2 s^2 - i a_3 s} \left[\cos\left(s - i\epsilon\right) + \alpha_-\right]^{-p}. \end{aligned} \tag{5.68}$$

Expanding the distributional kernel in the Gegenbauer-Fourier basis, integrating, and taking the limit $\epsilon \to 0^+$ (while absorbing extra factors into the definition of a_1) gives us

$$\boxed{C = a_1 \sum_{n=0}^{\infty} \left[C_n^p\left(\alpha_+\right) - \zeta C_n^p\left(-\alpha_-\right)\right] e^{-\frac{(n+p-a_3)^2}{4a_2}}} \tag{5.69}$$

5.1.5 Comparison

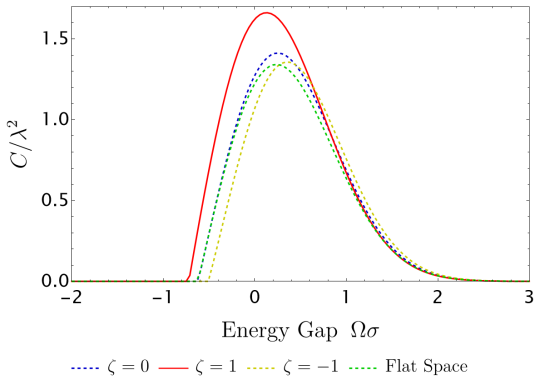
It is worthwhile to test the above formulas against pre-existing investigations into entanglement harvesting in AdS. A specific point of comparison is entanglement harvesting in AdS_3 by Henderson et al. [203]. The analytical series we derived replicated the numerical plots in that paper. Moreover, they allowed the plots to be generated remarkably quickly: in a matter of a few seconds. We present two such examples below in Fig. 5.1 It should be noted that the curve corresponding to Minkowski spacetime was also generated via an analytical series, as will be shown at the end of this chapter.

5.2 Solutions for dS_{d+1}

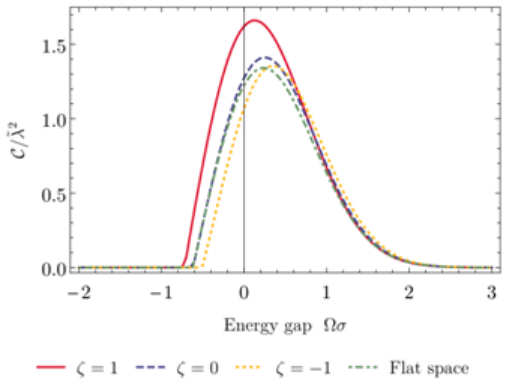
5.2.1 Wightman function

The Wightman function of a massless scalar field in dS_{d+1} in the Euclidean, or Bunch-Davies vacuum state is given by [274, 45]

$$W(x, x') = A_d \alpha^{1-d} \, {}_2F_1\left(\frac{d}{2} - \nu, \frac{d}{2} + \nu, \frac{d+1}{2}; 1 - c(x, x')\right), \tag{5.70}$$

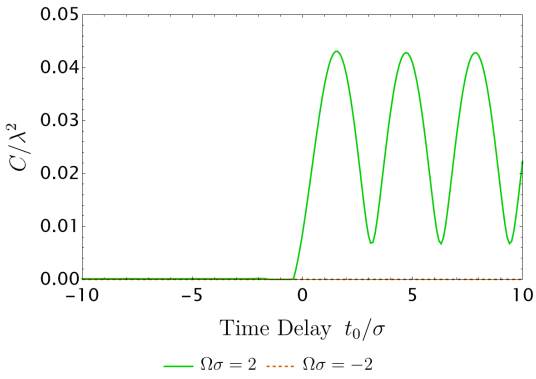


(a)

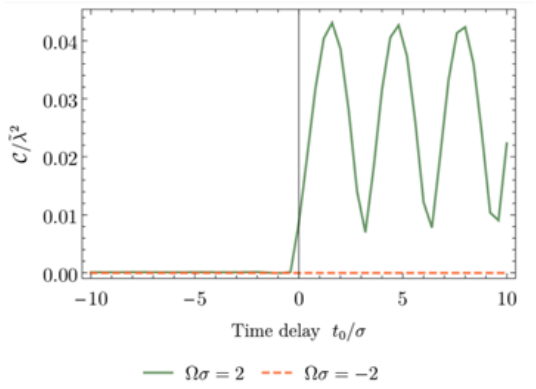


(b)

Figure 5.1: The concurrence of the final reduced density matrix of two static detectors with a given fixed proper distance between them, that reach peak interaction simultaneously in the field's frame (i.e., in the global time coordinate the global AdS vacuum is defined with), plotted as a function of their energy gap. All possible AdS boundary conditions are displayed. The AdS length scale ℓ is chosen to be equal to the switching width σ, and one detector is placed at the origin. Panel (a) shows the plots generated by the analytical formulas for the density matrix elements. Panel (b) is from the corresponding numerical plot in [203].



(a)



(b)

Figure 5.2: The final concurrence of the two detectors as a function of the the relative time delay in their switching functions t_0, where the AdS length scale is $\ell/\sigma = 1$, a proper distance of $5\sigma/2$ and where we impose Neumann boundary conditions ($\zeta = 1$) and an energy gap of $\Omega\sigma = 2$ and $\Omega\sigma = -2$. Panel (a) shows the plots generated by the analytical formulas. Panel (b) is from the corresponding numerical plot in [203]. Note the difference in the number of points, and that the analytical result took a few seconds to generate.

where

$$A_d = \frac{(4\pi)^{-(d+1)/2}}{\Gamma\left(\frac{d+1}{2}\right)}\Gamma\left(\frac{d}{2}-\nu\right)\Gamma\left(\frac{d}{2}+\nu\right), \tag{5.71}$$

$$\nu = \sqrt{\frac{d^2}{4}-\xi d(d+1)}, \tag{5.72}$$

α is the expansion rate parameter, and ξ is the coupling constant for the scalar field to the Ricci scalar. We'll work with conformal coupling, where $\xi = \frac{d-1}{4d}$. In that case, things reduce to $\nu = \frac{1}{2}$, so we have

$$W(x,x') = (4\pi)^{-(d+1)/2}\Gamma\left(\frac{d-1}{2}\right)\alpha^{1-d}\,{}_2F_1\left(\frac{d-1}{2},\frac{d+1}{2},\frac{d+1}{2};1-c(x,x')\right) \tag{5.73}$$

$$= (4\pi)^{-(d+1)/2}\Gamma\left(\frac{d-1}{2}\right)\alpha^{1-d}c(x,x')^{(1-d)/2} \tag{5.74}$$

Here, $c(x,x')$ is,

$$c(x,x') = \frac{|\Delta\mathbf{z}|^2 + r^2 + r'^2 - 2rr'\cos\Delta\phi - (\Delta\eta)^2}{4\eta\eta'}, \tag{5.75}$$

in flat slicing coordinates. Rewriting this in static coordinates, we have

$$c(x,x') = \frac{1}{2} - \frac{rr'\cos\Theta}{2\alpha^2} - \frac{1}{2}\sqrt{1-\frac{r^2}{\alpha^2}}\sqrt{1-\frac{r'^2}{\alpha^2}}\cosh\left(\frac{t-t'}{\alpha}\right). \tag{5.76}$$

We can write this as

$$c(x,x') = \frac{1}{2\alpha^2}\left[\alpha^2 - rr'\cos\Theta - \sqrt{\alpha^2-r^2}\sqrt{\alpha^2-r'^2}\cosh\left(\frac{t-t'}{\alpha}\right)\right] \tag{5.77}$$

$$= \frac{\gamma\gamma'}{2\alpha^2}\left[\kappa - \cosh\left(\frac{t-t'}{\alpha}\right)\right], \tag{5.78}$$

where we've defined $\gamma = \sqrt{\alpha^2-r^2}$, and $\kappa = \frac{\alpha^2 - rr'\cos\Theta}{\gamma\gamma'}$. So our Wightman function is

$$W(x,x') = 2^{-p-2}\pi^{-p-1}(\gamma\gamma')^{-p}\Gamma(p)\left[\kappa - \cosh\left(\frac{t-t'}{\alpha} - i\epsilon\right)\right]^{-p}, \tag{5.79}$$

where again, $p = \frac{d-1}{2}$, and we have inserted the regularization constant ϵ. To get the pullback onto a single static worldline, we let $\Theta = 0$ and take the limit of $r = r' = R$. We get

$$W(t,t') = (-1)^{-p}\Gamma(p)(4\pi)^{-p-1}\gamma^{-2p}\left[\sinh\left(\frac{t-t'}{2\alpha} - i\epsilon\right)\right]^{-2p}, \tag{5.80}$$

where $\gamma = \sqrt{\alpha^2 - R^2}$, and we used a hyperbolic trigonometric identity to simplify things. For the pullback onto two static detector worldlines,

$$W(t_A,t_B) = 2^{-p-2}\pi^{-p-1}(\gamma_A\gamma_B)^{-p}\Gamma(p)\left[\kappa - \cosh\left(\frac{t_A - t_B}{\alpha} - i\epsilon\right)\right]^{-p}, \tag{5.81}$$

where $\gamma_D = \sqrt{\alpha^2 - R^2}$, and $\kappa = \frac{\alpha^2 - R_A R_B \cos\Theta}{\gamma_A\gamma_B}$.

5.2.2 Excitation probability

Going through the same steps as in 5.1.2, we find that the excitation probability of a static detector is given by

$$P = (-1)^{-p}\sqrt{\pi}\sigma\lambda^2\Gamma(p)(4\pi)^{-p-1}\gamma^{-2p+1}\int \mathrm{d}s\; e^{-s^2\gamma^2/4\sigma^2}e^{-i\gamma\Omega s}\mathrm{csch}^{2p}\left(\frac{s}{2} - i\epsilon\right). \tag{5.82}$$

This does not admit an easy solution via exploiting the binomial expansion, since the resulting series does not converge, and the binomial expansions are not globally valid, requiring one to split the integral at $s = 0$, and deal with the pole contribution at that point separately.

In what follows we will make use of the following recursion relation

$$\mathrm{csch}^{2(p+1)}\left(\frac{s+x}{2}\right) = \frac{2}{p(2p+1)}\partial_x^2\mathrm{csch}^{2p}\left(\frac{s+x}{2}\right) - \frac{2p}{2p+1}\mathrm{csch}^{2p}\left(\frac{s+x}{2}\right). \tag{5.83}$$

We may generalize (5.82) to $P(p;x)$, solve for the base cases of $p = 1/2$ and $p = 1$ (corresponding to dS_3 and dS_4 respectively), and then use (5.83) to bootstrap up to larger values of p in steps of one. Upon reaching the desired value of p, one may set $x = 0$ (this does not involve taking a complicated limit) and recover the series for the excitation probability. In this sense, we have reduced the problem from finding P_D for any de Sitter spacetime with spatial dimension $d \geq 2$ to simply solving the specific cases of $d = 2$ and $d = 3$.

For $p = 1/2$ we may use the expansion

$$\operatorname{csch}\left(\frac{s+x}{2} - i\epsilon\right) = \sum_{n=-\infty}^{\infty} (-1)^n \left(i\pi n + \frac{s+x}{2} - i\epsilon\right)^{-1}. \tag{5.84}$$

Likewise for $p = 1$,

$$\operatorname{csch}^2\left(\frac{s+x}{2} - i\epsilon\right) = \sum_{n=-\infty}^{\infty} \left(i\pi n + \frac{s+x}{2} - i\epsilon\right)^{-2}. \tag{5.85}$$

Note that (5.82) is really just the Fourier transform (in $\gamma\Omega$) of the product of a Gaussian and a power of the hyperbolic cosecant function. Exploiting the series expansions above, and the convolution theorem, we may calculate the Fourier transform of each term in the series and convolve it with the Fourier transformed Gaussian to get valid series expansions for $P(x)$ for $p = 1/2$ and $p = 1$.

After carrying this out, one is left with

$$\begin{aligned} P\left(\frac{1}{2}; x\right) &= \sum_{n=-\infty}^{\infty} \mathcal{F}_n\left(\frac{1}{2}; x\right), \\ P\left(1; x\right) &= \sum_{n=-\infty}^{\infty} \mathcal{F}_n\left(1; x\right), \end{aligned} \tag{5.86}$$

where

$$\mathcal{F}_n\left(\frac{1}{2}; x\right) = -2\pi i \alpha_1 (-1)^n \left(\operatorname{erf}\left(\frac{\alpha_3 - 2\alpha_2 f_n}{2\sqrt{\alpha_2}}\right) + \operatorname{sgn}\left(n - \frac{1}{2}\right)\right) e^{-(f_n(\alpha_3 - \alpha_2 f_n))} \tag{5.87}$$

where $f_n = 2\pi n - ix$, and

$$\mathcal{F}_n\left(1; x\right) = -8\alpha_1\sqrt{\pi\alpha_2} e^{-\frac{\alpha_3^2}{4\alpha_2}} \left(\sqrt{\pi} e^{g_n^2} g_n \left(\operatorname{erf}\left(g_n\right) + \operatorname{sgn}\left(\frac{1}{2} - n\right)\right) + 1\right) \tag{5.88}$$

where $g_n = (\alpha_2(4\pi n + 2ix) - \alpha_3)/(2\sqrt{\alpha_2})$. The symbols α_n are defined to be

$$\begin{aligned} \alpha_1 &= (-1)^{-p}\sqrt{\pi}\sigma\lambda^2\Gamma(p)(4\pi)^{-p-1}\gamma^{-2p+1}, \\ \alpha_2 &= \frac{\gamma^2}{4\sigma^2}, \\ \alpha_3 &= \gamma\Omega. \end{aligned} \tag{5.89}$$

The terms in series for larger values of p can be built by applying the recursion relation (5.83) to the individual terms in the series, and then setting $x = 0$ to recover the specific series for an excitation probability.

5.2.3 Correlation term: X

The correlation term may be reduced to the form

$$X = \beta_1 \int_0^\infty \mathrm{d}s\; e^{-\beta_2 s^2} \cos(\beta_3 s)[\kappa - \cosh(s - i\epsilon)]^{-p} \tag{5.90}$$

where

$$\begin{aligned}
\beta_1 =& -\frac{(2\pi)^{-p-\frac{1}{2}} \sigma \gamma_A \gamma_B \Gamma(p) \left(\gamma_A \gamma_B\right)^{-p}}{\sqrt{\gamma_A^2 + \gamma_B^2}} \\
&\times \exp\left(-\frac{\sigma^2 \Omega^2 \left(\gamma_A + \gamma_B\right)^2 + \frac{t_0^2 \gamma_A^2 \gamma_B^2}{\alpha^2 \sigma^2} + \frac{i t_0 \Omega (\gamma_B - \gamma_A)(\gamma_A + \gamma_B)^2}{\alpha}}{2\left(\gamma_A^2 + \gamma_B^2\right)} \right) \\
\beta_2 =& \frac{\gamma_A^2 \gamma_B^2}{2\sigma^2 \left(\gamma_A^2 + \gamma_B^2\right)} \\
\beta_3 =& \frac{\gamma_A \gamma_B \left(\alpha \sigma^2 \Omega \left(\gamma_A - \gamma_B\right) + i t_0 \gamma_A \gamma_B\right)}{\alpha \sigma^2 \left(\gamma_A^2 + \gamma_B^2\right)}
\end{aligned} \tag{5.91}$$

Despite its similarities to the correlation term for AdS, (5.90) cannot be solved in the same manner. Instead, one must work with the base cases of $p = 1/2$ and $p = 1$ and bootstrap up to larger values via repeated differentiation with respect to κ, which must be treated like a Feynman parameter. The general form is

$$X(p; y) = \beta_1 \int_0^\infty \mathrm{d}s\; e^{-\beta_2 s^2} \cos(\beta_3 s)[y - \cosh(s - i\epsilon)]^{-p} \tag{5.92}$$

The relevant bootstrap is

$$X(p) = \frac{(-1)^{p-m}}{(p-m)!} \frac{\mathrm{d}^{p-m}}{\mathrm{d}y^{p-m}} X\left(m; y\right)|_{y=\kappa} \tag{5.93}$$

where $m = 1$ when p is an integer (d is odd) and $m = 1/2$ when p is a half-integer (d is even).

It should be noted that $X(p; y)$ satisfies the heat equation when β_2 is treated like time and β_3 is treated like position

$$\frac{\partial X(p; y)}{\partial \beta_2} = \frac{\partial^2 X(p; y)}{\partial \beta_3^2}. \tag{5.94}$$

This suggests that we may solve the base cases for the "initial condition" $\beta_2 = 0$ and then evolve the solution forward in β_3 using the heat kernel. The initial condition is given by

$$I(p; y) = \beta_1 \int_0^\infty \mathrm{d}s \ \cos(\beta_3 s)[y - \cosh(s - i\epsilon)]^{-p} \tag{5.95}$$

Let $y = \cosh\theta$. Also expand the hyperbolic cosine to first order in ϵ,

$$I(p; y) = \beta_1 \int_0^\infty \mathrm{d}s \ \cos(\beta_3 s)(\cosh\theta - \cosh s + i\epsilon \sinh s)^{-p}. \tag{5.96}$$

Since we're integrating over the positive half line, $\sinh s$ does not change sign and we can absorb it into our infinitesimal ϵ,

$$I(p; y) = \beta_1 \int_0^\infty \mathrm{d}s \ \cos(\beta_3 s)(\cosh\theta - \cosh s + i\epsilon)^{-p}. \tag{5.97}$$

The integrand is now even in s, so we can regard it as half of the Fourier transform of the kernel,

$$I(p; y) = \frac{1}{2}\beta_1 \int \mathrm{d}s \ e^{-\beta_3 s}(\cosh\theta - \cosh s + i\epsilon)^{-p}. \tag{5.98}$$

The base case of $p = 1$ is easier, so we shall deal with it first. Using the inverse Laplace transform we find that

$$[\cosh\theta - \cosh(s - i\epsilon)]^{-1} = -2 \ \mathrm{csch}(\theta) \sum_{n=-\infty}^{\infty} \frac{\theta - 2i\pi n}{(2\pi n + i\theta)^2 + (s - i\epsilon)^2}. \tag{5.99}$$

Each term in the series may be half-line cosine transformed to give its contribution to the "initial value", and then convolved with the heat kernel. The end result is

$$X\left(1; y\right) = \sum_{n=-\infty}^{\infty} \mathcal{G}_n\left(1; y\right), \tag{5.100}$$

where

$$\begin{aligned} \mathcal{G}_n(1; y) =& \frac{1}{2} i\pi\beta_1 \mathrm{csch}(\theta) e^{h_n(\beta_2 h_n - \beta_3)} \\ & \times \left(\mathrm{erf}\left(\frac{2\beta_2 h_n - \beta_3}{2\sqrt{\beta_2}} \right) + e^{2\beta_3 h_n} \mathrm{erf}\left(\frac{\beta_3 + 2\beta_2 h_n}{2\sqrt{\beta_2}} \right) \right. \\ & \left. - \mathrm{sgn}\left(n - \frac{1}{2} \right) \left(e^{2\beta_3 h_n} + 1 \right) \right). \end{aligned} \tag{5.101}$$

For the base case of $p = 1/2$, we may perform the variable transformation

$$x = \tanh\left(\frac{s}{2}\right) \in (0, 1). \tag{5.102}$$

Under this transformation,

$$\cosh s = \frac{1+x^2}{1-x^2}, \qquad \sinh s = \frac{2x}{1-x^2}, \qquad ds = \frac{2\,dx}{1-x^2}. \tag{5.103}$$

The base of the distributional kernel becomes

$$y - \cosh(s - i\epsilon) = y + i\epsilon + \frac{1+x^2}{1-x^2} \tag{5.104}$$

where we exploit the fact that $\sinh(s)$ is always positive over the domain of integration, and absorb the factor into ϵ. The test function the distribution acts on becomes

$$H(x) = \exp\left[-\beta_2 \left(2\,\mathrm{artanh}\, x\right)^2\right] \cos\left[\beta_3 \left(2\,\mathrm{artanh}\, x\right)\right]. \tag{5.105}$$

So the correlation term is

$$X\left(\frac{1}{2}; y\right) = 2\beta_1 \int_0^1 \mathrm{d}x \frac{H(x)}{\sqrt{x^4 + (x^2-1)^2\, y - 1}} \tag{5.106}$$

We have absorbed the infinitesimal regulator into y. Its purpose is to define the analytic structure of the integral. The function $H(x)$ is even and analytic on $|x| < 1$. We may therefore perform a Taylor expansion about $x = 0$.

$$H(x) = \sum_{n=0}^{\infty} b_{2n}\, x^{2n} \tag{5.107}$$

where b_{2n} is the series coefficient (a polynomial in β_2 and β_3). We may insert (5.107) in (5.106) and integrate term-by-term:

$$X\left(\frac{1}{2}; y\right) = 2\beta_1 \sum_{n=0}^{\infty} b_{2n} I_{2n} \tag{5.108}$$

where

$$\begin{aligned} I_{2n} &= \int_0^1 \mathrm{d}x \frac{x^{2n}}{\sqrt{x^4 + (x^2-1)^2\, y - 1}} \\ &= -\frac{1}{2} i \sqrt{\frac{\pi}{1-\kappa}} \Gamma\left(n + \frac{1}{2}\right)\, {}_2\tilde{F}_1\left(\frac{1}{2}, n + \frac{1}{2}; n+1; \frac{\kappa+1}{\kappa-1}\right) \end{aligned} \tag{5.109}$$

Once more, the analytical series shown here allow one to calculate density matrix elements in a fraction of the time it would take to perform the same investigation using numerical integration.

5.3 Solutions for the BTZ black hole

5.3.1 Wightman function

In Schwarzschild-like coordinates, $t \in (-\infty, \infty)$, $r \in (0, \infty)$, and $\phi \in (0, 2\pi)$, the static BTZ black hole has the metric [201],

$$\mathrm{d}s^2 = -\left(\frac{r^2 - r_h^2}{\ell^2}\right)\mathrm{d}t^2 + \left(\frac{\ell^2}{r^2 - r_h^2}\right)\mathrm{d}r^2 + r^2\mathrm{d}\phi^2, \tag{5.110}$$

where $r_h = \ell\sqrt{M}$, with M being the black hole mass, and ℓ being related to the cosmological constant by $\Lambda = -1/\ell^2$. The Wightman function for the conformally coupled real scalar field in the BTZ black hole spacetime, corresponding to the field being in the Hawking-Hartle vacuum state, is given by [201]

$$W_{\mathrm{BTZ}}(x, x') = \frac{1}{4\pi\sqrt{2}\ell}\sum_{n=-\infty}^{\infty}\left(\frac{1}{\sqrt{\sigma_n}} - \frac{\zeta}{\sqrt{\sigma_n + 2}}\right), \tag{5.111}$$

with σ_n in the image sum given by

$$\begin{aligned}\sigma_n(x, x') =& \frac{rr'}{r_h^2}\cosh\left(\frac{r_h}{\ell}\phi_n\right) - 1 - \frac{\sqrt{(r^2 - r_h^2)(r'^2 - r_h^2)}}{r_h^2}\cosh\left(\frac{r_h}{\ell^2}\Delta t\right) \\ =& \frac{\sqrt{(r^2 - r_h^2)(r'^2 - r_h^2)}}{r_h^2}\left[\frac{rr'\cosh\left(\frac{r_h}{\ell}\phi_n\right) - r_h^2}{\sqrt{(r^2 - r_h^2)(r'^2 - r_h^2)}} - \cosh\left(\frac{r_h}{\ell^2}\Delta t\right)\right]\end{aligned} \tag{5.112}$$

where $\phi_n = \Delta\phi - 2\pi n$, with $\Delta\phi = \phi - \phi'$, and $\Delta t = t - t'$. The term $\sigma_n + 2$ is

$$\sigma_n(x, x') + 2 = \frac{\sqrt{(r^2 - r_h^2)(r'^2 - r_h^2)}}{r_h^2}\left[\frac{rr'\cosh\left(\frac{r_h}{\ell}\phi_n\right) + r_h^2}{\sqrt{(r^2 - r_h^2)(r'^2 - r_h^2)}} - \cosh\left(\frac{r_h}{\ell^2}\Delta t\right)\right]. \tag{5.113}$$

If we pull both functions back onto a single static worldline $x[t] = (t, R, \Phi)$, we may write them as,

$$\begin{aligned}\sigma_n(x[t], x[t']) =& \chi^2\left[\mu_n^{(-)} - \cosh\left(\frac{r_h}{\ell^2}\Delta t\right)\right] \\ \sigma_n(x[t], x[t']) + 2 =& \chi^2\left[\mu_n^{(+)} - \cosh\left(\frac{r_h}{\ell^2}\Delta t\right)\right],\end{aligned} \tag{5.114}$$

where $\chi = (\sqrt{R^2 - r_h^2})/r_h$, and $\mu_n^{(\pm)} = \left[R^2 \cosh\left(2\pi r_h n/\ell\right) \pm r_h^2\right]/(R^2 - r_h^2)$. For the purposes of calculating the excitation probability, we will use this pullback of the Wightman function

$$W(x[t], x[t']) = \frac{1}{4\pi\sqrt{2}\ell\chi} \sum_{n=-\infty}^{\infty} \Bigg[\left[\mu_n^{(-)} - \cosh\left(\frac{r_h}{\ell^2}\Delta t - i\epsilon\right)\right]^{-1/2} - \zeta \left[\mu_n^{(+)} - \cosh\left(\frac{r_h}{\ell^2}\Delta t - i\epsilon\right)\right]^{-1/2} \Bigg], \tag{5.115}$$

where we have inserted the regularizing constant. For the case of two static detectors, the relevant Wightman pullback is

$$W(x[t_A], x[t_B]) = \frac{1}{4\pi\sqrt{2\chi_A\chi_B}\ell} \sum_{n=-\infty}^{\infty} \Bigg[\left[\kappa_n^{(-)} - \cosh\left(\frac{r_h}{\ell^2}\Delta t_{AB} - i\epsilon\right)\right]^{-1/2} \tag{5.116}$$

$$- \zeta \left[\kappa_n^{(+)} - \cosh\left(\frac{r_h}{\ell^2}\Delta t_{AB} - i\epsilon\right)\right]^{-1/2} \Bigg], \tag{5.117}$$

where

$$\kappa_n^{(\pm)} = \frac{R_A R_B \cosh\left[\frac{r_h}{\ell}(\Delta\phi - 2\pi n)\right] \pm r_h^2}{\sqrt{(R_A^2 - r_h^2)(R_B^2 - r_h^2)}}. \tag{5.118}$$

Note that the form of each image term in (5.115) and (5.116) are identical to the corresponding Wightman pullbacks in dS_3, for which we have analytical series. This means that the excitation probability and correlation term for static detectors in the BTZ black hole spacetime may be calculated as image sums of the excitation probabilities and correlation terms respectively, of static detectors in dS_3.

The coordinate and proper time are related by $\tau = \eta t$, where in the BTZ black hole spacetime, $\eta = \gamma_D/\ell$, where $\gamma_D = \sqrt{R_D^2 - r_h^2}$. To recover the expressions relevant to entanglement harvesting, we may use (5.108), though with the definitions of β_i adjusted to

$$\begin{aligned}
\beta_1 =& -\frac{\lambda^2\sigma\sqrt{\gamma_A\gamma_B}}{4\sqrt{\pi}\sqrt{\gamma_A^2 + \gamma_B^2}} \exp\left(-\frac{\sigma^2\Omega^2\left(\gamma_A + \gamma_B\right)^2 + \frac{t_0^2\gamma_A^2\gamma_B^2}{\sigma^2\ell^2} + \frac{it_0\Omega(\gamma_B - \gamma_A)(\gamma_A + \gamma_B)^2}{\ell}}{2\left(\gamma_A^2 + \gamma_B^2\right)}\right) \\
\beta_2 =& \frac{\ell^2\gamma_A^2\gamma_B^2}{2\sigma^2 r_h^2\left(\gamma_A^2 + \gamma_B^2\right)} \\
\beta_3 =& \frac{\gamma_A\gamma_B\left(\sigma^2\Omega\ell\left(\gamma_A - \gamma_B\right) + it_0\gamma_A\gamma_B\right)}{\sigma^2 r_h\left(\gamma_A^2 + \gamma_B^2\right)}
\end{aligned} \tag{5.119}$$

The $n = 0$ image term for the excitation probability corresponding to $\zeta = 0$ is found by using (5.89) (setting $x = 0$), with new definitions for the symbols α_i,

$$\begin{aligned}\alpha_1 =& \frac{\sigma\lambda^2}{4\sqrt{2\pi}} \\ \alpha_2 =& \frac{\ell^2\gamma^2}{4r_h^2\sigma^2} \\ \alpha_3 =& \frac{\Omega\gamma\ell}{r_h}\end{aligned} \tag{5.120}$$

Fundamentally, the manner of calculation is unchanged from dS_3. In fact, the analytical formulas replicate the results found in [201], where the distributional integrals in question were numerically evaluated.

5.4 Solutions for Minkowski Spacetime

5.4.1 Wightman function

A mode decomposition of a massless scalar field in flat spacetime gives the Wightman function[398]

$$W(x, x') = \int \frac{d^d|\mathbf{k}|}{(2\pi)^k} \frac{1}{2|\mathbf{k}|} e^{-i(|\mathbf{k}|(t-t'-i\epsilon)-\mathbf{k}\cdot(\mathbf{x}-\mathbf{x}'))} \tag{5.121}$$

Letting the spatial displacement $\mathbf{r} = \mathbf{x} - \mathbf{x}'$ align with the polar axis, and writing the integral in spherical coordinates, gives us an angular integral, which may be evaluated as

$$\int d\Omega_{d-1} e^{i|\mathbf{k}||\mathbf{r}|\cos\theta} = (2\pi)^{d/2}(|\mathbf{k}||\mathbf{r}|)^{1-d/2} J_{d/2-1}(|\mathbf{k}||\mathbf{r}|). \tag{5.122}$$

Substituting this in, and carrying out the remaining integral over $|\mathbf{k}|$ leaves us with

$$W(x, x') = \frac{\Gamma(p)}{4\pi^{p+1}}[|\mathbf{r}|^2 - (\Delta t - i\epsilon)^2]^{-p}. \tag{5.123}$$

Pulled back to a single static worldline

$$W(t, t') = \frac{\Gamma(p)}{4\pi^{p+1}} e^{-ip\pi}(\Delta t - i\epsilon)^{-2p}, \tag{5.124}$$

and pulled back for two static UDW detectors with a spatial separation of L,

$$W(t_A, t_B) = \frac{\Gamma(p)}{4\pi^{p+1}}[L^2 - (\Delta t_{AB} - i\epsilon)^2]^{-p}. \tag{5.125}$$

5.4.2 Excitation Probability

The excitation probability is given by

$$P = \lambda^2 \frac{\Gamma(p)}{4\pi^{p+1}} e^{-ip\pi} \sqrt{\pi}\sigma \int_{-\infty}^{\infty} \mathrm{d}s \; e^{-s^2/4\sigma^2 - i\Omega s} (s - i\epsilon)^{-2p}. \tag{5.126}$$

When $s > 0$, we may represent the distributional kernel as

$$(s - i\epsilon)^{-2p} = \frac{1}{\Gamma(2p)} \int_0^{\infty} \mathrm{d}u \; u^{2p-1} e^{-u(s-i\epsilon)}. \tag{5.127}$$

We can insert this into (5.126), and analytically continue to s being either positive or negative,

$$P = \lambda^2 \frac{\Gamma(p)}{\Gamma(2p) 4\pi^{p+1}} e^{-ip\pi} \sqrt{\pi}\sigma \int_{-\infty}^{\infty} \mathrm{d}s \int_0^{\infty} \mathrm{d}u \; e^{-s^2/4\sigma^2 - i\Omega s} u^{2p-1} e^{-u(s-i\epsilon)}. \tag{5.128}$$

Carrying out the integral over s, leaves us with

$$P = \lambda^2 \frac{e^{-i\pi p} \pi^{-p} \sigma^2 \Gamma(p)}{2\Gamma(2p)} e^{-\sigma^2\Omega^2} \int_0^{\infty} \mathrm{d}u \; u^{2p-1} e^{\sigma^2 u^2 + iu\left(2\sigma^2\Omega + \epsilon\right)}. \tag{5.129}$$

We may carry out the integral as though $\sigma^2 < 0$ and then analytically continue the result to the physical $\sigma^2 > 0$. After carrying out the integral over u, and letting $\epsilon \to 0^+$, we are left with

$$\begin{aligned} P = & \frac{\lambda^2 2^{-2p-1} \pi^{\frac{1}{2}-p} \sigma^{2-2p} \Gamma(p) \, {}_1F_1\left(\frac{1}{2} - p; \frac{1}{2}; -\sigma^2\Omega^2\right)}{\Gamma\left(p + \frac{1}{2}\right)} \\ & - \lambda^2 4^{-p} \pi^{\frac{1}{2}-p} \Omega \sigma^{3-2p} \, {}_1F_1\left(1 - p; \frac{3}{2}; -\sigma^2\Omega^2\right), \end{aligned} \tag{5.130}$$

where ${}_1F_1$ is the Kummer confluent hypergeometric function. As a test, we may consider 3+1 dimensional flat space, for which the excitation probability is known [398], and confirm that it matches. Setting $p = 1$ gives us

$$P = \frac{\lambda^2}{4\pi} \left(e^{-\sigma^2\Omega^2} - \sqrt{\pi}\sigma\Omega \, \mathrm{erfc}(\sigma\Omega) \right), \tag{5.131}$$

which indeed matches the result in [398].

An alternative path to the excitation probability is to take the limit of the sum (5.26) (under transparent boundary conditions) in the limit of the AdS length scale $\ell \to \infty$. This

is the same as taking the limit $\gamma \to \infty$ in (5.26)[456]. Labeling P explicitly as a function of γ,

$$P(\gamma) = \frac{2^{-d}\lambda^2 d\pi^{1-\frac{d}{2}}\sigma^2\gamma^{1-d}}{\Gamma\left(\frac{d}{2}+1\right)} \sum_{n=0}^{\infty} \frac{\Gamma(d+n-1)}{\Gamma(n+1)} e^{-\sigma^2\left(\Omega+\frac{d+2n-1}{2\gamma}\right)^2} \tag{5.132}$$

Define $x_n = \frac{n}{\gamma}$, so then $\Delta x_n = \frac{1}{\gamma}$. Multiply and divide the sum by γ, to get

$$P(\gamma) = \frac{2^{-d}\lambda^2 d\pi^{1-\frac{d}{2}}\sigma^2\gamma^{2-d}}{\Gamma\left(\frac{d}{2}+1\right)} \sum_{n=0}^{\infty} \frac{\Gamma(d+\gamma x_n-1)}{\Gamma(\gamma x_n+1)} e^{-\sigma^2\left(\Omega+\frac{d-1}{2\gamma}+x_n\right)^2} \tag{5.133}$$

We recognize this as a Riemann sum, that in the limit of large γ, approaches an integral. The integral it approaches can be seen to be

$$\sum_{n=0}^{\infty} \frac{\Gamma(d+\gamma x_n-1)}{\Gamma(\gamma x_n+1)} e^{-\sigma^2\left(\Omega+\frac{d-1}{2\gamma}+x_n\right)^2} \Delta x_n \longrightarrow \int_0^{\infty} \mathrm{d}x\, \frac{\Gamma(\gamma x+d-1)}{\Gamma(\gamma x+1)} e^{-\sigma^2\left(\Omega+\frac{d-1}{2\gamma}+x\right)^2} \tag{5.134}$$

In the limit of large γ, the ratio $\frac{\Gamma(\gamma x+d-1)}{\Gamma(\gamma x+1)}$ behaves like

$$\frac{\Gamma(\gamma x+d-1)}{\Gamma(\gamma x+1)} \sim \gamma^{d-2} x^{d-2}. \tag{5.135}$$

This comes from the fact that for large arguments $\Gamma(z+A)/\Gamma(z+B) \sim z^{A-B}$. The factor of γ^{d-2} cancels out the constant factor γ^{2-d} in front of our sum. It's clear that the term $\frac{d-1}{2\gamma}$ in the exponential becomes zero in the limit of large γ. Replacing the Riemann sum with the exact integral then shows us

$$\lim_{\gamma\to\infty} P(\gamma) = \frac{2^{-d}\lambda^2 d\pi^{1-\frac{d}{2}}\sigma^2}{\Gamma\left(\frac{d}{2}+1\right)} \int_0^{\infty} dx\, x^{d-2} e^{-\sigma^2(\Omega+x)^2}. \tag{5.136}$$

This integral can be evaluated exactly, so we get, for P (the excitation probability in Minkowski spacetime)

$$P = 2^{-d}\pi^{\frac{1}{2}-\frac{d}{2}}\lambda^2\Omega\sigma^{4-d}\Gamma\left(\frac{d-1}{2}\right) e^{-\sigma^2\Omega^2} U\left(\frac{d}{2}, \frac{3}{2}, \sigma^2\Omega^2\right), \tag{5.137}$$

where U is the Tricomi confluent hypergeometric function. In terms of p, this is

$$P = \lambda^2 2^{-2p-1}\pi^{-p}\Omega\sigma^{3-2p}\Gamma(p) e^{-\sigma^2\Omega^2} U\left(p+\frac{1}{2}, \frac{3}{2}, \sigma^2\Omega^2\right) \tag{5.138}$$

5.4.3 Correlation term: X

For simplicity, we will consider the case where the offset in the switching functions t_0 is zero. Going through the usual steps, we find that the correlation term X is given by

$$X = -\frac{\lambda^2}{2}\pi^{-p-\frac{1}{2}}\sigma\Gamma(p)e^{-\sigma^2\Omega^2}\int_0^\infty \mathrm{d}s\; e^{-s^2/4\sigma^2}[L^2-(s-i\epsilon)^2]^{-p}. \tag{5.139}$$

Using the Mellin transform representation of the distributional kernel again, and carrying out the integral over u first, just as when evaluating the excitation probability, gives us

$$X = \lambda^2\left(-2^{-2p-1}\right)\left(-\frac{1}{\pi}\right)^p\sigma^{2-2p}\Gamma(p)e^{-\sigma^2\Omega^2}U\left(p,p+\frac{1}{2},-\frac{L^2}{4\sigma^2}\right). \tag{5.140}$$

The Minkowski terms for the concurrence were used in Fig. 5.1, and found to match a previous result in [203].

5.5 Concluding remarks

The methods and formulas of this chapter facilitate a remarkable speed-up in calculations for entanglement harvesting. Beyond their intrinsic technical value, these results open the door to future investigations into geon spacetimes, and other quotient spacetimes of AdS and dS. They also allow for easy calculation of entanglement harvesting in higher dimensions. It should be noted that these formulas allow for the calculation of the density matrix elements necessary to quantify ~~magic harvesting~~the generation of magic by a single qutrit. Indeed, this has been shown in [456] for AdS_{d+1} which presented formulas for the calculation of (2.92) and (2.93). It is worth noting however that β essentially corresponds to X in the spatial coincident limit, which makes it unsuited for calculation via numerical integration. (the results diverge). The analytical series method allows one to identify the divergent part, and perform a renormalization to get a finite result.

Chapter 6

Braneworld Holography and Quantum Black Holes

The aim of this chapter is to provide a self-contained review of the theoretical framework in which the remainder of Part II is set: the construction and analysis of charged, rotating *quantum* black hole asymptotically AdS spacetimes. Here the term "quantum" refers not to a speculative Planck-scale model, but to semiclassical solutions of the gravitational field equations that include the backreaction of the stress tensor due to conformal fields, to all orders of perturbation theory. In the braneworld holography program, this stress tensor is that of a large-N, strongly coupled conformal field theory (CFT), for which the AdS/CFT correspondence provides a calculable and universal description. This union of semiclassical gravity with holography gives us a controlled setting to explore black holes whose geometry and thermodynamic properties are shaped by quantum effects.

In AdS spacetimes, the thermodynamics of black holes is encoded in the dual CFT as the thermodynamics of a thermal state. The Hawking–Page transition is reinterpreted as a confinement/deconfinement phase transition, and the bulk quantities T, S, Ω, and Φ acquire precise field-theoretic counterparts. In braneworld holography, a lower-dimensional brane is embedded in a higher-dimensional AdS bulk, and the effective field equations on the brane contain, in addition to the Einstein tensor, the expectation value of the dual CFT stress tensor. When the brane hosts a black hole, this expectation value encodes the quantum backreaction of the strongly coupled matter sector. The result is a spacetime that is a genuine solution of semiclassical gravity on the brane, with quantum effects already built in via the holographic dictionary.

This framework is particularly powerful for black hole thermodynamics. The brane

black hole inherits the rich phase structure of AdS black holes—Van der Waals–like critical points, re-entrant phase transitions, triple points—and it does so in a setting where the thermodynamic variables are understood through holography. Furthermore, when one promotes the cosmological constant to a thermodynamic pressure and the ADM mass to an enthalpy, the first law of black hole mechanics extends to include a $V\,dP$ term, and the entire black hole chemistry program becomes available. This extended thermodynamic framework provides a natural language in which to discuss the charged, rotating quantum black holes that will be our primary focus, and it links the semiclassical bulk description to chemical potentials and conjugate variables in the dual CFT.

The present chapter is therefore expository in nature. Its role is to assemble, in one place, the holographic, semiclassical, and thermodynamic ingredients needed for the construction and analysis of charged, rotating quantum black holes. We begin with the essential elements of AdS/CFT and the holographic stress tensor, proceed to the effective field equations for gravity on a brane in AdS, and review the known results on static, charged, and rotating brane-localized black holes. We then outline the working definition of a quantum black hole in this context, and conclude with a review of extended black hole thermodynamics in AdS. The discussion is deliberately compact but technically complete for the purposes of subsequent chapters. The exposition of holography largely follows Panella [350] and Hubeny [224], while the background on quantum black holes follows [351], and the background on black hole chemistry follows Mann [306].

It must be stressed that the term "quantum black hole" does not refer to a black hole whose description relies on a quantum theory of gravity, but rather to a black hole solution that is modified by taking into account the backreaction of conformal quantum fields onto the spacetime. From this vantage point, a more accurate term for these objects might be "quantum backreaction-corrected black holes." In what follows, we use the term quantum black hole to remain consistent with existing literature on the subject such as [147].

6.1 Holographic preliminaries

6.1.1 the AdS/CFT correspondence

The AdS/CFT correspondence posits a non-perturbative equivalence between a gravitational theory on an asymptotically anti–de Sitter spacetime of dimension $d{+}1$ ($\mathcal{M}$) and a conformal field theory (CFT) living on its d-dimensional conformal boundary, ($\partial\mathcal{M}$) [301]. In its canonical form, the duality relates type IIB string theory on $\mathrm{AdS}_5 \times S^5$ to $\mathcal{N}{=}4$

supersymmetric Yang–Mills theory with gauge group $SU(N)$ in four dimensions [224]. In this section, we briefly summarize the key features of the duality without any reference to string theory, following [224, 217].

The duality between the gravitational theory in the bulk and the conformal field theory on the boundary exists at the level of their partition functions. Consider a bulk field Φ over $\mathcal{M}$, with fixed boundary value on $\partial\mathcal{M}$, $\phi_{(0)}$. The standard AdS/CFT dictionary, as summarized by Gubser, Klebanov, Polyakov and Witten, states that

$$\left\langle e^{-\int_{\partial\mathcal{M}} \mathcal{O}\phi_{(0)}} \right\rangle_{\text{CFT}} = Z_{\text{grav}}[\phi_{(0)}]|_{\mathcal{M}}, \tag{6.1}$$

where the term on the right-hand side of the equation is the gravitational partition function of the bulk field Φ subject to the fixed boundary condition $\phi_{(0)}$, and the term on the left-hand side is the generating functional of the dual CFT, where $\mathcal{O}$ is field theory operator dual to the bulk field [350, 224]. The correspondence provides a precise, calculable bridge between strongly coupled field theories, on the conformal boundary, which is a non-dynamical background, and a weakly coupled theory of classical gravity. This simplification arises because the holographic field theories of interest are typically non-abelian gauge theories with gauge group $SU(N)$. In such theories the microscopic gauge coupling is g_{YM}, but in the large-N limit the relevant effective parameter is the *'t Hooft coupling*

$$\lambda \equiv g_{\text{YM}}^2 N\,. \tag{6.2}$$

In this large-N limit, where λ is fixed, it is natural to classify Feynman diagrams according to their topology, with planar diagrams dominating the expansion. The strong coupling limit $\lambda \gg 1$ corresponds, via the holographic dictionary, to an AdS bulk with curvature radius much larger than the string length, so that the dual description is well-approximated by classical supergravity. In this regime, $\mathcal{O}(1/N)$ corrections to the dual gauge field theory are mapped to $\mathcal{O}(G)$ quantum gravity corrections in the bulk. Thus, the correspondence becomes computationally powerful when both N and λ are taken large: the boundary theory is strongly coupled, but the dual bulk dynamics reduce to weakly coupled gravity [350].

The number of effective degrees of freedom in the boundary CFT is captured by its *central charge*. In two dimensions the central charge c appears as the coefficient of the Virasoro algebra's central extension and fixes the normalization of the stress tensor two-point function. In higher dimensions there are analogous anomaly coefficients (such as the a and c charges in four-dimensional CFTs), but in all cases the central charge plays the role of measuring the density of degrees of freedom. For all known holographic theories, c scales with N as $c \sim N^{\alpha}$ where α is some positive real number. This means that the large-c limit

coincides with the classical limit in the bulk. In this limit, the right-hand side of (6.1) may be approximated as a sum over the classical saddles $\{\Phi_i\}$, which are the solutions to the bulk classical gravity equations of motion that respect the prescribed boundary conditions

$$\lim_{c\to\infty} \left\langle e^{-\int_{\partial\mathcal{M}} \mathcal{O}_{\phi_{(0)}}} \right\rangle_{\text{CFT}} = \sum_i e^{-I_{\text{grav}}^{\text{on shell}}}. \tag{6.3}$$

When all sources $\phi_(0)$ but the boundary value of the bulk metric are taken to zero, the large-c limit corresponds to getting rid of all the bulk fields, except the metric. In this limit, the bulk is described by a purely gravitational theory.

6.1.2 Holographic Renormalization

The tree level gravitational partition function (6.3) suffers from infrared (IR) divergences, which corresponds to ultraviolet (UV) divergences in the correlation functions of the CFT. The holographic renormalization procedure removes these divergences by introducing an IR cutoff surface in the bulk, which corresponds to a UV cutoff for the CFT on the brane [350]. A brief sketch of the process is given below. The action governing a bulk asymptotically AdS_{d+1} spacetime $\mathcal{M}$ with length scale L_{d+1} and cosmological constant $\Lambda_{d+1} = -d(d-1)/L_{d+1}^2$ is given by

$$I_{\text{bulk}} = \frac{1}{16\pi G_{d+1}} \int_{\mathcal{M}} d^{d+1}x \sqrt{-\hat{g}} \left(\hat{R} - 2\Lambda_{d+1}\right) + \frac{1}{8\pi G_{d+1}} \int_{\partial\mathcal{M}} d^d x \sqrt{-h}\, K. \tag{6.4}$$

where G_{d+1} is the bulk Newton's constant, $\hat{g}_{ab}$ is the metric on $\mathcal{M}$. The second term is the Gibbons-Hawking-York (GHY) term, and K is the trace of the extrinsic curvature of the boundary submanifold $\partial\mathcal{M}$, which has the induced metric h_{ij}. This bulk gravitational theory is dual (in the large-N/planar diagram and large-c limit) to a CFT_d on the conformal boundary $\partial\mathcal{M}$.

The near–boundary geometry of any asymptotically AdS space is universal, and in Fefferman–Graham coordinates the metric admits an expansion [146]

$$ds^2 = \hat{g}_{ab}\, dx^a dx^b = L_{d+1}^2 \left(\frac{d\rho^2}{4\rho^2} + \frac{1}{\rho} g_{ij}(x,\rho)\, dx^i dx^j\right), \tag{6.5}$$

where the conformal boundary is located at $\rho = 0$, and $g_{ij}(x,\rho)$ may be expanded as $g_{ij}(x,\rho) = g_{ij}^{(0)}(x) + \rho g_{ij}^{(2)}(x) + \cdots + \rho^{d/2} g_{ij}^{(d)}(x)$. The higher order terms may be written in terms of $g_{ij}^{(0)}$ and its derivatives, after perturbatively solving the bulk Einstein field

equations. The bulk action (6.4) suffers from an IR divergence at $\rho = 0$ when the metric is on-shell. This divergence is then removed by introducing an IR cutoff surface near the boundary, at $\rho = \epsilon$ where $\epsilon \ll 1$. The regularized action is then defined by restricting the integral in the bulk coordinate ρ to be over $\rho > \epsilon$,

$$I^{\text{reg}}_{\text{bulk}} = \frac{1}{16\pi G_{d+1}} \left[\int_{\rho>\epsilon} d^{d+1}x \sqrt{-\hat{g}} \left(\hat{R} - 2\Lambda_{d+1} \right) + 2 \int_{\rho=\epsilon} d^d x \sqrt{-h}\, K \right] \tag{6.6}$$

We may then use the perturbative expansion for $g_{ij}(x, \rho)$ to split the regulated action into a part that stays finite I_{fin} and a part which diverges I_{div} in the limit where $\epsilon \to 0$

$$I^{\text{reg}}_{\text{bulk}} = I_{\text{fin}} + I_{\text{div}}. \tag{6.7}$$

Note that the finite component will typically include higher-curvature terms. The renormalized action is then defined by the minimal subtraction scheme, where a counterterm action is added to cancel out I_{div}

$$I^{\text{ren}}_{\text{bulk}} = \lim_{\epsilon \to 0} \left(I^{\text{reg}}_{\text{bulk}} + I_{\text{ct}} \right). \tag{6.8}$$

The standard AdS/CFT dictionary then shows that varying the renormalized action (6.8) with respect to the boundary metric h_{ij} yields the expectation value of the stress-tensor of the holographic CFT,

$$\langle T^{\text{CFT}}_{ij} \rangle = \lim_{\epsilon \to 0} \left(-\frac{2}{\sqrt{\hat{g}(x,\rho)}} \frac{\delta I^{\text{ren}}_{\text{bulk}}}{\delta \hat{g}^{ij}(x,\epsilon)} \right) \equiv -\frac{2}{\sqrt{h}} \frac{\delta W_{\text{CFT}}[h]}{\delta h^{ij}}\,. \tag{6.9}$$

where $W_{\text{CFT}}[h]$ is the quantum effective action of the CFT.

6.1.3 Braneworld Holography

Braneworld holography implements the holographic renormalization group by replacing the IR cutoff surface with an end–of–the–world (ETW) brane $\mathcal{B}$ at finite radial position. The physical spacetime is the region bounded by $\mathcal{B}$, and there are no more IR divergences to be removed. This brane is taken to have the action

$$I_\tau = -\tau \int_{\mathcal{B}} d^d x \sqrt{-h}, \tag{6.10}$$

where τ is the tension of the brane. To complete the geometry, one glues a second copy of AdS_{d+1} along the cutoff surface. Doing so induces a jump in the extrinsic curvature of the brane determined by the Israel junction condition

$$\Delta K_{ij} - h_{ij}\, \Delta K = 8\pi G_{d+1} S_{ij} = -8\pi G_{d+1} \tau\, h_{ij}\,. \tag{6.11}$$

where $\Delta K_{ij} = K^+_{ij} - K^-_{ij}$ is the difference between the extrinsic curvatures across the two sides of the brane, and S_{ij} is the brane stress tensor. In the simplest (purely tensional) set-up, the brane position is fixed by τ. A boundary CFT_d (BCFT_d) is defined on the AdS_{d+1} boundary $\partial\mathcal{M}$, which is coupled to a defect CFT_{d-1}, (DCFT_{d-1}), which is itself defined where $\mathcal{B}$ intersects $\partial\mathcal{M}$.

An induced theory on the brane is built by adding (6.4) to (6.10), and then integrating out the bulk up to the ETW brane $\mathcal{B}$, on both sides. The induced theory consists of a higher-derivative theory of gravity, and a large-c CFT with a UV cutoff, set by the brane's position, which is minimally coupled to the brane metric. The total action of the induced theory is given by

$$I \equiv I_{\mathrm{Bgrav}}[\mathcal{B}] + I_{\mathrm{CFT}}[\mathcal{B}], \tag{6.12}$$

where the gravitational theory on the brane is governed by the action (cf. [73, 91])

$$\begin{aligned} I_{B\mathrm{grav}} &= 2I_{\mathrm{div}} + I_\tau \\ &= \frac{1}{16\pi G_d}\int_{\mathcal{B}} d^dx\sqrt{-h}\left[R - 2\Lambda_d + \frac{L^2_{d+1}}{(d-4)(d-2)}\left(R^2_{ij} - \frac{dR^2}{4(d-1)}\right) + \cdots\right] \end{aligned} \tag{6.13}$$

where the factor of two is present since the bulk theory is integrated out on both sides of the brane, G_d is the effective Newton's constant on the brane,

$$G_d = \frac{d-2}{2L_{d+1}}G_{d+1}, \tag{6.14}$$

and Λ_d is the effective cosmological constant on the brane

$$\Lambda_d = -\frac{(d-1)(d-2)}{2L_d^2}, \tag{6.15}$$

which is itself related to the effective curvature scale on the brane L_d,

$$\frac{1}{L_d^2} = \frac{2}{L^2_{d+1}}\left(1 - \frac{4\pi G_{d+1}L_{d+1}}{d-1}\tau\right). \tag{6.16}$$

Higher curvature terms in (6.13) are coupled to higher powers of L^2_{d+1}. These higher-derivative terms generally make brane gravitational theory massive, since a massive graviton bound state will localize on the brane. For a brane near the boundary, this mass is negligible [350, 243]. A subset of the bulk graviton fluctuations localized on the brane

are light, with their mass being controlled by the brane tension, while the remaining bulk graviton modes appear as a tower of Kaluza-Klein modes with masses set by the effective AdS_d brane length scale $1/L_d$ [367, 368, 350].

The CFT part of the action I_{CFT} is equal to the finite piece of the regulated bulk action after integrating out the bulk, since

$$I \equiv 2I^{\mathrm{bulk}}_{\mathrm{bulk}} + I_\tau = \underbrace{(2I^{\mathrm{bulk}}_{\mathrm{bulk}} - 2I_{\mathrm{div}})}_{2I_{\mathrm{fin}}=I_{\mathrm{CFT}}} + \underbrace{(I_\tau + 2I_{\mathrm{div}})}_{I_{\mathrm{Bgrav}}}. \tag{6.17}$$

To leading order in the cutoff ϵ, I_{CFT} may be identified with the quantum effective action of the CFT,

$$I_{\mathrm{CFT}} = W_{\mathrm{CFT}} + \mathcal{O}(\epsilon). \tag{6.18}$$

Usually, one works in the limit of ϵ being negligible, which is to say that the brane is close to the original AdS_{d+1} boundary, and the matter field on the brane has a good approximate description as a large-c holographic CFT. As Panella says, this may heuristically be described by a portion of the the conformal boundary $\partial\mathcal{M}$ being pushed into the bulk, so that the dual CFT_d now resides on the brane. Owing to duality, since the ETW brane is an IR cutoff, the CFT on the brane is one with a UV cutoff [350].

6.1.4 Double Holography

The construction so far has assumed a negative cosmological constant on the brane—a Karch-Randall brane. In contrast, a Randall-Sundrum brane may have a non-negative cosmological constant. The Karch-Randall braneworld may be described in three equivalent ways, termed the bulk, brane, and boundary perspectives [350]. From the bulk perspective, the theory we deal with is that of classical gravity in AdS_{d+1}, coupled to an ETW brane (that is itself asymptotically AdS_d) with tension τ. From the brane perspective (which is intermediate between the bulk and boundary), the theory is one of dynamical gravity coupled to a CFT_d with a UV cutoff. This cutoff CFT on the brane communicates with a boundary CFT_d (BCFT_d) [416, 162, 170] on the conformal boundary of the bulk space via transparent boundary conditions. Finally, from the boundary perspective, the object of interest is the BCFT_d. This perspective is viable when the gravitational theory on the ETW brane gravitational theory is itself dual to a defect CFT_{d-1} (DCFT_{d-1}) [455], as described previously. The brane gravitational theory is replaced by a conformal defect by integrating out the bulk and brane. Therefore, the boundary perspective is that of a CFT living on the fixed conformal boundary (as opposed to the dynamical ETW brane), which is coupled to the conformal defect.

6.2 Quantum black holes

The effective induced theory on the brane, governed by (6.12) may be interpreted from the bulk and brane perspectives. From the bulk perspective, the theory describes a $(d+1)$-dimensional system obeying Einstein gravity coupled to an ETW brane obeying boundary conditions. From the brane perspective, the theory describes a d-dimensional higher curvature gravitational theory coupled to a large-c, UV cutoff CFT which backreacts to the brane metric h_{ij}. The higher derivative terms in (6.13) represent quantum corrections induced by this backreaction. The term corrections is appropriate, since the theory on the brane is treated as an effective theory, and one assumes that $L_d \gg L_{d+1}$, which means the higher derivative terms are suppressed [350]. Since, according to double holography, these perspectives are equivalent, we may solve the (complicated) semi-classical field equations on the brane which incorporate backreaction, by solving the (comparatively simple) classical gravitational field equations of the $(d+1)$-dimensional bulk theory (i.e., the theory of the bulk coupled to an ETW brane).

Duff and Liu observed that, in the Randall-Sundrum model, the massive Kaluza-Klein modes lead to a $\sim 1/r^3$ correction to the four-dimensional Newtonian gravitational potential which coincide with the one-loop quantum correction of the graviton propagator [130]. Taking this in conjunction with the double-holography perspective on the problem of backreaction in semiclassical gravity influenced Emparan, Fabbri and Kaloper to make the following conjecture, which lies at the heart of the quantum black hole research program: classical AdS_{d+1} black holes which are localized on a brane are dual to d-dimensional *quantum corrected* black holes in an asymptotically AdS_d spacetime, including all orders of backreaction [133, 350]. It must be stressed again that quantum black holes are solutions to the semi-classical gravitational theory on the brane, and that 'quantum' here refers to the quantum corrections due to backreaction of quantum fields, and does not mean that the black holes are solutions to a fully quantum theory of gravity.

It is helpful to elaborate on the central conjecture with a more detailed description. In the context of braneworld holography, the ETW brane removes a portion of the bulk, and a second copy is glued to complete the geometry. This brane intersects a bulk black hole. This intersection induces the formation of an horizon on the brane. It is this brane black hole that is a quantum black hole, which may be described by studying the classical bulk black hole, via the double holographic duality [350]. The conjecture was corroborated by the discovery of exact AdS_4 braneworld black holes, discovered by Emparan, Horowitz, and Myers [135, 136]. The projection of this black hole onto the brane which intersects it, is interpreted as a three-dimensional quantum black hole. It is worth noting that the neutral-static (i.e., no electric charge and no angular momentum) quantum black

holes have quantum backreaction corrections that are in keeping with a non-holographic (and necessarily perturbative) analysis. However, the rotating quantum black holes, and charged quantum black holes obtained via holography do not agree with non-holographic perturbation theory (i.e., the corresponding models of the black holes that treat backreaction perturbatively, and do not rely on double holography) [350]. For example, the perturbative backreaction effects on the rotating BTZ black hole caused by a conformally coupled scalar field is far more complicated than the corresponding (exact) quantum black hole solution with a holographic CFT [350].

6.2.1 The AdS C-metric

We shall focus on three-dimensional quantum black holes: the case of a holographic AdS_4 bulk with a three-dimensional ETW brane. We assume the brane satisfies Israel junction conditions. As the previous section indicated, the black holes may be interpreted as quantum black holes which solve a semiclassical gravitational theory with non-perturbative backreaction due to a large-c CFT_3 with a UV cutoff. Braneworld quantum black holes are constructed from the bulk geometry of the AdS_4 C-metric coupled to an ETW brane. It is illustrative to consider the example of the neutral-static quantum BTZ black hole, and some aspects of its construction from this bulk solution.

The bulk gravitational theory is taken to be Einstein–Maxwell theory. The most general solution to Einstein–Maxwell theory in the presence of a cosmological constant is given by the Plebiánski–Demiánski type-D metric [360]. The AdS_4 C-metric is a specific type of this solution which, depending on the parameter values, may be interpreted as one or two accelerating black holes in an AdS_4 background [350]. Recall that a black hole localized on a brane requires a bulk geometry whose horizon intersects the ETW brane at finite radius. The AdS C-metric is singled out within the Plebiánski–Demiánski family because, as we will see further in this section, the acceleration of the AdS black holes is sourced by a cosmic string, so there is a tunable acceleration parameter that balances the AdS pull and allows a horizon to be suspended so as to cut the brane. Furthermore, it admits a surface that automatically solves the Israel junction condition, with the brane tension fixed by the acceleration scale. The parameter values of the C-metric also map cleanly to brane data. Other classes of solutions (or global AdS–Schwarzschild without acceleration) either fail to admit such an umbilic embedding at fixed tension or instead produce extended horizons along the brane (black strings) rather than localized holes [135, 136, 134, 350].

The neutral and static (i.e, non-rotating) C-metric takes the following form in Boyer-

Lindquist-like coordinates [134],

$$ds^2 = \frac{\ell^2}{(\ell + xr)^2}\left[-H(r)\,dt^2 + \frac{dr^2}{H(r)} + r^2\left(\frac{dx^2}{G(x)} + G(x)\,d\phi^2\right)\right] \tag{6.19}$$

where

$$H(r) = \frac{r^2}{\ell_3^2} + \kappa - \frac{\mu\ell}{r}\,, \qquad G(x) = 1 - \kappa x^2 - \mu x^3\,. \tag{6.20}$$

In these coordinates, the position of the conformal boundary is not at $r \to \infty$, but depends on the value of the angular variable x. The coordinate r has the range $r \in (-\infty, r_{\text{bdry}}) \cup (0, \infty)$, where $r_{\text{bdry}} = -\ell/x$ is the location of the conformal boundary, and ϕ is an azimuthal coordinate [350].

The parameters $\mu > 0$, κ, $\ell > 0$, and $\ell_3 > 0$ in (6.19) are real numbers that characterize the solution. Here $\kappa \in \{-1, 0, 1\}$ denotes the curvature parameter of the 2-dimensional angular sections of the metric ($\kappa = -1$ recovers classical BTZ geometry on the brane), μ is related to the mass of the black hole in the bulk geometry, ℓ_3 is related to the curvature scale of the brane (which is asymptotically AdS_3), and ℓ is the inverse acceleration of the bulk black hole (when the C-metric describes an accelerating black hole). It is related to the AdS_4 length scale by

$$L_4 = \left(\frac{1}{\ell^2} + \frac{1}{\ell_3^2}\right)^{-1/2}. \tag{6.21}$$

The determining factor for whether (6.19) is a black hole solution is the root structure of the metric functions (6.20)[350]. The roots of $H(r)$ are Killing horizons generated by $\partial/\partial t$ (the time-translation Killing vector). Positive roots correspond to physical black holes. To get rid of the non-compact Rindler horizon associated with the acceleration of the black hole, one works with the case where $\ell < L_4$. In this case, $H(r)$ has a single positive root r_+, which is the black hole horizon. A consequence of working in this regime is that the metric describes a black hole with small acceleration, suspended from the center of AdS_4 by a cosmic string which is attached to the horizon [350]. This acceleration makes the horizon conical.

The real roots of $G(x)$ are associated with the axes of symmetry of the Killing vector $\xi = \partial/\partial_\phi$, the norm of which vanishes when $G(x) = 0$. For the bulk black hole to have a finite horizon, $G(x)$ must have at least one positive root. The smallest of the positive roots

x_1 is then selected, and one must then work in the range $0 < x < x_1$. The mass parameter μ is written in terms of x_1 by solving the equation $G(x_1) = 0$,

$$\mu = \frac{1 - \kappa x_1^2}{x_1^3}. \tag{6.22}$$

The requirements that $x_1 > 0$ and $\mu > 0$ mean that $x_1 \in (0, 1]$ when $\kappa = 1$, and $x_1 \in (0, \infty)$ when $\kappa \in \{-1, 0\}$. Since $G(x_1) = 0$, the space pinches off at this point as an axis. To ensure the absence of conical singularities, we must periodically identify the azimuthal coordinate $\phi \sim \phi + 2\pi\Delta$, where

$$\Delta = \frac{2}{|G'(x_1)|} = \frac{2x_1}{3 - \kappa x_1^2}\,. \tag{6.23}$$

It is now possible to construct the corresponding braneworld three-dimensional quantum black hole. In (6.19), the surface $x = 0$ is always totally umbilic, i.e. it satisfies $K_{ab} \propto h_{ab}$ where K_{ab} is the extrinsic curvature. Such a surface automatically solves the Israel junction conditions arising from a purely tensional brane. It is then a simple matter to relate the brane tension to the parameters of the solution. We have [229, 263]

$$[K_{ab} - K h_{ab}] = 8\pi G_4 T_{ab}\,, \tag{6.24}$$

where

$$T_{ab} = -\frac{2}{\sqrt{-h}} \frac{\delta I_{\text{brane}}}{\delta h^{ab}} = -\tau h_{ab} \tag{6.25}$$

is the brane stress tensor and $[F(z)]$ measures the discontinuity

$$[F] = \lim_{\epsilon \to 0} \left(F|_{z+\epsilon} - F|_{z-\epsilon} \right)$$

of F at z [263]. Then, using the fact that

$$K_{ab} = -\frac{1}{\ell} h_{ab} \tag{6.26}$$

we find the tension of the brane is given by

$$\tau = \frac{1}{2\pi G_4 \ell}\,. \tag{6.27}$$

The brane tension is therefore directly proportional to the acceleration of the bulk black hole, and vanishes in the limit of $\ell \to \infty$. Conversely, the high tension limit of $\ell \to 0$

corresponds to the brane being pushed near the boundary. The metric of the brane is found by setting $x = 0$ in (6.19),

$$ds^2\big|_{x=0} = -\left(\frac{r^2}{\ell_3^2} + \kappa - \frac{\mu\ell}{r}\right) dt^2 + \left(\frac{r^2}{\ell_3^2} + \kappa - \frac{\mu\ell}{r}\right)^{-1} dr^2 + r^2 d\phi^2 \,. \tag{6.28}$$

When $\kappa = -1$, this describes a static black hole. Specifically, this represents the static-neutral quantum BTZ black hole [350].

Applying the braneworld holographic procedure described in 6.1.3 to the three dimensional Karch-Randall brane gives the induced action

$$I = \frac{1}{16\pi G_3} \int_{\mathcal{B}} d^3x\sqrt{-h}\left[R - 2\Lambda_3 + L_4^2\left(\tfrac{3}{8}R^2 - R_{ij}^2\right) + \cdots\right] + I_{\text{CFT}} \,. \tag{6.29}$$

The limit where $L_3 \sim \ell_3$ corresponds to the gravitons on the brane being effectively massless, since the brane is very close to the boundary. This is the limit we will work in. The length scale L_3 is given by (6.16) with $d = 3$. Substituting in (6.27) for the brane tension, and (6.21) for L_4, and then recalling that the limit of the brane being near the boundary corresponds to $\ell \to 0$, and performing a Taylor expansion in ℓ/ℓ_3 gives us the approximation

$$\frac{1}{L_3^2} = \frac{1}{\ell_3^2}\left[1 + \frac{\ell^2}{4\ell_3^2} + \mathcal{O}\left(\frac{\ell^4}{\ell_3^4}\right)\right]. \tag{6.30}$$

The induced action (6.29) then becomes

$$I = \frac{1}{16\pi G_3} \int_{\mathcal{B}} d^3x\sqrt{-h}\left[R + \frac{2}{\ell_3^2} + \ell^2\left(\tfrac{3}{8}R^2 - R_{ij}^2\right) + \cdots\right] + I_{\text{CFT}} \,. \tag{6.31}$$

The crucial point is that the higher curvature corrections to the Einstein-Hilbert action are associated with higher powers of ℓ, which has become an effective UV cutoff scale [350].

The three-dimensional CFT on the brane has its central charge c_3 normalized to

$$c_3 = \frac{L_4^2}{G_4}. \tag{6.32}$$

Substituting (6.21) for L_4, and defining a new symbol $\nu = \ell/\ell_3$, we can write this as

$$c_3 = \frac{\ell}{G_3\sqrt{1+\nu^2}}. \tag{6.33}$$

Performing a Taylor expansion in ν gives

$$2c_3G_3 = L_4 = \ell\left[1 - \frac{1}{2}\nu^2 + \mathcal{O}(\nu^4)\right]. \tag{6.34}$$

The scale of the matter part of the action is given by $|I_{\text{CFT}}| \sim c_3$ while the scale of the gravitational part is $|I_{\mathcal{B}\text{grav}}| \sim L_3/G_3$ [350]. Taking the ratio of these two scales gives us a parameter that determines the contribution of the CFT to the geometry of the brane, G_3c_3/L_3. When $\ell \ll \ell_3$, (so $\nu \ll 1$) this ratio is very small, and the backreaction effects are considered to be in the perturbative regime. Conversely, when $\nu \geq 1$, the backreaction effects are large. We therefore refer to ν as our dimensionless backreaction parameter.

It should be noted that, despite what the form of (6.34) might suggest, our braneworld holographic requirement for a large-c CFT is not violated when we consider $\nu \ll 1$. Recall that the large-c requirement corresponds to semiclassical gravity in the bulk being a good approximation. Indeed, the central charge is normalized according to (6.33), where the right hand side is equal to $L_4^2/L_P^{(4)2}$, since $L_P^{(4)} = \sqrt{G_4}$ is the Planck length in four-dimensional spacetime. The Planck length in three-dimensions is given by $L_P^{(3)} = G_3$. So long as $L_4 \sim \ell \gg G_3$, semiclassical gravity will remain a good approximation. In other words, we work in the regime where the UV cutoff scale ℓ is much greater than the Planck length, which is consistent with taking c_3 to be large[350]. Note that (6.34) implies that for a fixed c_3 gravity becomes weak as $\ell \to 0$.

Further details on quantum black holes are relegated to the next chapter, in which we construct the charged and rotating quantum BTZ black hole.

6.3 Black hole thermodynamics

The development of black hole thermodynamics represents one of the most remarkable discoveries in theoretical physics. It remains a cornerstone of modern quantum gravity research, since the entropy of thermodynamic systems must count underlying microstates in statistical mechanics, and uncovering this microstate origin of black hole entropy promises to illuminate the nature of a consistent quantum theory of gravity.

6.3.1 Classical Black Holes and the Laws of Mechanics

Black holes were originally understood as purely geometric objects: regions of spacetime bounded by event horizons, from which nothing can escape. The discovery that black

holes possess temperature and entropy solved the apparent violation of the second law of thermodynamics implicit in the assumption that black holes have a temperature of absolute zero. In the early 1970s, Bardeen, Carter, and Hawking formulated the four laws of black hole mechanics, which closely mirror the familiar laws of thermodynamics [39, 306]:

- The **zeroth law**: the surface gravity κ of a stationary black hole is constant over its event horizon.
- The **first law**: A change in the mass of a black hole dM is given by

$$dM = \frac{\kappa}{8\pi G} dA + \Omega_H dJ + \Phi_H dQ + \cdots \tag{6.35}$$

  where M is the ADM mass, A the horizon area, J the angular momentum, Ω_H the angular velocity of the black hole horizon, Q the charge, and Φ_H the electrostatic potential at the horizon.
- The **second law**: Hawking's area theorem states that the horizon area A never decreases in classical general relativity.
- The **third law**: it is impossible to reduce the surface gravity κ to zero by any finite sequence of physical processes.

This parallel with the laws of thermodynamics motivated the identification of area with entropy, and surface gravity with temperature.

6.3.2 Hawking radiation

The decisive breakthrough came in 1974 when Hawking demonstrated (using QFTCS) that black holes radiate as black bodies with a temperature [192]

$$T_H = \frac{\hbar \kappa}{2\pi c k_B}. \tag{6.36}$$

This result conferred a physical interpretation upon the earlier analogy: the surface gravity *is* a temperature, and the horizon area corresponds to entropy. Bekenstein had already argued, on information-theoretic grounds, that black holes must possess an entropy proportional to horizon area [41]. Hawking's discovery fixed the proportionality constant, giving the celebrated Bekenstein–Hawking entropy:

$$S_{BH} = \frac{k_B c^3}{4G\hbar} A. \tag{6.37}$$

6.4 Black hole chemistry

In the standard formulation of black hole thermodynamics, the the ADM mass M of the black hole is identified with the internal energy of the spacetime, the surface gravity κ is identified with the temperature $T = \kappa/2\pi$, and the horizon area A is identified with the entropy $S = A/4G$. In asymptotically AdS spacetimes however, it has proven fruitful to enlarge this dictionary by promoting the cosmological constant Λ to a thermodynamic variable, related to a pressure. This extension, known as *black hole chemistry*, provides a consistent and powerful framework for analyzing black hole phase structure in direct analogy with laboratory thermodynamics [260, 261, 306].

6.4.1 Pressure–Volume Thermodynamics

The central step is to interpret the cosmological constant as a pressure,

$$P \equiv -\frac{\Lambda}{8\pi G}, \tag{6.38}$$

which is positive for the AdS case since $\Lambda < 0$. The conjugate quantity is the thermodynamic volume V, defined through the extended first law as

$$dM = T\,dS + \Omega\,dJ + \Phi\,dQ + V\,dP + \cdots, \tag{6.39}$$

where Ω and J are the horizon angular velocity and angular momentum, and Φ and Q are the electrostatic potential and charge, with ellipses denoting possible additional conserved charges. The appearance of the $V\,dp$ term implies that the ADM mass M is most naturally interpreted as the *enthalpy* of the spacetime rather than its internal energy:

$$M = H = U + PV. \tag{6.40}$$

This reinterpretation is consistent with scaling arguments and the Smarr relation, to which we now turn.

6.4.2 Smarr Relation

In d spacetime dimensions, dimensional analysis yields the generalized Smarr formula

$$(d-3)M = (d-2)TS + (d-2)\Omega J - 2PV + (d-3)\Phi Q + \cdots, \tag{6.41}$$

which has been explicitly verified for a wide class of AdS black holes. The appearance of the $-2PV$ term is characteristic of the extended thermodynamic framework and ensures consistency with the first law.

6.4.3 Phase Structure and Critical Phenomena

Treating AdS black holes as genuine thermodynamic systems with (P, V, T) variables reveals a striking phase structure. For example, the charged Reissner–Nordström–AdS black hole exhibits a small/large black hole transition that is directly analogous to the liquid–gas transition in a van der Waals fluid.

The Gibbs free energy develops the characteristic swallowtail structure, and the associated equation of state

$$P = \frac{T}{v} - \frac{1}{2\pi v^2} + \frac{Q^2}{\pi v^4}, \tag{6.42}$$

where v is the specific volume, defined as $6V/N$ where V is the thermodynamic volume and $N == A/L_P^2$ is the "number of states", counting the degrees of freedom associated with the black hole horizon, possesses critical points with mean-field critical exponents [306, 260],

$$\alpha = 0, \qquad \beta = \tfrac{1}{2}, \qquad \gamma = 1, \qquad \delta = 3. \tag{6.43}$$

Furthermore, the Hawking–Page transition between thermal AdS and a large, stable Schwarzschild-AdS black hole is shown to be the analogue of a solid/liquid transition. This is because, in the P–T plane its coexistence line does not terminate at a critical point but persists for all pressures (equivalently, all $\Lambda < 0$). This framing complements the confinement/deconfinement interpretation on the CFT side [260]. These features demonstrate that black hole chemistry provides not only a conceptual extension of black hole thermodynamics but also a precise laboratory for studying analogues of condensed matter phase transitions in a gravitational setting.

6.4.4 Holographic Interpretation

From the holographic perspective, the cosmological constant is related to the number of degrees of freedom in the dual CFT. Varying Λ corresponds to varying the central charge, or equivalently the rank N of the gauge group in large-N holography [245]. Thus, the pressure–volume sector of black hole chemistry encodes information about the microscopic structure of the dual field theory in a manner complementary to entropy and temperature. In braneworld holography, this viewpoint is especially natural: the brane black hole inherits the full extended thermodynamic structure of its bulk progenitor, but in a setting where the dual degrees of freedom are manifestly those of a cutoff CFT.

Black hole chemistry therefore provides a unifying framework in which to analyze the thermodynamics of semiclassical braneworld black holes. Its language of enthalpy, pressure, and volume will be essential in subsequent chapters, where we study charged and rotating quantum black holes and their associated phase behavior.

In the rest of Part II, we turn to the construction of charged and rotating quantum black holes, and perform an analysis of its thermodynamics and phase structure in the language of black hole chemistry.

Chapter 7

Charged and Rotating Quantum Black Holes

In this chapter, we present a construction of the charged-rotating quantum black hole, as well as a calculation of its thermodynamic quantities as expressed in terms of dimensionless parameters characterizing its size, charge, spin, and the backreaction of the fields.

7.1 Solution and braneworld embedding

We begin with the four-dimensional Einstein-Maxwell action with the following conventions,

$$I_{\rm bulk} = \frac{1}{16\pi G_4}\int_{\mathcal{M}} \mathrm{d}^4x\sqrt{-g}\left(\mathcal{R}+\frac{6}{L_4^2}\right) - \frac{1}{4g_4^2}\int_{\mathcal{M}}\mathrm{d}^4x\sqrt{-g}F_{ab}F^{ab}\,, \tag{7.1}$$

where $\mathcal{R}$ is the Ricci scalar of the bulk spacetime with metric g_{ab}, the cosmological constant Λ_4 is related with the AdS length ℓ_3 via $3/\ell_4^2$, and the curvature of the electromagnetic field $\mathbf{F}$ is coupled with the Einstein term via a dimensionless coupling constant g_4, which is related with a length scale $\ell_\star$ via $\ell_\star^2 \equiv 16\pi G_4/g_4^2$. Here we are interested in the charged and rotating C-metric [117, 360, 182], which is a solution of the above Einstein-Maxwell action with the metric

$$\begin{aligned}\mathrm{d}s^2 = \frac{1}{\Omega^2}\Bigg[&-\frac{H(r)}{\Sigma(x,r)}\left(\mathrm{d}t+ax^2\mathrm{d}\phi\right)^2+\frac{\Sigma(x,r)}{H(r)}\mathrm{d}r^2\\ &+r^2\left(\frac{\Sigma(x,r)}{G(x)}\mathrm{d}x^2+\frac{G(x)}{\Sigma(x,r)}\left(\mathrm{d}\phi-\frac{a}{r^2}\mathrm{d}t\right)^2\right)\Bigg]\,,\end{aligned} \tag{7.2}$$

where

$$H(r) = \frac{a^2}{r^2} + \kappa + \frac{\ell^2 q^2}{r^2} + \frac{r^2}{\ell_3^2} - \frac{\ell\mu}{r}\,, \tag{7.3}$$

$$G(x) = \frac{a^2 x^4}{\ell_3^2} - q^2 x^4 - \mu x^3 - \kappa x^2 + 1\,, \tag{7.4}$$

$$\Sigma(x,r) = 1 + \frac{a^2 x^2}{r^2}\,, \tag{7.5}$$

$$\Omega = 1 + \frac{xr}{\ell}\,. \tag{7.6}$$

The gauge field takes the form

$$A_\mu dx^\mu = \frac{2}{\ell_\star}\left(-\frac{\ell q r}{a^2x^2 + r^2}\,,\, 0\,,\, 0\,,\, -\frac{a\ell q r x^2}{a^2x^2 + r^2}\right)\,. \tag{7.7}$$

The metric (7.2) and gauge field (7.7) satisfy the Einstein equation

$$R_{ab} + \frac{\ell_\star^2}{2} F_a{}^c F_{cb} + \frac{\ell_\star^2}{8} F^{cd} F_{cd} g_{ab} = -3\left(\frac{1}{\ell^2} + \frac{1}{\ell_3^2}\right) g_{ab} = -\frac{3}{L_4^2} g_{ab} \tag{7.8}$$

and the Maxwell equation

$$\nabla \cdot \mathbf{F} = \mathbf{0}\,. \tag{7.9}$$

Recall that, in the above solution, μ encodes the mass of the black hole, ℓ is the inverse of the acceleration for the C-metric, ℓ_3 is related with (but not equal to) the cosmological constant, and κ parametrizes the topology of the black hole horizon. Further note that q is the charge parameter, a the angular momentum parameter.

The parameter ranges are determined by ensuring that the metric signature remains invariant in the domain of communication. The inner and outer horizons $r_\mp$ are determined by $H(r_\mp) = 0$, and the conformal boundary r_c is determined by $\Omega = 0$. The condition we have stated corresponds to $H(r)$ not changing signs between $r_+ < r < r_c$. On the other hand, to ensure proper metric signature we must have $G(x) \geq 0$. While the metric is fairly complicated, this constraint on $G(x)$ leads to nothing conceptually new when compared with the neutral-rotating or static charged metrics considered in previous works. That is, we take the range of x to be

$$0 \leq x \leq x_1\,, \tag{7.10}$$

where x_1 is the smallest positive root of $G(x)$. We shall also consider the mass parameter μ to be positive and take it to be a 'derived' parameter. That is, solving for μ by setting $G(x_1) = 0$ we obtain

$$\mu = \frac{-\left(q^2 - a^2/\ell_3^2\right) x_1^4 - \kappa x_1^2 + 1}{x_1^3} \geq 0\,. \tag{7.11}$$

On the other hand, since $G(x_1) = 0$, the space pinches off at this point as an axis. Hence, to ensure the absence of conical singularities, we must periodically identify the azimuthal coordinate $\phi \in [0, 2\pi\Delta]$ where

$$\Delta = \frac{2}{|G'(x_1)|} = \frac{2}{|-2\kappa x_1 - 3\mu x_1^2 - 4\,(q^2 - a^2/\ell_3^2)\,x_1^3|}\,. \tag{7.12}$$

Having made these global considerations, it is possible to apply the braneworld 'algorithm' to construct the corresponding three-dimensional quantum black hole. To do this, we first must couple the Einstein-Maxwell action to a brane, which we take to be purely tensional with tension τ. The total action therefore have three pieces,

$$I = I_{\rm bulk}[\mathcal{M}] + I_{\rm GHY}[\partial\mathcal{M}] + I_{\rm brane}[\mathcal{B}]\,, \tag{7.13}$$

which are respectively, the Einstein-Maxwell bulk term given in (7.1), the Gibbons-Hawking-York (GHY) boundary term (which is necessary for the variational problem to be well defined),

$$I_{\rm GHY} = \frac{1}{8\pi G_4}\int_{\partial\mathcal{M}} \mathrm{d}^3x\sqrt{-h}K\,, \tag{7.14}$$

where K is the extrinsic curvature scalar and h is the determinant of the induced metric on the brane $\mathcal{B}$, and the brane term,

$$I_{\rm brane} = -\tau\int_{\mathcal{B}} \mathrm{d}^3x\sqrt{-h}\,, \tag{7.15}$$

where τ is the tension of the brane. The variation of the bulk and boundary parts of this action yield the Einstein-Maxwell equations plus the junction conditions at the brane interface. Recall that in the case of the C-metric written in the chart (7.2), the surface $x = 0$ is always totally umbilic, and therefore solves the junction conditions arising from a purely tensional brane. The brane tension is still given by (6.27).

The induced metric on the brane is

$$\mathrm{d}s^2 = -H(r)\mathrm{d}t^2 + \frac{1}{H(r)}\mathrm{d}r^2 + r^2\left(\mathrm{d}\phi - \frac{a}{r}\mathrm{d}t\right)^2\,, \tag{7.16}$$

where $H(r)$ is given by

$$H(r) = \frac{r^2}{\ell_3^2} + \kappa - \frac{\mu\ell}{r} + \frac{q^2\ell^2}{r^2} + \frac{a^2}{r^2}\,. \tag{7.17}$$

In order for the azimuthal coordinate to have the range $[0, 2\pi]$, and take on the canonical asymptotic form of a rotating AdS black hole, we define [350]

$$a = \frac{\ell_3 \bar{a}}{x_1^2}\,, \quad r_s = \ell_3 \frac{\bar{a}\Delta}{x_1}\sqrt{2 - \kappa x_1^2}\,. \tag{7.18}$$

and employ the coordinate transformations

$$t = \Delta(\bar{t} - \bar{a}\ell_3\bar{\phi})\,, \quad r = \sqrt{\frac{\bar{r}^2 - r_s^2}{(1-\bar{a}^2)\Delta^2}}\,, \quad \phi = \Delta(\bar{\phi} - \bar{a}\bar{t}/\ell_3)\,, \tag{7.19}$$

yielding

$$\begin{aligned} \mathrm{d}s^2 = &-\left(\frac{\bar{r}^2}{\ell_3^2} + \frac{q^2\ell^2\Delta^2}{r^2} - \Delta^2\left(\frac{4\bar{a}^2}{x_1^2} - (1+\bar{a}^2)\kappa\right) - \frac{\ell\Delta^2\mu}{r}\right)\mathrm{d}\bar{t}^2 \\ &+ \frac{\bar{r}^2}{(\bar{a}^2-1)^2\Delta^4 r^2}\left(\kappa + \frac{r^2}{\ell_3^2} + \frac{q^2\ell^2 x_1^2 + \bar{a}^2\ell_3^2}{x_1^4 r^2} - \frac{\ell\mu}{r}\right)^{-1}\mathrm{d}\bar{r}^2 \\ &+ \left(\bar{r}^2 - \bar{a}^2\Delta^2\ell_3^2\left(\frac{q^2\ell^2}{r^2} - \frac{\ell\mu}{r}\right)\right)\mathrm{d}\bar{\phi}^2 \\ &- 2\bar{a}x_1\ell_3\Delta^2(q^2x_1+\mu)\left(1 + \frac{\ell}{rx_1} - \frac{q^2\ell(rx_1+\ell)}{r^2x_1(q^2x_1+\mu)}\right)\mathrm{d}\bar{t}\mathrm{d}\bar{\phi} \end{aligned} \tag{7.20}$$

for the metric on the brane, where $r = r(\bar{r})$ from (7.19).

Examining the $\bar{t}\bar{t}$-component of the metric (specifically, taking note of the term that is independent of radius $\bar{r}$), allows us to make the following identification for the black hole mass,

$$8\mathcal{G}_3 M = -\kappa\Delta^2\left(1 + \bar{a}^2 - \frac{4\bar{a}^2}{\kappa x_1^2}\right)\,, \tag{7.21}$$

where $\mathcal{G}_3 \equiv G_4/2\ell$ is the renormalized Newton's constant [147], which can be related to the effective three-dimensional Newton's constant G_3 on the brane as

$$G_3 = \frac{1}{2L_4}G_4 = \frac{\ell}{L_4}\mathcal{G}_3\,. \tag{7.22}$$

Note that the effect of electric charge on the mass is hidden in Δ as there is functionally no difference between the mass (7.21) of our charged rotating black hole, and the mass of the neutral-rotating black hole. The mass M of the black hole here is related to the conical deficit angle [135, 136], as confirmed in [263] via the Euclidean formulation. The result should be the same if one uses the Ashtekar-Das conformal mass [32, 112] or the

holographic stress tensor [369], as studied in [29, 26] for the four-dimensional accelerating black holes when suitably adapted to account for the presence of the brane, though it would be interesting to confirm this.

The angular momentum is then found from the $\bar{t}\bar{\phi}$ element in the limit of $\bar{r} \to \infty$,

$$4\mathcal{G}_3 J = \bar{a} x_1 \ell_3 \Delta^2 (q^2 x_1 + \mu)\,. \tag{7.23}$$

Unlike the expression for the mass, the angular momentum explicitly depends on the charge parameter q. We can then rewrite the metric in terms of the mass and angular momentum as

$$\begin{aligned} ds^2 = &-\left(\frac{\bar{r}}{\ell_3^2} - 8\mathcal{G}_3 M - \ell\Delta^2\left(\frac{\mu}{r} - \frac{q^2\ell}{r^2}\right)\right)\mathrm{d}\bar{t}^2 + \left(\bar{r}^2 + \bar{a}^2\ell_3^2\ell\Delta^2\left(\frac{\mu}{r} - \frac{q^2\ell}{r^2}\right)\right)\mathrm{d}\bar{\phi}^2 \\ &-8\mathcal{G}_3 J\left(1 + \frac{\ell}{x_1 r} - \frac{q^2\ell(x_1 r + \ell)}{r^2 x_1 (q^2 x_1 + \mu)}\right)\mathrm{d}\bar{t}\mathrm{d}\bar{\phi} \\ &+\left(\frac{\bar{r}^2}{\ell_3^2} - 8\mathcal{G}_3 M + \frac{(4\mathcal{G}_3 J)^2}{\bar{r}^2} + (\bar{a}^2 - 1)^2\ell\Delta^4\frac{(q^2\ell - r\mu)}{\bar{r}^2}\right)^{-1}\mathrm{d}\bar{r}^2\,. \end{aligned} \tag{7.24}$$

The above three-dimensional metric is a solution of the semiclassical Einstein equations on the brane. More specifically, it solves the following effective action:

$$I = I_{\mathrm{CFT}}[\mathcal{B}] + I_{\mathrm{Bgrav}}\,[\mathcal{B}]\,, \tag{7.25}$$

where $I_{\mathrm{CFT}}[\mathcal{B}]$ stands for the action of the holographic CFT_3 on the brane and $I_{\mathrm{Bgrav}}\,[\mathcal{B}]$ is the gravitational action

$$I_{\mathrm{Bgrav}} = \frac{\ell_4}{8\pi \mathrm{G}_4}\int \mathrm{d}^3x\sqrt{-h}\left[\frac{4}{\ell_4^2}\left(1 - \frac{\ell_4}{\ell}\right) + R + \ell_4^2\left(\frac{3}{8}R^2 - R_{ab}R^{ab}\right) + \cdots\right] + I_{\mathrm{EM}}\,, \tag{7.26}$$

where I_{EM} represents the induced electromagnetic action on the brane, which was first given in [418] and reads

$$\begin{aligned} I_{\mathrm{EM}} = \frac{\ell_4\ell_\star^2}{8\pi G_4}\int \mathrm{d}^3x\sqrt{-h}\Big[&-\frac{5}{16}\tilde{F}^2 + \ell_4^2\Big(\frac{1}{288}R\tilde{F}^2 - \frac{5}{8}R^a_b\tilde{F}_{ac}\tilde{F}^{bc} \\ &+ \frac{3}{98}\tilde{F}^{ab}\left(\nabla_b\nabla^c\tilde{F}_{ca} - \nabla_a\nabla^c\tilde{F}_{cb}\right) + \frac{5}{24}\nabla_a\tilde{F}^{ab}\nabla_c\tilde{F}^c_b\Big) + \mathcal{O}(\ell_4^3)\Big]\,, \end{aligned} \tag{7.27}$$

where $\widetilde{\mathbf{F}} = \mathrm{d}\bar{\mathcal{A}}$ with $\bar{\mathcal{A}}$ the induced gauge potential on the brane

From the brane effective action we can directly read off the three-dimensional coupling constants in terms of their four-dimensional counterparts. For the three-dimensional Newton constant we already did this earlier in (7.22). It is useful to define a three-dimensional gauge coupling constant g_3 to describe the non-linear electromagnetic field on the brane through

$$g_3^2 = \frac{2g_4^2}{5L_4}\,. \tag{7.28}$$

Writing the brane action in terms of the intrinsically three-dimensional quantities G_3, L_3 and g_3 we have

$$\begin{aligned} I_{\rm Bgrav} =& \frac{1}{16\pi G_3}\int \mathrm{d}^3x\sqrt{-h}\left[\frac{2}{L_3^2}+R+\ell^2\left(\frac{3}{8}R^2-R_{ab}R^{ab}\right)\right] \\ &+\int \mathrm{d}^3x\sqrt{-h}\Bigg[-\frac{1}{4g_3^2}\widetilde{\mathbf{F}}^2+\frac{4\ell^2}{5g_3^2}\Bigg(\frac{1}{288}R\widetilde{\mathbf{F}}^2-\frac{5}{8}R^a_b\widetilde{F}_{ac}\widetilde{F}^{bc}+\frac{5}{24}(\nabla\cdot\widetilde{\mathbf{F}})^2 \\ &+\frac{3}{98}\widetilde{F}^{ab}\left(\nabla_b\nabla^c\widetilde{F}_{ca}-\nabla_a\nabla^c\widetilde{F}_{cb}\right)\Bigg)+\cdots\Bigg]\,. \end{aligned}$$

7.2 Thermodynamic quantities

Note that the presence or absence of electric charge does not change the functional form of (7.16), only the function $H(r)$. This is in contrast to the black hole's spin, since the rotation parameter a explicitly enters the metric, outside of $H(r)$. Because of this, many of the parameters derived from the metric, including the angular velocity and temperature of the black hole's outer horizon, have the same functional form as in the neutral-rotating quantum BTZ black hole, and their calculation can be carried over from the analysis performed in [134] with no change.

The original form for the induced metric on the brane (7.16) manifestly had the Killing vectors ∂_t and ∂_ϕ. Under the coordinate transformation (7.19), these Killing vectors are written as

$$\begin{aligned} \frac{\partial}{\partial t} &= \frac{1}{\Delta(1-\bar{a}^2)}\left(\frac{\partial}{\partial\bar{t}}+\frac{\bar{a}}{\ell_3}\frac{\partial}{\partial\bar{\phi}}\right)\,, \\ \frac{\partial}{\partial \phi} &= \frac{1}{\Delta(1-\bar{a}^2)}\left(\frac{\partial}{\partial\bar{\phi}}+\bar{a}\ell_3\frac{\partial}{\partial\bar{t}}\right)\,, \end{aligned} \tag{7.29}$$

as shown in [134, 350]. The outer horizon of the black hole corresponds to those points with the coordinate $r = r_+$, where r_+ is the largest positive root of $H(r)$. It is the Killing

horizon of the Killing vector

$$k = \frac{\partial}{\partial t} + \frac{a}{r_+^2}\frac{\partial}{\partial \phi}\,. \tag{7.30}$$

Given (7.29), we can see that the canonically normalized Killing vector $\bar{k}$, which generates the outer horizon, takes the form

$$\bar{k} = \frac{\Delta(1-\bar{a}^2)}{1+\frac{a^2x_1^2}{r_+^2}}k = \frac{\partial}{\partial \bar{t}} + \Omega_H \frac{\partial}{\partial \bar{\phi}}\,, \tag{7.31}$$

where Ω_H, the angular velocity of the outer horizon, is

$$\Omega_H \equiv \frac{a}{r_+^2 + a^2x_1^2}\left(1 + \frac{r_+^2x_1^2}{\ell_3^2}\right)\,. \tag{7.32}$$

The temperature of the outer horizon, relative to $\bar{k}$ is

$$T = \frac{\Delta(1-\bar{a}^2)}{1+\frac{a^2x_1^2}{r_+^2}}\frac{H'(r_+)}{4\pi} = \frac{\Delta\left(2r_+^4 - 2\ell_3^2\left(a^2+q^2\ell^2\right) + \mu r_+\ell\ell_3^2\right)}{4\pi r_+\ell_3^2\left(a^2x_1^2+r_+^2\right)}\,. \tag{7.33}$$

To calculate the entropy of the quantum charged rotating black hole, we compute the entropy of the bulk horizon using the bulk metric (7.2). The Bekenstein-Hawking entropy is given by

$$\begin{aligned} S_{\text{gen}} =& \frac{\text{Area}(r_+)}{4G_4} \\ =& \frac{1}{2G_4}\int_0^{2\pi\Delta} \mathrm{d}\phi \int_0^{x_1} \mathrm{d}x \frac{r_+^2\ell^2}{(\ell+r_+x)^2}\left(1+\frac{a^2x_1^2}{r_+^2}\right) \\ =& \frac{\pi}{G_4}\Delta\frac{\ell x_1(r_+^2+a^2x_1^2)}{\ell+r_+x_1}\,. \end{aligned} \tag{7.34}$$

This can be interpreted as a generalized entropy that incorporates the backreaction of quantum fields on the black hole spacetime, to all orders of perturbation theory.

The electric charge of the black hole on the brane is identified with the charge of the bulk, which is given by

$$Q = \frac{1}{g_4^2}\int *\mathbf{F} = \frac{4\pi\Delta q x_1 \ell}{g_4^2\ell_\star}\,. \tag{7.35}$$

To calculate the conjugate electric potential, we first see that, on the brane (located at $x=0$), the gauge field (7.7) becomes

$$\bar{\mathcal{A}}_\mu \mathrm{d}\bar{x}^\mu = -\frac{2\ell q\Delta}{\ell_\star r(\bar{r})}\mathrm{d}\bar{t} + \frac{2\bar{a}\ell_3\ell q\Delta}{\ell_\star r(\bar{r})}\mathrm{d}\bar{\phi}\,, \tag{7.36}$$

where $r(\bar{r})$, is given by the coordinate transformation (7.19). The electric potential conjugate to the electric charge on the brane is given by the difference in the inner product between this one-form and the Killing vector

$$\zeta^{\mu} = \frac{\partial}{\partial \bar{t}} + \frac{\bar{a}}{\ell_3}\frac{\partial}{\partial \bar{\phi}}\,, \tag{7.37}$$

evaluated at $r \to \infty$ and $r = r_+$. This gives

$$\Phi = \bar{\mathcal{A}}_{\mu}\zeta^{\mu}\Big|_{r=r_+}^{r\to\infty} = (1-\bar{a}^2)\frac{2\ell q \Delta}{\ell_* r_+}\,. \tag{7.38}$$

We now possess several of the physical parameters of the charged rotating quantum black hole.

7.2.1 Brane expressions

We can write the expressions found in the preceding subsection as functions of dimensionless variables as

$$z = \frac{\ell_3}{r_+ x_1}\,, \quad \nu = \frac{\ell}{\ell_3}\,, \quad \chi = q x_1^2\,, \quad \alpha = \frac{\bar{a}}{\sqrt{-\kappa}x_1}\,, \tag{7.39}$$

where χ and α are the new parameters for electric charge and spin respectively. By combining the above definitions with $H(r_+) = 0$ and $G(x_1) = 0$, we obtain the expressions for x_1^2, r_+^2 and μx_1 as

$$\begin{aligned}
x_1^2 =& \frac{\nu z^3\left(\chi^2(\nu z+1)-1\right)+1}{\kappa z^2\left(\alpha^2 z^2-(\alpha^2+1)\nu z-1\right)}\,,\\
r_+^2 =& \frac{\kappa \ell_3{}^2\left(\alpha^2 z^2-(\alpha^2+1)\nu z-1\right)}{\nu z^3\left(\chi^2(\nu z+1)-1\right)+1}\,,\\
\mu x_1 =& \frac{\kappa\left(\left(z^2+1\right)\left(\alpha^2\left(z^2-1\right)-1\right)-\chi^2 z^2\left(z^2\left(\alpha^2\left(\nu^2+1\right)+\nu^2\right)-1\right)\right)}{\nu z^3\left(\chi^2(\nu z+1)-1\right)+1}\,.
\end{aligned} \tag{7.40}$$

It is convenient to define [147]

$$\kappa = -\mathrm{sgn}(\nu^2\chi^2 z^4 + \nu\chi^2 z^3 - \nu z^3 + 1)\,, \tag{7.41}$$

where sgn is the sign function. Since $r_+^2 > 0$, the rotation parameter α is bounded from above as

$$\alpha^2 \leq \frac{1+\nu z}{z(z-\nu)}\,, \tag{7.42}$$

which is the same restriction found for the neutral-rotating black hole in [134]. Given the definition in (7.39), we can see that the case of $\kappa = +1$ corresponds to imaginary values of α. These states correspond to naked closed timelike curves, and are not black hole solutions [134]. The central charge of the CFT_3 is given by

$$c_3 = \frac{L_4^2}{G_4} = \frac{\nu \ell_3}{2G_3\sqrt{\nu^2+1}}\,, \tag{7.43}$$

as expressed in terms of the AdS_3 radius ℓ_3. The dependence of the central charge on the backreaction parameter ℓ suggests that it may be regarded as a thermodynamic variable of the system. We employ the extended thermodynamic phase space treatment of black hole chemistry described in the preceding chapter [261] in which the pressure P_3 of the system on the brane is identified with the cosmological constant Λ_3 as

$$P_3 = -\frac{\Lambda_3}{8\pi G_3} = \frac{\sqrt{\nu^2+1}}{4\pi G_3 \ell_3^2(\sqrt{\nu^2+1}+1)}\,. \tag{7.44}$$

With (7.40) at hand, we can find the mass (7.21), entropy (7.34), angular momentum (7.23), and charge (7.35) of the quantum charged rotating black hole on the brane in terms of our dimensionless variables respectively as

$$\begin{aligned} M = \; & \frac{1}{2G_3}(-\alpha^2 + z^2\left(\chi^2 + z^2\left(\nu^2\chi^2 - \alpha^2\left(\left(\nu^2+1\right)\chi^2+3\right)\right)\right. \\ & \left.+2\nu z\left(2\alpha^2+\chi^2+1\right)+3\right)+1\Big)^{-2} \\ & \times\Big[\sqrt{\nu^2+1}(\nu z^3(\chi^2(\nu z+1)-1)+1)\left(\alpha^2+z^2\left(4\alpha^4 z(\nu-z)\right.\right. \\ & \left.\left.+\alpha^2\left(z\left(4\nu+\nu\chi^2(\nu z+1)-z\right)+4\right)+\nu z+1\right)\right)\Big]\,, \end{aligned} \tag{7.45}$$

$$\begin{aligned} S_{\text{gen}} = \; & -\frac{\pi}{G_3}\left[\sqrt{\nu^2+1} z\ell_3\left(\alpha^2\left(z^2\left(\nu\chi^2 z-1\right)+1\right)+1\right)\right] \\ & \times\Big[\Big(\alpha^2+z^2\left(-\chi^2+z\left(-2\nu\left(2\alpha^2+\chi^2+1\right)\right.\right. \\ & \left.\left.+\chi^2 z\left(\left(\alpha^2-1\right)\nu^2+\alpha^2\right)+3\alpha^2 z\right)-3\right)-1\Big)\Big]^{-1}\,, \end{aligned} \tag{7.46}$$

$$\begin{aligned} J = & \frac{1}{G_3}\left[\alpha z\ell_3\left(\alpha^2-\alpha^2 z^4+\left(\alpha^2+1\right)\nu\chi^2 z^3(\nu z+1)+z^2+1\right)\right. \\ & \left.\times\sqrt{\left(\nu^2+1\right)\left(z\left(\nu+\alpha^2(\nu-z)\right)+1\right)\left(\nu z^3\left(\chi^2(\nu z+1)-1\right)+1\right)}\right] \\ & \Big[-\alpha^2+z^2\left(\chi^2+z^2\left(\nu^2\chi^2-\alpha^2\left(\left(\nu^2+1\right)\chi^2+3\right)\right)\right. \\ & \left.+2\nu z\left(2\alpha^2+\chi^2+1\right)+3\right)+1\Big]^{-2}\,, \end{aligned} \tag{7.47}$$

$$
\begin{aligned}
Q =& -\left[4\sqrt{\pi}\chi z^2\sqrt{\nu^2+1}\left(z\left(\nu+\alpha^2(\nu-z)\right)+1\right)\right] \\
&\times\left[\sqrt{5G_3}g_3\left(\alpha^2+z^2\left(-\chi^2+z\left(-2\nu\left(2\alpha^2+\chi^2+1\right)\right.\right.\right.\right. \\
&\left.\left.\left.\left.+\chi^2 z\left(\left(\alpha^2-1\right)\nu^2+\alpha^2\right)+3\alpha^2 z\right)-3\right)-1\right)\right]^{-1}.
\end{aligned}
\tag{7.48}
$$

Given these quantities, we can obtain the temperature T, angular velocity Ω_H, electric potential Φ, three-dimensional thermodynamic volume V_3 and three-dimensional chemical potential μ_3 as

$$
\begin{aligned}
T =& \left(\frac{\partial M}{\partial S_{\rm gen}}\right)_{P_3,c_3,Q,J} \\
=&\left[\left(z\Big(\nu\chi^2 z^2\left(z^2\left(\alpha^2\left(\nu^2+1\right)+\nu^2\right)+2\nu z+1\right)\right.\right. \\
&\left.-\nu\left(\alpha^2\left(z^4+3\right)+z^2+3\right)+4\alpha^2 z\right)-2\Big) \\
&\left.\times\left(\alpha^2+z^2\left(\alpha^2 z\left(-2\nu+\nu\chi^2(\nu z+1)+z\right)-\nu z-1\right)\right)\right] \\
&\times\left[2\pi z\ell_3(\nu z+1)\left(\alpha^2\left(z^2\left(\nu\chi^2 z-1\right)+1\right)+1\right)\right. \\
&\times\left(\alpha^2+z^2\Big(-\chi^2+z\Big(-2\nu\Big(2\alpha^2+\chi^2+1\Big)\right.\right. \\
&\left.\left.\left.+\chi^2 z\left(\left(\alpha^2-1\right)\nu^2+\alpha^2\right)+3\alpha^2 z\right)-3\right)-1\right)\Big]^{-1},
\end{aligned}
\tag{7.49}
$$

$$
\begin{aligned}
\Phi =& \left(\frac{\partial M}{\partial Q}\right)_{S_{\rm gen},P_3,c_3,J} \\
=&-\left[\sqrt{5}g_3\nu\chi z\left(\alpha^2 z^2-\left(\alpha^2+1\right)\nu z-1\right)\right. \\
&\left.\times\left(\alpha^2+z^2\left(\alpha^2 z\left(-2\nu+\nu\chi^2(\nu z+1)+z\right)-\nu z-1\right)\right)\right] \\
&\times\left[2\sqrt{G_3\pi}(\nu z+1)\left(\alpha^2\left(z^2\left(\nu\chi^2 z-1\right)+1\right)+1\right)\right. \\
&\times\left(\alpha^2+z^2\Big(-\chi^2+z\Big(-2\nu\left(2\alpha^2+\chi^2+1\right)\right.\right. \\
&\left.\left.\left.+\chi^2 z\left(\left(\alpha^2-1\right)\nu^2+\alpha^2\right)+3\alpha^2 z\right)-3\right)-1\right)\Big]^{-1},
\end{aligned}
\tag{7.50}
$$

$$
\begin{aligned}
\Omega_H = & \left(\frac{\partial M}{\partial J}\right)_{S_{\rm gen},P_3,c_3,Q} \qquad (7.51)\\
=& \frac{\alpha\left(z^2+1\right)\sqrt{\left(z\left(\nu+\alpha^2(\nu-z)\right)+1\right)\left(\nu z^3\left(\chi^2(\nu z+1)-1\right)+1\right)}}{z\ell_3(\nu z+1)\left(\alpha^2\left(z^2\left(\nu\chi^2 z-1\right)+1\right)+1\right)}\,,\\
V_3 = & \left(\frac{\partial M}{\partial P_3}\right)_{S_{\rm gen},c_3,Q,J}\\
=& \frac{4\pi z^2\ell_3^2\left(\alpha^2\left(z^2-1\right)-1\right)^2}{\left(\alpha^2+\left(\chi^2+3\right)z^2\left(\alpha^2z^2-1\right)-1\right)^2} - \Bigg[4\nu\left(\alpha^2+\left(\chi^2+3\right)z^2\left(\alpha^2z^2-1\right)-1\right)^{-3}\\
&\times\Bigg(\pi z\ell_3^2\left(\alpha^2+\left(\chi^2-1\right)z^2\left(\alpha^2z^2-1\right)+1\right)\\
&\times\left(\alpha^4-\alpha^2+2\alpha^4\left(\chi^2+3\right)z^6-\alpha^2z^4\left(\left(\alpha^2+2\right)\chi^2+\alpha^2+8\right)\right.\\
&\left.-z^2\left(2\alpha^4+\alpha^2\left(\chi^2+3\right)-2\right)\right)\Bigg)\Bigg]+\mathcal{O}\left(\nu^2\right)\,,
\end{aligned}
$$

$$
\begin{aligned}
\mu_3 = & \left(\frac{\partial M}{\partial c_3}\right)_{S_{\rm gen},P_3,Q,J} \\
= & -\Big[\nu\Big(4z\left(\alpha^2\left(z^4+1\right)-z^2\right)\left(\chi^2 z^2(\alpha z-1)(\alpha z+1)\left(\alpha^2\left(z^2+1\right)-1\right)\right. \\
& \left.-\left(z^2-1\right)\left(\alpha^2\left(z^2-1\right)-1\right)^2\right)\Big(\left(-\alpha^2-\left(\left(\chi^2+3\right)z^2\left(\alpha^2 z^2-1\right)\right)+1\right) \\
& \times\left(\alpha^2 z\left(\left(\chi^2-1\right)z^2+1\right)+z\right)+4z^3\left(2\alpha^2+\chi^2+1\right)\left(1-\alpha^2\left(z^2-1\right)\right)\Big) \\
& +\left(1-\alpha^2\left(z^2-1\right)\right)\left(4\alpha^4+4\alpha^2-4\left(2\alpha^6+\alpha^4\right)z^{10}\right. \\
& +\left(34\alpha^6+28\alpha^4+8\alpha^2\right)z^8-2\left(19\alpha^6+35\alpha^4+12\alpha^2+2\right)z^6 \\
& \left.+\left(22\alpha^6+44\alpha^4+38\alpha^2+4\right)z^4-2\left(5\alpha^6+9\alpha^4+5\alpha^2+3\right)z^2\right. \\
& -4\chi^2 z^4\left(\alpha^2\left(z^4+1\right)-z^2\right)\left(\alpha^2\left(5-4z^2\right)+\alpha^4\left(z^4-9z^2+2\right)+3\right) \\
& -4\alpha^2\chi^4 z^6(\alpha z-1)(\alpha z+1)\left(-z^2+\alpha^2\left(z^4+z^2+2\right)-1\right)\Big) \\
& \times\left(-\alpha^2-\left(\left(\chi^2+3\right)z^2\left(\alpha^2 z^2-1\right)\right)+1\right)\Big)-4z\left(1-\alpha^2\left(z^2-1\right)\right) \\
& \times\left(\alpha^2\left(z^4+1\right)-z^2\right)\Big(\chi^2 z^2(\alpha z-1)(\alpha z+1)\left(\alpha^2\left(z^2+1\right)-1\right) \\
& -\left(z^2-1\right)\left(\alpha^2\left(z^2-1\right)-1\right)^2\Big)\left(-\alpha^2-\left(\left(\chi^2+3\right)z^2\left(\alpha^2 z^2-1\right)\right)+1\right)\Big] \\
& \times\left[4\ell_3\left(\alpha^2\left(z^2-1\right)-1\right)^2\left(\alpha^2+\left(\chi^2+3\right)z^2\left(\alpha^2 z^2-1\right)-1\right)^3\right]^{-1}+\mathcal{O}(\nu^2)\,,
\end{aligned}
\tag{7.52}
$$

keeping the three-dimensional Newton's constant G_3 fixed. We have written V_3 and μ_3 only to the first order in the backreaction parameter ν, owing to their size; the complete expressions are given in Appendix B. These thermodynamic expressions (when using the complete forms of V_3 and μ_3) satisfy the first law of black hole thermodynamics

$$
\mathrm{d}M = T\mathrm{d}S_{\rm gen}+\Phi\mathrm{d}Q+\Omega_H\mathrm{d}J+V_3\mathrm{d}P_3+\mu_3\mathrm{d}c_3 \tag{7.53}
$$

on the brane and the corresponding Smarr relation

$$
0 = TS_{\rm gen}-2P_3V_3+\mu_3c_3+\Omega_H J\,. \tag{7.54}
$$

The mass M and charge Q are absent from the Smarr relation since G_3M and Q are dimensionless. Here we have taken the central charge as a variable, as was done in the standard holographic black hole chemistry [245]; see [302] for other solutions.

7.2.2 Bulk expressions

From the bulk perspective, there is a black hole sliced by an ETW brane with tension (6.27), which is a thermodynamic variable. The charged rotating quantum black hole on the brane is associated with the classical solution of the bulk gravitational theory coupled to the brane, and contains all orders of backreaction from the CFT_3 on the brane. Just as in the brane perspective, we work in the extended thermodynamic phase space, which means that

$$P_4 = -\frac{\Lambda_4}{8\pi G_4} = \frac{3(\nu^2+1)}{8\pi G_4 \ell^2}\,, \tag{7.55}$$

where the four-dimensional bulk pressure P_4 is a variable. Tuning the brane tension τ is done by altering the position of the brane in the bulk (with the rest following from the Israel junction conditions). The thermodynamic variable conjugate to τ will be referred to as the thermodynamic area of the brane, and will be denoted as A_τ.

Given our previous expressions (7.21), (7.34), (7.35), and (7.23), the charged rotating quantum black hole's mass M, entropy S, electric charge Q, and spin J can be written as

$$\begin{aligned} M =& \frac{\ell}{G_4}\Big[\left(\nu z^3\left(\chi^2(\nu z+1)-1\right)+1\right)\Big(\alpha^2+z^2\Big(4\alpha^4 z(\nu-z) \\ &+\alpha^2\left(z\left(4\nu+\nu\chi^2(\nu z+1)-z\right)+4\right)+\nu z+1\Big)\Big)\Big] \\ &\times\Big[\Big(-\alpha^2+z^2\Big(\chi^2+z^2\left(\nu^2\chi^2-\alpha^2\left(\left(\nu^2+1\right)\chi^2+3\right)\right) \\ &+2\nu z\left(2\alpha^2+\chi^2+1\right)+3\Big)+1\Big)\Big]^{-2}\,, \end{aligned} \tag{7.56}$$

$$\begin{aligned} S_{\mathrm{gen}} =& -\frac{2\pi\ell^2}{G_4}\Big[z\left(\alpha^2\left(z^2\left(\nu\chi^2 z-1\right)+1\right)+1\right)\Big] \\ &\times\Big[\nu\Big(\alpha^2+z^2\Big(-\chi^2+z\Big(-2\nu\left(2\alpha^2+\chi^2+1\right) \\ &+\chi^2 z\left(\left(\alpha^2-1\right)\nu^2+\alpha^2\right)+3\alpha^2 z\Big)-3\Big)-1\Big)\Big]^{-1}\,, \end{aligned} \tag{7.57}$$

$$
\begin{aligned}
Q =& -\frac{4\ell}{g_4}\sqrt{\frac{\pi}{G_4}}\Big[\chi z^2\left(z\left(\nu+\alpha^2(\nu-z)\right)+1\right)\Big] \qquad (7.58)\\
&\times\Big[\alpha^2+z^2\Big(-\chi^2+z\Big(-2\nu\left(2\alpha^2+\chi^2+1\right)\\
&\quad+\chi^2 z\left(\left(\alpha^2-1\right)\nu^2+\alpha^2\right)+3\alpha^2 z\Big)-3\Big)-1\Big]^{-1},\\
J =& \frac{2\ell^2}{G_4}\Big[\alpha z\left(\alpha^2-\alpha^2 z^4+\left(\alpha^2+1\right)\nu\chi^2 z^3(\nu z+1)+z^2+1\right) \qquad (7.59)\\
&\quad\times\sqrt{\left(\nu^2+1\right)\left(z\left(\nu+\alpha^2(\nu-z)\right)+1\right)\left(\nu z^3\left(\chi^2(\nu z+1)-1\right)+1\right)}\Big]\\
&\times\Big[\nu\sqrt{\nu^2+1}\Big(-\alpha^2+z^2\Big(\chi^2+z^2\left(\nu^2\chi^2-\alpha^2\left(\left(\nu^2+1\right)\chi^2+3\right)\right)\\
&\quad+2\nu z\left(2\alpha^2+\chi^2+1\right)+3\Big)+1\Big)^2\Big]^{-1},
\end{aligned}
$$

where G_4 is the four-dimensional Newton constant.

The above expressions allow us to write down the bulk temperature T, electric potential Φ, angular velocity Ω_H, thermodynamic volume V_4, and thermodynamic area A_τ as, respectively

$$
\begin{aligned}
T =& \left(\frac{\partial M}{\partial S_{\rm gen}}\right)_{P_4,\tau,Q,J} \qquad (7.60)\\
=& -\Big[\nu\Big(z\Big(\nu\chi^2 z^2\left(z^2\left(\alpha^2\left(\nu^2+1\right)+\nu^2\right)+2\nu z+1\right)\\
&\quad-\nu\left(\alpha^2\left(z^4+3\right)+z^2+3\right)+4\alpha^2 z\Big)-2\Big)\\
&\quad\times\left(\alpha^2+z^2\left(\alpha^2 z\left(-2\nu+\nu\chi^2(\nu z+1)+z\right)-\nu z-1\right)\right)\Big]\\
&\times\Big[2\pi z\ell(\nu z+1)\left(\alpha^2\left(z^2\left(\nu\chi^2 z-1\right)+1\right)+1\right)\\
&\quad\times\Big(\alpha^2+z^2\Big(-\chi^2+z\Big(-2\nu\left(2\alpha^2+\chi^2+1\right)\\
&\quad+\chi^2 z\left(\left(\alpha^2-1\right)\nu^2+\alpha^2\right)+3\alpha^2 z\Big)-3\Big)-1\Big)\Big]^{-1},
\end{aligned}
$$

$$\Phi = \left(\frac{\partial M}{\partial Q}\right)_{S_{\rm gen},P_4,\tau,J} \tag{7.61}$$
$$\begin{aligned}
=&\frac{g_4}{\sqrt{\pi G_4}}\Bigg[\nu\chi z\left(z\left(\nu+\alpha^2(\nu-z)\right)+1\right)\\
&\qquad\times\left(\alpha^2+z^2\left(\alpha^2 z\left(-2\nu+\nu\chi^2(\nu z+1)+z\right)-\nu z-1\right)\right)\Bigg]\\
&\times\Bigg[(\nu z+1)\left(\alpha^2\left(z^2\left(\nu\chi^2 z-1\right)+1\right)+1\right)\\
&\quad\times\Big(\alpha^2+z^2\Big(-\chi^2+z\Big(-2\nu\left(2\alpha^2+\chi^2+1\right)\\
&\quad+\chi^2 z\left(\left(\alpha^2-1\right)\nu^2+\alpha^2\right)+3\alpha^2 z\Big)-3\Big)-1\Big)\Bigg]^{-1},
\end{aligned}$$

$$\Omega_H = \left(\frac{\partial M}{\partial J}\right)_{S_{\rm gen},P_4,\tau,Q} \tag{7.62}$$
$$=\frac{\alpha\nu\left(z^2+1\right)\sqrt{\left(z\left(\nu+\alpha^2(\nu-z)\right)+1\right)\left(\nu z^3\left(\chi^2(\nu z+1)-1\right)+1\right)}}{z\ell(\nu z+1)\left(\alpha^2\left(z^2\left(\nu\chi^2 z-1\right)+1\right)+1\right)},$$

$$
\begin{aligned}
V_4 = \quad & \left(\frac{\partial M}{\partial P_4}\right)_{S_{\rm gen},\tau,Q,J} \qquad (7.63)\\
=& \Bigg[8\pi z\ell^3\Big(\alpha^2\nu^2\chi^4 z^5(\nu z+1)\left(\nu z\left(\left(\alpha^2+1\right)\nu z+2\right)+1\right)\\
&+\left(\alpha^2\left(z^2-1\right)-1\right)\left(\nu\left(\alpha^2+z^2\left(\alpha^2\left(3z^2-2\right)-3\right)\right)\right.\\
&\left.+z\left(\alpha^2\left(z^2-1\right)-1\right)+\nu^2z^3\left(\alpha^2\left(z^2-3\right)-2\right)\right)\\
&+\alpha^2\nu\chi^2z^2\Big(z\Big(-\left(\left(\alpha^2+1\right)\nu^3z^4\right)+\nu\left(-\alpha^2\left(1-2z^2\right)^2+4z^2+1\right)\\
&+z\left(\alpha^2\left(1-2z^2\right)+2\right)+\nu^2z^3\left(1-\alpha^2\left(z^2-4\right)\right)\Big)+1\Big)\Big)\Bigg]\\
&\times\Bigg[3\nu^2(\nu z+1)\Big(\alpha^2+z^2\Big(-\chi^2+z\Big(-2\nu\left(2\alpha^2+\chi^2+1\right)\\
&+\chi^2z\left(\left(\alpha^2-1\right)\nu^2+\alpha^2\right)+3\alpha^2z\Big)-3\Big)-1\Big)^2\Bigg]^{-1},
\end{aligned}
$$

$$
\begin{aligned}
A_\tau = \quad & \left(\frac{\partial M}{\partial \tau}\right)_{S_{\rm gen},P_4,Q,J} \qquad (7.64)\\
=& \Big[2\pi\ell^2\Big(-\alpha^2\nu^2+\alpha^2\nu^2 z^8\left(\left(\nu^2+2\right)\chi^2+1\right)\left(2\alpha^2-\nu^2\chi^2\right)\\
&+\nu z^7\Big(2\alpha^4\left(-3\nu^2-\left(\nu^4+\nu^2-2\right)\chi^2-2\right)\\
&-\alpha^2\nu^2\left(2\left(\nu^2+2\right)\chi^4-\left(\nu^2-1\right)\chi^2+3\right)+\nu^4\chi^2\Big)\\
&+z^6\Big(-2\alpha^4\left(\nu^4\left(\chi^2-2\right)+\nu^2\left(3\chi^2-2\right)+1\right)\\
&-\alpha^2\nu^2\left(\nu^2\left(\chi^4+\chi^2-4\right)+2\left(\chi^2+1\right)^2\right)+\nu^4\left(2\chi^2+1\right)\Big)\\
&+\nu z^5\left(2\alpha^4\left(\left(\nu^2-1\right)\chi^2+3\right)+\alpha^2\left(6\nu^2-4\chi^2+8\right)+\nu^2\left(\chi^2+3\right)\right)\\
&+\alpha^2 z^4\left(2\alpha^2\left(\nu^2\left(\chi^2-1\right)+2\right)-2\nu^4\chi^2-7\nu^2+4\right)\\
&+\nu z^3\left(-2\alpha^4\left(\nu^2+2\right)+\alpha^2\left(-2\left(\nu^2+1\right)\chi^2+\nu^2-6\right)+\nu^2-4\right)\\
&+z^2\left(-2\alpha^2\left(\alpha^2+\nu^2+2\right)+\nu^2-2\right)+2\alpha^2\left(\alpha^2+1\right)\nu z\Big)\Big]\\
&\times\Big[\nu^2\Big(-\alpha^2+z^2\Big(\chi^2+z^2\left(\nu^2\chi^2-\alpha^2\left(\left(\nu^2+1\right)\chi^2+3\right)\right)\\
&+2\nu z\left(2\alpha^2+\chi^2+1\right)+3\Big)+1\Big)^2\Big]^{-1},
\end{aligned}
$$

where just as in the brane perspective, we keep Newton's constant fixed. The above expressions satisfy the first law

$$
{\rm d}M = T{\rm d}S_{\rm gen}+\Phi{\rm d}Q+\Omega_H{\rm d}J+V_4{\rm d}P_4+A_\tau{\rm d}\tau\,, \qquad (7.65)
$$

and the Smarr relation

$$
M = 2TS-2V_4P_4+2\Omega_H J+\Phi Q-A_\tau\tau\,. \qquad (7.66)
$$

The latter can be derived from the former by applying Euler's theorem for homogeneous functions [247, 156, 189].

7.2.3 Boundary expressions

The double holography prescription states that the DCFT$_2$ (which, recall, results from the intersection of the ETW brane in the bulk with the boundary) coupled to the BCFT$_3$,

provides another description of the thermodynamics of the quantum charged rotating black hole on the brane. The degrees of freedom of the DCFT$_2$ are related to the three-dimensional Newtonian constant G_3 and the three-dimensional cosmological constant L_3 via the holographic correspondence formula [69]

$$c_2 = \frac{3L_3}{2G_3} = \frac{3\ell}{2G_3\sqrt{2\nu^2 - 2\sqrt{\nu^2+1}+2}}\,. \tag{7.67}$$

The holographic dictionary tells us that the energy E, entropy $\mathcal{S}$, electric charge $\mathcal{Q}$, and volume V_2 of the DCFT$_2$ are given by

$$\begin{aligned} E = M = \frac{1}{2G_3}\Big(&- \alpha^2 + z^2\Big(\chi^2 + z^2\left(\nu^2\chi^2 - \alpha^2\left(\left(\nu^2+1\right)\chi^2+3\right)\right) \\ &+ 2\nu z\left(2\alpha^2+\chi^2+1\right)+3\Big)+1\Big)^{-2} \\ &\times\Bigg[\sqrt{\nu^2+1}\left(\nu z^3\left(\chi^2(\nu z+1)-1\right)+1\right)\Big(\alpha^2+z^2\Big(4\alpha^4 z(\nu-z) \\ &+\alpha^2\left(z\left(4\nu+\nu\chi^2(\nu z+1)-z\right)+4\right)+\nu z+1\Big)\Big)\Bigg], \end{aligned} \tag{7.68}$$

$$\begin{aligned} \mathcal{S} = S_{\rm gen} = &-\left[\pi\sqrt{\nu^2+1}z\ell\left(\alpha^2\left(z^2\left(\nu\chi^2 z-1\right)+1\right)+1\right)\right] \\ &\times\Bigg[G_3\nu\Big(\alpha^2+z^2\Big(-\chi^2+z\Big(-2\nu\left(2\alpha^2+\chi^2+1\right) \\ &+\chi^2 z\left(\left(\alpha^2-1\right)\nu^2+\alpha^2\right)+3\alpha^2 z\Big)-3\Big)-1\Big)\Bigg]^{-1}, \end{aligned} \tag{7.69}$$

$$\begin{aligned} \mathcal{Q} = QL_3 = &-\left[2\sqrt{2\pi}\sqrt{\nu^2+1}\chi z^2\ell\left(z\left(\nu+\alpha^2(\nu-z)\right)+1\right)\right] \\ &\times\Bigg[g_3\sqrt{5G_3}\sqrt{\nu^2-\sqrt{\nu^2+1}+1} \\ &\times\Big(\alpha^2+z^2\Big(-\chi^2+z\Big(-2\nu\left(2\alpha^2+\chi^2+1\right) \\ &+\chi^2 z\left(\left(\alpha^2-1\right)\nu^2+\alpha^2\right)+3\alpha^2 z\Big)-3\Big)-1\Big)\Bigg]^{-1}, \end{aligned} \tag{7.70}$$

$$\mathcal{J} = \Bigg[\alpha z\ell\left(\alpha^2 - \alpha^2 z^4 + \left(\alpha^2+1\right)\nu\chi^2 z^3(\nu z+1) + z^2 + 1\right) \tag{7.71}$$
$$\times \sqrt{\left(\nu^2+1\right)\left(z\left(\nu+\alpha^2(\nu-z)\right)+1\right)\left(\nu z^3\left(\chi^2(\nu z+1)-1\right)+1\right)}\Bigg]$$
$$\times \Bigg[G_3\nu\Big(-\alpha^2 + z^2\Big(\chi^2 + z^2\left(\nu^2\chi^2 - \alpha^2\left(\left(\nu^2+1\right)\chi^2+3\right)\right)$$
$$+ 2\nu z\left(2\alpha^2+\chi^2+1\right)+3\Big)+1\Big)^2\Bigg]^{-1},$$
$$V_2 = 2\pi L_3 = \frac{2\pi\ell}{G_3\sqrt{2\nu^2 - 2\sqrt{\nu^2+1}+2}}\,. \tag{7.72}$$

The form of E for the DCFT$_2$ was chosen to match the brane expression for the mass, and the charge $\mathcal{Q}$ is rescaled by L_3. The temperature T, electric potential Φ, angular velocity Ω_H, two-dimensional thermodynamic pressure P_2, and two-dimensional chemical potential μ_2 are

$$T = \left(\frac{\partial E}{\partial \mathcal{S}}\right)_{\ell,V_2,c_2,\mathcal{Q},\mathcal{J}} \tag{7.73}$$
$$= -\Bigg[\nu\Big(z\Big(\nu\chi^2 z^2\left(z^2\left(\alpha^2\left(\nu^2+1\right)+\nu^2\right)+2\nu z+1\right)$$
$$-\nu\left(\alpha^2\left(z^4+3\right)+z^2+3\right)+4\alpha^2 z\Big)-2\Big)$$
$$\times\left(\alpha^2+z^2\left(\alpha^2 z\left(-2\nu+\nu\chi^2(\nu z+1)+z\right)-\nu z-1\right)\right)\Bigg]$$
$$\times\Bigg[2\pi z\ell(\nu z+1)\left(\alpha^2\left(z^2\left(\nu\chi^2 z-1\right)+1\right)+1\right)$$
$$\times\Big(\alpha^2+z^2\Big(-\chi^2+z\Big(-2\nu\left(2\alpha^2+\chi^2+1\right)$$
$$+\chi^2 z\left(\left(\alpha^2-1\right)\nu^2+\alpha^2\right)+3\alpha^2 z\Big)-3\Big)-1\Big)\Bigg]^{-1},$$

$$\Phi = \left(\frac{\partial E}{\partial \mathcal{Q}}\right)_{\ell,\mathcal{S},V_2,c_2,\mathcal{J}} \tag{7.74}$$
$$\begin{aligned}
=&\Bigg[\sqrt{5}g_3\nu\chi z\sqrt{\nu^2-\sqrt{\nu^2+1}+1}\left(z\left(\nu+\alpha^2(\nu-z)\right)+1\right)\\
&\times\left(\alpha^2+z^2\left(\alpha^2 z\left(-2\nu+\nu\chi^2(\nu z+1)+z\right)-\nu z-1\right)\right)\Bigg]\\
&\times\Bigg[\sqrt{2\pi G_3}\ell(\nu z+1)\left(\alpha^2\left(z^2\left(\nu\chi^2 z-1\right)+1\right)+1\right)\\
&\times\Big(\alpha^2+z^2\Big(-\chi^2+z\Big(-2\nu\left(2\alpha^2+\chi^2+1\right)\\
&+\chi^2 z\left(\left(\alpha^2-1\right)\nu^2+\alpha^2\right)+3\alpha^2 z\Big)-3\Big)-1\Big)\Bigg]^{-1},
\end{aligned}$$

$$\Omega_H = \left(\frac{\partial E}{\partial \mathcal{J}}\right)_{\ell,\mathcal{S},V_2,c_2,\mathcal{Q}} \tag{7.75}$$
$$=\frac{\alpha\nu\left(z^2+1\right)\sqrt{\left(z\left(\nu+\alpha^2(\nu-z)\right)+1\right)\left(\nu z^3\left(\chi^2(\nu z+1)-1\right)+1\right)}}{z\ell(\nu z+1)\left(\alpha^2\left(z^2\left(\nu\chi^2 z-1\right)+1\right)+1\right)},$$

$$P_2 = \left(\frac{\partial E}{\partial V_2}\right)_{\ell,\mathcal{S},c_2,\mathcal{Q},\mathcal{J}} \tag{7.76}$$
$$=\frac{\nu\left(\alpha^2-\left(4\alpha^2+1\right)z^2\left(\alpha^2z^2-1\right)\right)}{4\pi G_3\ell\left(\alpha^2+\left(\chi^2+3\right)z^2\left(\alpha^2z^2-1\right)-1\right)^2}+\mathcal{O}(\nu^2),$$

$$\mu_2 = \left(\frac{\partial E}{\partial c_2}\right)_{\ell,\mathcal{S},V_2,\mathcal{Q},\mathcal{J}} \tag{7.77}$$
$$\begin{aligned}
=&-\Bigg[\sqrt{-2\left(\left(\nu^2+1\right)\left(-\nu^2+\sqrt{\nu^2+1}-1\right)\right)}\\
&\times\Big(\alpha^2\nu z^5\left(\left(\nu^2+1\right)\chi^2+1\right)-\left(2\alpha^2+1\right)\nu^2z^4-2\nu z^3\\
&+2\alpha^2z^2-\left(\alpha^2+2\right)\nu z-1\Big)\\
&\times\left(\alpha^2+z^2\left(\alpha^2z\left(-2\nu+\nu\chi^2(\nu z+1)+z\right)-\nu z-1\right)\right)\Bigg]\\
&\times\Bigg[3\ell(\nu z+1)\Big(\alpha^2+z^2\Big(-\chi^2+z\Big(-2\nu\left(2\alpha^2+\chi^2+1\right)\\
&+\chi^2 z\left(\left(\alpha^2-1\right)\nu^2+\alpha^2\right)+3\alpha^2 z\Big)-3\Big)-1\Big)^2\Bigg]^{-1},
\end{aligned}$$

where we have written P_2 to linear order in the backreaction parameter ν owing to its size; the full expression is written in Appendix B. In the above expressions, the parameter ℓ is kept fixed. This does not mean that the brane tension is kept constant, since in the boundary perspective, we let the three-dimensional Newton constant G_3 be a variable. This seems to be the only choice we have in order to obtain cohomogeneity thermodynamics. This means that the central charge on the brane c_3 is variable.

The above expressions satisfy the first law of black hole thermodynamics on the DCFT$_2$ as

$$\mathrm{d}E = T\mathrm{d}\mathcal{S} - P_2\mathrm{d}V_2 + \mu_2\mathrm{d}c_2 + \Phi\mathrm{d}\mathcal{Q} + \Omega_H\mathrm{d}\mathcal{J}\,. \tag{7.78}$$

Note the presence of a work term P_2dV_2 as opposed to V_2dP_2. This indicates that E plays the role of the thermodynamic internal energy, in contrast to M in the other perspectives, which played the role of enthalpy in the extended thermodynamic phase space, where pressure is a variable. The integral internal energy formula for the DCFT$_2$ reads

$$E = T\mathcal{S} + \mu_2 c_2 + \frac{1}{2}\mathcal{Q}\Phi + \Omega_H\mathcal{J}\,, \tag{7.79}$$

where V_2 is absent since V_2/G_3 is dimensionless.

Chapter 8

Phase Transitions and Criticality

With the expressions for all the thermodynamic variables in the brane, bulk, and boundary perspectives respectively, at hand, we may investigate the phase transitions and critical points of the quantum black hole. Since our expressions are general, we may obtain functions for the charged-static, neutral-rotating, and neutral-static quantum black holes by setting $\alpha = 0$, $\chi = 0$, and $\alpha = \chi = 0$, respectively. Our investigation of the phase structure of these black hole systems is carried out through the use of phase diagrams. In particular, we locate the second order critical points in phase space and calculate their associated critical exponents. Owing to the complicated nature of the functions we derived in the previous section, it is impossible to obtain closed-form equations of state, which means that the investigation must be carried out numerically.

8.1 Brane perspective

We focus on the so-called canonical ensemble, in which the temperature T, pressure P_3, central charge c_3, electric charge Q, and angular momentum J are all fixed. Looking at the first law of black hole thermodynamics on the brane (7.53), and noting again that in the extended thermodynamic phase space, the black hole mass corresponds to enthalpy, and not the internal energy, this means that the relevant thermodynamic potential for the ensemble is the Gibbs free energy $G = M - TS_{\text{gen}}$. The path the system traces out in the phase space can be parameterized by the variable z. Given values for P_3, c_3, Q, J, and z, we are left with a system of four equations for four variables, ν, χ, α, ℓ_3. Adjusting the value of z, but keeping the same values for P_3, c_3, Q, and J, we can see how the other thermodynamic variables of the system, including the temperature and Gibbs free

energy, evolve as we move from one system to another within the ensemble. We start with the simplest possible system, the neutral-static quantum BTZ black hole (so $Q = 0$, and $J = 0$). This is the only black hole that can transition to thermal AdS. The ensemble is one in which electric charge is fixed. This prevents any black hole carrying electric charge from making the transition. For the sake of consistency between different cases, we will not compare the neutral-static quantum BTZ black hole to quantum thermal AdS, (i.e., AdS_3 spacetime including backreaction from the CFT_3 on the brane), as was done in [157]. This will not affect our analysis of phase behavior or our calculation of critical exponents.

Keeping the central charge c_3 fixed at an arbitrary value, we may observe the behavior of the curves the system is constrained to be on in the $G - T$ plane, as we move from an ensemble with one value for the thermodynamic pressure P_3 to another. The cusps on the curve correspond to where $\frac{\partial G}{\partial z} = 0$, and $\frac{\partial T}{\partial z} = 0$. With the exception of the curve corresponding to the system being kept at the critical pressure P_c, each curve will have two cusps, and one point at which it self-intersects. As the critical pressure is approached (i.e., we move to copies of the system within the ensemble with fixed pressures that are closer and closer to P_c), these cusps will approach each other on the plane, until at the critical pressure, they merge and disappear, leaving a smooth curve with no self-intersections. Crucially, as the thermodynamic pressure of the neutral-static black hole on the brane exceeds P_c, the cusps will immediately reappear and the curve will self-intersect once more. On either side of the critical pressure, the self-intersection of the curve presents as an inverted swallowtail. This corresponds to the re-entrant phase transitions observed in [157]. The coexistence curve between two phases of the black hole will extend past the critical point in the $P_3 - T$ plane, and not simply terminate, as it does in the case for ordinary phase behavior. We stress that this phenomenon is unique to the neutral-static quantum BTZ black hole. The addition of any electric charge or spin into the system removes the critical point associated with this re-entrant phase transition. This is shown in section 8.4.

The second order critical points of the system in the canonical ensemble are those where

$$\left(\frac{\partial T}{\partial S}\right)_{P_3,c_3,Q,J} = \left(\frac{\partial^2 T}{\partial S^2}\right)_{P_3,c_3,Q,J} = 0\,. \tag{8.1}$$

Keeping c_3 fixed at some value, and setting the first two partial derivatives to zero gives us three equations to solve for the three parameters $(z_c, \nu_c, \ell_{3,c})$ (in the neutral-static limit, we know that $\chi = \alpha = 0$). After numerically finding these parameters, we can calculate the critical values for the various thermodynamic variables. With this at hand, we will be able to define an order parameter and reduced temperature $\tilde{t} = \frac{T-T_c}{T_c} = \tau - 1$. We select the reduced chemical potential $\frac{\mu_3-\mu_{3,c}}{\mu_{3,c}}$ as our order parameter, where the subscript c indicates

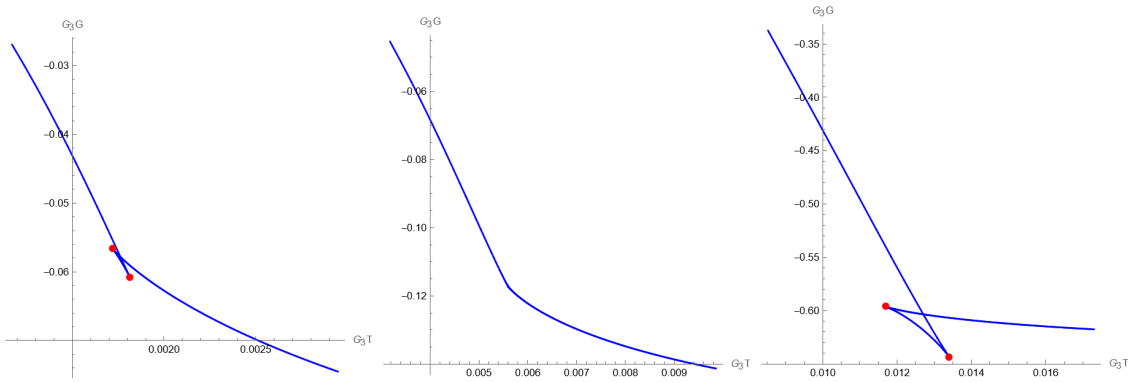


Figure 8.1: Free energy-temperature curves for neutral-static systems in the canonical ensemble with different pressures. The central charge for each curve is kept at $c_3 = 10$. The cusps on each curve are highlighted in red. From left to right are curves at $P < P_C$, $P = P_c$, and $P > P_c$.

the value of the thermodynamic variable at criticality. In order to calculate the values of the critical exponents $\tilde{\alpha}$, β, and γ (where $\tilde{\alpha}$ the critical exponent is not to be confused with the rotation parameter α), the critical point must be approached in phase space along the coexistence curve. The critical exponent δ is found by approaching the critical point along the critical isotherm (so constrained to $t = 0$ in phase space). Having chosen an order parameter, we can define the functions used to extract the critical exponents. Since we are working in the fixed (P_3, c_3) ensemble, the heat capacity (based on which $\tilde{\alpha}$ is calculated) is

$$C_{P_3,\mu_3} = T\left(\frac{\partial S}{\partial T}\right)_{P_3,\mu_3} \propto |t|^{-\tilde{\alpha}}\,, \tag{8.2}$$

where we have chosen to keep the order parameter constant when evaluating the heat capacity. The critical exponent β is calculated based on the power-law behavior of the order parameter with respect to t near the critical point,

$$|\mu_3 - \mu_{3,c}| \propto |t|^{\beta}\,. \tag{8.3}$$

The analogue for isothermal compressibility that we use (the susceptibility) is

$$\chi = -\frac{1}{\mu_3}\left(\frac{\partial \mu_3}{\partial c_3}\right)_{P_3,T} \propto |t|^{-\gamma}\,. \tag{8.4}$$

Finally, δ governs how the source function $\frac{c_3 - c_{3,c}}{c_{3,c}}$ is related to the order parameter near the critical point, along the critical isotherm $T = T_c$ (we also constrain the approach to be

along the critical isobar $P_3 = P_{3,c}$),

$$|c_3 - c_{3,c}| \propto |\mu_3 - \mu_{3,c}|^{\delta} . \tag{8.5}$$

The coexistence curve corresponds to where the Gibbs free energy surface intersects itself in natural variables space, with coordinates (S, P_3, c_3). As stated previously, owing to the fact that our thermodynamic variables are expressed as complicated, non-invertible functions of independent parameters, we do not have the luxury of turning to an explicit equation of state to find the coexistence curve and critical exponents. With this in mind, we must resort to using numerical methods, just as we did when locating the critical point to begin with. We have used two such methods with consistent results.

The first method uses the fact that along a coexistence curve, the two phases of the system will have equal temperature, pressure, and free-energy, but different thermodynamic volumes. The self-intersection of free energy-temperature curves will disappear at the critical point. Since we selected the chemical potential μ_3 to form the order parameter, we will keep the central charge constant for each of these curves (fixing it to be its critical value) so that the source function $\frac{c_3 - c_{3,c}}{c_{3,c}}$ is kept at a value of zero. The pressure is varied. Since we want to focus on the coexistence curve very close to the critical point, in order to calculate the order of various divergences, the pressures we use will be very close to the critical pressure. The point of self-intersection is tracked, and the two separate sets of values of the parameters (z, ν, ℓ_3) that map on to the point of self-intersection are recorded. Then one list of values for the variables (corresponding to a single coexistence curve in (z, ν, ℓ_3) space) is used to calculate the heat capacity, order parameter, and susceptibility. Note that due to the phenomenon of re-entrant phase transitions for the quantum BTZ black hole, the coexistence curves do not actually terminate at the critical point, but extend beyond them. In practice when calculating the critical exponents α, β, and γ, we will work on the side of the coexistence curve where the reduced temperature $t = \frac{T - T_c}{T_c}$ is negative.

The second method is simply to implement Maxwell's equal area construction numerically. We take the system and solve for the $P - V$ curves numerically, for temperatures close to the critical temperature (such that $t \to 0^-$), again holding the central charge at its critical value. Along the $P - V$ isothermal curves, the places where the curve does not monotonically decrease (i.e., where $\frac{\partial P}{\partial V} > 0$) must be corrected, and the metastable states removed, with an isobar that is positioned according to Maxwell's equal area construction. The ends of this isobar will be positioned at the two thermodynamic volumes of the two respective coexistent phases. As the temperature of the isotherms approaches the critical temperature, the isobar's position varies. Keeping track of the position of the isobar, and the values of the two coexistent volumes allows one to form a coexistence curve.

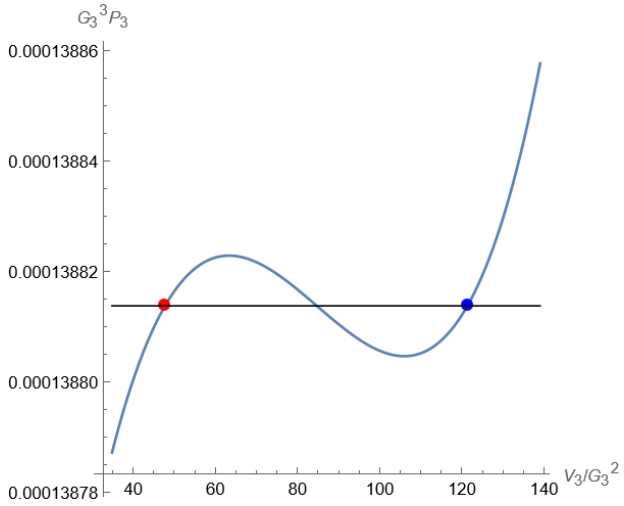


Figure 8.2: An isobar that corrects the presence of metastable states in the isotherm. The area above and below the isobar are equal. The smaller volume is marked in red while the larger volume is marked in blue. These are points on the coexistence curve. For the sake of visibility, this is far away from the critical point, and the curve corresponds to $\tilde{t} = -1/10$. When calculating the critical exponents, we take these points to be very close.

As stated previously, both numerical methods agree. We found values of the critical exponents for the second order critical point of the neutral-static quantum BTZ black hole in the canonical ensemble (up to some negligible numerical error) as

$$\tilde{\alpha} = 0, \quad \beta = 1, \quad \gamma = 2, \quad \delta = 3 \tag{8.6}$$

that curiously are the same values that occur for a particular type of black hole in 3rd order Lovelock gravity [124]. These unorthodox values differ from those predicted by mean-field theory, but satisfy both the Rushbrooke inequality

$$\tilde{\alpha} + 2\beta + \gamma \geq 2\,, \tag{8.7}$$

and the Widom relation

$$\gamma = \beta(\delta - 1)\,. \tag{8.8}$$

Moving on to the charged-static quantum BTZ black hole, we find that the presence of any electric charge introduces an upper bound on the temperature. This is in contrast to the neutral-static black hole, where the temperature of the black hole grows unbounded as a function of z past a second turning point [157]. The introduction of charge into the system

gives rise to another turning point in the curve, past which the temperature decreases. The requirement that temperature be greater than or equal to zero means electric charge also introduces an upper bound on z. There is a critical point associated with a large value of electric charge for the quantum black hole. This point is found by solving (8.1) and $P_3 = P_{3,0}$, $c_3 = c_{3,0}$ for z, ν, χ, and ℓ_3. As opposed to the neutral-static case, this critical point is not associated with a re-entrant phase transition, i.e., when the critical electric charge is exceeded, the cusps and self-intersection in the free energy-temperature curve do not reappear. The critical exponents for this second-order critical point were calculated numerically using the same methods as in the neutral-static case. They are

$$\tilde{\alpha} = 0\,, \quad \beta = \frac{1}{2}\,, \quad \gamma = 1\,, \quad \delta = 3\,. \tag{8.9}$$

Notably, these agree with the critical exponents found in [259] for the classical charged AdS_4 black hole, which has the same critical exponents as the van der Waals gas.

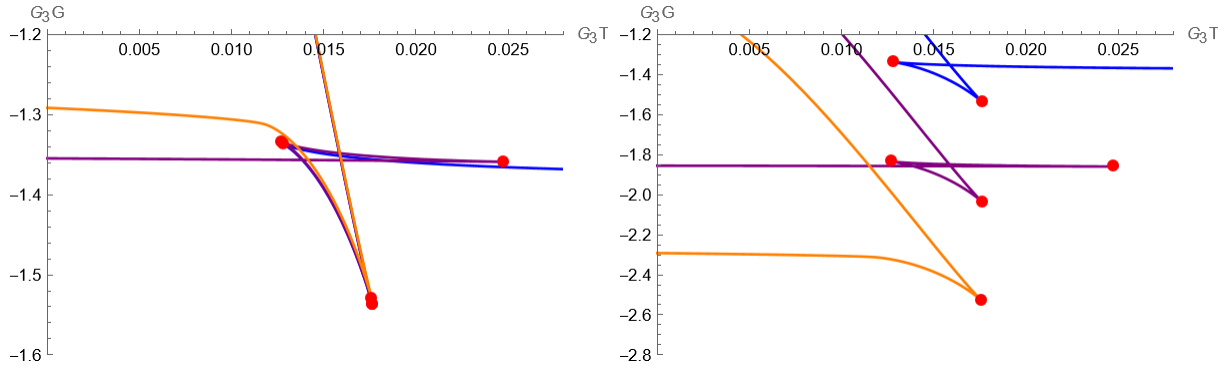


Figure 8.3: (Left) Free energy-temperature curves for the charged-static quantum black hole, with central charge $c_3 = 10$ and pressure $G_3^3 P_3 = 1.81 \times 10^{-4}$, for three different charges: (blue) $\sqrt{G_3}Q = 0$, (purple) $\sqrt{G_3}Q = \frac{1}{10}$, (orange) $\sqrt{G_3}Q = \frac{1}{3}$. The last of these has an electric charge that exceeds the critical electric charge value Q_c, and the cusp does not reappear, signifying a non-re-entrant phase transition. (Right) The same curves separated by vertical offsets for the sake of visibility. Note how the neutral curve extends to $T \to \infty$, but the charged curves have a maximum possible temperature. Note also how increasing the electric charge of the system pulls the new turning point/cusp towards another, until (at criticality) they merge and disappear.

The case of the neutral-rotating black hole has a subtlety, in that its critical point (associated with a large spin) has an imaginary value for the rotation parameter α. This remains a formal solution, but corresponds to a closed timelike curve formed from the

rotation of a naked singularity, not a black hole [134]. Attempting to restrict the search for critical points to real values of α leads to the location of an artificial critical point with a value of α_c that exceeds the upper bound (7.42), which in turn means that the associated critical value of the angular momentum is imaginary. Treating the original critical point (with imaginary α) as a formal solution, we find that it is associated with a phase transition that is not re-entrant, just as the critical point for the charged-static quantum black hole. The critical exponents for this are the orthodox ones (8.9), and the corresponding free-energy curves have an identical form to those of the charged-static black hole, shown in Fig. 8.3.

We restrict our treatment of the charged rotating quantum black hole to the boundary perspective for the sake of brevity, though an analysis from the brane and bulk perspectives was carried out and confirmed to give the same results.

8.2 Bulk perspective

The calculation of the critical exponents of the thermodynamic system from the bulk perspective proceeds in the same way as in the brane perspective, with minimal changes. We work in the canonical ensemble, with fixed temperature T, fixed charge Q, fixed angular momentum J, fixed pressure P_4, and fixed brane tension τ. Calculations proceed using the bulk perspective formulas. Using V_4 as the order parameter, we can define the relevant heat capacity and susceptibility in the same manner as previously,

$$C_{V_4,P_4} = T\left(\frac{\partial S}{\partial T}\right)_{V_4,P_4} \propto |t|^{-\tilde{\alpha}}\,, \tag{8.10}$$

$$\chi = -\frac{1}{V_4}\left(\frac{\partial V_4}{\partial P_4}\right)_{\tau,T} \propto |t|^{-\gamma}\,. \tag{8.11}$$

The neutral-static system's critical exponents, calculated from the bulk perspective, match those of the brane perspective (8.6). This is insensitive to the choice of order parameter, as long as the susceptibility and heat capacity are defined consistently. The charged-static and neutral-rotating critical exponents are also consistent with the values found in the previous section (8.9). We again stress that the introduction of charge and spin into the system does not merely perturb the position of the re-entrant critical point in phase space or variable space; rather, it eliminates the point altogether. Instead, new critical points are found in the regime of large charge or large angular momentum.

8.3 Boundary perspective

From the boundary perspective we work in the microcanonical ensemble, where $\mathcal{S}$, V_2, c_2, $\mathcal{Q}$ and $\mathcal{J}$ are fixed. The critical point is found using Maxwell's equal area construction in the $T-\mathcal{S}$ plane, where the presence of metastable states with negative heat capacity are replaced by an isotherm. The two coexisting phases of the DCFT_2 are distinguished by different values of the entropy $\mathcal{S}$. The coexistence curve is found numerically by adjusting the thermodynamic volume of the system and keeping track of the movement of the isotherm (based on the equal area requirement) and where it intersects the curve. The critical exponent values for the neutral-static, charged-static, and neutral-rotating quantum black holes are the same as in the brane and bulk perspectives.

The charged rotating black hole poses the same subtlety as the neutral-rotating black hole, in that the critical points in parameter space have imaginary values of α, which means that the critical state is not a black hole. Treating it as a formal solution, the corresponding critical exponents are found to be the same as in the charged-static, and neutral-rotating cases (8.9).

8.4 Elimination of re-entrant phase transitions

The elimination of re-entrant phase transitions with the introduction of electric charge or spin in the thermodynamic system may be shown analytically as follows. We begin with electric charge, and for simplicity, focus on the charged-static quantum BTZ black hole. The following analysis is performed in the brane perspective, but is expected to hold true in the boundary and bulk perspectives as well. The partial derivatives $\left(\frac{\partial T}{\partial S}\right)|_{P_3,c_3,Q}$ and $\left(\frac{\partial^2 T}{\partial S^2}\right)|_{P_3,c_3,Q}$ are expressed as functions of z, ν, ℓ_3, and χ. The condition for criticality is that these functions vanish, and the critical points in parameter space are precisely those points where this occurs. If electric charge did not destroy the critical point associated with re-entrant phase transitions, then we would expect a very small charge to merely perturb its position. Instead, any non-zero electric charge (corresponding to any non-zero value of χ) removes the point entirely.

The partial derivatives may be written as rational expressions of polynomials. We can extract the numerators of these rational expressions, which are multivariate polynomials. Any root of the original system of equations will obviously be a root of the system of polynomial equations. Due to the structure of the equations, ℓ_3 is not one of the variables in these polynomials. The original critical point in the neutral-static case had the coordinates

z_c, and ν_c. Treating χ as a new parameter in the equations, it may be demonstrated that these roots take on complex values when $\chi \neq 0$.

We may calculate the resultant of our two polynomials with respect to ν. This leaves us with a very high-degree polynomial in z and χ. The resultant will only vanish when the two polynomials share a common root. We can factor the resultant into numerous polynomials. One of those factors has a root with $z = z_c$, when we set $\chi = 0$. This is the factor that we shall focus on. We will make the assumption that z-coordinate of our original root varies smoothly with χ. To that end, we can Taylor expand the relevant factor of the resultant to third-order in z, about $z = z_c$. This leaves us with a cubic equation in z, whose roots can be obtained analytically. This gives us three roots, but only two of them smoothly converge to $z = z_c$ as we take the limit $\chi \to 0$. Any non-zero value of χ introduces an imaginary part to the roots. This can be visualized in the complex plane. At $\chi = 0$, the root sits on the real axis. As χ takes on a very small value (it may be seen from the definition of χ that it must be real), the root splits into two, and each point moves off the real-axis and takes on an imaginary part. Since z is physically restricted to take on real values, as may be seen from its definition (7.39), this means the critical point has been destroyed, as far as physics is concerned. This analytic approximation can be tested against a numerical solution to the original two equations, and the agreement is found to be excellent for small values of χ. We conclude that electric charge gets rid of re-entrant phase transitions.

The introduction of angular momentum to the system also gets rid of the re-entrant critical point, but in a different manner than charge. It should be noted that the angular momentum function vanishes when we substitute in the values of the neutral-static critical coordinates, no matter what the value of the rotation parameter α is. This means that for an ensemble with non-zero angular momentum, the original critical point cannot be a valid solution. For the sake of simplicity, we will focus on the neutral-rotating case. We proceed as before, calculating the first two partial derivatives of T with respect to S as functions of z, ν, α, and ℓ_3, and extract the numerator polynomials. Unlike in the charged case, where non-zero values of χ pulled the original root off the real-axis, a non-zero value of α does not add an imaginary part to the original root. This may be confirmed numerically. So at first glance, it would appear that the introduction of angular momentum does not destroy our interesting critical point. The resultant method does give us one insight however: it has a factor of $(z-1)$. This means that $z_c = 1$ will remain a root of the two polynomials for any value of α. Substituting this into our two polynomials and solving for ν, confirms that the ν coordinate of the critical point remains invariant here too, at $\nu_c = 1$, for any value of α. The original critical point remains a root insofar as the partial derivatives vanish there. It is only disqualified when we demand that the angular momentum be non-zero.

We proceed as follows. The relevant functions and variables, along with the conditions that we place on them, are

$$\left.\frac{\partial T}{\partial S}\right|_{P_3,c_3,J} = 0\,, \tag{8.12}$$

$$\left.\frac{\partial^2 T}{\partial S^2}\right|_{P_3,c_3,J} = 0\,, \tag{8.13}$$

$$J \in \mathbb{R}\,,\ J \neq 0\,,\ T > 0\,,\ z > 0\,,\ \nu > 0\,,\ \ell_3 > 0\,. \tag{8.14}$$

These conditions are obviously all physically motivated. We take these functions and expand everything to first order in α about $\alpha = 0$. Due to the structure of the functions, this means that only the series for J will be a function of α. By analyzing the resulting system of equations, it may be seen that it is impossible for all of these conditions to be satisfied. This shows that for any small but non-zero angular momentum, there are no critical points. This should not be taken to imply that rotating black holes have no critical points. Once we increase the allowed angular momentum to be outside of the perturbative range of small α, then the linear expansion in α is no longer valid, and the above conclusion no longer holds true. The fact that the above system of equations and conditions are inconsistent in the limit of small α however, demonstrates that angular momentum removes the original re-entrant critical point of the neutral-static system.

Chapter 9

Validity of the Semiclassical Approximation

Braneworld methods allow for a convenient solution of the semiclassical problem incorporating backreaction of quantum matter to all orders. However, just like in any semiclassical approach, the results are expected to remain valid only when it is legitimate to treat the metric classically, that is, when quantum fluctuations of the geometry remain small.

It has been recently understood that extremal black holes are highly quantum objects [227]. In the case of extremal black holes in Einstein gravity, the low temperature dynamics is described by a Jackiw-Teitelboim theory that governs the fluctuations of the throat. In the absence of supersymmetry, these quantum fluctuations drive the extremal entropy from its semiclassical value down to zero.

The rotating quantum BTZ black hole and its charged generalization presented here admit extremal limits, akin to their higher-dimensional counterparts [326]. Here we will not study the quantum fluctuations of the geometry, but we will characterize when one can expect the semiclassical description to break down. On general grounds, the black hole entropy near extremality admits an expansion

$$S = S_0 + \frac{4\pi^2}{M_{\rm gap}} T + \cdots . \tag{9.1}$$

Here S_0 is extremal entropy in the semiclassical approximation, which is just given by the area of the four-dimensional bulk horizon. The energy scale $M_{\rm gap}$ determines when quantum fluctuations of the geometry become important. We can expect the semiclassical approximation to breakdown when $T < |M_{\rm gap}|$.

Here we will study the behaviour of $M_{\rm gap}$ for the charged and rotating quantum BTZ black hole, taking account of different cases in turn. We will define the $M_{\rm gap}$ as a simple derivative of the entropy,

$$M_{\rm gap} \equiv 4\pi^2 \left[\left(\frac{\partial S}{\partial T} \right)_{W_i; T=0} \right]^{-1} , \tag{9.2}$$

where here the subscript W_i indicates the various thermodynamic potentials that are held fixed in the differentiation — here we will be mostly interested in the case where the conserved charges (Q, J) are held fixed, along with theory specific parameters such as ℓ_3 and G_3.

9.1 Static charged quantum black holes

Let us first consider the charged static quantum black hole with $\alpha = 0 \Rightarrow J = 0$. The behaviour of $M_{\rm gap}$ for this case was studied in [99], and we use this as an opportunity to benchmark our results.

In terms of the thermodynamic parameters, the temperature of the charged quantum black hole vanishes when

$$\chi^2_{\rm ext} = \frac{\nu z^3 + 3\nu z + 2}{\nu z^3 (\nu z + 1)^2} . \tag{9.3}$$

At fixed charge Q, we then obtain for $M_{\rm gap}$ the following

$$M_{\rm gap} = \frac{4G_3}{\ell_3^2} \frac{(\nu^2 z^4 + 6\nu^2 z^2 + 8\nu z + 3)}{\sqrt{\nu^2 + 1}(2\nu z + 1)} . \tag{9.4}$$

Here it is to be understood that the quantities are evaluated for an extremal black hole with a specified charge. This agrees with previous results [99]

9.2 Neutral rotating quantum black holes

Let us now consider the neutral rotating quantum black hole, i.e. with $\chi = 0 \Rightarrow Q = 0$. Notably, there are now *two* possible branches of zero temperature black holes. The condition $T = 0$ is satisfied when

$$\alpha^2_{\rm I} = \frac{z^2(\nu z + 1)}{z^4 - 2\nu z^3 + 1} , \quad \text{or} \quad \alpha^2_{\rm II} = \frac{-\nu z^3 - 3\nu z - 2}{z\,(3\nu + \nu z^4 - 4z)} . \tag{9.5}$$

The first of these two possibilities preserves the classical rotating BTZ extremality condition, or three-dimensional "Kerr bound". Specifically, we have

$$\frac{|J|}{M\ell_3} = 1 \quad \text{for} \quad \alpha^2 = \alpha_{\rm I}^2 \,. \tag{9.6}$$

As was explained already in [134], for this branch of extremal black holes the quantum matter stress tensor vanishes and the CFT does not backreact on the geometry. These zero temperature black holes have $\bar{a}^2 = 1$, and it is because of this relationship that the temperature vanishes. The function $H(r)$ of the four-dimensional metric does not have a double root in this case. However, restricting to the brane perspective, the near horizon geometry of this extremal solution does indeed exhibit the usual features.

On the other hand, the second branch of extremal solutions satisfies

$$\frac{|J|}{M\ell_3} = 1 + \frac{\nu\,(1-z^2)^2}{2z} + \mathcal{O}(\nu^2) \quad \text{for} \quad \alpha^2 = \alpha_{\rm II}^2 \,. \tag{9.7}$$

This branch saturates the three-dimensional Kerr bound in the limit of vanishing backreaction. For small but nonzero backreaction, these extremal solutions *exceed* the three-dimensional Kerr bound.

To allow for a better understanding of how these different zero temperature limits arise we plot the temperature as a function of the parameter α for fixed values of z and ν in Fig. 9.1. Given these parameters, we determined the range of α consistent with the physicality constraints of the metric. The behaviour of temperature and the set of physical solutions depends on the choice of (ν, z) parameters. We illustrate in Fig. 9.1 the two characteristic behaviours with blue and green curves.

Let us consider first the blue curve. Increasing α from zero, the temperature begins to decrease and crosses zero when $\alpha = \alpha_{\rm I}$. This corresponds to $\bar{a}^2 = 1$ and all larger values of α are unphysical, corresponding to $\bar{a}^2 > 1$. Turning next to the green curve, the temperature once again decreases as α is increased. This time, the temperature vanishes first when $\alpha = \alpha_{\rm II}$. Larger values of α are consistent with the most natural physical criteria, i.e. demanding $\mu x_1 > 0$, $r_+ > 0$, $\bar{a}^2 < 1$, but possess negative temperature and are therefore discarded. Now, when α is further increased we reach $\alpha = \alpha_{\rm I}$, indicated by the red circle on the green curve. This is a completely isolated but otherwise physically acceptable solution. We cannot increase α any further beyond this point as doing so would result in $\bar{a}^2 > 1$. On the other hand, the solution cannot have its value of α sensibly decreased as doing so would result in a negative temperature configuration.

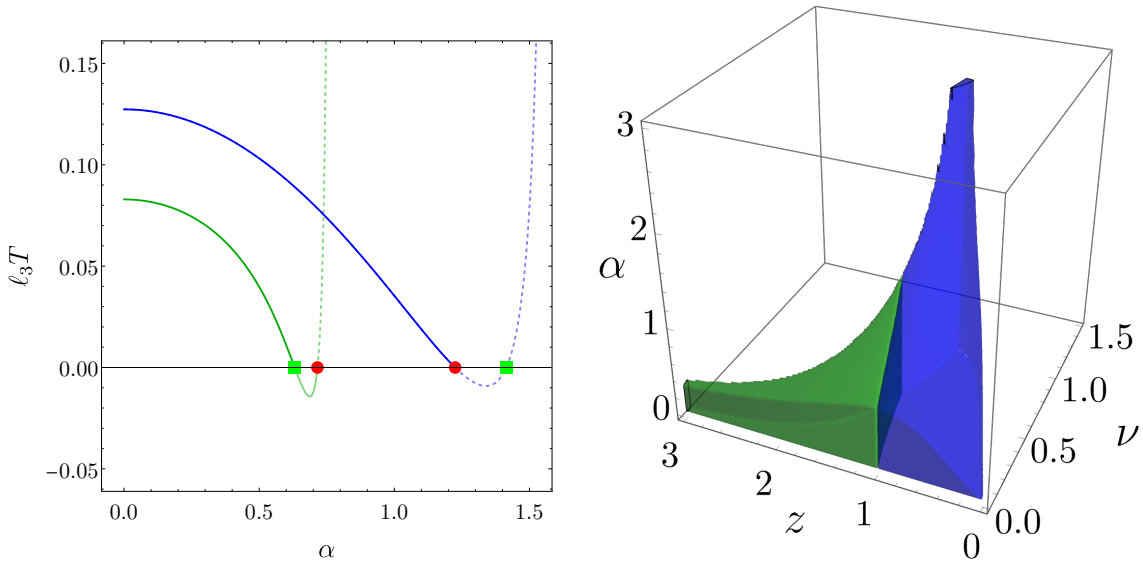


Figure 9.1: Left: A plot of the temperature as a function of α for the neutral rotating quantum black hole. Here the red dots indicate the extremal solutions with $\alpha = \alpha_{\rm I}$ while the green squares are the extremal solutions with $\alpha = \alpha_{\rm II}$. The blue curve corresponds to $(z, \nu) = (1, 1/2)$ while the green curve corresponds to $(z, \nu) = (1.5, 0.125)$. The dashed portions of the curves have $\bar{a}^2 > 1$ and are therefore unphysical. Right: The (z, ν, α) parameter space color-coded according to the type of extremal solutons. For those parameters in the green region (leftmost side of the plot) the $\alpha_{\rm II}$ extremal solution is reached first. For those parameters in the blue region (rightmost side of the plot) the $\alpha_{\rm I}$ extremal solution is reached first, while the $\alpha_{\rm II}$ solution is unphysical with $\bar{a}^2 > 1$.

Summarizing, for the neutral rotating black hole, there are two different choices of α that yield zero temperature quantum black holes, $\alpha_{\rm I}$ and $\alpha_{\rm II}$. Which of these extremal solutions exist depends on the combination of parameters. Generally, when $\alpha_{\rm I} < \alpha_{\rm II}$ then only $\alpha_{\rm I}$ is physical. When $\alpha_{\rm II} < \alpha_{\rm I}$ then both extremal solutions are technically physical, but the one corresponding to $\alpha_{\rm I}$ is highly exotic. It is completely isolated in parameter space, as the value of α cannot be made larger or smaller without violating physicality conditions. This exotic behaviour is consistent with the fact that, from the four-dimensional bulk perspective, the $\alpha_{\rm I}$ extremal solutions do not correspond to a double root of the $H(r)$ metric function. Moreover, in all cases, the $\alpha_{\rm I}$ solutions have completely vanishing backreaction, with vanishing quantum stress tensor. The most conservative perspective is that, while the $\alpha_{\rm II}$ extremal solutions are perfectly fine when physical, the $\alpha_{\rm I}$ must be regarded with care.

Let us now analyse when we expect the semiclassical approximation to break down in the vicinity of these black holes. Holding the angular momentum fixed, we can compute $M_{\rm gap}$ for each of the two types of extremal solution. We find

$$M^{\rm I}_{\rm gap} = \frac{4G_3}{\ell_3^2}\frac{\left(\nu z^3+2z^2-3\nu z-2\right)^2}{\sqrt{\nu^2+1}(\nu z+1)\left(z^4-4\nu z^3-2z^2+1\right)}\,, \tag{9.8}$$

$$M^{\rm II}_{\rm gap} = \frac{G_3}{\ell_3^2}\frac{\left(\nu z^3+2z^2-3\nu z-2\right)\left(-3\nu+\nu z^4+6\nu z^2+8z\right)}{\sqrt{\nu^2+1}(z-1)z(z+1)(\nu z+1)}\,. \tag{9.9}$$

In the limit of small backreaction, both $M^{\rm I}_{\rm gap}$ and $M^{\rm II}_{\rm gap}$ limit to the expected value for the classical rotating BTZ black hole,

$$M^{\rm I}_{\rm gap} = \frac{16G_3}{\ell_3^2}\left[1+\frac{2\nu\left(z^3+z\right)}{\left(z^2-1\right)^2}+\mathcal{O}(\nu^2)\right]\,, \tag{9.10}$$

$$M^{\rm II}_{\rm gap} = \frac{16G_3}{\ell_3^2}\left[1-\frac{\nu\left(z^6+z^4-13z^2+3\right)}{8z-8z^3}+\mathcal{O}(\nu^2)\right]\,. \tag{9.11}$$

We see that the corrections to the classical result differ.

Although it is not obvious from inspection, when implementing all physicality conditions $M^{\rm II}_{\rm gap}$ can be shown to be strictly positive. This is in line with all the well-known higher-dimensional black holes. On the other hand, $M^{\rm I}_{\rm gap}$ is *not* always positive — see Fig. 9.2. This bizarre feature further solidifies the exotic nature of these solutions. We shall comment in more detail on this feature and its relation to weak cosmic censorship below.

We consider the dependence of $M_{\rm gap}$ on the angular momentum in Fig. 9.3. The left plot shows the result for $M^{\rm I}_{\rm gap}$. As mentioned above, this extremal solution does not have a strictly positive $M_{\rm gap}$. For a given value of the backreaction parameter ν, $M^{\rm I}_{\rm gap}$ initially increases as the angular momentum increases. This continues until, at a finite value of J, $M^{\rm I}_{\rm gap}$ diverges to infinity. For J just larger than this critical value, $M^{\rm I}_{\rm gap}\to-\infty$. As the angular momentum is further increased, $M^{\rm I}_{\rm gap}$ increases but remains negative, terminating at $M^{\rm I}_{\rm gap}=0$ for the maximum value of J.

The behaviour of $M^{\rm II}_{\rm gap}$ is shown in the right panel of the same figure. The behaviour in this case is more reasonable, with $M^{\rm II}_{\rm gap}$ exhibiting a monotonic behaviour, decreasing as the angular momentum increases toward its maximum value. Note that in this case, the physical parameter space terminates at $z=1/\nu^3$, which is indicated by the solid black line in the figure. For fixed ν, the blue curves originate along this line and then tend toward zero as J is increased.

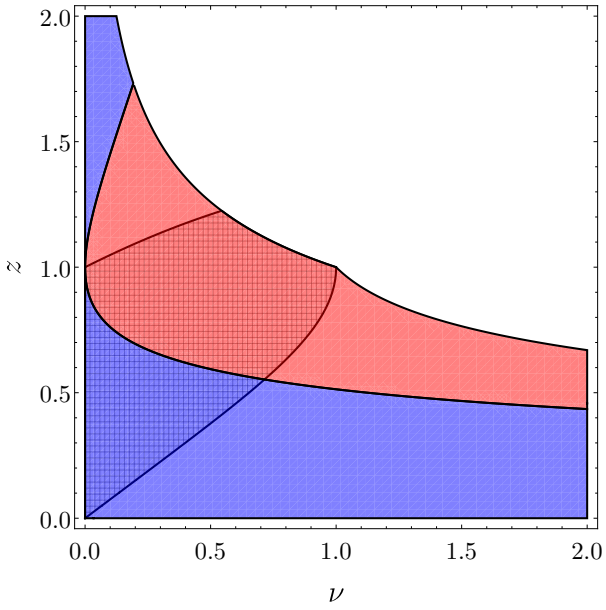


Figure 9.2: We show the (ν, z) parameter space for the neutral rotating quantum black hole characterizing the regions where $M^{\rm I}_{\rm gap}$ is negative (red) and positive (blue). The black cross-hatched portion of the parameter space shows where $\alpha_{\rm I} < \alpha_{\rm II}$.

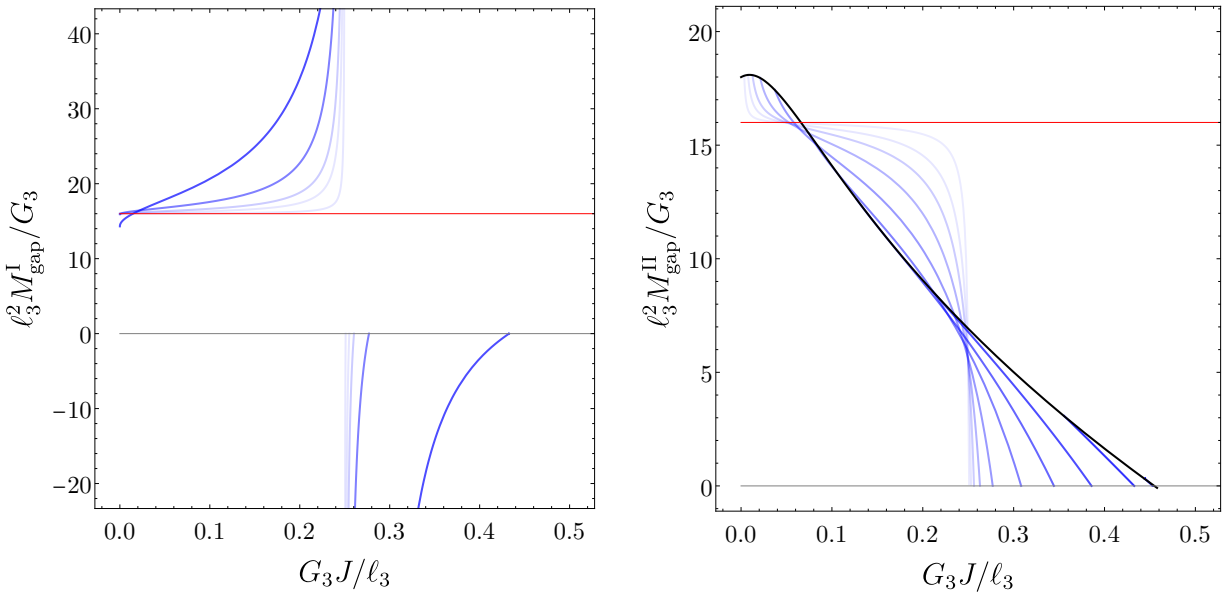


Figure 9.3: Left: $M^{\rm I}_{\rm gap}$ as a function of the angular momentum for difference choices of backreaction parameter ν. Right: $M^{\rm II}_{\rm gap}$ as a function of the angular momentum for difference choices of backreaction parameter ν. In each case, the darker the shade of blue, the larger the value of ν for that curve. The thin red lines in each plot show the value of $M^{\rm BTZ}_{\rm gap} = 16 G_3/\ell_3^2$ for the classical rotating BTZ black hole. On the right plot, the black line is $z = \nu^{-1/3}$ which marks the boundary of the physical parameter space. In both cases, $M_{\rm gap} \to 0$ when the angular momentum takes its largest value for a given ν.

9.3 Charged and rotating quantum black holes

We now extend the preceding results to the case with non-zero charge. The conditions for $T = 0$ generalize from (9.5) to

$$\begin{aligned} \alpha_{\rm I}^2 &= \frac{z^2(\nu z+1)}{z^3\left(-2\nu+\nu\chi^2(\nu z+1)+z\right)+1}\,, \\ \alpha_{\rm II}^2 &= \frac{\nu z\left(z^2\left(1-(\chi+\nu\chi z)^2\right)+3\right)+2}{z\left(-3\nu+\nu z^4\left(\left(\nu^2+1\right)\chi^2-1\right)+4z\right)}\,, \end{aligned} \tag{9.12}$$

and the respective mass gaps for these extremal cases become

$$M_{\rm gap}^{\rm I} = \frac{4G_3}{\ell_3^2}\frac{\Xi^2}{\sqrt{\nu^2+1}\left(z^2+1\right)^2(\nu z+1)\left(z^2\left(z\left(-4\nu+\nu\chi^2(\nu z+1)+z\right)-2\right)+1\right)}\,, \tag{9.13}$$

$$M_{\rm gap}^{\rm II} = \frac{4G_3}{\ell_3^2}\frac{\Xi\left(3\nu+\nu\left(\nu^2+1\right)\chi^2z^4-z\left(\nu z\left(z^2+6\right)+8\right)\right)}{\sqrt{\nu^2+1}z(\nu z+1)\left(z^2\left(\nu\chi^2z+2\right)-2\right)\left(z^2\left(\nu\chi^2z(\nu z+1)-2\right)-2\right)}\,, \tag{9.14}$$

where $\Xi = z^3\left(-2\nu+\nu(\chi+\nu\chi z)^2+z(\nu z+2)\right)-3\nu z-2$. Just as for the neutral rotating quantum black holes, $M_{\rm gap}^{\rm II}$ is strictly positive under physical conditions, while $M_{\rm gap}^{\rm I}$ is not always positive. Fig. 9.2 can be shown to evolve under non-zero χ, with the effect that in the limit of large positive χ, the region in (ν, z) parameter space where $M_{\rm gap}^{\rm I}$ is negative shrinks — see Fig. 9.4.

Note that the extremal solution parameters $\alpha_{\rm I}^2$ and $\alpha_{\rm II}^2$ are equal when

$$\chi_1^2 = \frac{\nu z^3-1}{\nu z^3(\nu z+1)}\,, \quad \text{or} \quad \chi_2^2 = \frac{-\nu z^5-2z^4+2\nu z^3+3\nu z+2}{\nu z^3(\nu z+1)^2}\,. \tag{9.15}$$

The corresponding values that the extremal rotation parameter takes are

$$\alpha_1^2 = \frac{\nu z+1}{z^2-\nu z}\,, \quad \text{or} \quad \alpha_2^2 = -\frac{z^2(\nu z+1)^2}{\left(2\nu^2+1\right)z^4-4\nu z-3}\,. \tag{9.16}$$

The pair (χ_1, α_1) can be dismissed, since their substitution yields divergent x_1^2 and r_+^2. However, the second pair (χ_2, α_2) is physically acceptable, since it admits solutions that satisfy all physical conditions. The (coincident) mass gap that results from this value of χ is

$$M_{\rm gap}^{\rm I}(\chi_2, \alpha_2) = M_{\rm gap}^{\rm II}(\chi_2, \alpha_2) = 0\,. \tag{9.17}$$

This is an extremal value of the mass gap itself, as under physical conditionsis impossible for $M_{\rm gap}^{\rm II}$ to be negative. The mass gap vanishing at extremality only occurs in this coincident limit for the charged and rotating black hole. This implies that quantum fluctuations

of the geometry become arbitrarily important even at infinitesimally small temperatures, which may signal a deeper, nontrivial quantum gravitational regime, distinct from conventional semiclassical black hole thermodynamics. Specifically, the coincident limit marks a boundary in parameter space at which the usual semiclassical picture fails entirely, suggesting that these particular extremal charged rotating quantum black holes could serve as a window into a novel quantum gravitational phase.

9.4 Connection with weak cosmic censorship

Weak cosmic censorship (WCC) — the idea that there are no "naked" singularities — is a cornerstone of our modern perspective on gravitational collapse and black holes. However, there is to date no *proof* that weak cosmic censorship is true. Instead, over the last half century, WCC has been subjected to a battery of consistency tests. Largely, these tests have shown that WCC is robust, and in those cases where counterexamples have been found in the classical theory, one is forced into a regime where quantum gravitational corrections ultimately cannot be ignored [132].

A popular class of tests of WCC are the *gedankenexperiments* where one attempts to overcharge or overspin an (near) extremal black hole by throwing in a test particle carrying charge or angular momentum [435]. It was once believed that these thought experiments *could* succeed in creating a naked singularity [223]. However, in recent years it has been understood that this is an artifact of failing to account for higher-order perturbations induced by the test particle [402].

Taking this idea further, a series of recent studies have identified a connection between the robustness of WCC in gedankenexperiments and the positivity of a single parameter — called "W" in their notation [450, 299]. As defined in, e.g., eq. (9) of [450],

$$W \equiv \lim_{T\to 0}\left(\frac{\partial S}{\partial T}\right)_{Q_i} , \tag{9.18}$$

where Q_i denote conserved charges which are held fixed during the physical process. These investigations find that gedankenexperiments cannot succeed if $W > 0$, while if $W < 0$ then it may be the case that a black hole can be overcharged/overspun. Obviously, the parameter W is, up to unimportant factors, the same as $M_{\rm gap}$ as we defined it in (9.2). We will make several comments about this, though a full analysis of these ideas would take us well outside the scope of the present article.

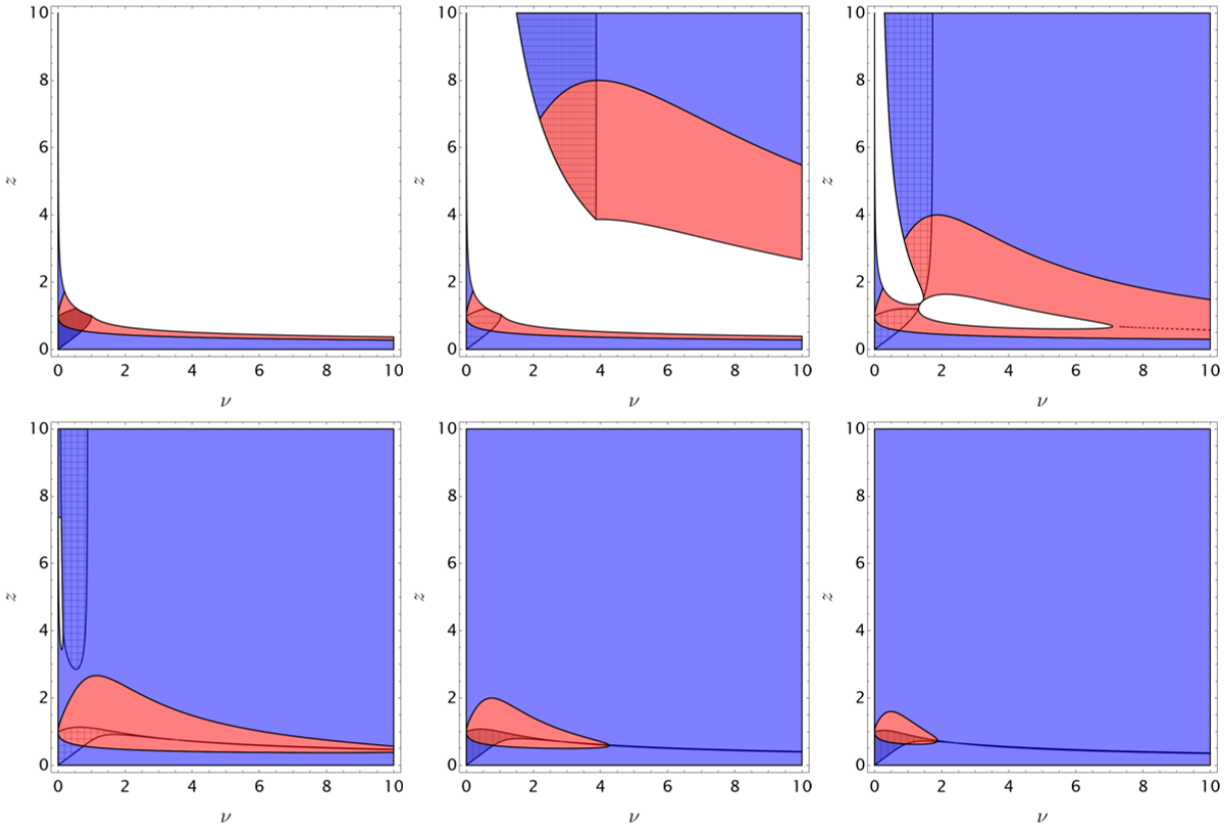


Figure 9.4: We extend Fig. 9.2 to show how the regions in (ν, z) parameter space where $M^{\rm I}_{\rm gap}$ is negative evolves as χ increases. From the top left across and down, we have shown the regions for $\chi = 0, 1/4, 1/2, 3/4, 1, 5/4$. Just as before, the red-shaded portion of the parameter space corresponds to $M^{\rm I}_{\rm gap} < 0$ and the black cross-hatched portion of the parameter space shows where $\alpha_{\rm I} < \alpha_{\rm II}$. Note that increasing χ increases the portion of parameter space where there exist solutions satisfying physicality conditions, and shrinks the portion where $M^{\rm I}_{\rm gap}$ is negative. The apparent dashed curve is a thin section of meshed area.

First let us note the following. In [158], the authors studied gedankenexperiments for the neutral rotating quantum black hole. Their work focused entirely on the physically sensible $\alpha_{\rm II}$ extremal solutions. The results presented there are consistent with the neutral, rotating quantum BTZ respecting WCC. It is not immediately obvious that the results of [450, 299] apply directly to quantum black holes, and it would be interesting to analyze this carefully. That is, to assess whether $W > 0$ remains a sufficient condition for robustness of WCC against perturbations due to classical test particles. Our finding that $M^{\rm II}_{\rm gap}$ is strictly positive for the neutral rotating quantum black hole is fully consistent with the explicit results obtained in [158]. We also observed that $M_{\rm gap}$ is strictly positive for the charged static quantum black hole, suggesting that WCC will be robust to overcharging experiments.

On the other hand, we observed that for the rotating solutions it is possible for $M^{\rm I}_{\rm gap}$ to be *negative*. As we have explained at several instances, these black holes are highly exotic. The extremality condition is met due to $\bar{a}^2 = 1$ and the four-dimensional bulk solution does not have a double root for the metric function $H(r)$ in this case. The stress tensor of the quantum matter vanishes for these extremal solutions, and the brane geometry is identical to the extremal classical rotating BTZ black hole. Nonetheless, supposing that a connection such as that outlined in [450, 299] remains valid, then this suggests that these black holes are candidates for overspinning/overcharging. However, what is less clear is whether such a gedankenexperiment would potentially result in the creation of a naked singularity or if this would signal the onset of a dynamical instability instead.

A closely related point is the following. Since it is now known that quantum fluctuations of the geometry are non-negligible for $T < M_{\rm gap}$, it is not sensible to treat black holes very close to extremality as having a well-defined semiclassical geometry. This calls for a reconsideration of the classical gedankenexperiments to see whether they continue to hold up in this regime. Supposing that the exotic quantum black holes continue to admit a Schwarzian description at low temperatures, then the fact that $M^{\rm I}_{\rm gap} < 0$ is suggestive of a dynamical instability. This is because in the one-dimensional effective description provided by the Schwarzian, $M_{\rm gap}$ plays the role of a coupling — see, for example, eq. (5.2) of [227] or eq. (3.13) of [138]. Thus changing the sign of $M_{\rm gap}$ suggests the Schwarzian mode becomes a ghost.

We can speculate a bit further on how such a potential instability could manifest. Let us recall the structure of the semiclassical theory living on the brane. This consists of an infinite tower of higher-curvature terms coupled to a CFT. As explained in [1, 72], in the absence of the CFT, the spectrum of the gravitational theory on the brane consists of an infinite tower of massive ghost modes. Combining this action with the CFT cures the otherwise pathological behaviour of the purely gravitational theory. However, as mentioned

above, the exotic extremal solutions have $\bar{a}^2 = 1$ and there is therefore no coupling with the CFT. These black holes are therefore solutions of the corresponding purely gravitational theory on the brane. It thus seems at least plausible that perturbations of these exotic extremal solutons that do not excite the CFT could succumb to ghost instabilities. It would be interesting, though rather complicated, to understand the stability of these solutions from both a bulk and brane perspective. Since the four-dimensional configuration is a solution of the Einstein (Maxwell) equations, there could be an interesting and intricate connection between the two perspectives.

Chapter 10

Quantum Inequalities

10.1 Quantum Penrose inequality

The classical black holes of general relativity obey a number of geometric inequalities that place bounds on their physical properties. Perhaps the most famous of these is the Penrose inequality, which is a conjectured bound on the mass of an asymptotically flat spacetime in terms of the area of black hole horizons it contains [356],

$$G_4 M_{\rm ADM} \geq \sqrt{\frac{A}{16\pi}}\,. \tag{10.1}$$

Besides providing a lower bound on the mass, the Penrose inequality is important for the role it plays in the weak cosmic censorship hypothesis. Specifically, assuming weak cosmic censorship and assuming gravitational collapse produces a Kerr black hole, then (10.1) must follow. Therefore, establishing a counterexample to the Penrose inequality would suggest that at least one of these two assumptions must be wrong. In turn, a proof of the Penrose inequality is generally expected to greatly inform our understanding of weak cosmic censorship.

A more subtle question concerns what happens when quantum effects become important. Since many expect that quantum gravity will cure the singularity problem entirely, it is perhaps reasonable to expect that weak quantum effects should not make the classical singularity problem *worse*. A sharp question is whether there exists a version of weak cosmic censorship that holds in semiclassical gravity. While this is at present not clear, there

have been attempts to construct generalizations of the Penrose inequality valid in semiclassical gravity, called *quantum* Penrose inequalities. The hope is that these inequalities, if true, will contribute to our understanding of quantum cosmic censorship [133, 141, 154].

The first such construction was carried out in [56, 57], where it was also shown that the classical Penrose inequality is *badly* violated by quantum effects. Instead, it was argued, a valid inequality can be obtained in $D \geq 4$ by replacing the area term in the Penrose inequality by the corresponding generalized entropy,

$$A \to 4\mathcal{G}_{\rm D} S_{\rm gen}\,. \tag{10.2}$$

There is evidence that the resulting inequalities are indeed satisfied, but this is limited to the perturbative regime due to the general complexities of semiclassical gravity.

Braneworld holography offers a promising avenue for testing such inequalities beyond the perturbative regime. Indeed, already in the context where the bulk is classical, strong holographic arguments have been obtained in favor of the validity of the Penrose inequality, e.g., [142, 140, 148]. Considering semiclassical gravity, a quantum Penrose inequality was recently proposed in three-dimensions [153],

$$8\mathcal{G}_3\left(M - M_{\rm cas}\right) \geq \frac{1}{\ell_3^2}\left(\frac{2\mathcal{G}_3 S_{\rm gen}}{\pi}\right)^2\,, \tag{10.3}$$

where $M_{\rm cas}$ is the Casimir contribution to the mass. In [153], it was demonstrated that (10.3) holds for all known quantum black holes constructed via braneworld holography, even non-perturbatively in the backreaction. This does not prove that a quantum Penrose inequality exists in three-dimensions, but it does provide strong evidence in favour of it.

To further stress-test this proposal, here we examine its validity for the charged and rotating quantum black hole. This turns out to be a more complicated endeavor than any of the quantum black holes considered in [153]. In that case, the solutions and parameter constraints were sufficiently simple that Mathematica could be used to prove the validity of (10.3) exactly. Here, we find this to be impossible, and we resort to a combination of numerical techniques.

The first technique makes use of Mathematica's "NMinimize" routine. We specify particular values of the charge and rotation parameters (χ, α) and then require Mathematica to find a minimum of the functional

$$8\mathcal{G}_3\left(M - M_{\rm cas}\right) - \frac{1}{\ell_3^2}\left(\frac{2\mathcal{G}_3 S_{\rm gen}}{\pi}\right)^2\,, \tag{10.4}$$

subject to constraints that ensure the physical viability of the solution. Specifically, we require the positivity of $x_1^2, r_+^2, \mu x_1$, as given in eq. (7.40), along with the positivity of the temperature, z, and ν. We repeat the minimization procedure for a large set of (χ, α) parameters. We find in all cases that the minimum of the functional is positive, indicating no violation of the conjectured quantum Penrose inequality.

The second method makes use of Mathematica's "FindInstance" routine. We specify two parameters of the solution, e.g., (α, χ) and then use FindInstance to generate a large set of the remaining parameters such that all the constraints just described are satisfied. We then test the validity of (10.3) on the numerically constructed data. We repeat the same procedure for different choices of the manually specified parameter values. In no cases do we find violations of (10.3).

In summary: our numerical investigations are consistent with the validity of (10.3) for charged and rotating quantum black holes.

10.2 Penrose inequality with angular momentum

The Penrose inequality is one member of a hierarchy of conjectured inequalities that bound the mass in terms of the horizon area and additional conserved charges [309]. For example, in four-dimensional Einstein-Maxwell theory, the following generalized Penrose inequality is expected to hold [110],

$$m^2 \geq \frac{A}{16\pi} + \frac{q^2}{2} + \frac{\pi\left(q^4 + 4J^2\right)}{A} \quad \text{when} \quad A \geq 4\pi\sqrt{q^4 + 4J^2}\,. \tag{10.5}$$

(We refer the reader to [110] for a discussion of the conventions in this formula). The inequality is saturated by the Kerr-Newman solution. The constraint on the area arises because it is only when $A \geq 4\pi\sqrt{q^4 + 4J^2}$ that the functional on the right-hand-side of the inequality is monotonically increasing as a function of A. When the charge and rotation vanish, the inequality reduces to the familiar Penrose inequality but otherwise is a stricter constraint.

It is natural to wonder whether there exist quantum inequalities that incorporate additional conserved charges. The charged and rotating quantum black hole provides us with a means to check the viability of such statements. To obtain one such inequality, we will follow the same chain of reasoning that led to the inequality (10.5).

We shall pursue an inequality that incorporates the angular momentum. The first step is to obtain an identity that holds for the *classical* rotating BTZ geometry. It is

straightforward to verify that

$$8\mathcal{G}_3 M = \frac{A^2}{4\pi^2\ell_3^2} + \frac{64\pi^2\mathcal{G}_3^2 J^2}{A^2} \quad \text{for classical rotating BTZ}\,. \tag{10.6}$$

The function on the right-hand-side is an increasing function of A provided that

$$A \geq 4\pi\sqrt{\mathcal{G}_3\ell_3 J}\,. \tag{10.7}$$

This suggests the following "naive" quantum Penrose inequality with angular momentum

$$8\mathcal{G}_3 M \geq \frac{1}{\ell_3^2}\left(\frac{2\mathcal{G}_3 S_{\rm gen}}{\pi}\right)^2 + \left(\frac{2\pi J}{S_{\rm gen}}\right)^2 \quad \text{when} \quad S_{\rm gen} \geq \pi\sqrt{\frac{\ell_3 J}{\mathcal{G}_3}} \quad \text{(naive)}\,. \tag{10.8}$$

The above naive inequality does not hold for quantum black holes. The reason for this is simple: saturation of the inequality by the classical solution is too strong a requirement in three dimensions. In four and higher dimensions, the case $A = 0$ corresponds to the vacuum. But this is not so in three dimensions, as there is a mass gap: there exist naked conical singularities whenever [83]

$$-\sqrt{1+(8\mathcal{G}_3 J)^2} \leq 8\mathcal{G}_3 M < 0\,. \tag{10.9}$$

These naked singularities become cloaked by event horizons when quantum matter backreacts on the geometry. This generates horizons of non-vanishing area in regions of parameter space where they would be classically forbidden. The naive inequality fails to account for this fact, and this is the reason why it fails to hold. To remedy this, the mass appearing in the inequality must be shifted so that the zero point now coincides with the boundary of the parameter space containing naked conical singularities. The same reasoning applies to the nonrotating case, as explained in [153]. The result is then,

$$8\mathcal{G}_3\left(M + \frac{\sqrt{1+(8\mathcal{G}_3 J)^2}}{8\mathcal{G}_3}\right) \geq \frac{1}{\ell_3^2}\left(\frac{2\mathcal{G}_3 S_{\rm gen}}{\pi}\right)^2 + \left(\frac{2\pi J}{S_{\rm gen}}\right)^2 \quad \text{when} \quad S_{\rm gen} \geq \pi\sqrt{\frac{\ell_3 J}{\mathcal{G}_3}}\,. \tag{10.10}$$

When $J \to 0$, this inequality recovers the quantum Penrose inequality (10.3) first presented in [153]. With the mass shifted as above, the inequality is no longer saturated in the classical limit, but it is still satisfied.

If the above proposal is to be considered viable, then it must hold for all quantum black holes. We have numerically investigated the validity of the inequality for the neutral and

charged rotating quantum black holes using the same techniques described in the previous section. We have found no counterexamples within the scanned parameter space.

In fact we have found that a slightly stronger inequality holds for the charged and rotating quantum black hole

$$8\mathcal{G}_3\left(M-M_{\rm cas}\right)\geq\frac{1}{\ell_3^2}\left(\frac{2\mathcal{G}_3S_{\rm gen}}{\pi}\right)^2+\left(\frac{2\pi J}{S_{\rm gen}}\right)^2\quad\text{when}\quad S_{\rm gen}\geq\pi\sqrt{\frac{\ell_3 J}{\mathcal{G}_3}}\,, \tag{10.11}$$

where

$$M_{\rm cas}=-\frac{1}{8\mathcal{G}_3}\,. \tag{10.12}$$

To assess whether this stronger inequality holds in general will require a study of the $\kappa=+1$ quantum black holes. This would be a good target for future work.

10.3 Quantum reverse isoperimetric inequality

Within the context of extended phase space thermodynamics, it was conjectured that asymptotically AdS black holes obey the *reverse* of the familiar isoperimetric inequality for surfaces in Euclidean space [109],

$$\mathcal{R}\equiv\left(\frac{(D-1)V_{\rm th}}{\Omega_{D-2}}\right)^{\frac{1}{D-3}}\left(\frac{\Omega_{D-2}}{A}\right)^{\frac{1}{D-2}}\geq 1\,. \tag{10.13}$$

Physically, this conjecture captures the idea that, at fixed thermodynamic volume, the entropy is maximized for the Schwarzschild-AdS black hole.

Over the last decade, this inequality has been subjected to a variety of tests and has largely held up. In four and higher dimensions, there exists no robust counterexample of the conjecture for asymptotically AdS black holes in Einstein gravity.[1] In three-dimensions, the classical charged BTZ metric is a potential counterexample [233]. However, as already explained in [155], this case is ambiguous and depends on how the length scale associated with the charge is defined.

[1]The 'super entropic' black holes first studied in [207] were initially thought to be a counterexample to the inequality. However, it was later realized that these black holes have degenerate thermodynamics, calling into question their status as a counterexample to the inequality [206, 28]. Moreover, beside this point, those solutions are actually asymptotically *locally* AdS.

In [153], a quantum generalization of the reverse isoperimetric inequality was proposed and tested against all known three-dimensional quantum black holes. The quantum reverse isoperimetric conjecture states,

$$\mathcal{R}_{\mathcal{Q}} \equiv \left(\frac{(D-1)V_{\rm th}}{\Omega_{D-2}}\right)^{\frac{1}{D-3}} \left(\frac{\Omega_{D-2}}{4\mathcal{G}_D S_{\rm gen}}\right)^{\frac{1}{D-2}} \geq 1 \quad \text{for thermally stable BHs.} \tag{10.14}$$

In understanding the ingredients in this formula, it is important to recall how the thermodynamic volume is defined. The thermodynamic volume has a zero point ambiguity that is directly tied to the zero point ambiguity of the mass. In higher dimensions, the "interesting" thermodynamic volume is the one that is obtained when the mass is defined according to the Ashtekar-Magnon-Das (AMD) prescription, which assigns zero mass to the global AdS vacuum [109]. This is equivalent to assigning zero thermodynamic volume to the vacuum. The conventions used in three-dimensions do not adhere to this prescription, and we must subtract a Casimir contribution from the volume,

$$V_{\rm th} = V - V_{\rm cas}\,, \quad V_{\rm cas} = \left(\frac{\partial M_{\rm cas}}{\partial P_D}\right)_{S_{\rm gen},\ldots}\,. \tag{10.15}$$

For the quantum black holes considered here, we have

$$M_{\rm cas} = -\frac{1}{8\mathcal{G}_3} \quad \Rightarrow \quad V_{\rm cas} = -\frac{\pi\nu^2\ell_3^2}{2}\,. \tag{10.16}$$

We have tested the quantum reverise isoperimetric inequality for the charged and rotating quantum black holes. We have done this numerically, using the same constraints as for the Penrose inequality. That is, we demand positive temperature, and select our data such that $z > 0$, $\nu > 0$ along with positivity of the quantities in eq. (7.40). We also demand that $\bar{a}^2 < 1$, since this is implicitly assumed in the derivation of the coordinate chart and subsequent thermodynamic expressions.

In [153] it was found that there exist some black holes that violate (10.14) but are thermally unstable (adhering to Johnson's revised version of the classical reverse isoperimetric conjecture [232]). Here we find that such examples actually have $\bar{a}^2 > 1$, and are therefore pathological. In summary, we find strong numerical evidence that the quantum reverse isoperimetric inequality holds robustly for these solutions. When $\bar{a}^2 < 1$ and the other physicality constraints hold, we find not a single violation of the inequality.

Chapter 11

The Gyromagnetic Ratio of the Charged and Rotating Quantum Black Hole

11.1 The renormalized gyromagnetic ratio

It is possible to make a preliminary investigation into the gyromagnetic ratio of the quantum black hole. In the appropriate coordinates $(\bar{t}, \bar{r}, \bar{\phi})$ where the metric is manifestly asymptotically AdS_3, the expression for the magnetic dipole moment may be extracted from the asymptotic expansion of the angular component of the gauge field on the brane as

$$\bar{\mathcal{A}}_{\bar{\phi}} \sim \frac{\mu_m}{\bar{r}}\,, \quad \bar{r} \to \infty\,. \tag{11.1}$$

Using the gauge field around the black hole (7.36), we find that

$$\mu_m = \frac{2\bar{a}\sqrt{1-\bar{a}^2}q\ell\ell_3\Delta^2}{\ell_*}\,. \tag{11.2}$$

We define the gyromagnetic ratio g_m of the quantum black hole via

$$\mu_m = g_m \frac{g_4 QJ}{8\pi(M - M_{\rm cas})}\,, \tag{11.3}$$

where M, J, Q are given in (7.21), (7.23), and (7.35), respectively. This formula takes into account the fact that the definition for the electric charge of the black hole used in this thesis differs from that of the standard literature by a factor of $4\pi/g_4$. The standard formula $\mu_m = g_m QJ/2M$ is appropriate when the mass of the black hole is defined such that the vacuum has zero energy. This is not the case here, where the vacuum has an energy contribution of $M_{\text{cas}} = -1/8\mathcal{G}_3$ which must be substracted to ensure the ratio is positive.

We have verified that the above definition of the gyromagnetic ratio passes a non-trivial consistency check. Specifically, when one carefully takes the $\ell \to \infty$ limit of the charged and rotating C-metric, the result is the Kerr-Newman(-AdS) black hole — see Appendix B.2. In this limit, our expression for the gyromagnetic ratio reproduces well-established results in the literature, e.g. limiting to $g_m = 2$ for the Kerr-Newman solution [436].

Evaluating the above ratio for the thermodynamic quantities we have computed earlier, we obtain

$$g_m = \frac{2g_4\sqrt{1-\bar{a}^2}\left(4\Delta^2\bar{a}^2 + x_1^2\left(1-\Delta^2\kappa\left(\bar{a}^2+1\right)\right)\right)}{\Delta x_1^4\left(\mu + q^2 x_1\right)}. \tag{11.4}$$

This in turn can be written in terms of the dimensionless variables z, ν, χ, and α, as well as the gauge constant on the brane g_3. In the limit of large backreaction, this expression diverges as $\sqrt{\nu}$. Holding fixed the 'bare' parameters $\mu, \bar{a}, q$ and examining each term in the expression shows that while Q and μ_m are well behaved and finite in the limit of large backreaction, the mass and spin diverge like $M \sim \nu$, and $J \sim \sqrt{\nu}$.

Of course, the 'bare' quantities are not physical, and so we should instead examine the behaviour of the gyromagnetic ratio as a function of the physical mass, charge and angular momentum as the backreaction varies. Unfortunately, the necessary analysis cannot be carried out analytically, and therefore we study this problem numerically. By fixing physically measurable quantities such as the mass difference $M - M_{\text{cas}}$, electric charge Q, and angular momentum J, we let the underlying geometric parameters z, χ, and α vary with the backreaction parameter ν. Due to the algebraic complexity of the parameter dependencies, the necessary inverse relationships, e.g. $z(\nu, Q, J, M)$, etc., must be obtained numerically. The resulting numerically computed gyromagnetic ratio as a function of the backreaction parameter is presented in Fig. 11.1. A significant result of this analysis is that the structure of the g_m curve proves robust against variations of fixed physical parameters. Importantly, for large values of backreaction parameter ν, the renormalized gyromagnetic ratio exhibits a clear universal behavior, asymptotic to 2π. A good approximation to the curve is $2\pi\sqrt{\nu}/(\nu^2+1)^{1/4}$.

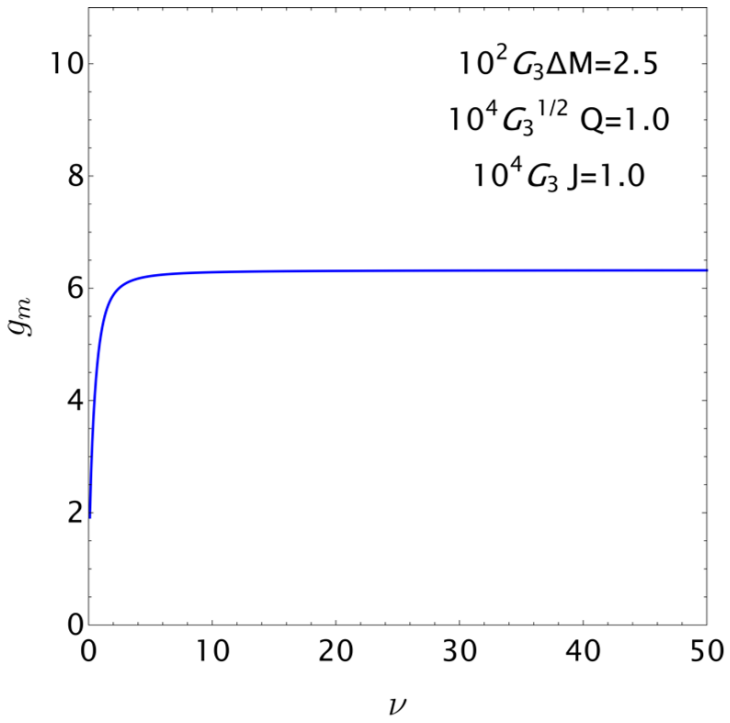


Figure 11.1: The renormalized gyromagnetic ratio of the quantum black hole on the brane as a function of the backreaction parameter ν for the displayed values of the Casimir subtracted mass ΔM, charge Q and spin J. The structure of this curve is insensitive to the fixed physical values that an observer would measure, of the black hole on the brane. The gauge coupling g_3 has been set to unity.

11.2 Discussion

We studied aspects of the thermodynamic properties of the charged rotating quantum black holes in the braneworld. The charged rotating quantum black hole can be obtained by incorporating an ETW brane in the charged rotating AdS C-metric. The quantum black hole then serves as an exact solution to the semi-classical gravitational field equation on the ETW brane, which includes the quantum backreaction from the quantum matter on the brane at all orders.

First, we calculated the thermodynamic quantities, such as the mass, and generalized entropy for the black holes. The mass of the black hole is determined by the conical deficit of the three-dimensional geometry. The generalized entropy of the black hole incorporates all-order of backreaction from the holographic CFT on the brane. Working with the methods of black hole chemistry, where the cosmological constant is treated as a thermodynamic variable, we found both the thermodynamic first law and its integral form (Smarr formula) for the quantum black hole, from three perspectives: the brane, the bulk, and the boundary. From the brane perspective, where there is a quantum black hole coupled to quantum matter, the central charge of the holographic quantum field was considered as a thermodynamic variable; from the bulk perspective, where there is a tensional brane, the tension of the brane was taken to be variable; from the boundary perspective, we studied the thermodynamics of the two-dimensional DCFT.

A numerical analysis of thermodynamic phase diagrams allowed us to identify second-order critical points and calculate their associated critical exponents. The neutral-static quantum BTZ black hole's re-entrant phase transitions were found to be characterized by unorthodox critical exponents $\tilde{\alpha} = 0$, $\beta = 1$, $\gamma = 2$ and $\delta = 3$, which, however, still satisfy classical thermodynamic scaling relations–the Rushbrooke inequality and the Widom relation. Notably, to the best of our knowledge, this is the first and only example of a black hole in General Relativity with critical exponents outside of the mean field theory class. While similar non-standard critical exponents have indeed been observed elsewhere, these examples always require modifications of Einstein's theory [124, 208, 131, 222]. However, it must be emphasized that here the corresponding black holes do not dominate the thermodynamic ensemble, as they have positive free energy. We found that the introduction of any electric charge or spin into the system changes the thermodynamics of the black hole system such that to eliminate the re-entrant phase transitions, and introduce non-re-entrant phase transitions which have conventional critical behavior, with the van der Waals type orthodox critical exponents of mean-field theory $\tilde{\alpha} = 0$, $\beta = 1/2$, $\gamma = 1$ and $\delta = 3$. This was confirmed across all three perspectives with consistent results.

The braneworld approach offers a mechanism by which one can solve the equations of

semiclassical gravity via holography. However, the semiclassical approximation will remain valid only insofar as the quantum fluctuations of the metric remain under control. This is particularly relevant in our case because we have seen it is possible to construct *extremal* quantum black holes. Generally speaking, a key development of the last decade has been the understanding that the semiclassical approximation cannot be fully trusted for low temperature horizons. To study the limitations of the semiclassical approximation, we used the mass gap $M_{\rm gap}$ near extremality which defines a temperature scale above which the semiclassical approximation can be relied on.

Concerning extremal solutions, we showed that in the presence of rotation there are two branches of extremal horizons while in the presence of charge alone there is a single extremal branch. Of the two branches of extremal solutions for (charged)-rotating black holes, one behaves analogous to familiar higher-dimensional extremal rotating solutions, while the other is highly exotic. In particular, while we demonstrated that (upon imposing physicality conditions) $M_{\rm gap}$ is always positive for the 'sensible' extremal solutions, it can become negative for the exotic ones. Since $M_{\rm gap}$ plays the role of a coupling in the Schwarzian action that governs the fluctuations of quantum zero modes of extremal black hole throats, this suggests likely semiclassical instabilities of the exotic extremal solutions. We also speculated about the connection between this observation and recent results in weak cosmic censorship 'Gedankenexperiments'. In that context, it has been shown via completely unrelated methods, that the positivity of $M_{\rm gap}$ is a sufficient condition to ensure that *classical* black holes cannot be overspun or overcharged. Hence, there may be a connection between the outcome of classical weak cosmic censorship gedankenexperiments and the quantum stability of extremal horizons.

In the same vein, we also used the charged-rotating quantum black hole as a testbed for recent proposals of quantum inequalities that generalize certain geometric inequalities in classical general relativity. A three-dimensional quantum Penrose inequality was proposed in [153] and tested against charged and rotating quantum black holes, finding agreement. Here, for the charged-rotating quantum black hole, the complexity of the expressions involved precluded the ability to directly confirm that the inequality is always satisfied, but a wide-spread sampling of the parameter space found no violations. More significantly, here we proposed and tested a *generalized* quantum Penrose inequality that bounds the mass in terms of both the generalized entropy *and* the angular momentum. While such generalized Penrose inequalities have long been studied classically, we believe our proposal is the first of its kind for semiclassical gravity (certainly the first to be tested *nonperturbatively*). In classical general relativity, the Penrose inequality plays an important role in the weak cosmic censorship conjecture. The hope is that their quantum generalizations can serve as a guiding light for quantum weak cosmic censorship [154]. Beyond the Penrose inequality

and its generalized version, we also examined the quantum reverse isoperimetric inequality, proposed in [153], with the inclusion of charge and spin. Numerical tests confirm the validity of the inequality for all physically admissible quantum black holes. Violations of this inequality were found in [153], but noted to be thermally unstable. We find that these violations actually occur within the unphysical region of the parameter space and, hence, the quantum reverse isoperimetric inequality is true in all known examples.

Finally, we investigated the gyromagnetic ratio g_m of the charged and rotating quantum black hole, defined by obtaining the magnetic dipole moment from the asymptotic behavior of the gauge field on the brane, and studied its behaviour as a function of the backreaction parameter. To ensure physicality of the result, we fixed the Casimir subtracted mass, electric charge, and spin leaving only the backreaction parameter to vary. Under these constraints, g_m is finite as $\nu \to \infty$, with the limiting value of 2π. This is a robust feature, in that adjusting the Casimir subtracted mass, charge, and spin of the black hole does not change the limiting behaviour of the curve, which is approximated well by $2\pi\sqrt{\nu}/(\nu^2+1)^{-1/4}$.

Chapter 12

Conclusion

This thesis examined how spacetime geometry imprints itself on observables of quantum fields. Part I approached the question operationally, using UDW detectors as localized probes of field correlations; Part II approached it holographically, constructing and analyzing charged and rotating quantum black holes in a doubly holographic AdS braneworld. The two parts differ in method and motivation, but both treat quantum fields on curved backgrounds and translate geometric features into measurable quantities.

Part I (Relativistic Quantum Information)

Chapter 3 studied two initially entangled UDW detectors in Minkowski spacetime and in a gravitational shockwave background. The analysis found that weakly entangled initial states can gain entanglement after interacting with the field, while strongly entangled initial states exhibit only degradation. In the shock wave spacetime the enhancement of weak initial entanglement persists at larger detector separations than in flat spacetime.

Chapter 4 turned to a single-detector observable. By comparing detector transition rates in locally identical but globally distinct geometries—specifically, $\mathbb{R}\mathrm{P}^2$ and Swedish geons constructed as quotients of BTZ—it was shown that the response encodes global identifications hidden behind the horizon. Thus, localized measurements can register global topology.

Chapter 5 provided analytic expressions, at leading order in the detector–field coupling, for the reduced density matrix of two static detectors coupled to a massless conformally coupled scalar in AdS_{d+1}, dS_{d+1}, and BTZ spacetimes. These formulas enable exact evaluations of standard entanglement measures and agree with prior numerical calculations of entanglement harvesting in these settings.

Part II (Braneworld Quantum Black Holes)

Chapter 6 reviewed AdS/CFT and set up the doubly holographic braneworld in which black holes localized on the brane admit codimension-one duals. On the brane side these are exact solutions of a semiclassical effective theory with higher-derivative terms encoding the backreaction of conformal matter. These are quantum black holes.

Building on the AdS C-metric restricted to the brane, Chapter 7 constructed solutions carrying both electric charge and angular momentum, identified the physical parameters directly from the metric, and used a consistent set of dimensionless variables to present thermodynamics from bulk, brane, and boundary perspectives.

Chapter 8 mapped the phase structure using free-energy matching and the Maxwell equal-area construction. The neutral-static quantum black hole exhibits re-entrant phase transitions with critical exponents that were found to differ from mean-field values. Introducing charge or rotation removes the re-entrant behavior and yields criticality consistent with mean-field theory. This constitutes the first appearance of non-mean-field critical exponents within a theory of Einstein gravity, to our knowledge.

Chapter 9 quantified the regime of validity of the semiclassical description by extracting a mass-gap scale from a near-extremal expansion of the entropy, analyzed the associated extremal limits, and related these considerations to the weak cosmic censorship conjecture.

Chapter 10 extended geometric (quantum Penrose-type and reverse isoperimetric) inequalities to include charge and angular momentum, and a numerical sweep found them to be satisfied by the charged and rotating quantum black holes considered here.

Chapter 11 introduced a renormalized gyromagnetic ratio g and showed that at large backreaction this tends to 2π.

Scope and limitations

The detector calculations in Part I are leading order in the coupling, with static worldlines and a massless, conformally coupled scalar. The topology probe relies on specific BTZ quotients. The analytic harvesting formulas address those same field and trajectory assumptions. In Part II, conclusions are drawn within a specific doubly holographic braneworld built from the AdS C-metric; phase diagrams were inferred from standard free-energy and equal-area methods, and inequality checks were numerical.

Outlook

Several directions follow naturally:

- Extend harvesting beyond static detectors and conformal coupling, and test whether the qualitative enhancement seen for shock waves persists for other backgrounds or switching profiles.
- Generalize the single-detector topology probe to other quotient geometries and to arrays of detectors to map global identifications more systematically.
- On the braneworld side, explore families of solutions beyond the C-metric construction to test the robustness of the non-mean-field critical exponents found for the neutral-static case and to delineate precisely how charge or spin restore mean-field behavior in the sense of removing the critical points associated with the non-mean field critical exponents from thermodynamic phase space.
- Combine the mass-gap criterion with dynamical diagnostics (e.g., quasinormal spectra) to cross-check the semiclassical validity regime identified from entropy.
- Study near-saturation regimes of the extended inequalities and track the renormalized gyromagnetic ratio along controlled parameter sweeps to clarify how quantum backreaction modifies classical relations.

At a high level, the two halves of the thesis realize the same program from different angles: translate properties of spacetime into quantities that are calculable and physically meaningful. In Part I the map is explicit—detector response functionals of the Wightman two-point function transcribe local curvature and global identifications into measurable rates and correlation measures. In Part II the doubly holographic setup packages quantum backreaction into a semiclassical effective theory on the brane, whose black hole thermodynamics and phase structure are computable. In both cases, geometry is not described abstractly, but through its imprint on operational or thermodynamic data.

Two general lessons follow. First, global structure leaves local signatures, in the sense of affecting the transition rate of detectors locally coupled to the field, because the field state stores nonlocal information. This sensitivity to the topology of BTZ quotients illustrates that global identifications can be diagnosed by local observers. Second, the character of thermodynamic criticality depends sensitively on how quantum backreaction reshapes the effective dynamics. In the neutral–static branch of the quantum black hole family studied here, higher-derivative terms from conformal matter result in re-entrant phase transitions

with non-mean-field critical exponents, and introducing charge or rotation restores mean field behavior.

A broader set of questions emerges from these results. On the detector side, the natural next step is to ask whether entanglement harvesting can serve as a diagnostic of global structure: do the correlations registered by two detectors distinguish between spacetimes that are locally identical but globally distinct, in the same way that single-detector responses can? Here, the analytical results presented in Chapter 5 may facilitate an investigation that would otherwise be hampered by numerical difficulties associated with accurately evaluating the action of the Wightman distribution on smooth test functions, particularly given the method of images.

On the quantum black hole side, the appearance of non-mean-field exponents in the neutral–static branch raises the sharper question of mechanism: which specific higher-derivative terms in the semiclassical brane effective action, induced by conformal matter backreaction, are responsible for the departure from mean-field criticality, and why are these effects eliminated when charge or rotation is introduced?

Taken together, the results of this thesis show that geometric input—curvature, topology, and boundary conditions on the one hand; charge, rotation, and backreaction on the other—leaves structured, calculable traces in detector observables and black hole chemistry respectively. The tools developed here make some of those traces explicit and provide a clear path for sharpening them further.

References

[1] Sergio E. Aguilar-Gutierrez, Pablo Bueno, Pablo A. Cano, Robie A. Hennigar, and Quim Llorens. Aspects of higher-curvature gravities with covariant derivatives. *Phys. Rev. D*, 108(12):124075, 2023.

[2] Yakir Aharonov, Jeeva Anandan, Sandu Popescu, and Lev Vaidman. Superpositions of time evolutions of a quantum system and a quantum time-translation machine. *Phys. Rev. Lett.*, 64:2965–2968, Jun 1990.

[3] Ofer Aharony, Steven S. Gubser, Juan Martin Maldacena, Hirosi Ooguri, and Yaron Oz. Large N field theories, string theory and gravity. *Phys. Rept.*, 323:183–386, 2000.

[4] Aida Ahmadzadegan, Eduardo Martin-Martinez, and Robert B. Mann. Cavities in curved spacetimes: The response of particle detectors. *Phys. Rev. D*, 89(2):024013, 2014.

[5] Moaathe Belhaj Ahmed, Wan Cong, David Kubiznak, Robert B. Mann, and Manus R. Visser. Holographic CFT phase transitions and criticality for rotating AdS black holes. *JHEP*, 08:142, 2023.

[6] Moaathe Belhaj Ahmed, Wan Cong, David Kubizňák, Robert B. Mann, and Manus R. Visser. Holographic Dual of Extended Black Hole Thermodynamics. *Phys. Rev. Lett.*, 130(18):181401, 2023.

[7] Peter C Aichelburg and Roman Ulrich Sexl. On the gravitational field of a massless particle. *Gen. Relativ. Gravit.*, 2(4):303–312, 1971.

[8] Aghil Alaee and Hari K. Kunduri. A Penrose-Type Inequality with Angular Momenta for Black Holes with 3-Sphere Horizon Topology. *J. Geom. Anal.*, 33(7):231, 2023.

[9] Álvaro M. Alhambra, Achim Kempf, and Eduardo Martín-Martínez. Casimir forces on atoms in optical cavities. *Phys. Rev. A*, 89:033835, Mar 2014.

[10] A. N. Aliev. Gyromagnetic Ratio of Charged Kerr-Anti-de Sitter Black Holes. *Class. Quant. Grav.*, 24:4669–4678, 2007.

[11] A. N. Aliev and Valeri P. Frolov. Five-dimensional rotating black hole in a uniform magnetic field: The Gyromagnetic ratio. *Phys. Rev. D*, 69:084022, 2004.

[12] Alikram N. Aliev. Electromagnetic Properties of Kerr-Anti-de Sitter Black Holes. *Phys. Rev. D*, 75:084041, 2007.

[13] B. Allen and A. Folacci. Massless minimally coupled scalar field in de Sitter space. *Phys. Rev. D*, 35:3771–3778, Jun 1987.

[14] Bruce Allen. Vacuum states in de Sitter space. *Phys. Rev. D*, 32:3136, 1985.

[15] Ahmed Almheiri, Netta Engelhardt, Donald Marolf, and Henry Maxfield. The entropy of bulk quantum fields and the entanglement wedge of an evaporating black hole. *JHEP*, 12:063, 2019.

[16] Ahmed Almheiri, Thomas Hartman, Juan Maldacena, Edgar Shaghoulian, and Amirhossein Tajdini. Replica Wormholes and the Entropy of Hawking Radiation. *JHEP*, 05:013, 2020.

[17] Ahmed Almheiri, Thomas Hartman, Juan Maldacena, Edgar Shaghoulian, and Amirhossein Tajdini. The entropy of Hawking radiation. *Rev. Mod. Phys.*, 93(3):035002, 2021.

[18] Ahmed Almheiri, Raghu Mahajan, Juan Maldacena, and Ying Zhao. The Page curve of Hawking radiation from semiclassical geometry. *JHEP*, 03:149, 2020.

[19] Ahmed Almheiri, Donald Marolf, Joseph Polchinski, and James Sully. Black holes: Complementarity or firewalls? *J. High Energy Phys.*, 02:62, 2013.

[20] P. M. Alsing, I. Fuentes-Schuller, R. B. Mann, and T. E. Tessier. Entanglement of dirac fields in noninertial frames. *Phys. Rev. A*, 74:032326, Sep 2006.

[21] Paul M. Alsing and Ivette Fuentes. Observer-dependent entanglement. *Classical and Quantum Gravity*, 29(22):224001, 2012.

[22] Paul M. Alsing and G. J. Milburn. Teleportation with a uniformly accelerated partner. *Phys. Rev. Lett.*, 91:180404, Oct 2003.

[23] Natacha Altamirano, David Kubiznak, and Robert B. Mann. Reentrant phase transitions in rotating anti–de Sitter black holes. *Phys. Rev. D*, 88(10):101502, 2013.

[24] Stefan Åminneborg, Ingemar Bengtsson, Dieter Brill, Sören Holst, and Peter Peldán. Black holes and wormholes in 2+1 dimensions. *Class. Quantum Grav.*, 15(3):627–644, mar 1998.

[25] Masaya Amo, Antonia M. Frassino, and Robie A. Hennigar. Entropy Bounds for Rotating AdS Black Holes. *Phys. Rev. Lett.*, 131(24):241401, 2023.

[26] Andrés Anabalón, Finnian Gray, Ruth Gregory, David Kubizňák, and Robert B. Mann. Thermodynamics of Charged, Rotating, and Accelerating Black Holes. *JHEP*, 04:096, 2019.

[27] Edoardo Anastasi, Roberta Angius, Jesús Huertas, Angel Uranga, and Chuying Wang. Relative Quantum Gravity: Localized Gravity and the Swampland. 1 2025.

[28] Michael Appels, Leopoldo Cuspinera, Ruth Gregory, Pavel Krtouš, and David Kubizňák. Are "Superentropic" black holes superentropic? *JHEP*, 02:195, 2020.

[29] Michael Appels, Ruth Gregory, and David Kubiznak. Thermodynamics of Accelerating Black Holes. *Phys. Rev. Lett.*, 117(13):131303, 2016.

[30] Juan Sebastián Ardenghi. Entanglement harvesting in double-layer graphene by vacuum fluctuations in a microcavity. *Phys. Rev. D*, 98:045006, Aug 2018.

[31] Philip C. Argyres and Chiara R. Nappi. Massive Spin-2 Bosonic String States in an Electromagnetic Background. *Phys. Lett. B*, 224:89–96, 1989.

[32] Abhay Ashtekar and Saurya Das. Asymptotically Anti-de Sitter space-times: Conserved quantities. *Class. Quant. Grav.*, 17:L17–L30, 2000.

[33] S. J. Avis, C. J. Isham, and D. Storey. Quantum Field Theory in anti-De Sitter Space-Time. *Phys. Rev. D*, 18:3565, 1978.

[34] Maximo Bañados, Marc Henneaux, Claudio Teitelboim, and Jorge Zanelli. Geometry of the (2+1) black hole. *Phys. Rev. D*, 48:1506–1525, 1993. [Erratum: Phys.Rev.D 88, 069902 (2013)].

[35] Máximo Bañados, Marc Henneaux, Claudio Teitelboim, and Jorge Zanelli. Geometry of the 2+1 black hole. *Phys. Rev. D*, 48:1506–1525, Aug 1993.

[36] Máximo Bañados, Claudio Teitelboim, and Jorge Zanelli. Black hole in three-dimensional spacetime. *Phys. Rev. Lett.*, 69:1849–1851, Sep 1992.

[37] Máximo Bañados, Claudio Teitelboim, and Jorge Zanelli. Black hole in three-dimensional spacetime. *Phys. Rev. Lett.*, 69:1849–1851, Sep 1992.

[38] Maximo Banados, Claudio Teitelboim, and Jorge Zanelli. The Black hole in three-dimensional space-time. *Phys. Rev. Lett.*, 69:1849–1851, 1992.

[39] James M. Bardeen, B. Carter, and S. W. Hawking. The Four laws of black hole mechanics. *Commun. Math. Phys.*, 31:161–170, 1973.

[40] Dipankar Barman, Angshuman Choudhury, Bhushan Kad, and Bibhas Ranjan Majhi. Spontaneous entanglement leakage of two static entangled unruh-dewitt detectors. *Phys. Rev. D*, 107:045001, Feb 2023.

[41] Jacob D. Bekenstein. Black holes and entropy. *Phys. Rev. D*, 7:2333–2346, Apr 1973.

[42] Dionigi M. T. Benincasa, Leron Borsten, Michel Buck, and Fay Dowker. Quantum information processing and relativistic quantum fields. *Classical and Quantum Gravity*, 31(7):075007, 2014.

[43] Charles H. Bennett, David P. DiVincenzo, John A. Smolin, and William K. Wootters. Mixed-state entanglement and quantum error correction. *Physical Review A*, 54(5):3824–3851, November 1996.

[44] Cédric Bény, Christopher T Chubb, Terry Farrelly, and Tobias J Osborne. Energy cost of entanglement extraction in complex quantum systems. *Nat. Commun.*, 9(1):1–9, 2018.

[45] E. R. Bezerra de Mello and A. A. Saharian. Vacuum polarization by a cosmic string in de Sitter spacetime. *JHEP*, 04:046, 2009.

[46] Dyuman Bhattacharya, Kensuke Gallock-Yoshimura, Laura J. Henderson, and Robert B. Mann. Extraction of entanglement from quantum fields with entangled particle detectors. *Phys. Rev. D*, 107:105008, May 2023.

[47] Dyuman Bhattacharya, Robie A. Hennigar, Robert B. Mann, and Ming Zhang. Charged rotating quantum black holes. 6 2025.

[48] Dyuman Bhattacharya, Jorma Louko, and Robert B. Mann. Probing hidden topology with quantum detectors. *Phys. Rev. D*, 111:045005, Feb 2025.

[49] Dyuman Bhattacharya, Jorma Louko, and Robert B. Mann. Probing hidden topology with quantum detectors. *Phys. Rev. D*, 111(4):045005, 2025.

[50] N. D. Birrell and P. C. W. Davies. *Quantum Fields in Curved Space*. Cambridge Monographs on Mathematical Physics. Cambridge University Press, 1982.

[51] N.D. Birrell and P.C.W. Davies. *Quantum Fields in Curved Space*. Cambridge Monographs on Mathematical Physics. Cambridge University Press, Cambridge, England, 1984.

[52] Ana Blasco, Luis J. Garay, Mercedes Martín-Benito, and Eduardo Martín-Martínez. Violation of the Strong Huygen's Principle and Timelike Signals from the Early Universe. *Phys. Rev. Lett.*, 114:141103, Apr 2015.

[53] Ana Blasco, Luis J. Garay, Mercedes Martín-Benito, and Eduardo Martín-Martínez. Timelike information broadcasting in cosmology. *Phys. Rev. D*, 93:024055, Jan 2016.

[54] Vicente J Bolós. Intrinsic definitions of "relative velocity" in general relativity. *Commun. Math. Phys.*, 273(1):217–236, 2007.

[55] David G. Boulware. Quantum Field Theory in Schwarzschild and Rindler Spaces. *Phys. Rev. D*, 11:1404, 1975.

[56] Raphael Bousso, Arvin Shahbazi-Moghaddam, and Marija Tomasevic. Quantum Penrose Inequality. *Phys. Rev. Lett.*, 123(24):241301, 2019.

[57] Raphael Bousso, Arvin Shahbazi-Moghaddam, and Marija Tomašević. Quantum Information Bound on the Energy. *Phys. Rev. D*, 100(12):126010, 2019.

[58] Fernando G. S. L. Brandão and Gilad Gour. Reversible framework for quantum resource theories. *Phys. Rev. Lett.*, 115:070503, Aug 2015.

[59] Daniel Braun. Creation of entanglement by interaction with a common heat bath. *Phys. Rev. Lett.*, 89:277901, Dec 2002.

[60] Daniel Braun. Entanglement from thermal blackbody radiation. *Phys. Rev. A*, 72:062324, Dec 2005.

[61] Sergey Bravyi and Alexei Kitaev. Universal quantum computation with ideal clifford gates and noisy ancillas. *Physical Review A*, 71(2), February 2005.

[62] W.G. Brenna, Robert B. Mann, and Eduardo Martín-Martínez. Anti-Unruh phenomena. *Physics Letters B*, 757:307 – 311, 2016.

[63] Wilson G. Brenna, Eric G. Brown, Robert B. Mann, and Eduardo Martín-Martínez. Universality and thermalization in the unruh effect. *Phys. Rev. D*, 88:064031, Sep 2013.

[64] HW Brinkmann. On riemann spaces conformal to euclidean space. *Proc. Natl. Acad. Sci. U.S.A*, 9:1–3, 1923.

[65] Jacques Bros, Henri Epstein, and Ugo Moschella. Scalar tachyons in the de Sitter universe. *Letters in Mathematical Physics*, 93(2):203–211, Aug 2010.

[66] Eric G. Brown. Thermal amplification of field-correlation harvesting. *Phys. Rev. A*, 88:062336, Dec 2013.

[67] Eric G. Brown, Eduardo Martín-Martínez, Nicolas C. Menicucci, and Robert B. Mann. Detectors for probing relativistic quantum physics beyond perturbation theory. *Phys. Rev. D*, 87:084062, Apr 2013.

[68] Eric G. Brown, Eduardo Martín-Martínez, Nicolas C. Menicucci, and Robert B. Mann. Detectors for probing relativistic quantum physics beyond perturbation theory. *Phys. Rev. D*, 87:084062, Apr 2013.

[69] J. David Brown and M. Henneaux. Central Charges in the Canonical Realization of Asymptotic Symmetries: An Example from Three-Dimensional Gravity. *Commun. Math. Phys.*, 104:207–226, 1986.

[70] David Edward Bruschi and Jorma Louko. Charged Unruh effect on geon spacetimes. In *12th Marcel Grossmann Meeting on General Relativity*, pages 2359–2361, 3 2010.

[71] Dagmar. Bruss and Gerd. Leuchs. *Lectures on quantum information*. Wiley-VCH, Weinheim ;, 2007.

[72] Pablo Bueno, Pablo A. Cano, and Robie A. Hennigar. Nonlocal Massive Gravity from Einstein Gravity. *Phys. Rev. Lett.*, 132(19):191402, 2024.

[73] Pablo Bueno, Roberto Emparan, and Quim Llorens. Higher-curvature gravities from braneworlds and the holographic c-theorem. *Phys. Rev. D*, 106(4):044012, 2022.

[74] T. S. Bunch and P. C. W. Davies. Quantum field theory in de Sitter space: renormalization by point splitting. *Proc. Roy. Soc. Lond. A*, 360:117–134, 1978.

[75] Lissa de Souza Campos and Claudio Dappiaggi. Ground and thermal states for the klein-gordon field on a massless hyperbolic black hole with applications to the anti-hawking effect. *Phys. Rev. D*, 103:025021, Jan 2021.

[76] Raúl Carballo-Rubio, Luis J. Garay, Eduardo Martín-Martínez, and José de Ramón. Unruh effect without thermality. *Phys. Rev. Lett.*, 123:041601, Jul 2019.

[77] Steven Carlip. The (2+1)-Dimensional black hole. *Class. Quantum Grav.*, 12:2853–2880, 1995.

[78] Steven Carlip. *Quantum Gravity in* $2+1$ *Dimensions*. Cambridge Monographs on Mathematical Physics. Cambridge University Press, 1998.

[79] S.M. Carroll. *Spacetime and Geometry: An Introduction to General Relativity*. Cambridge University Press, Cambridge, England, 2019.

[80] Brandon Carter. Global structure of the Kerr family of gravitational fields. *Phys. Rev.*, 174:1559–1571, 1968.

[81] Casey Cartwright, Umut Gürsoy, Juan F. Pedraza, and Guim Planella Planas. Perturbing a quantum black hole. 8 2024.

[82] Casey Cartwright, Umut Gürsoy, Juan F. Pedraza, and Andrew Svesko. Quantum induced superradiance. 1 2025.

[83] Marc Casals, Alessandro Fabbri, Cristián Martínez, and Jorge Zanelli. Quantum-corrected rotating black holes and naked singularities in (2+1) dimensions. *Phys. Rev. D*, 99(10):104023, 2019.

[84] Horacio Casini, Marina Huerta, and Robert C. Myers. Towards a derivation of holographic entanglement entropy. *JHEP*, 05:036, 2011.

[85] L. C. Céleri, A. G. S. Landulfo, R. M. Serra, and G. E. A. Matsas. Sudden change in quantum and classical correlations and the unruh effect. *Phys. Rev. A*, 81:062130, Jun 2010.

[86] Andrew Chamblin, Roberto Emparan, Clifford V. Johnson, and Robert C. Myers. Charged AdS black holes and catastrophic holography. *Phys. Rev. D*, 60:064018, 1999.

[87] K. C. K. Chan and Robert B. Mann. Static charged black holes in (2+1)-dimensional dilaton gravity. *Phys. Rev. D*, 50:6385, 1994. [Erratum: Phys.Rev.D 52, 2600 (1995)].

[88] S. Chandrasekhar. *The Mathematical Theory of Black Holes*. International Series of Monographs on Physics. Clarendon Press, Oxford, 1998.

[89] Jing-Cheng Chang, Song He, Yu-Xiao Liu, and Long Zhao. Island formula in Planck brane. *JHEP*, 11:006, 2023.

[90] Hong Zhe Chen, Zachary Fisher, Juan Hernandez, Robert C. Myers, and Shan-Ming Ruan. Evaporating Black Holes Coupled to a Thermal Bath. *JHEP*, 01:065, 2021.

[91] Hong Zhe Chen, Robert C. Myers, Dominik Neuenfeld, Ignacio A. Reyes, and Joshua Sandor. Quantum Extremal Islands Made Easy, Part I: Entanglement on the Brane. *JHEP*, 10:166, 2020.

[92] Hong Zhe Chen, Robert C. Myers, Dominik Neuenfeld, Ignacio A. Reyes, and Joshua Sandor. Quantum Extremal Islands Made Easy, Part II: Black Holes on the Brane. *JHEP*, 12:025, 2020.

[93] N. A. Chernikov and E. A. Tagirov. Quantum theory of scalar fields in de Sitter space-time. *Ann. Inst. H. Poincare A Phys. Theor.*, 9:109, 1968.

[94] Eric Chitambar and Gilad Gour. Quantum resource theories. *Rev. Mod. Phys.*, 91:025001, Apr 2019.

[95] Pratyusha Chowdhury and Bibhas Ranjan Majhi. Fate of entanglement between two Unruh-DeWitt detectors due to their motion and background temperature. *J. High Energy Phys.*, 05(2022):025, 2022.

[96] Maria E. Gabach Clement, Jose Luis Jaramillo, and Martin Reiris. Proof of the area-angular momentum-charge inequality for axisymmetric black holes. *Class. Quant. Grav.*, 30:065017, 2013.

[97] M. Cliche and A. Kempf. Relativistic quantum channel of communication through field quanta. *Phys. Rev. A*, 81:012330, Jan 2010.

[98] M. Cliche and A. Kempf. Vacuum entanglement enhancement by a weak gravitational field. *Phys. Rev. D*, 83:045019, Feb 2011.

[99] Ana Climent, Roberto Emparan, and Robie A. Hennigar. Chemical potential and charge in quantum black holes. *JHEP*, 08:150, 2024.

[100] Ana Climent, Robie A. Hennigar, Emanuele Panella, and Andrew Svesko. Nucleation of charged quantum de-Sitter$_3$ black holes. *JHEP*, 05:086, 2025.

[101] Geoffrey Compère, Jiang Long, and Max Riegler. Invariance of Unruh and Hawking radiation under matter-induced supertranslations. *Journal of High Energy Physics*, 2019(5):53, May 2019.

[102] Wan Cong, David Kubiznak, and Robert B. Mann. Thermodynamics of AdS Black Holes: Critical Behavior of the Central Charge. *Phys. Rev. Lett.*, 127(9):091301, 2021.

[103] Wan Cong, David Kubiznak, Robert B. Mann, and Manus R. Visser. Holographic CFT phase transitions and criticality for charged AdS black holes. *JHEP*, 08:174, 2022.

[104] Wan Cong, Chen Qian, Michael R.R. Good, and Robert B. Mann. Effects of horizons on entanglement harvesting. *J. High Energy Phys.*, 10(2020):067, Oct 2020.

[105] Wan Cong, Erickson Tjoa, and Robert B Mann. Entanglement harvesting with moving mirrors. *J. High Energy Phys.*, 06(2019):021, 2019.

[106] Aindriú Conroy and Peter Taylor. Response of an unruh-dewitt detector near an extremal black hole. *Phys. Rev. D*, 105:085001, Apr 2022.

[107] Luís C. B. Crispino, Atsushi Higuchi, and George E. A. Matsas. The Unruh effect and its applications. *Rev. Mod. Phys.*, 80:787–838, Jul 2008.

[108] Hong-Ming Cui and Zhong-Ying Fan. Critical phenomenon of quantum BTZ black holes. 5 2025.

[109] M. Cvetic, G. W. Gibbons, D. Kubiznak, and C. N. Pope. Black Hole Enthalpy and an Entropy Inequality for the Thermodynamic Volume. *Phys. Rev. D*, 84:024037, 2011.

[110] Sergio Dain, Marcus Khuri, Gilbert Weinstein, and Sumio Yamada. Lower Bounds for the Area of Black Holes in Terms of Mass, Charge, and Angular Momentum. *Phys. Rev. D*, 88:024048, 2013.

[111] Ester Dalvit. Punctured Torus. https://www.youtube.com/watch?v=P5RLa3g-nwQ, September 2010.

[112] Saurya Das and Robert B. Mann. Conserved quantities in Kerr-anti-de Sitter space-times in various dimensions. *JHEP*, 08:033, 2000.

[113] P. C. W. Davies and Adrian C. Ottewill. Detection of negative energy: 4-dimensional examples. *Phys. Rev. D*, 65:104014, May 2002.

[114] Sebastian de Haro, Kostas Skenderis, and Sergey N. Solodukhin. Gravity in warped compactifications and the holographic stress tensor. *Class. Quant. Grav.*, 18:3171–3180, 2001.

[115] Sebastian de Haro, Sergey N. Solodukhin, and Kostas Skenderis. Holographic reconstruction of space-time and renormalization in the AdS / CFT correspondence. *Commun. Math. Phys.*, 217:595–622, 2001.

[116] Lissa de Souza Campos and Claudio Dappiaggi. The anti-hawking effect on a btz black hole with robin boundary conditions. *Physics Letters B*, 816:136198, 2021.

[117] Robert Debever. On type d expanding solutions of einstein-maxwell equations. *Bulletin de la Société mathématique de Belgique*, 23:360–376, 1971.

[118] Marco del Rey, Diego Porras, and Eduardo Martín-Martínez. Simulating accelerated atoms coupled to a quantum field. *Phys. Rev. A*, 85:022511, Feb 2012.

[119] B. S. DeWitt. Quantum gravity: The new synthesis. In S. W. Hawking and W. Israel, editors, *General Relativity: An Einstein Centenary Survey*, pages 680–745. Cambridge University Press, Cambridge, England, 1979.

[120] Oscar J. C. Dias and Jose P. S. Lemos. Pair of accelerated black holes in anti-de Sitter background: AdS C metric. *Phys. Rev. D*, 67:064001, 2003.

[121] Robbert Dijgraaf, Herman Verlinde, and Erik Verlinde. String propagation in black hole geometry. *Nuclear Physics B*, 371(1-2):269–314, 1992.

[122] *NIST Digital Library of Mathematical Functions.* http://dlmf.nist.gov/, Release 1.0.27 of 2020-06-15. F. W. J. Olver, A. B. Olde Daalhuis, D. W. Lozier, B. I. Schneider, R. F. Boisvert, C. W. Clark, B. R. Miller, B. V. Saunders, H. S. Cohl, and M. A. McClain, eds.

[123] Brian P. Dolan. The cosmological constant and the black hole equation of state. *Class. Quant. Grav.*, 28:125020, 2011.

[124] Brian P. Dolan, Anna Kostouki, David Kubiznak, and Robert B. Mann. Isolated critical point from Lovelock gravity. *Class. Quant. Grav.*, 31(24):242001, 2014.

[125] Daniela D. Doneva and Stoytcho S. Yazadjiev. New Gauss-Bonnet Black Holes with Curvature-Induced Scalarization in Extended Scalar-Tensor Theories. *Phys. Rev. Lett.*, 120(13):131103, 2018.

[126] Xi Dong. Holographic Entanglement Entropy for General Higher Derivative Gravity. *JHEP*, 01:044, 2014.

[127] Jason Doukas and Benedict Carson. Entanglement of two qubits in a relativistic orbit. *Phys. Rev. A*, 81:062320, Jun 2010.

[128] Tevian Dray and Gerard 't Hooft. The gravitational shock wave of a massless particle. *Nucl. Phys.*, B253:173–188, 1985.

[129] M. J. Duff. Quantum corrections to the schwarzschild solution. *Phys. Rev. D*, 9:1837–1839, Mar 1974.

[130] M. J. Duff and James T. Liu. Complementarity of the Maldacena and Randall-Sundrum pictures. *Phys. Rev. Lett.*, 85:2052–2055, 2000.

[131] Hannah Dykaar, Robie A. Hennigar, and Robert B. Mann. Hairy black holes in cubic quasi-topological gravity. *JHEP*, 05:045, 2017.

[132] Roberto Emparan. Predictivity lost, predictivity regained: a Miltonian cosmic censorship conjecture. *Int. J. Mod. Phys. D*, 29(14):2043021, 2020.

[133] Roberto Emparan, Alessandro Fabbri, and Nemanja Kaloper. Quantum black holes as holograms in AdS brane worlds. *JHEP*, 08:043, 2002.

[134] Roberto Emparan, Antonia Micol Frassino, and Benson Way. Quantum BTZ black hole. *JHEP*, 11:137, 2020.

[135] Roberto Emparan, Gary T. Horowitz, and Robert C. Myers. Exact description of black holes on branes. *JHEP*, 01:007, 2000.

[136] Roberto Emparan, Gary T. Horowitz, and Robert C. Myers. Exact description of black holes on branes. 2. Comparison with BTZ black holes and black strings. *JHEP*, 01:021, 2000.

[137] Roberto Emparan, Clifford V. Johnson, and Robert C. Myers. Surface terms as counterterms in the AdS / CFT correspondence. *Phys. Rev. D*, 60:104001, 1999.

[138] Roberto Emparan and Javier M. Magan. Tearing down spacetime with quantum disentanglement. *JHEP*, 03:078, 2024.

[139] Roberto Emparan, Juan F. Pedraza, Andrew Svesko, Marija Tomašević, and Manus R. Visser. Black holes in dS_3. *JHEP*, 11:073, 2022.

[140] Netta Engelhardt and Åsmund Folkestad. Holography abhors visible trapped surfaces. *JHEP*, 07:066, 2021.

[141] Netta Engelhardt, Åsmund Folkestad, Adam Levine, Evita Verheijden, and Lisa Yang. Cryptographic Censorship. *JHEP*, 01:122, 2025.

[142] Netta Engelhardt and Gary T. Horowitz. Holographic argument for the Penrose inequality in AdS spacetimes. *Phys. Rev. D*, 99(12):126009, 2019.

[143] Netta Engelhardt and Aron C. Wall. Quantum Extremal Surfaces: Holographic Entanglement Entropy beyond the Classical Regime. *JHEP*, 01:073, 2015.

[144] Valerio Faraoni and Edgard Gunzig. Tales of tails in cosmology. *Int. J. Mod. Phys. D*, 08(02):177–188, 1999.

[145] Thomas Faulkner, Aitor Lewkowycz, and Juan Maldacena. Quantum corrections to holographic entanglement entropy. *JHEP*, 11:074, 2013.

[146] Charles Fefferman and C. Robin Graham. The ambient metric, 2008.

[147] Yiji Feng, Hao Ma, Robert B. Mann, Yesheng Xue, and Ming Zhang. Quantum charged black holes. *JHEP*, 08:184, 2024.

[148] Åsmund Folkestad. Penrose Inequality as a Constraint on the Low Energy Limit of Quantum Gravity. *Phys. Rev. Lett.*, 130(12):121501, 2023.

[149] Joshua Foo, Sho Onoe, Robert B. Mann, and Magdalena Zych. Thermality, causality and the quantum-controlled unruh-dewitt detector. 2020.

[150] Joshua Foo, Sho Onoe, and Magdalena Zych. Unruh-dewitt detectors in quantum superpositions of trajectories. *Phys. Rev. D*, 102:085013, Oct 2020.

[151] P. Francesco, P. Mathieu, and D. Senechal. *Conformal Field Theory*. Graduate Texts in Contemporary Physics. Springer New York, 2012.

[152] J. D. Franson. Generation of entanglement outside of the light cone. *Journal of Modern Optics*, 55(13):2117–2140, 2008.

[153] Antonia M. Frassino, Robie A. Hennigar, Juan F. Pedraza, and Andrew Svesko. Quantum Inequalities for Quantum Black Holes. *Phys. Rev. Lett.*, 133(18):181501, 2024.

[154] Antonia M. Frassino, Robie A. Hennigar, Juan F. Pedraza, and Andrew Svesko. Quantum censors: backreaction builds horizons. 5 2025.

[155] Antonia M. Frassino, Robert B. Mann, and Jonas R. Mureika. Lower-Dimensional Black Hole Chemistry. *Phys. Rev. D*, 92(12):124069, 2015.

[156] Antonia M. Frassino, Juan F. Pedraza, Andrew Svesko, and Manus R. Visser. Higher-Dimensional Origin of Extended Black Hole Thermodynamics. *Phys. Rev. Lett.*, 130(16):161501, 2023.

[157] Antonia M. Frassino, Juan F. Pedraza, Andrew Svesko, and Manus R. Visser. Reentrant phase transitions of quantum black holes. *Phys. Rev. D*, 109(12):124040, 2024.

[158] Antonia M. Frassino, Jorge V. Rocha, and Andrea P. Sanna. Weak cosmic censorship and the rotating quantum BTZ black hole. *JHEP*, 07:226, 2024.

[159] Valeri P. Frolov. Notes on nonsingular models of black holes. *Phys. Rev. D*, 94:104056, Nov 2016.

[160] C. Fronsdal. Completion and embedding of the Schwarzschild solution. *Phys. Rev.*, 116:778–781, Nov 1959.

[161] I. Fuentes-Schuller and R. B. Mann. Alice falls into a black hole: Entanglement in noninertial frames. *Phys. Rev. Lett.*, 95:120404, Sep 2005.

[162] Mitsutoshi Fujita, Tadashi Takayanagi, and Erik Tonni. Aspects of AdS/BCFT. *JHEP*, 11:043, 2011.

[163] Masafumi Fukuma, Sotaro Sugishita, and Yuho Sakatani. Master equation for the Unruh-DeWitt detector and the universal relaxation time in de Sitter space. *Phys. Rev. D*, 89:064024, Mar 2014.

[164] Kensuke Gallock-Yoshimura and Robert B. Mann. Entangled detectors nonperturbatively harvest mutual information. *Phys. Rev. D*, 104:125017, Dec 2021.

[165] Kensuke Gallock-Yoshimura, Erickson Tjoa, and Robert B. Mann. Harvesting entanglement with detectors freely falling into a black hole. *Phys. Rev. D*, 104:025001, Jul 2021.

[166] Luis J. Garay, Eduardo Martín-Martínez, and José de Ramón. Thermalization of particle detectors: The Unruh effect and its reverse. *Phys. Rev. D*, 94:104048, Nov 2016.

[167] Hao Geng and Andreas Karch. Massive islands. *JHEP*, 09:121, 2020.

[168] Hao Geng, Andreas Karch, Carlos Perez-Pardavila, Suvrat Raju, Lisa Randall, Marcos Riojas, and Sanjit Shashi. Information Transfer with a Gravitating Bath. *SciPost Phys.*, 10(5):103, 2021.

[169] Hao Geng, Andreas Karch, Carlos Perez-Pardavila, Suvrat Raju, Lisa Randall, Marcos Riojas, and Sanjit Shashi. Entanglement phase structure of a holographic BCFT in a black hole background. *JHEP*, 05:153, 2022.

[170] Hao Geng, Lisa Randall, and Erik Swanson. BCFT in a black hole background: an analytical holographic model. *JHEP*, 12:056, 2022.

[171] G. W. Gibbons and S. W. Hawking. Action Integrals and Partition Functions in Quantum Gravity. *Phys. Rev. D*, 15:2752–2756, 1977.

[172] G. W. Gibbons and S. W. Hawking. Cosmological event horizons, thermodynamics, and particle creation. *Phys. Rev. D*, 15:2738–2751, May 1977.

[173] Ting-Feng Gong, Jie Jiang, and Ming Zhang. Holographic thermodynamics of rotating black holes. *JHEP*, 06:105, 2023.

[174] Kanato Goto and Yoichi Kazama. On the observer dependence of the Hilbert space near the horizon of black holes. *Prog. Theor. Exp. Phys.*, 2019(2), 02 2019. 023B01.

[175] I. S. Gradshteyn and I. M. Ryzhik. *Table of Integrals, Series, and Products*. Academic Press, 2014.

[176] Finnian Gray, David Kubizňák, Taillte May, Sydney Timmerman, and Erickson Tjoa. Quantum imprints of gravitational shockwaves. *J. High Energy Phys.*, 11(2021):054, 2021.

[177] Finnian Gray, David Kubizňák, Taillte May, Sydney Timmerman, and Erickson Tjoa. Quantum imprints of gravitational shockwaves. *Journal of High Energy Physics*, 2021(11), November 2021.

[178] Ruth Gregory. Braneworld black holes. *Lect. Notes Phys.*, 769:259–298, 2009.

[179] Ruth Gregory and Andrew Scoins. Accelerating Black Hole Chemistry. *Phys. Lett. B*, 796:191–195, 2019.

[180] Ruth Gregory, Richard Whisker, Kris Beckwith, and Chris Done. Observing braneworld black holes. *JCAP*, 10:013, 2004.

[181] J. B. Griffiths and J. Podolsky. A New look at the Plebanski-Demianski family of solutions. *Int. J. Mod. Phys. D*, 15:335–370, 2006.

[182] Jerry B Griffiths and Jiří Podolskỳ. *Exact space-times in Einstein's general relativity*. Cambridge University Press, 2009.

[183] Guglielmo Grimaldi, Juan Hernandez, and Robert C. Myers. Quantum extremal islands made easy. Part IV. Massive black holes on the brane. *JHEP*, 03:136, 2022.

[184] Steven S. Gubser. AdS / CFT and gravity. *Phys. Rev. D*, 63:084017, 2001.

[185] Steven S. Gubser and Indrajit Mitra. The Evolution of unstable black holes in anti-de Sitter space. *JHEP*, 08:018, 2001.

[186] Rudolf Haag. *Local Quantum Physics*. Theoretical and Mathematical Physics. Springer, Berlin, 1996.

[187] Rudolf Haag and Daniel Kastler. An algebraic approach to quantum field theory. *J. Math. Phys.*, 5(7):848–861, 1964.

[188] Sasha Haco, Stephen W Hawking, Malcolm J Perry, and Andrew Strominger. Black hole entropy and soft hair. *J. High Energy Phys.*, 2018(12):98, 2018.

[189] Tomáš Hale, David Kubizňák, Jana Menšíková, Robert B. Mann, and Jiayue Yang. Thermodynamics of charged and accelerating black holes. *Phys. Rev. D*, 111(10):104004, 2025.

[190] J. B. Hartle and S. W. Hawking. Path Integral Derivation of Black Hole Radiance. *Phys. Rev. D*, 13:2188–2203, 1976.

[191] Allen Hatcher. *Algebraic Topology*. Cambridge University Press, 2002.

[192] S. W. Hawking. Particle Creation by Black Holes. *Commun. Math. Phys.*, 43:199–220, 1975. [Erratum: Commun.Math.Phys. 46, 206 (1976)].

[193] S. W. Hawking. Breakdown of Predictability in Gravitational Collapse. *Phys. Rev. D*, 14:2460–2473, 1976.

[194] Stephen W. Hawking and George F. R. Ellis. *The Large Scale Structure of Space-Time*. Cambridge University Press, 1973.

[195] S.W. Hawking. Particle creation by black holes. *Communications in Mathematical Physics*, 43(3):199–220, 1975.

[196] Sean A. Hayward. Formation and evaporation of nonsingular black holes. *Phys. Rev. Lett.*, 96:031103, Jan 2006.

[197] L Henderson and V Vedral. Classical, quantum and total correlations. *J. Phys. A*, 34(35):6899–6905, aug 2001.

[198] Laura J. Henderson. *What can detectors detect?* PhD thesis, Waterloo U., 2021.

[199] Laura J. Henderson, Alessio Belenchia, Esteban Castro-Ruiz, Costantino Budroni, Magdalena Zych, Časlav Brukner, and Robert B. Mann. Quantum temporal superposition: The case of quantum field theory. *Phys. Rev. Lett.*, 125:131602, Sep 2020.

[200] Laura J. Henderson, Su Yu Ding, and Robert B. Mann. Entanglement harvesting with a twist. *AVS Quantum Sci.*, 4(1):014402, 2022.

[201] Laura J. Henderson, Robie A. Hennigar, Robert B. Mann, Alexander R. H. Smith, and Jialin Zhang. Harvesting Entanglement from the Black Hole Vacuum. *Class. Quant. Grav.*, 35(21):21LT02, 2018.

[202] Laura J Henderson, Robie A Hennigar, Robert B Mann, Alexander R H Smith, and Jialin Zhang. Harvesting entanglement from the black hole vacuum. *Classical Quantum Gravity*, 35(21):21LT02, oct 2018.

[203] Laura J Henderson, Robie A Hennigar, Robert B Mann, Alexander RH Smith, and Jialin Zhang. Entangling detectors in anti-de Sitter space. *J. High Energy Phys.*, 05(2019):178, 2019.

[204] Laura J. Henderson, Robie A. Hennigar, Robert B. Mann, Alexander R.H. Smith, and Jialin Zhang. Anti-hawking phenomena. *Physics Letters B*, 809:135732, 2020.

[205] M. Henneaux and C. Teitelboim. Asymptotically anti-De Sitter Spaces. *Commun. Math. Phys.*, 98:391–424, 1985.

[206] Robie A. Hennigar. *Explorations in black hole chemistry and higher curvature gravity.* PhD thesis, Waterloo U., 2018.

[207] Robie A. Hennigar, David Kubizňák, and Robert B. Mann. Entropy Inequality Violations from Ultraspinning Black Holes. *Phys. Rev. Lett.*, 115(3):031101, 2015.

[208] Robie A. Hennigar, Erickson Tjoa, and Robert B. Mann. Thermodynamics of hairy black holes in Lovelock gravity. *JHEP*, 02:070, 2017.

[209] Juan Hernandez, Robert C. Myers, and Shan-Ming Ruan. Quantum extremal islands made easy. Part III. Complexity on the brane. *JHEP*, 02:173, 2021.

[210] Lee Hodgkinson. Particle detectors in curved spacetime quantum field theory. *arXiv:1309.7281*, 2013.

[211] Lee Hodgkinson and Jorma Louko. Static, stationary and inertial Unruh-DeWitt detectors on the BTZ black hole. *Phys. Rev. D*, 86:064031, 2012.

[212] Lee Hodgkinson and Jorma Louko. Static, stationary, and inertial Unruh-DeWitt detectors on the BTZ black hole. *Phys. Rev. D*, 86:064031, Sep 2012.

[213] Lee Hodgkinson, Jorma Louko, and Adrian C. Ottewill. Static detectors and circular-geodesic detectors on the Schwarzschild black hole. *Phys. Rev. D*, 89:104002, May 2014.

[214] Michael Horodecki, Peter W. Shor, and Mary Beth Ruskai. Entanglement breaking channels. *Rev. Math. Phys.*, 15(06):629–641, 2003.

[215] Michał Horodecki, Paweł Horodecki, and Ryszard Horodecki. Separability of mixed states: necessary and sufficient conditions. *Phys. Lett. A*, 223(1):1–8, 1996.

[216] Michał Horodecki, Paweł Horodecki, and Ryszard Horodecki. Separability of mixed states: necessary and sufficient conditions. *Physics Letters A*, 223(1–2):1–8, November 1996.

[217] Gary T. Horowitz and Joseph Polchinski. Gauge/gravity duality. pages 169–186, 2 2006.

[218] Seyed Ali Hosseini Mansoori, Juan F. Pedraza, and Morteza Rafiee. Criticality and thermodynamic geometry of quantum BTZ black holes. *Phys. Rev. D*, 111(2):024012, 2025.

[219] Masahiro Hotta. Quantum measurement information as a key to energy extraction from local vacuums. *Phys. Rev. D*, 78:045006, Aug 2008.

[220] Masahiro Hotta, Achim Kempf, Eduardo Martín-Martínez, Takeshi Tomitsuka, and Koji Yamaguchi. Duality in dynamics of Unruh-DeWitt detectors in conformally related spacetimes. 2020.

[221] B L Hu, Shih-Yuin Lin, and Jorma Louko. Relativistic quantum information in detectors–field interactions. *Classical and Quantum Gravity*, 29(22):224005, oct 2012.

[222] Ya-Peng Hu, Yu-Sen An, Gao-Yong Sun, Wen-Long You, Da-Ning Shi, Hongsheng Zhang, Xiaosong Chen, and Rong-Gen Cai. Quantum anomaly triggers the violation of scaling laws in gravitational system. 10 2024.

[223] Veronika E. Hubeny. Overcharging a black hole and cosmic censorship. *Phys. Rev. D*, 59:064013, 1999.

[224] Veronika E. Hubeny. The AdS/CFT Correspondence. *Class. Quant. Grav.*, 32(12):124010, 2015.

[225] Veronika E. Hubeny, Mukund Rangamani, and Tadashi Takayanagi. A Covariant holographic entanglement entropy proposal. *JHEP*, 07:062, 2007.

[226] Daniel Hümmer, Eduardo Martín-Martínez, and Achim Kempf. Renormalized Unruh-DeWitt particle detector models for boson and fermion fields. *Phys. Rev. D*, 93:024019, Jan 2016.

[227] Luca V. Iliesiu and Gustavo J. Turiaci. The statistical mechanics of near-extremal black holes. *JHEP*, 05:145, 2021.

[228] Wolfram Research, Inc. Mathematica, Version 10.0. Champaign, IL, 2020.

[229] W. Israel. Singular hypersurfaces and thin shells in general relativity. *Nuovo Cim. B*, 44S10:1, 1966. [Erratum: Nuovo Cim.B 48, 463 (1967)].

[230] W. Israel. Thermo field dynamics of black holes. *Phys. Lett. A*, 57:107–110, 1976.

[231] David Jennings. On the response of a particle detector in Anti-de Sitter spacetime. *Class. Quant. Grav.*, 27:205005, 2010.

[232] Clifford V. Johnson. Instability of super-entropic black holes in extended thermodynamics. *Mod. Phys. Lett. A*, 35(13):2050098, 2020.

[233] Clifford V. Johnson, Victoria L. Martin, and Andrew Svesko. Microscopic description of thermodynamic volume in extended black hole thermodynamics. *Phys. Rev. D*, 101(8):086006, 2020.

[234] Robert H Jonsson. Quantum signaling in relativistic motion and across acceleration horizons. *Journal of Physics A: Mathematical and Theoretical*, 50(35):355401, 2017.

[235] Robert H. Jonsson, David Q. Aruquipa, Marc Casals, Achim Kempf, and Eduardo Martín-Martínez. Communication through quantum fields near a black hole. 2 2020.

[236] Robert H. Jonsson, David Q. Aruquipa, Marc Casals, Achim Kempf, and Eduardo Martín-Martínez. Communication through quantum fields near a black hole. 2020.

[237] Robert H. Jonsson, Eduardo Martín-Martínez, and Achim Kempf. Quantum signaling in cavity QED. *Phys. Rev. A*, 89:022330, Feb 2014.

[238] Robert H. Jonsson, Eduardo Martín-Martínez, and Achim Kempf. Quantum signaling in cavity QED. *Phys. Rev. A*, 89:022330, Feb 2014.

[239] Robert H. Jonsson, Eduardo Martín-Martínez, and Achim Kempf. Information transmission without energy exchange. *Phys. Rev. Lett.*, 114:110505, Mar 2015.

[240] Benito A Juárez-Aubry and Jorma Louko. Onset and decay of the 1+1 Hawking-Unruh effect: What the derivative-coupling detector saw. *Classical and Quantum Gravity*, 31(24):245007, nov 2014.

[241] Benito A. Juárez-Aubry and Jorma Louko. Quantum fields during black hole formation: How good an approximation is the Unruh state? *J. High Energy Phys.*, 05(2018):140, May 2018.

[242] Wolfgang Junker and Elmar Schrohe. Adiabatic vacuum states on general spacetime manifolds: Definition, construction, and physical properties. *Annales Henri Poincaré*, 3:1113–1182, 2002.

[243] Andreas Karch and Lisa Randall. Locally localized gravity. *JHEP*, 05:008, 2001.

[244] Andreas Karch and Lisa Randall. Open and closed string interpretation of SUSY CFT's on branes with boundaries. *JHEP*, 06:063, 2001.

[245] Andreas Karch and Brandon Robinson. Holographic Black Hole Chemistry. *JHEP*, 12:073, 2015.

[246] Andreas Karch, Haoyu Sun, and Christoph F. Uhlemann. Double holography in string theory. *JHEP*, 10:012, 2022.

[247] David Kastor, Sourya Ray, and Jennie Traschen. Enthalpy and the Mechanics of AdS Black Holes. *Class. Quant. Grav.*, 26:195011, 2009.

[248] Bernard S. Kay and Robert M. Wald. Theorems on the Uniqueness and Thermal Properties of Stationary, Nonsingular, Quasifree States on Space-Times with a Bifurcate Killing Horizon. *Phys. Rept.*, 207:49–136, 1991.

[249] Igor Khavkine and Valter Moretti. *Algebraic QFT in Curved Spacetime and Quasifree Hadamard States: An Introduction*, pages 191–251. Springer International Publishing, Cham, 2015.

[250] W. Kinnersley and M. Walker. Uniformly accelerating charged mass in general relativity. *Phys. Rev. D*, 2:1359–1370, 1970.

[251] Klaus Kirsten and Jaume Garriga. Massless minimally coupled fields in de Sitter space: $O(4)$-symmetric states versus de Sitter–invariant vacuum. *Phys. Rev. D*, 48:567–577, Jul 1993.

[252] Sanved Kolekar and Jorma Louko. Gravitational memory for uniformly accelerated observers. *Phys. Rev. D*, 96:024054, Jul 2017.

[253] Sanved Kolekar and Jorma Louko. Quantum memory for rindler supertranslations. *Phys. Rev. D*, 97:085012, Apr 2018.

[254] Theodora Kolioni and Charis Anastopoulos. Detectors interacting through quantum fields: Non-Markovian effects, non-perturbative generation of correlations and apparent non-causality. 2019.

[255] Nikolai E. Korotkov and Alexander N. Korotkov. *Integrals Related to the Error Function*. Chapman and Hall/CRC, 2020.

[256] George T. Kottanattu and Jorma Louko. Topological geon black holes in Einstein-Yang-Mills theory. *Commun. Math. Phys.*, 303:127–148, 2011.

[257] Per Kraus, Finn Larsen, and Ruud Siebelink. The gravitational action in asymptotically AdS and flat space-times. *Nucl. Phys. B*, 563:259–278, 1999.

[258] M. D. Kruskal. Maximal extension of Schwarzschild metric. *Phys. Rev.*, 119:1743–1745, Sep 1960.

[259] David Kubiznak and Robert B. Mann. P-V criticality of charged AdS black holes. *JHEP*, 07:033, 2012.

[260] David Kubiznak and Robert B. Mann. Black hole chemistry. *Can. J. Phys.*, 93(9):999–1002, 2015.

[261] David Kubiznak, Robert B. Mann, and Mae Teo. Black hole chemistry: thermodynamics with Lambda. *Class. Quant. Grav.*, 34(6):063001, 2017.

[262] Ryogo Kubo. Statistical-mechanical theory of irreversible processes. i. general theory and simple applications to magnetic and conduction problems. *Journal of the Physical Society of Japan*, 12(6):570–586, 1957.

[263] Hideaki Kudoh and Yasunari Kurita. Thermodynamics of four-dimensional black objects in the warped compactification. *Phys. Rev. D*, 70:084029, 2004.

[264] S. Kukita and Y. Nambu. Harvesting large scale entanglement in de Sitter space with multiple detectors. *Entropy*, 19(9):449, Aug 2017.

[265] Hari K. Kunduri, Juan Margalef-Bentabol, and Sarah Muth. The Penrose inequality in spherical symmetry with charge and in Gauss-Bonnet gravity. 9 2024.

[266] André G. S. Landulfo. Nonperturbative approach to relativistic quantum communication channels. *Phys. Rev. D*, 93:104019, May 2016.

[267] André G. S. Landulfo and George E. A. Matsas. Sudden death of entanglement and teleportation fidelity loss via the Unruh effect. *Phys. Rev. A*, 80:032315, Sep 2009.

[268] Paul Langlois. *Imprints of spacetime topology in the Hawking-Unruh effect*. PhD thesis, University of Nottingham, 10 2005.

[269] Paul Langlois. Imprints of spacetime topology in the hawking-unruh effect. 2005.

[270] Paul Langlois. Causal particle detectors and topology. *Annals Phys.*, 321:2027–2070, 2006.

[271] Adam Lewandowski. The Wilsonian renormalization group in Randall-Sundrum 1. *Phys. Rev. D*, 71:024006, 2005.

[272] Aitor Lewkowycz and Juan Maldacena. Generalized gravitational entropy. *JHEP*, 08:090, 2013.

[273] Gilad Lifschytz and Miguel Ortiz. Scalar field quantization on the (2+1)-dimensional black hole background. *Phys. Rev. D*, 49:1929–1943, Feb 1994.

[274] Feng-Li Lin and Sayid Mondal. Entanglement harvesting and quantum discord of alpha vacua in de Sitter space. *JHEP*, 08:159, 2024.

[275] Shih-Yuin Lin. Notes on nonlocal projective measurements in relativistic systems. *Annals of Physics*, 351:773 – 786, 2014.

[276] Shih-Yuin Lin, Chung-Hsien Chou, and B. L. Hu. Disentanglement of two harmonic oscillators in relativistic motion. *Phys. Rev. D*, 78:125025, Dec 2008.

[277] Shih-Yuin Lin, Chung-Hsien Chou, and B. L. Hu. Quantum teleportation between moving detectors. *Phys. Rev. D*, 91:084063, Apr 2015.

[278] Shih-Yuin Lin, Chung-Hsien Chou, and B. L. Hu. Entanglement dynamics of detectors in an Einstein cylinder. *J. High Energ. Phys.*, 2016(3):47, Mar 2016.

[279] Shih-Yuin Lin and B. L. Hu. Temporal and spatial dependence of quantum entanglement from a field theory perspective. *Phys. Rev. D*, 79:085020, Apr 2009.

[280] Yi Ling, Yuxuan Liu, and Zhuo-Yu Xian. Island in Charged Black Holes. *JHEP*, 03:251, 2021.

[281] Zhihong Liu, Jialin Zhang, Robert B. Mann, and Hongwei Yu. Does acceleration assist entanglement harvesting? *Phys. Rev. D*, 105(8):085012, 2022.

[282] Zhihong Liu, Jialin Zhang, Robert B. Mann, and Hongwei Yu. Does acceleration assist entanglement harvesting? *Phys. Rev. D*, 105:085012, Apr 2022.

[283] Richard Lopp, Eduardo Martín-Martínez, and Don N. Page. Relativity and quantum optics: accelerated atoms in optical cavities. *Classical and Quantum Gravity*, 35(22):224001, 2018.

[284] Krzysztof Lorek, Daniel Pecak, Eric G. Brown, and Andrzej Dragan. Extraction of genuine tripartite entanglement from the vacuum. *Phys. Rev. A*, 90:032316, Sep 2014.

[285] Jorma Louko. Geon black holes and quantum field theory. *J. Phys. Conf. Ser.*, 222:012038, 2010.

[286] Jorma Louko. Unruh-DeWitt detector response across a Rindler firewall is finite. *J. High Energ. Phys.*, 2014(9):142, 2014.

[287] Jorma Louko, Robert B Mann, and Donald Marolf. Geons with spin and charge. *Class. Quantum Grav.*, 22(7):1451–1467, mar 2005.

[288] Jorma Louko and Donald Marolf. Inextendible Schwarzschild black hole with a single exterior: How thermal is the Hawking radiation? *Phys. Rev. D*, 58:024007, 1998.

[289] Jorma Louko and Donald Marolf. Inextendible schwarzschild black hole with a single exterior: How thermal is the hawking radiation? *Phys. Rev. D*, 58:024007, Jun 1998.

[290] Jorma Louko and Donald Marolf. Single exterior black holes and the AdS/CFT conjecture. *Phys. Rev. D*, 59:066002, 1999.

[291] Jorma Louko, Donald Marolf, and Simon F. Ross. On geodesic propagators and black hole holography. *Phys. Rev. D*, 62:044041, 2000.

[292] Jorma Louko and Alejandro Satz. How often does the Unruh-DeWitt detector click? Regularisation by a spatial profile . *Classical and Quantum Gravity*, 23:6321–6343, 2006.

[293] Jorma Louko and Alejandro Satz. Transition rate of the Unruh-DeWitt detector in curved spacetime . *Classical and Quantum Gravity*, 25:055012, 2007.

[294] Jorma Louko and Alejandro Satz. Transition rate of the Unruh-DeWitt detector in curved spacetime. *Class. Quantum Grav.*, 25:055012, 2008.

[295] Jorma Louko and Vladimir Toussaint. Unruh-DeWitt detector's response to fermions in flat spacetimes. *Phys. Rev. D*, 94:064027, Sep 2016.

[296] Jorma Louko and Vladimir Toussaint. Unruh-DeWitt detector's response to fermions in flat spacetimes. *Phys. Rev. D*, 94:064027, Sep 2016.

[297] Jorma Louko and Vladimir Toussaint. Unruh-DeWitt fermion detector on a (1+ 1)-dimensional cylindrical spacetime: Arbitrary worldlines and inequivalent spin structures. 2016.

[298] C.O. Loustó and N. Sánchez. Gravitational shock waves generated by extended sources: ultrarelativistic cosmic strings, monopoles and domain walls. *Nucl. Phys.*, B355(1):231–249, 1991.

[299] Kai-Peng Lu, Peng-Yu Wu, and H. Lu. WCCC in Gedankenexperiments at All Orders. 2 2025.

[300] Héctor Maeso-García, José Polo-Gómez, and Eduardo Martín-Martínez. Entanglement harvesting: State dependence and covariance. *Phys. Rev. D*, 106:105001, Nov 2022.

[301] Juan Martin Maldacena. The Large N limit of superconformal field theories and supergravity. *Adv. Theor. Math. Phys.*, 2:231–252, 1998.

[302] Robinson Mancilla. Generalized Euler Equation from Effective Action: Implications for the Smarr Formula in AdS Black Holes. 10 2024.

[303] Robert B. Mann. Pair production of topological anti-de Sitter black holes. *Class. Quant. Grav.*, 14:L109–L114, 1997.

[304] Robert B. Mann. Misner string entropy. *Phys. Rev. D*, 60:104047, 1999.

[305] Robert B. Mann. Recent Developments in Holographic Black Hole Chemistry. *JHAP*, 4(1):1–26, 2024.

[306] Robert B. Mann. Black hole chemistry: The first 15 years. *Int. J. Mod. Phys. D*, 34(09):2542001, 2025.

[307] Donald Marolf. The black hole information problem: Past, present, and future. *Rep. Prog. Phys.*, 80(9):092001, jul 2017.

[308] Donald Marolf and Aron C. Wall. State-dependent divergences in the entanglement entropy. *Journal of High Energy Physics*, 2016(10):109, 2016.

[309] Marc Mars. Present status of the Penrose inequality. *Class. Quant. Grav.*, 26:193001, 2009.

[310] Karl Martel and Eric Poisson. Regular coordinate systems for Schwarzschild and other spherical spacetimes. *Am. J. Phys.*, 69(4):476–480, 2001.

[311] Paul C. Martin and Julian Schwinger. Theory of many-particle systems. i. *Phys. Rev.*, 115:1342–1373, Sep 1959.

[312] Eduardo Martín-Martínez. Causality issues of particle detector models in QFT and quantum optics. *Phys. Rev. D*, 92:104019, Nov 2015.

[313] Eduardo Martín-Martínez, Eric G. Brown, William Donnelly, and Achim Kempf. Sustainable entanglement production from a quantum field. *Phys. Rev. A*, 88:052310, Nov 2013.

[314] Eduardo Martín-Martínez, Luis J. Garay, and Juan León. Unveiling quantum entanglement degradation near a schwarzschild black hole. *Phys. Rev. D*, 82:064006, Sep 2010.

[315] Eduardo Martín-Martínez and Juan León. Fermionic entanglement that survives a black hole. *Phys. Rev. A*, 80:042318, Oct 2009.

[316] Eduardo Martín-Martínez and Jorma Louko. Particle detectors and the zero mode of a quantum field. *Phys. Rev. D*, 90:024015, Jul 2014.

[317] Eduardo Martín-Martínez and Jorma Louko. $(1+1)$D calculation provides evidence that quantum entanglement survives a firewall. *Phys. Rev. Lett.*, 115:031301, Jul 2015.

[318] Eduardo Martín-Martínez, Miguel Montero, and Marco del Rey. Wavepacket detection with the unruh-dewitt model. *Phys. Rev. D*, 87:064038, Mar 2013.

[319] Eduardo Martín-Martínez, T. Rick Perche, and Bruno de S. L. Torres. Broken covariance of particle detector models in relativistic quantum information. 2020.

[320] Eduardo Martín-Martínez, T. Rick Perche, and Bruno de S. L. Torres. General relativistic quantum optics: Finite-size particle detector models in curved spacetimes. *Phys. Rev. D*, 101:045017, Feb 2020.

[321] Eduardo Martín-Martínez, T. Rick Perche, and Bruno de S. L. Torres. Broken covariance of particle detector models in relativistic quantum information. *Phys. Rev. D*, 103:025007, Jan 2021.

[322] Eduardo Martín-Martínez and Pablo Rodriguez-Lopez. Relativistic quantum optics: The relativistic invariance of the light-matter interaction models. *Phys. Rev. D*, 97:105026, May 2018.

[323] Eduardo Martín-Martínez and Pablo Rodriguez-Lopez. Relativistic quantum optics: The relativistic invariance of the light-matter interaction models. *Phys. Rev. D*, 97:105026, May 2018.

[324] Eduardo Martín-Martínez, Alexander R. H. Smith, and Daniel R. Terno. Spacetime structure and vacuum entanglement. *Phys. Rev. D*, 93:044001, Feb 2016.

[325] Cristian Martinez, Claudio Teitelboim, and Jorge Zanelli. Charged rotating black hole in three space-time dimensions. *Phys. Rev. D*, 61:104013, 2000.

[326] Sabyasachi Maulik, Xin Meng, and Leopoldo A. Pando Zayas. Quantum-Corrected Hawking Radiation from Near-Extremal Kerr-Newman Black Holes. 1 2025.

[327] Kirill Melnikov and Marvin Weinstein. On the evolution of a massless scalar field in a schwarzschild background: A new look at hawking radiation and the information paradox. *Int. J. Mod. Phys. D*, 13(08):1595–1635, 2004.

[328] Miguel Montero and Eduardo Martín-Martínez. Entanglement of arbitrary spin fields in noninertial frames. *Phys. Rev. A*, 84:012337, Jul 2011.

[329] V. Mukhanov and S. Winitzki. *Introduction to Quantum Effects in Gravity*. Cambridge University Press, 2007.

[330] Viatcheslav Mukhanov and Sergei Winitzki. *Introduction to Quantum Effects in Gravity*. Cambridge University Press, 6 2007.

[331] Robert C. Myers and M. J. Perry. Black Holes in Higher Dimensional Space-Times. *Annals Phys.*, 172:304, 1986.

[332] Robert C. Myers, Shan-Ming Ruan, and Tomonori Ugajin. Double holography of entangled universes. *JHEP*, 07:035, 2024.

[333] Dominik Neuenfeld. The Dictionary for Double Holography and Graviton Masses in d Dimensions. 4 2021.

[334] Keith K. Ng, Lee Hodgkinson, Jorma Louko, Robert B. Mann, and Eduardo Martín-Martínez. Unruh-DeWitt detector response along static and circular-geodesic trajectories for Schwarzschild–anti-de Sitter black holes. *Phys. Rev. D*, 90:064003, Sep 2014.

[335] Keith K. Ng, Robert B. Mann, and Eduardo Martín-Martínez. New techniques for entanglement harvesting in flat and curved spacetimes. *Phys. Rev. D*, 97:125011, Jun 2018.

[336] Keith K. Ng, Robert B. Mann, and Eduardo Martín-Martínez. Unruh-DeWitt detectors and entanglement: The anti–de Sitter space. *Phys. Rev. D*, 98:125005, Dec 2018.

[337] M.A. Nielsen and I.L. Chuang. *Quantum Computation and Quantum Information*. Cambridge Series on Information and the Natural Sciences. Cambridge University Press, Cambridge, England, 2000.

[338] Ron Nyström, Nicola Pranzini, and Esko Keski-Vakkuri. Harvesting magic from the vacuum, 2024.

[339] M. Okumura and Y. Yamanaka. Proper treatment of the zero mode in quantum field theory for trapped bose-einstein condensation. *Phys. Rev. A*, 68:013609, Jul 2003.

[340] Leandro A. Oliveira, Luís C. B. Crispino, and Atsushi Higuchi. Scalar radiation from a radially infalling source into a schwarzschild black hole in the framework of quantum field theory. *The European Physical Journal C*, 78(2):133, Feb 2018.

[341] Harold Ollivier and Wojciech H. Zurek. Quantum discord: A measure of the quantumness of correlations. *Phys. Rev. Lett.*, 88:017901, Dec 2001.

[342] S. Jay Olson and Timothy C. Ralph. Entanglement between the future and the past in the quantum vacuum. *Phys. Rev. Lett.*, 106:110404, Mar 2011.

[343] S. Jay Olson and Timothy C. Ralph. Extraction of timelike entanglement from the quantum vacuum. *Phys. Rev. A*, 85:012306, Jan 2012.

[344] David C. M. Ostapchuk, Shih-Yuin Lin, Robert B. Mann, and B. L. Hu. Entanglement dynamics between inertial and non-uniformly accelerated detectors. *J. High Energy Phys.*, 07(2012):072, 2012.

[345] Don N. Page. Information in black hole radiation. *Phys. Rev. Lett.*, 71:3743–3746, 1993.

[346] Don N. Page. Time Dependence of Hawking Radiation Entropy. *JCAP*, 09:028, 2013.

[347] Don N Page and Xing Wu. Massless scalar field vacuum in de Sitter spacetime. *J. Cosmol. Astropart. Phys.*, 2012(11):051–051, nov 2012.

[348] Qiyuan Pan and Jiliang Jing. Degradation of nonmaximal entanglement of scalar and dirac fields in noninertial frames. *Phys. Rev. A*, 77:024302, Feb 2008.

[349] Qiyuan Pan and Jiliang Jing. Hawking radiation, entanglement, and teleportation in the background of an asymptotically flat static black hole. *Phys. Rev. D*, 78:065015, Sep 2008.

[350] Emanuele Panella, Juan F. Pedraza, and Andrew Svesko. Three-Dimensional Quantum Black Holes: A Primer. *Universe*, 10(9):358, 2024.

[351] Emanuele Panella and Andrew Svesko. Quantum Kerr-de Sitter black holes in three dimensions. *JHEP*, 06:127, 2023.

[352] Ioannis Papadimitriou and Kostas Skenderis. AdS / CFT correspondence and geometry. *IRMA Lect. Math. Theor. Phys.*, 8:73–101, 2005.

[353] Ioannis Papadimitriou and Kostas Skenderis. Thermodynamics of asymptotically locally AdS spacetimes. *JHEP*, 08:004, 2005.

[354] Leonard Parker. Quantized fields and particle creation in expanding universes I. *Phys. Rev.*, 183:1057–1069, 1969.

[355] Geoffrey Penington. Entanglement Wedge Reconstruction and the Information Paradox. *JHEP*, 09:002, 2020.

[356] R. Penrose. Naked singularities. *Annals N. Y. Acad. Sci.*, 224:125–134, 1973.

[357] Asher Peres. Separability criterion for density matrices. *Physical Review Letters*, 77(8):1413–1415, August 1996.

[358] Asher Peres. Separability criterion for density matrices. *Phys. Rev. Lett.*, 77:1413–1415, Aug 1996.

[359] Malcolm J Perry and Edward Teo. Nonsingularity of the exact two-dimensional string black hole. *Physical review letters*, 70(18):2669, 1993.

[360] J. F. Plebanski and M. Demianski. Rotating, charged, and uniformly accelerating mass in general relativity. *Annals Phys.*, 98:98–127, 1976.

[361] Alejandro Pozas-Kerstjens, Jorma Louko, and Eduardo Martín-Martínez. Degenerate detectors are unable to harvest spacelike entanglement. *Phys. Rev. D*, 95:105009, May 2017.

[362] Alejandro Pozas-Kerstjens and Eduardo Martín-Martínez. Harvesting correlations from the quantum vacuum. *Phys. Rev. D*, 92:064042, Sep 2015.

[363] Alejandro Pozas-Kerstjens and Eduardo Martín-Martínez. Entanglement harvesting from the electromagnetic vacuum with hydrogenlike atoms. *Phys. Rev. D*, 94:064074, Sep 2016.

[364] Alejandro Pozas-Kerstjens and Eduardo Martín-Martínez. Entanglement harvesting from the electromagnetic vacuum with hydrogenlike atoms. *Phys. Rev. D*, 94:064074, 2016.

[365] María R. Preciado-Rivas, Manar Naeem, Robert B. Mann, and Jorma Louko. More excitement across the horizon. *Phys. Rev. D*, 110(2):025002, 2024.

[366] Marek J. Radzikowski. Micro-local approach to the Hadamard condition in quantum field theory on curved space-time. *Commun. Math. Phys.*, 179(3):529–553, Sep 1996.

[367] Lisa Randall and Raman Sundrum. A Large mass hierarchy from a small extra dimension. *Phys. Rev. Lett.*, 83:3370–3373, 1999.

[368] Lisa Randall and Raman Sundrum. An Alternative to compactification. *Phys. Rev. Lett.*, 83:4690–4693, 1999.

[369] Mukund Rangamani. Gravity and Hydrodynamics: Lectures on the fluid-gravity correspondence. *Class. Quant. Grav.*, 26:224003, 2009.

[370] Alpan Raval, B. L. Hu, and James Anglin. Stochastic theory of accelerated detectors in a quantum field. *Phys. Rev. D*, 53:7003–7019, Jun 1996.

[371] C. Reina and A. Treves. Gyromagnetic ratio of Einstein-Maxwell fields. *Phys. Rev. D*, 11:3031–3032, 1975.

[372] Benni Reznik. Entanglement from the vacuum. *Found. Phys.*, 33(1):167–176, 2003.

[373] Benni Reznik, Alex Retzker, and Jonathan Silman. Violating Bell's inequalities in vacuum. *Phys. Rev. A*, 71:042104, Apr 2005.

[374] Matthew P. G. Robbins, Laura J. Henderson, and Robert B. Mann. Entanglement amplification from rotating black holes. *Classical Quantum Gravity*, 39(2):02LT01, 2022.

[375] Matthew P. G. Robbins and Robert B. Mann. Anti-hawking phenomena around a rotating btz black hole, 2021.

[376] Sandra Robles and Javier Rodríguez-Laguna. Local quantum thermometry using Unruh–DeWitt detectors. *J. Stat. Mech.: Theory Exp.*, 2017(3):033105, 2017.

[377] C.D. Rodríguez-Camargo, G. Menezes, and N.F. Svaiter. Finite-time response function of uniformly accelerated entangled atoms. *Ann. Phys. (Amsterdam)*, 396:266–291, 2018.

[378] Shinsei Ryu and Tadashi Takayanagi. Aspects of Holographic Entanglement Entropy. *JHEP*, 08:045, 2006.

[379] Shinsei Ryu and Tadashi Takayanagi. Holographic derivation of entanglement entropy from AdS/CFT. *Phys. Rev. Lett.*, 96:181602, 2006.

[380] C. Sabín, J. J. García-Ripoll, E. Solano, and J. León. Dynamics of entanglement via propagating microwave photons. *Phys. Rev. B*, 81:184501, May 2010.

[381] Carlos Sabín, Borja Peropadre, Marco del Rey, and Eduardo Martín-Martínez. Extracting past-future vacuum correlations using circuit QED. *Phys. Rev. Lett.*, 109:033602, Jul 2012.

[382] Allison M. Sachs, Robert B. Mann, and Eduardo Martín-Martínez. Entanglement harvesting from multiple massless scalar fields and divergences in Unruh-DeWitt detector models. 8 2018.

[383] Abhisek Sahu, Irene Melgarejo-Lermas, and Eduardo Martín-Martínez. Sabotaging the harvesting of correlations from quantum fields. *Phys. Rev. D*, 105:065011, Mar 2022.

[384] Grant Salton, Robert B Mann, and Nicolas C Menicucci. Acceleration-assisted entanglement harvesting and rangefinding. *New J. Phys.*, 17(3):035001, mar 2015.

[385] Alejandro Satz. Then again, how often does the Unruh-DeWitt detector click if we switch it carefully? *Class. Quantum Grav.*, 24:1719–1732, 2007.

[386] Sebastian Schlicht. Considerations on the unruh effect: causality and regularization. *Classical and Quantum Gravity*, 21(19):4647–4660, September 2004.

[387] Sebastian Schlicht. Considerations on the unruh effect: causality and regularization. *Class. Quantum Grav.*, 21:4647, 2004.

[388] Matthew D. Schwartz. *Quantum Field Theory and the Standard Model*. Cambridge University Press, 3 2014.

[389] Marlan O. Scully, Stephen Fulling, David M. Lee, Don N. Page, Wolfgang P. Schleich, and Anatoly A. Svidzinsky. Quantum optics approach to radiation from atoms falling into a black hole. *Proc. Natl. Acad. Sci. U.S.A*, 115(32):8131–8136, 2018.

[390] Tetsuya Shiromizu, Takashi Torii, and Daisuke Ida. Brane world and holography. *JHEP*, 03:007, 2002.

[391] Petar Simidzija, Aida Ahmadzadegan, Achim Kempf, and Eduardo Martín-Martínez. Transmission of quantum information through quantum fields. *Phys. Rev. D*, 101:036014, Feb 2020.

[392] Petar Simidzija, Robert H. Jonsson, and Eduardo Martín-Martínez. General no-go theorem for entanglement extraction. *Phys. Rev. D*, 97:125002, Jun 2018.

[393] Petar Simidzija and Eduardo Martín-Martínez. Nonperturbative analysis of entanglement harvesting from coherent field states. *Phys. Rev. D*, 96:065008, Sep 2017.

[394] Petar Simidzija and Eduardo Martín-Martínez. Harvesting correlations from thermal and squeezed coherent states. *Phys. Rev. D*, 98:085007, Oct 2018.

[395] Kostas Skenderis. Lecture notes on holographic renormalization. *Class. Quant. Grav.*, 19:5849–5876, 2002.

[396] Kostas Skenderis and Sergey N. Solodukhin. Quantum effective action from the AdS / CFT correspondence. *Phys. Lett. B*, 472:316–322, 2000.

[397] Alexander R H Smith and Robert B Mann. Looking inside a black hole. *Class. Quantum Grav.*, 31(8):082001, apr 2014.

[398] Alexander RH Smith. *Detectors, reference frames, and time*. Springer, 2019.

[399] Smith, Alexander R. H. *Detectors, Reference Frames, and Time*. PhD thesis, University of Waterloo, 2017.

[400] M. S. Soares, N. F. Svaiter, and G. Menezes. Entanglement dynamics: Generalized master equation for uniformly accelerated two-level systems. *Phys. Rev. A*, 106:062440, Dec 2022.

[401] S. Sonego and V. Faraoni. Huygens' principle and characteristic propagation property for waves in curved space-times. *J. Math. Phys.*, 33(2):625–632, 1992.

[402] Jonathan Sorce and Robert M. Wald. Gedanken experiments to destroy a black hole. II. Kerr-Newman black holes cannot be overcharged or overspun. *Phys. Rev. D*, 96(10):104014, 2017.

[403] R. Sorkin. *Impossible Measurements on Quantum Fields*, volume 2, pages 293–305. Cambridge University Press, 1956.

[404] R. D. Sorkin. Introduction to topological geons. In P. G. Bergmann and V. De Sabbata, editors, *Topological properties and global structure of space-time*, Proceedings of the NATO Advanced Study Institute on Topological Properties and Global Structure of Space-Time, Erice, Italy, May 12–22 1985, page 249–70. Plenum, New York, 1986.

[405] Massimiliano Spadafora, Manar Naeem, María R. Preciado-Rivas, Robert B. Mann, and Jorma Louko. Deep in the Knotted Black Hole. 12 2024.

[406] Mark Srednicki. Entropy and area. *Physical Review Letters*, 71(5):666–669, August 1993.

[407] L. Sriramkumar and T. Padmanabhan. Response of finite-time particle detectors in non-inertial frames and curved spacetime. *Classical and Quantum Gravity*, 13:2061–2079, 1994.

[408] Greg Ver Steeg and Nicolas C. Menicucci. Entangling power of an expanding universe. *Phys. Rev. D*, 79:044027, Feb 2009.

[409] Alan R. Steif. The Quantum stress tensor in the three-dimensional black hole. *Phys. Rev. D*, 49:585–589, 1994.

[410] Stephen J. Summers and Reinhard Werner. Bell's inequalities and quantum field theory. i. general setting. *Journal of Mathematical Physics*, 28(10):2440–2447, 1985.

[411] Stephen J. Summers and Reinhard Werner. Bell's inequalities and quantum field theory. i. general setting. *J. Math. Phys. (N.Y.)*, 28(10):2440–2447, 1987.

[412] C. Suryaatmadja, R. B. Mann, and W. Cong. Entanglement harvesting of inertially moving unruh-dewitt detectors in minkowski spacetime. *Phys. Rev. D*, 106:076002, Oct 2022.

[413] Kenta Suzuki and Tadashi Takayanagi. BCFT and Islands in two dimensions. *JHEP*, 06:095, 2022.

[414] G Szekeres. "Golden Oldie": On the singularities of a Riemannian manifold. *Gen. Rel. Grav.*, 24:2001–2016, Nov 2002. Reprinted from Publ. Math. Debrecen **7** (1960), 285–301.

[415] Shin Takagi. Vacuum Noise and Stress Induced by Uniform Acceleration, Hawking-Unruh Effect in Rindler Manifold of Arbitrary Dimension. *Progress of Theoretical Physics Supplement*, 88:1–142, 1986.

[416] Tadashi Takayanagi. Holographic Dual of BCFT. *Phys. Rev. Lett.*, 107:101602, 2011.

[417] Tadashi Takayanagi. Essay: Emergent Holographic Spacetime from Quantum Information. *Phys. Rev. Lett.*, 134(24):240001, 2025.

[418] Marika Taylor. More on counterterms in the gravitational action and anomalies. 2 2000.

[419] Erickson Tjoa. Numerical contour integration. *The Mathematica Journal (to be published)*.

[420] Erickson Tjoa. *Aspects of Quantum Field Theory with Boundary Conditions* (*MSc. Thesis*). UWSpace, 2019.

[421] Erickson Tjoa, Irene López-Gutiérrez, Allison Sachs, and Eduardo Martín-Martínez. *, in preparation*

[422] Erickson Tjoa and Robert B Mann. Harvesting correlations in Schwarzschild and collapsing shell spacetimes. *J. High Energy Phys.*, 08(2020):155, 2020.

[423] Erickson Tjoa and Eduardo Martín-Martínez. Zero mode suppression of superluminal signals in light-matter interactions. *Phys. Rev. D*, 99:065005, Mar 2019.

[424] Erickson Tjoa and Eduardo Martín-Martínez. When entanglement harvesting is not really harvesting. *Phys. Rev. D*, 104:125005, Dec 2021.

[425] Erickson Tjoa and Eduardo Martín-Martínez. When entanglement harvesting is not really harvesting. *Physical Review D*, 104(12), December 2021.

[426] Richard C. Tolman. On the weight of heat and thermal equilibrium in general relativity. *Phys. Rev.*, 35:904–924, Apr 1930.

[427] Richard C. Tolman and Paul Ehrenfest. Temperature equilibrium in a static gravitational field. *Phys. Rev.*, 36:1791–1798, Dec 1930.

[428] W. G. Unruh. Notes on black-hole evaporation. *Phys. Rev. D*, 14:870–892, Aug 1976.

[429] Antony Valentini. Non-local correlations in quantum electrodynamics. *Phys. Lett.*, 153A(6):321 – 325, 1991.

[430] Victor Veitch, S A Hamed Mousavian, Daniel Gottesman, and Joseph Emerson. The resource theory of stabilizer quantum computation. *New Journal of Physics*, 16(1):013009, jan 2014.

[431] G. Vidal and R. F. Werner. Computable measure of entanglement. *Phys. Rev. A*, 65:032314, Feb 2002.

[432] G. Vidal and R. F. Werner. Computable measure of entanglement. *Phys. Rev. A*, 65:032314, Feb 2002.

[433] Manus R. Visser. Holographic thermodynamics requires a chemical potential for color. *Phys. Rev. D*, 105(10):106014, 2022.

[434] R.M. Wald. *General Relativity*. University of Chicago Press, 2010.

[435] Robert Wald. Gedanken experiments to destroy a black hole. *Annals Phys.*, 82(2):548–556, 1974.

[436] Robert M. Wald. Black hole in a uniform magnetic field. *Phys. Rev. D*, 10:1680–1685, 1974.

[437] Jieci Wang and Jiliang Jing. Quantum decoherence in noninertial frames. *Phys. Rev. A*, 82:032324, Sep 2010.

[438] Jieci Wang, Qiyuan Pan, Songbai Chen, and Jiliang Jing. Entanglement of coupled massive scalar field in background of dilaton black hole. *Physics Letters B*, 677(3):186–189, 2009.

[439] Jieci Wang, Qiyuan Pan, and Jiliang Jing. Entanglement redistribution in the schwarzschild spacetime. *Physics Letters B*, 692(3):202–205, 2010.

[440] Qingdi Wang and William G. Unruh. Motion of a mirror under infinitely fluctuating quantum vacuum stress. *Phys. Rev. D*, 89:085009, Apr 2014.

[441] Sijia Wang, María Rosa Preciado-Rivas, Massimiliano Spadafora, and Robert B. Mann. Singular excitement beyond the horizon of a rotating black hole. *Phys. Rev. D*, 110(6):065013, 2024.

[442] J. Watrous. *The Theory of Quantum Information*. Cambridge University Press, 2018.

[443] Marvin Weinstein. Moving mirrors, black holes, hawking radiation and all that .... *Nucl. Phys. B, Proc. Suppl.*, 108:68–73, 2002. lignt-cone physics: Particles and strings Proceedings of the International Workshop TRENTO 2001.

[444] H. Arthur Weldon. Thermal Green functions in coordinate space for massless particles of any spin. *Phys. Rev. D*, 62:056010, Aug 2000.

[445] E. P. Wigner. On unitary representations of the inhomogeneous Lorentz group. *Annals of Mathematics*, 40(1):149–204, 1939.

[446] Edward Witten. String theory and black holes. *Phys. Rev. D*, 44:314–324, Jul 1991.

[447] Edward Witten. APS Medal for Exceptional Achievement in Research: Invited article on entanglement properties of quantum field theory. *Rev. Mod. Phys.*, 90(4):045003, 2018.

[448] William K. Wootters. Entanglement of formation of an arbitrary state of two qubits. *Physical Review Letters*, 80(10):2245–2248, March 1998.

[449] William K. Wootters. Entanglement of formation of an arbitrary state of two qubits. *Phys. Rev. Lett.*, 80:2245–2248, Mar 1998.

[450] Peng-Yu Wu, H. Khodabakhshi, and H. Lu. Weak cosmic censorship conjecture cannot be violated in gedanken experiments. *Phys. Rev. D*, 110(10):104019, 2024.

[451] Shan-Ping Wu and Shao-Wen Wei. Thermodynamical topology of quantum BTZ black hole. *Phys. Rev. D*, 110(2):024054, 2024.

[452] Qidong Xu, Shadi Ali Ahmad, and Alexander R. H. Smith. Gravitational waves affect vacuum entanglement. *Phys. Rev. D*, 102:065019, Sep 2020.

[453] Zhen-Ming Xu, Pan-Pan Zhang, Bin Wu, and Xing Zhang. Thermodynamic bounce effect in quantum BTZ black hole. *JHEP*, 12:181, 2024.

[454] Karen Yagdjian. Huygens' principle for the Klein-Gordon equation in the de Sitter spacetime. *J. Math. Phys.*, 54(9):091503, 2013.

[455] Satoshi Yamaguchi. Holographic RG flow on the defect and g theorem. *JHEP*, 10:002, 2002.

[456] Jiayue Yang, Dyuman Bhattacharya, Ming Zhang, and Robert B. Mann. Analytic Tools for Harvesting Magic Resource in Curved Spacetime. 8 2025.

[457] Yasaman K. Yazdi. Zero modes and entanglement entropy. *J. High Energ. Phys.*, 2017(4):140, Apr 2017.

[458] Peiter Zatko, Ivan Poupyrev, Rachid El Guerrab, and Regina Dugan. Google I/O 2015. A little badass. Beautiful. Tech and human. Work and love. ATAP. https://www.youtube.com/watch?v=mpbWQbkl8_g, May 2015.

[459] Ming Zhang, Wen-Di Tan, Mengqi Lu, Dyuman Bhattacharya, Jiayue Yang, and Robert B. Mann. Finite-cutoff Holographic Thermodynamics. 7 2025.

APPENDICES

Appendix A

Explicit construction of the Swedish geon

A.1 Swedish geon generators

In this appendix we construct a convenient pair of free generators of the isometry group by which the Swedish geon is quotiented from AdS_3. We first consider the spacelike hypersurface on which the geometry is locally that of the Poincaré disk, and we then extend the generators to the spacetime.

A.1.1 Fundamental domain on the Poincaré disk

Recall that the Poincaré metric on the open unit disk $|z| < 1$ of $\mathbb{C}$ is

$$ds^2 = \frac{4|dz|^2}{(1-|z|^2)^2}\,. \tag{A.1}$$

The metric has constant negative curvature, with Ricci scalar -2. The metric is invariant under the fractional linear $SU(1,1)$ action

$$z \mapsto U(z) = \frac{\alpha z + \overline{\beta}}{\beta z + \overline{\alpha}}, \tag{A.2}$$

where $U \in SU(1,1)$ is written as

$$U = \begin{pmatrix} \alpha & \overline{\beta} \\ \beta & \overline{\alpha} \end{pmatrix}, \tag{A.3}$$

where α and β are complex numbers with $|\alpha|^2 - |\beta|^2 = 1$. The only degeneracy in this action is that U and $-U$ give the same fractional linear transformation. The isometry group of the Poincaré disc is hence $PSU(1,1)$, and elements in $PSU(1,1)$ may be represented as in (A.3) when understood modulo overall sign.

To establish notation, we define three one-parameter families of $SU(1,1)$ matrices by

$$R(\theta) := \begin{pmatrix} e^{i\theta/2} & 0 \\ 0 & e^{-i\theta/2} \end{pmatrix}, \tag{A.4a}$$

$$D_H(\psi) := \begin{pmatrix} \cosh(\psi/2) & \sinh(\psi/2) \\ \sinh(\psi/2) & \cosh(\psi/2) \end{pmatrix}, \tag{A.4b}$$

$$D_V(\psi) := \begin{pmatrix} \cosh(\psi/2) & i\sinh(\psi/2) \\ -i\sinh(\psi/2) & \cosh(\psi/2) \end{pmatrix}. \tag{A.4c}$$

The action of $R(\theta)$ on the disk is a rotation about the origin, and θ is the rotation angle, measured positive counterclockwise. The action of $D_H(\psi)$ is a boost with fixed points at $z = \pm 1$, such that positive values of the rapidity ψ move points to the right, towards $z = 1$. The action of $D_V(\psi)$ is a boost with fixed points at $z = \pm i$, such that positive values of the rapidity ψ move points upwards, towards $z = i$. The subscripts H and V stand respectively for "horizontal" and "vertical."

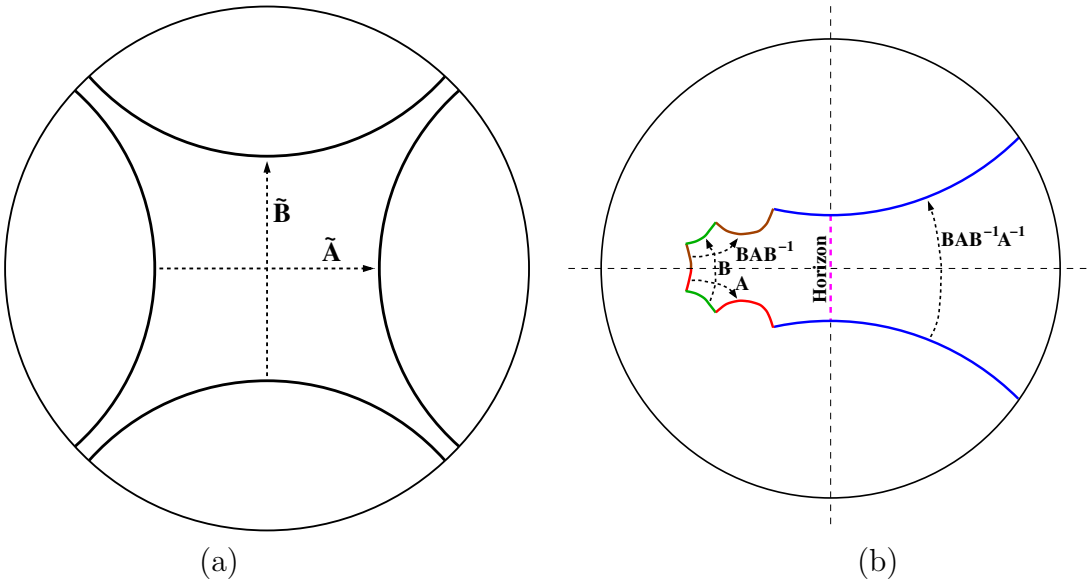
With this notation, let $a > 2\,\mathrm{arcsinh}(1)$, and let

$$\tilde{A} := D_H(a), \tag{A.5a}$$

$$\tilde{B} := D_V(a). \tag{A.5b}$$

$\tilde{A}$ and $\tilde{B}$ act on the disk as illustrated in Figure A.1 (a), mapping the four symmetrically-chosen geodesic circle segments to each other as shown. The condition $a > 2\,\mathrm{arcsinh}(1)$ is the condition for the circle segments not to intersect, neither on the open disk nor on its boundary. From the figure it is hence clear that the group generated by $\tilde{A}$ and $\tilde{B}$ acts on the disk freely and properly discontinuously, and the domain between the four circle segments in the figure serves as a fundamental domain for the group action. This is the construction given in [24].

The symmetric fundamental domain shown in Figure A.1 (a) intersects the boundary of the disk in four segments, but it is clear from the identifications that these four segments connect to form a circle, and the quotient space hence has a single trumpet-like infinity. A fundamental domain adapted to the infinity is displayed in Figure A.1 (b), where the



(a) (b)

Figure A.1: Two fundamental domains on the Poincaré disk. **(a)** In panel (a), the fundamental domain is between the four symmetrically-arranged geodesic circle segments, and the identifications of the segments use the generators $\tilde{A}$ and $\tilde{B}$ (A.5) as shown. The fundamental domain reaches the boundary of the disk in four segments, and the identifications join these segments into a circle. **(b)** In panel (b), the fundamental domain is between the seven geodesic circle segments, and the identifications of the segments use the generators A and B (A.6) as shown. The fundamental domain is adapted to the infinity, where it reaches the boundary of the disk in a single segment, and the identification by $BAB^{-1}A^{-1} = -D_V(\psi_h)$, with ψ_h given by (A.10), joins this segment into a circle. The horizon is on the axis of $D_V(\psi_h)$ as shown.

identifications of the boundary segments are as shown, and the $SU(1,1)$ matrices A and B are given by

$$A = R(q)D_H(-\chi_A)D_V(-a)D_H(\chi_A)R(-q)\,, \tag{A.6a}$$
$$B = D_H(-\chi_B)D_V(a)D_H(\chi_B)\,, \tag{A.6b}$$

with

$$q = \arctan\left(\frac{\sqrt{S^4-1}}{S}\right)\,, \tag{A.7a}$$
$$\chi_A = \operatorname{arctanh}\left(\frac{S^2}{\sqrt{S^4+S^2-1}}\right)\,, \tag{A.7b}$$
$$\chi_B = \operatorname{arctanh}\left(\frac{1}{S}\right)\,, \tag{A.7c}$$

where

$$S := \sinh(a/2), \quad C := \cosh(a/2)\,. \tag{A.8}$$

The map between the two infinity-reaching boundary segments is by

$$BAB^{-1}A^{-1} = -D_V(\psi_h)\,, \tag{A.9}$$

where

$$\psi_h = 4\,\operatorname{arcosh}\left(S^2\right)\,. \tag{A.10}$$

The transformations leading from Figure A.1 (a) with (A.5) to Figure A.1 (b) with (A.6) are given in A.2. In A.2 it is shown that the quotient surface is a punctured torus, and $A/\{\pm 1\}$ and $B/\{\pm 1\}$ are a pair of free generators of the fundamental group of this surface.

A.1.2 Generators in the spacetime

Recall that we realise AdS_3 as the hyperboloid (4.6) in $\mathbb{R}^{2,2}$ with the metric (4.7). We write the action of the $O(2,2)$ isometry group on AdS_3 in terms of the embedding space coordinates as

$$\begin{pmatrix} T_2 \\ T_1 \\ X_2 \\ X_1 \end{pmatrix} \mapsto \underset{\sim}{U} \begin{pmatrix} T_2 \\ T_1 \\ X_2 \\ X_1 \end{pmatrix}\,, \tag{A.11}$$

where $\underset{\sim}{U}$ denotes $O(2,2)$ elements in the defining matrix representation.

In terms of this realization, we embed the Poincaré disc of Figure A.1(b) in AdS_3 by

$$T_2 = 0\,, \tag{A.12a}$$

$$\frac{T_1}{\ell} = \frac{1+|z|^2}{1-|z|^2}\,, \tag{A.12b}$$

$$\frac{X_2 + iX_1}{\ell} = \frac{2z}{1-|z|^2}\,, \tag{A.12c}$$

as the spacelike hypersurface $T_2 = 0$ with $T_1 > 0$. The induced metric on this hypersurface is ℓ^2 times (A.1). The isometries of the Poincaré disk by the $SU(1,1)$ matrices (A.4) are induced from the AdS_3 isometries by the respective $O(2,2)$ matrices

$$\underset{\sim}{R}(\theta) = \begin{pmatrix} 1 & 0 & 0 & 0 \\ 0 & 1 & 0 & 0 \\ 0 & 0 & \cos\theta & -\sin\theta \\ 0 & 0 & \sin\theta & \cos\theta \end{pmatrix}, \tag{A.13a}$$

$$\underset{\sim}{D_H}(\psi) = \begin{pmatrix} 1 & 0 & 0 & 0 \\ 0 & \cosh\psi & \sinh\psi & 0 \\ 0 & \sinh\psi & \cosh\psi & 0 \\ 0 & 0 & 0 & 1 \end{pmatrix}, \tag{A.13b}$$

$$\underset{\sim}{D_V}(\psi) = \begin{pmatrix} 1 & 0 & 0 & 0 \\ 0 & \cosh\psi & 0 & \sinh\psi \\ 0 & 0 & 1 & 0 \\ 0 & \sinh\psi & 0 & \cosh\psi \end{pmatrix}. \tag{A.13c}$$

It can then be verified that the Poincaré disc isometries by A and B (A.6) are induced from the respective AdS_3 isometries by

$$\underset{\sim}{A} = \begin{pmatrix} 1 & 0 & 0 & 0 \\ 0 & \dfrac{\cosh(6z)+2\cosh(4z)+\cosh(2z)}{4\sinh^2(z)} & \dfrac{\sqrt{\cosh(2z)}\cosh(4z)}{\sinh^2(z)} & \sinh(4z) \\ 0 & -\dfrac{\sqrt{\cosh(2z)}}{\sinh^2(z)} & -\coth^2(z) & 0 \\ 0 & -\dfrac{\cosh(5z)+3\cosh(3z)+4\cosh(z)}{2\sinh(z)} & -4[\cosh(2z)]^{3/2}\coth(z) & -\cosh(4z) \end{pmatrix}, \tag{A.14a}$$

$$\underset{\sim}{B} = \begin{pmatrix} 1 & 0 & 0 & 0 \\ 0 & \dfrac{\cosh(4z)+\cosh(2z)}{2\sinh^2(z)} & \dfrac{[\cosh(2z)]^{3/2}}{\sinh^2(z)} & \dfrac{\cosh(3z)+\cosh(z)}{\sinh(z)} \\ 0 & -\dfrac{[\cosh(2z)]^{3/2}}{\sinh^2(z)} & -\coth^2(z) & -2\sqrt{\cosh(2z)}\coth(z) \\ 0 & \dfrac{\cosh(3z)+\cosh(z)}{\sinh(z)} & 2\sqrt{\cosh(2z)}\coth(z) & 2\cosh(2z)+1 \end{pmatrix}, \tag{A.14b}$$

where $z = \frac{1}{8}\psi_h$. The Poincaré disc isometry by $BAB^{-1}A^{-1}$ (A.9) is induced from the AdS_3 isometry by $\underset{\sim}{D}_V(\psi_h)$. It follows that the quotient of the Poincaré disc evolves into a single-exterior spinless BTZ black whole with $2\pi\sqrt{M} = \psi_h$, where M is the mass, and the exterior is covered by the BTZ coordinates (t, r, ϕ) in (4.11) and (4.12), with the identification $(t, r, \phi) \sim (t, r, \phi + 2\pi)$. In terms of M, (A.14) then has $z = \frac{1}{4}\pi\sqrt{M}$.

A.2 Fundamental domain deformation

In this appendix we describe the deformation between the two fundamental domains shown in Figure A.1.

We start from the Poincaré disc of Figure A.1(a), with $\tilde{A}$ and $\tilde{B}$ given by (A.5). We map the disc to the upper half-plane by the fractional linear transformation

$$w = V \times \frac{\big(1 - i(C+S)\big)z + i - (C+S)}{\big(1 + i(C+S)\big)z + i + (C+S)}, \tag{A.15}$$

where S and C are given by (A.8), and $V := \sqrt{\frac{S+1}{S-1}}$. Writing $w = u + iv$, where $u \in \mathbb{R}$ and $v > 0$, the metric (A.1) is mapped to the upper half-plane hyperbolic metric

$$ds^2 = \frac{du^2 + dv^2}{v^2}. \tag{A.16}$$

The fractional linear transformations by $\tilde{A}$ and $\tilde{B}$ are mapped respectively to fractional linear transformations by the $SL(2, \mathbb{R})$ matrices

$$\hat{A} = \begin{pmatrix} -C(S-1) & -S^2V \\ S^2V^{-1} & C(S+1) \end{pmatrix}, \tag{A.17a}$$

$$\hat{B} = \begin{pmatrix} C & SV \\ SV^{-1} & C \end{pmatrix}. \tag{A.17b}$$

The fixed points $z = \pm 1$ of $\tilde{A}$ are mapped to the fixed points of $\hat{A}$, which are respectively at $w = -V(C-1)S^{-1}$ and $w = -V(C+1)S^{-1}$, and the fixed points $z = \pm i$ of $\tilde{B}$ are mapped to the fixed points of $\hat{B}$, which are respectively at $w = \pm V$. The fundamental domain in Figure A.1(a) is mapped to the fundamental domain D_1 in Figure A.2, with the identifications described in the caption. Figures A.2–A.4 then show how D_1 can be replaced by the new fundamental domain D_3 in Figure A.4(b), as described in the captions. In particular, it follows that there is a horizon, generated by the boost

$$\hat{B}\hat{A}\hat{B}^{-1}\hat{A}^{-1} = -\begin{pmatrix} 2S^4 - 1 & 2CS^2\sqrt{S^2-1} \\ 2CS^2\sqrt{S^2-1} & 2S^4 - 1 \end{pmatrix}, \tag{A.18}$$

which has fixed points $w = \pm 1$ and the boost parameter ψ_h (A.10).

Finally, we map D_3 in the upper half-plane back to the Poincaré disk by the fractional linear transformation

$$z = \frac{iw + 1}{-iw + 1}, \tag{A.19}$$

which maps $w = 0$ to $z = 1$, $w = i$ to $z = 0$ and $w = \infty$ to $z = -1$. This gives the fundamental domain in Figure A.1(b). A and B are boosts with rapidity a, with fixed points respectively at

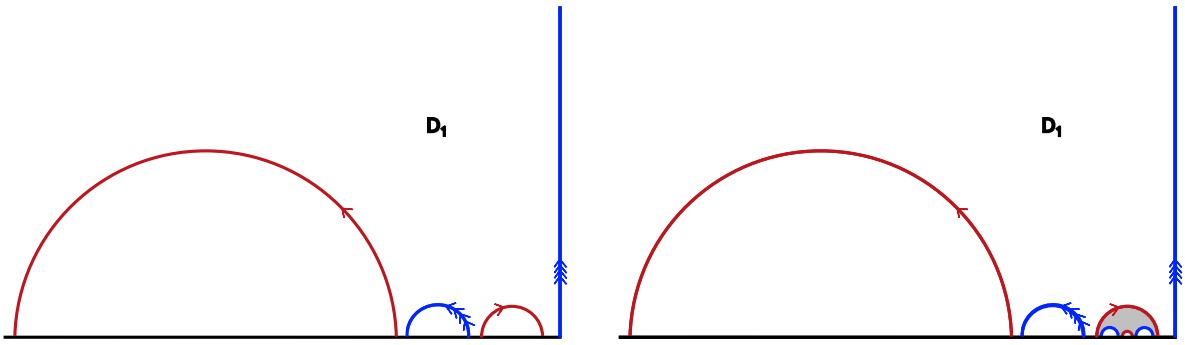
$$A: \quad e^{iq}\frac{-S^2 \mp i\sqrt{S^2-1}}{\sqrt{S^4+S^2-1}}, \tag{A.20a}$$

$$B: \quad \frac{-1 \pm i\sqrt{S^2-1}}{S}, \tag{A.20b}$$

where q is given by (A.7a). From this it follows that A and B have the expressions given in (A.6)–(A.8), using the fact that $D_H(\psi)$ maps the fixed points $\pm i$ of $D_V(\psi)$ to respectively $\tanh\psi \pm i/\cosh\psi$.

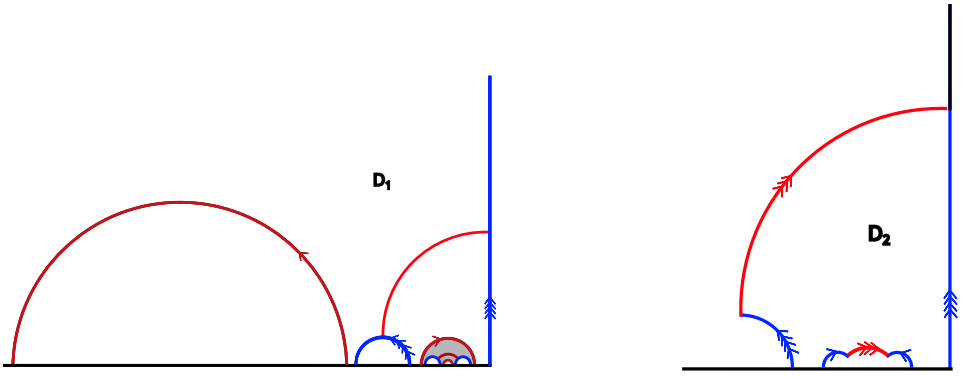
A.3 Topology

In this appendix we show that the quotient surface of the Poincaré disc is a punctured torus, and its fundamental group is the free group generated by $A/\{\pm 1\}$ and $B/\{\pm 1\}$, were A and B are given in (A.6).



(a) (b)

Figure A.2: **(a)** The upper half-plane fundamental domain D_1 to which the fundamental domain in Figure A.1(a) is mapped by the fractional linear transformation (A.15). $\hat{A}$ maps the left single-arrowed semicircle to the right one, and $\hat{B}$ maps the quadruple-arrowed semicircle to the positive imaginary axis. **(b)** D_1 together with its image under $\hat{A}$, shown shaded.

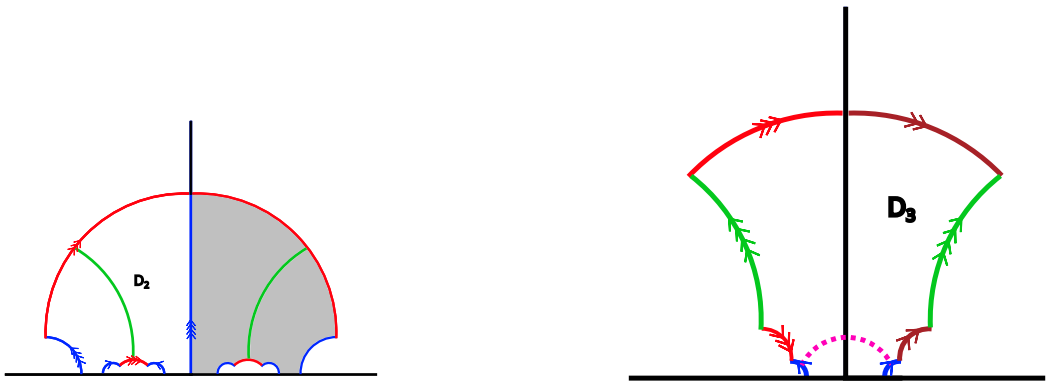


(a) (b)

Figure A.3: **(a)** As in Figure A.2 (b), but showing also a geodesic arc (in red) that cuts D_1 in two symmetric halves, and the image of this arc in the shaded image of D_1. **(b)** A new fundamental domain D_2, combining half of D_1 and half of the shaded image of D_1. The upper triple-arrowed boundary is mapped to the lower triple-arrowed boundary by $\hat{A}$. The left single-arrowed boundary is mapped to the right single-arrowed boundary by $\hat{A}\hat{B}\hat{A}^{-1}$.

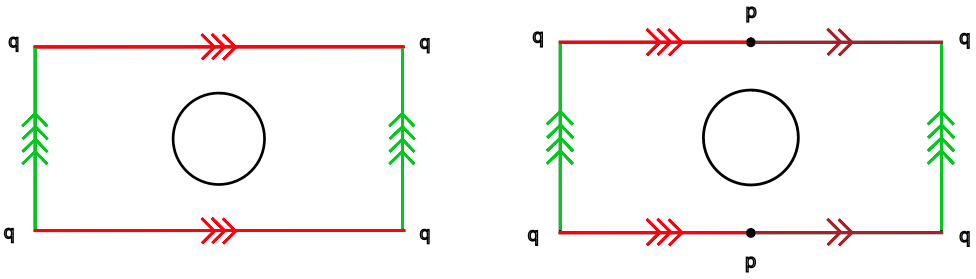
We start by representing the punctured torus as shown in Figure A.5(a), as a punctured rectangle with the opposing sides pairwise identified as shown. We then perform a sequence of cut-and paste deformations as shown in Figures A.5(b)–A.7(a). The fundamental domain in Figure A.7(a) is topologically identical to that in Figure A.1(b), and the identifications by A and B in Figure A.1(b) correspond to the pair of identifications across the boundaries of the fundamental domain in Figure A.5(a). A perspective picture of the fundamental domain of Figure A.4(b) glued across the identifications is shown in Figure A.7(b).

As the fundamental group of the punctured torus is the free group generated by the two identifications shown in Figure A.5(a) [191, Section 1.2][111], it follows that $A/\{\pm 1\}$ and $B/\{\pm 1\}$ provide a pair of free generators for the action of the fundamental group on the Poincaré disc.



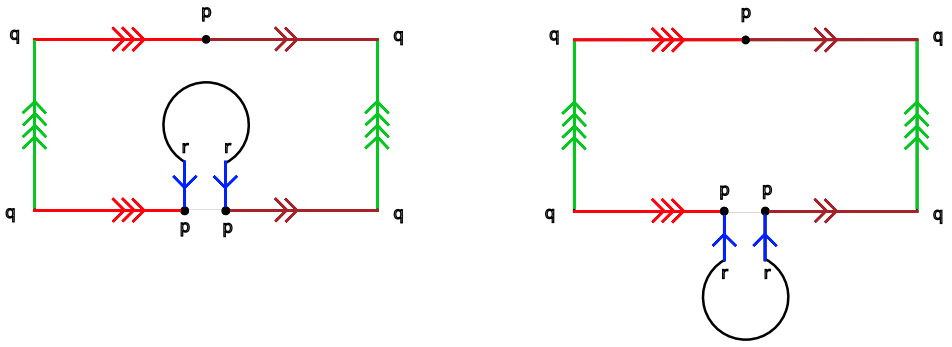
(a) (b)

Figure A.4: **(a)** D_2 together with its image under $\hat{B}$, shown shaded. Also shown is a geodesic arc (in green) that cuts D_2 in two symmetric halves, and the image of this arc in the shaded image of D_2. **(b)** A new fundamental domain D_3, combining half of D_2 and half of the shaded image of D_2. The left quadruple-arrowed boundary is mapped to the right quadruple-arrowed boundary by $\hat{B}$. The left single-arrowed boundary is mapped to the right single-arrowed boundary by $\hat{B}\hat{A}\hat{B}^{-1}\hat{A}^{-1}$, whose fixed points are $w = \pm 1$. The dashed curve is the geodesic circle joining $w = \pm 1$ and forming the horizon.



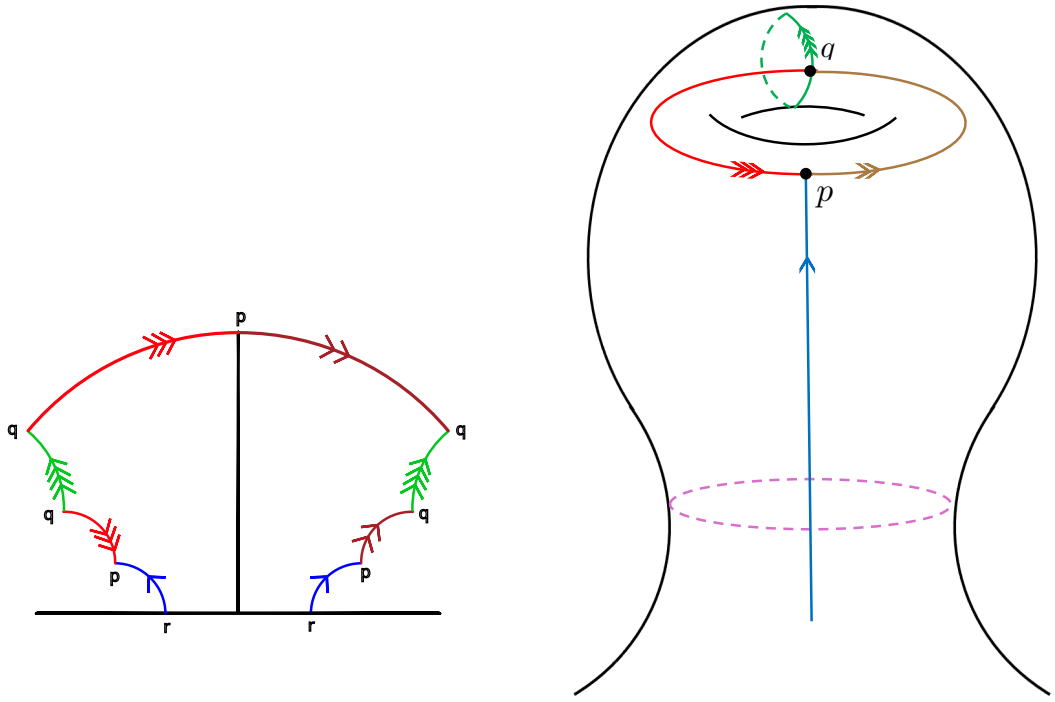
(a) (b)

Figure A.5: **(a)** Fundamental domain of a punctured torus, realised as a rectangle with a hole in the middle. The arrows show the pairwise identifications of the sides. All the four corner points, labelled q, are identified. **(b)** A pair of identified points labelled p on the boundary are chosen. The double-arrowed boundary segments are identified, and the triple-arrowed boundary segments are identified.



(a) (b)

Figure A.6: **(a)** A cut is introduced from one of the points p to the puncture. **(b)** The surface is continuously deformed around the new cut.



(a) (b)

Figure A.7: **(a)** The straight boundary segments of Figure A.6 (b) are deformed to curved boundary segments that match those in the upper half-plane fundamental domain in Figure A.4 (b). **(b)** A perspective picture in which the fundamental domain of panel (a) has been embedded in $\mathbb{R}^3$ and glued across the identified boundaries. The top side of the surface in panel (a) has become the inner side in panel (b).

Appendix B

Explicit Expressions for the Charged Rotating Quantum Black Hole

B.1 Explicit expressions

B.1.1 Brane volume and chemical potential

The thermodynamic volume on the brane, V_3 is given by

$$V_3 = \frac{2\pi\ell_3^2}{O_V^2}\sum_{n=0}^{8} N_{V,n} z^n \,, \tag{B.1}$$

where

$$N_{V,0} = \alpha^2\nu^2 \tag{B.2}$$

$$N_{V,1} = -2\alpha^2\left(\alpha^2+1\right)\nu \tag{B.3}$$

$$N_{V,2} = 2\alpha^2\left(\alpha^2+\nu^2+2\right)-\nu^2+2 \tag{B.4}$$

$$N_{V,3} = \nu\left(2\alpha^4\left(\nu^2+2\right)+\alpha^2\left(2\left(\nu^2+1\right)\chi^2-\nu^2+6\right)-\nu^2+4\right) \tag{B.5}$$

$$N_{V,4} = \alpha^2\left(2\alpha^2\left(\nu^2\left(1-\chi^2\right)-2\right)+2\nu^4\chi^2+7\nu^2-4\right) \tag{B.6}$$

$$N_{V,5} = \nu\left(2\alpha^4\left(-\nu^2\chi^2+\chi^2-3\right)+\alpha^2\left(-6\nu^2+4\chi^2-8\right)-\nu^2\left(\chi^2+3\right)\right) \tag{B.7}$$

$$N_{V,6} = -\nu^4\left(2\chi^2+1\right)+2\alpha^4\left(\nu^4\left(\chi^2-2\right)+\nu^2\left(3\chi^2-2\right)+1\right) \tag{B.8}$$

$$
\begin{aligned}
&+\alpha^2\nu^2\left(\nu^2\left(\chi^4+\chi^2-4\right)+2\left(\chi^2+1\right)^2\right)\\
N_{V,7}=&\nu\left(2\alpha^4\left(3\nu^2+\left(\nu^4+\nu^2-2\right)\chi^2+2\right)\right.\\
&\left.+\alpha^2\nu^2\left(2\left(\nu^2+2\right)\chi^4-\left(\nu^2-1\right)\chi^2+3\right)-\nu^4\chi^2\right)
\end{aligned}
\tag{B.9}
$$

$$
N_{V,8}=-\alpha^2\nu^2\left(\left(\nu^2+2\right)\chi^2+1\right)\left(2\alpha^2-\nu^2\chi^2\right)
\tag{B.10}
$$

and

$$
\begin{aligned}
O_V=&\alpha^2+z^2\left(\chi^2+z^2\left(\nu^2\chi^2-\alpha^2\left(\left(\nu^2+1\right)\chi^2+3\right)\right)\right.\\
&\left.+2\nu z\left(2\alpha^2+\chi^2+1\right)+3\right)+1
\end{aligned}
\tag{B.11}
$$

Let $f(x)=\sqrt{1+x^2}$. The chemical potential on the brane μ_3 is

$$
\mu_3=\frac{1}{\ell_3 O_\mu}\sum_{n=0}^{12}N_{\mu,n}z^n\,,
\tag{B.12}
$$

where

$$
N_{\mu,0}=2\alpha^2\nu f(\alpha)^2f(\nu)^2(f(\nu)+1)\,,
\tag{B.13}
$$

$$
N_{\mu,1}=\alpha^2f(\alpha)^2f(\nu)^2\left(\alpha^2\left(-2f(\nu)+\nu^2-2\right)+\nu^2(2f(\nu)+3)-2(f(\nu)+1)\right)\,,
\tag{B.14}
$$

$$
N_{\mu,2}=-2\nu f(\nu)^2\left(\alpha^6(2f(\nu)+3)+3\alpha^4(f(\nu)+2)+\alpha^2(f(\nu)+4)+f(\nu)+2\right)\,,
\tag{B.15}
$$

$$
\begin{aligned}
N_{\mu,3}=&f(\nu)^2\Big(\alpha^6\left(\left(4\nu^2+6\right)f(\nu)-\nu^2+6\right)+\alpha^4\Big(\nu^2\left(\chi^2(6f(\nu)+5)+4f(\nu)-9\right)\\
&+2\left(\chi^2+5\right)(f(\nu)+1)\Big)+\alpha^2\Big(\nu^2\left(\left(4\chi^2-2\right)f(\nu)+\chi^2-15\right)\\
&-2\left(\chi^2-3\right)(f(\nu)+1)\Big)-\nu^2(4f(\nu)+9)+2(f(\nu)+1)\Big)\,,
\end{aligned}
\tag{B.16}
$$

$$
\begin{aligned}
N_{\mu,4}=&\nu f(\nu)^2\Big(2\alpha^6\left(2f(\nu)\left(\nu^2-\chi^2+2\right)+\left(\nu^2-2\right)\chi^2+7\right)\\
&+\alpha^4\left(2f(\nu)\left(5\left(\nu^2-1\right)\chi^2+\nu^2+8\right)+\nu^2\left(7\chi^2-9\right)-10\chi^2+28\right)\\
&+\alpha^2\left(\nu^2\left(\left(8\chi^2-4\right)f(\nu)+3\chi^2-14\right)-6\chi^2(f(\nu)+1)+16f(\nu)+22\right)\\
&-\nu^2(2f(\nu)+5)+2(f(\nu)+1)\Big)\,,
\end{aligned}
\tag{B.17}
$$

$$
\begin{aligned}
N_{\mu,5} =& f(\nu)^2\Big(-\Big(\alpha^6\Big(\nu^2\left(\chi^2(16f(\nu)+21)-12\right) \\
&+2\left(\chi^2+4\right)(f(\nu)+1)+2\nu^4\chi^2\Big)\Big) \\
&+\alpha^4\Big(4\nu^4\chi^2 f(\nu)+\nu^2\left(-2\chi^2(10f(\nu)+13)+4f(\nu)+29\right) \\
&+2\left(2\chi^2-7\right)(f(\nu)+1)\Big)+\alpha^2\Big(2\nu^4\chi^2(2f(\nu)+1) \\
&+\nu^2\left(13-\chi^2(8f(\nu)+15)\right) \\
&-2\left(\chi^2+5\right)(f(\nu)+1)\Big)-\nu^2\left(2\left(\chi^2+3\right)f(\nu)+\chi^2+7\right) \\
&+2\left(\chi^2-1\right)(f(\nu)+1)\Big), \\
N_{\mu,6} =& \nu f(\nu)^2\Big(\alpha^6\Big(\nu^2\left(4\left(\chi^2-3\right)f(\nu)-3\chi^2-4\right) \\
&+2\left(9\chi^2(f(\nu)+1)-8f(\nu)-11\right)\Big) \\
&+\alpha^4\Big(\nu^2\left(\left(6\chi^4-4\chi^2-26\right)f(\nu)+4\chi^4-22\chi^2-13\right) \\
&+4\chi^2\left(\chi^2+3\right)(f(\nu)+1)-32f(\nu)-38\Big)+\alpha^2\Big(\nu^2\Big(2\left(\chi^4-4\chi^2-13\right)f(\nu) \\
&-\left(\left(\chi^2+17\right)\chi^2\right)-22\Big)-2\left(\chi^4-5\chi^2+6\right)(f(\nu)+1)\Big) \\
&-\nu^2\left(\chi^2(6f(\nu)+3)+8f(\nu)+9\right)+2\left(3\chi^2-1\right)(f(\nu)+1)\Big),
\end{aligned}
\tag{B.18}
$$

$$
\tag{B.19}
$$

$$
\begin{aligned}
N_{\mu,7} =& f(\nu)^2\Big(\alpha^6\Big(\nu^4\left(2\chi^2(6f(\nu)+1)-8(f(\nu)+1)+\chi^4\right) \\
&+\nu^2\left(-2\chi^4(f(\nu)+1)+\chi^2(16f(\nu)+25)-12\right) \\
&-2\left(\chi^2-4\right)(f(\nu)+1)\Big) \\
&+\alpha^4\Big(\nu^4\left(2\left(7\chi^4+\chi^2-8\right)f(\nu)+6\chi^4-7\chi^2-16\right) \\
&+\nu^2\left(\chi^2(34f(\nu)+48)+12f(\nu)+1\right)+2\left(2\chi^2+7\right)(f(\nu)+1)\Big) \\
&+\alpha^2\Big(nu^4\left(\chi^4(6f(\nu)-3)-4\chi^2(2f(\nu)+1)-10(f(\nu)+1)\right) \\
&+\nu^2\left(-6\chi^4(f(\nu)+1)+\chi^2(28f(\nu)+25)+16f(\nu)+19\right) \\
&-6\left(\chi^2-1\right)(f(\nu)+1)\Big)-\nu^4\left(\left(6\chi^2+2\right)f(\nu)+3\chi^2+2\right) \\
&+6\nu^2\chi^2(f(\nu)+1)\Big),
\end{aligned}
\tag{B.20}
$$

$$
\begin{aligned}
N_{\mu,8} =& \nu f(\nu)^2\Big(\alpha^6\Big(\nu^4\chi^2\left(4f(\nu)-3\chi^2+8\right) \\
&+\nu^2\left(\chi^2\left(-2\chi^2(7f(\nu)+9)+12f(\nu)+35\right)+4(5f(\nu)+4)\right) \\
&-2\chi^2\left(2\chi^2+3\right)(f(\nu)+1)+16f(\nu)+18\Big) \\
&+\alpha^4\Big(\nu^4\chi^2\left(2\chi^2(5f(\nu)-1)+2f(\nu)+11\right) \\
&+\nu^2\left(2\chi^2\left(-7\chi^2(f(\nu)+1)+11f(\nu)+18\right)+38f(\nu)+37\right) \\
&+2\left(2\left(\chi^2-7\right)\chi^2+7\right)(f(\nu)+1)\Big) \\
&+\alpha^2\Big(\nu^4\chi^2\left(3\chi^2-2\right)(2f(\nu)-1) \\
&+\nu^2\left(2\left(-4\chi^4+8\chi^2+7\right)f(\nu)-9\chi^4+9\chi^2+16\right) \\
&-2\left(\chi^4+7\chi^2-2\right)(f(\nu)+1)\Big)-\nu^2\chi^2\left(2\left(\nu^2-1\right)f(\nu)+\nu^2-2\right)\Big),
\end{aligned}
\tag{B.21}
$$

$$
\begin{aligned}
N_{\mu,9} =& -\alpha^2 f(\nu)^2\Big(\alpha^4\Big(\nu^4\left(\left(6\chi^4+20\chi^2-8\right)f(\nu)+9\left(\chi^2+2\right)\chi^2-8\right) \\
&+\nu^2\left(-10\chi^4(f(\nu)+1)+\chi^2(40f(\nu)+47)+8f(\nu)+5\right) \\
&+2\left(\chi^2+3\right)(f(\nu)+1)+3\nu^6\chi^4\Big)+\alpha^2\Big(-2\nu^6\chi^4(f(\nu)-2) \\
&-\nu^4\left(2\left(\chi^6-6\chi^4-11\chi^2+4\right)f(\nu)+\chi^6-11\chi^4-27\chi^2+8\right) \\
&+\nu^2\left(40\chi^2f(\nu)-2\left(\chi^2+3\right)\chi^4(f(\nu)+1)+14f(\nu)+37\chi^2+17\right) \\
&-6\left(\chi^2-1\right)(f(\nu)+1)\Big)+\nu^6\chi^4(1-2f(\nu))+\nu^4\Big(\chi^4(8f(\nu)+11) \\
&-2(f(\nu)+1)+3\chi^2\Big)+6\nu^2\chi^2(f(\nu)+1)f(\chi)^2\Big),
\end{aligned}
\tag{B.22}
$$

$$
\begin{aligned}
N_{\mu,10} =& \alpha^2\nu f(\nu)^2\Big(\alpha^4\Big(\nu^4\chi^2\left(\chi^2(8f(\nu)+7)-12(f(\nu)+1)\right) \\
&+\nu^2\left(\chi^2\left(\chi^2(14f(\nu)+17)+4f(\nu)-1\right)-12(f(\nu)+1)\right) \\
&-2\left(\chi^4-9\chi^2+2\right)(f(\nu)+1)\Big) \\
&+\alpha^2\Big(\nu^4\chi^2\left(6\left(\chi^4-\chi^2-1\right)f(\nu)+3\chi^4-5\chi^2-5\right) \\
&+\nu^2\left(6\chi^6(f(\nu)+1)+\chi^2(8f(\nu)+13)-6f(\nu)+2\chi^4-7\right) \\
&+2\left(2\chi^4+5\chi^2-1\right)(f(\nu)+1)\Big) \\
&+\nu^2\chi^2\left(-6\chi^2f(\nu)^3+2f(\nu)-3\left(3\nu^2+2\right)\chi^2+\nu^2+2\right)\Big),
\end{aligned}
\tag{B.23}
$$

$$
\begin{aligned}
N_{\mu,11} =&\alpha^2 f(\nu)^2\Big(\alpha^4\Big(\nu^6\chi^4\left(4f(\nu)-\chi^2+5\right) \\
&+\nu^4\chi^2\left(2\left(-\chi^4+\chi^2+8\right)f(\nu)-3\chi^4+10\chi^2+14\right) \\
&+\nu^2\left(-2\chi^6(f(\nu)+1)+\chi^2(8f(\nu)+7)+4f(\nu)+5\right) \\
&-2\left(\chi^2-1\right)(f(\nu)+1)\Big)+\alpha^2\nu^2\chi^2\Big(\nu^4\chi^2\Big(\chi^2(6f(\nu)+3) \\
&-4(f(\nu)+1)\Big)+\nu^2\left(6\chi^4(f(\nu)+1)+4(f(\nu)+1)+3\chi^2\right) \\
&+6\chi^2(f(\nu)+1)\Big)-\nu^4\chi^4\left(2f(\nu)^3+3\nu^2+2\right)\Big)\,, \qquad \text{(B.24)}\\
N_{\mu,12} =&-\alpha^4\nu\chi^2 f(\nu)^2\Big(\nu^2\Big(\left(\nu^2+2\right)\chi^4\left(\left(\alpha^2-1\right)\nu^2+\alpha^2\right) \\
&+\chi^2\left(\alpha^2\left(2\nu^2+5\right)-3\nu^2-2\right)+5\alpha^2\Big) \\
&+2f(\nu)\left(\nu^2\chi^2+1\right)\left(\alpha^2\left(2\nu^2+1\right)+\chi^2(\alpha-\nu)(\alpha+\nu)f(\nu)^2\right)+2\alpha^2 f(\chi)^2\Big)\,, \qquad \text{(B.25)}
\end{aligned}
$$

and

$$
\begin{aligned}
O_\mu =&(f(\nu)+1)^2(\nu z+1)\left(\alpha^2\left(z^2\left(\nu\chi^2 z-1\right)+1\right)+1\right)\Big(\alpha^2+\alpha^2\chi^2 z^4 f(\nu)^2 \qquad \text{(B.26)}\\
&-z^2\left(-3\alpha^2 z^2+4\alpha^2\nu z+(\chi+\nu\chi z)^2+2\nu z+3\right)-1\Big)^2\,.
\end{aligned}
$$

B.1.2 Boundary pressure

The boundary pressure P_2 is given by

$$
P_2 =\frac{1}{2\sqrt{2}G_3\ell\nu O_P}\sum_{n=0}^{12}N_{P,n}z^n\,, \qquad \text{(B.27)}
$$

where

$$
\begin{aligned}
N_{P,0} =&\alpha^2\nu^2 f(\alpha)^2 f(\nu)^3\left(7f(\nu)-4\nu^2-7\right)\,, \qquad \text{(B.28)}\\
N_{P,1} =&-\alpha^2\nu f(\alpha)^2 f(\nu)^2\Big(\alpha^2\left(\nu^2(9-5f(\nu))-8f(\nu)+\nu^4+8\right) \qquad \text{(B.29)}\\
&+2\nu^2\left(\nu^2(2f(\nu)-3)+f(\nu)+1\right)-8f(\nu)+8\Big)\,, \\
N_{P,2} =&f(\nu)^2\Big(\nu^2\Big(\alpha^2\left(\alpha^4\left(2-6\nu^2\right)+3\alpha^2\left(\nu^2+9\right)+17\nu^2+41\right) \qquad \text{(B.30)}\\
&+\left(\alpha^2\left(4\left(\alpha^4-2\right)\nu^2+2\alpha^4-15\alpha^2-29\right)-5\right)f(\nu)+\nu^2+9\Big) \\
&-8f(\alpha)^6(f(\nu)-1)\Big)\,,
\end{aligned}
$$

$$
\begin{aligned}
N_{P,3} =& \nu f(\nu)^4\Big(\alpha^6\left(25\nu^2+32\right)+\alpha^4\left(\nu^2\left(22\chi^2+51\right)+8\left(\chi^2+9\right)\right) \\
&+\alpha^2\left(\nu^2\left(11\chi^2+36\right)+8\left(\chi^2+8\right)\right)+3\left(\nu^2+8\right)\Big) \\
&-\nu f(\nu)^3\Big(\alpha^6\left(12\nu^4+41\nu^2+32\right)+\alpha^4\Big(\nu^2\left(12\nu^2\left(\chi^2+2\right)+26\chi^2+87\right) \\
&+8\left(\chi^2+9\right)\Big)+\alpha^2\left(\nu^2\left(4\nu^2\left(\chi^2+4\right)+15\chi^2+68\right)+8\left(\chi^2+8\right)\right) \\
&+3\left(5\nu^2+8\right)\Big), \qquad \text{(B.31)} \\
N_{P,4} =& f(\nu)^4\Big(-2\alpha^6\left(\nu^4\left(\chi^2-12\right)+\nu^2\left(8\chi^2-7\right)+12\right) \\
&+\alpha^4\left(\nu^4\left(26\chi^2+36\right)+\nu^2\left(37-8\chi^2\right)-48\right)+\alpha^2\Big(7\nu^4\left(3\chi^2+2\right) \\
&+\nu^2\left(8\chi^2+60\right)-24\Big)+2\nu^2\left(\nu^2+8\right)\Big)-f(\nu)^3\Big(2\alpha^6\Big(6\nu^6+\nu^4\left(16-5\chi^2\right) \\
&+\nu^2\left(1-8\chi^2\right)-12\Big)+\alpha^4\Big(4\nu^6\left(3\chi^2+4\right)+\nu^4\left(22\chi^2+56\right) \\
&+\nu^2\left(13-8\chi^2\right)-48\Big)+\alpha^2\Big(\nu^6\left(8\chi^2+4\right)+\nu^4\left(25\chi^2+46\right) \\
&+8\nu^2\left(\chi^2+6\right)-24\Big)+2\nu^2\left(5\nu^2+8\right)\Big), \qquad \text{(B.32)} \\
N_{P,5} =& \nu f(\nu)^3\Big(\alpha^6\left(16\nu^4+68\nu^2+\left(4\nu^6+16\nu^4+11\nu^2-16\right)\chi^2+64\right) \\
&+\alpha^4\left(28\nu^4-2\left(7\left(\nu^2+2\right)\nu^2+16\right)\chi^2+129\nu^2+128\right) \\
&+\alpha^2\left(16\nu^4+73\nu^2-\left(4\nu^6+18\nu^4+29\nu^2+24\right)\chi^2+72\right) \\
&-f(\nu)\Big(\alpha^6\left(36\nu^2+\left(4\nu^4+19\nu^2-16\right)\chi^2+64\right) \\
&+\alpha^4\left(65\nu^2-2\left(3\nu^4+6\nu^2+16\right)\chi^2+128\right) \\
&+\alpha^2\left(37\nu^2-\left(10\nu^4+17\nu^2+24\right)\chi^2+72\right) \\
&+4\nu^2\chi^2 f(\nu)+2\nu^2\left(7-2\chi^2\right)\Big)+8\nu^4+14\nu^2\Big), \qquad \text{(B.33)}
\end{aligned}
$$

$$
\begin{aligned}
N_{P,6} =& f(\nu)^4\Big(\alpha^6\left(\nu^4\left(51\chi^2-56\right)+\nu^2\left(64\chi^2-46\right)+24\right) \\
&+\alpha^4\left(\nu^4\left(23\chi^4+76\chi^2-110\right)+\nu^2\left(16\chi^2\left(\chi^2+6\right)-107\right)+24\right) \\
&+\alpha^2\nu^2\left(\nu^2\left(4\chi^4+65\chi^2-89\right)+8\left(\chi^4+7\chi^2-5\right)\right)+3\nu^4\left(4\chi^2-7\right)\Big) \\
&-f(\nu)^3\Big(\alpha^6\left(28\nu^6\left(\chi^2-1\right)+\nu^4\left(83\chi^2-80\right)+\nu^2\left(64\chi^2-34\right)+24\right) \\
&+\alpha^4\Big(4\nu^6\left(3\chi^4+10\chi^2-14\right)+\nu^4\left(31\chi^2\left(\chi^2+4\right)-166\right) \\
&+\nu^2\left(16\chi^2\left(\chi^2+6\right)-95\right)+24\Big) \\
&+\alpha^2\nu^2\left(8\nu^4\left(5\chi^2-6\right)+\nu^2\left(8\chi^4+93\chi^2-109\right)+8\left(\chi^4+7\chi^2-5\right)\right) \\
&+3\nu^4\left(4\nu^2\left(\chi^2-1\right)+4\chi^2-7\right)\Big), \qquad \text{(B.34)} \\
N_{P,7} =& -\nu f(\nu)^3\Big(\alpha^6\Big(4\nu^6\left(9\chi^2-4\right)+\nu^4\left(-5\chi^4+86\chi^2-12\right) \\
&+\nu^2\left(-8\chi^4+13\chi^2+68\right)-40\chi^2+64\Big)+\alpha^4\Big(4\nu^6\left(5\chi^2\left(\chi^2+3\right)-8\right) \\
&+\nu^4\left(61\chi^4+132\chi^2-24\right)+\nu^2\left(32\chi^4+36\chi^2+101\right)-48\chi^2+72\Big) \\
&+\alpha^2\nu^2\left(24\chi^4 f(\nu)^2+\left(52\nu^4+74\nu^2+19\right)\chi^2-5\left(4\nu^4+3\nu^2-7\right)\right) \\
&+f(\nu)\Big(\alpha^6\left(\nu^4\left(\chi^4-70\chi^2+28\right)+\nu^2\left(8\chi^4-33\chi^2-36\right)+8\left(5\chi^2-8\right)\right) \\
&-\alpha^4\left(\nu^4\left(45\chi^4+100\chi^2-56\right)+\nu^2\left(32\chi^4+60\chi^2+65\right)-48\chi^2+72\right) \\
&-\alpha^2\nu^2\left(\nu^2\left(12\chi^4+70\chi^2-35\right)+24\chi^4+19\chi^2+35\right) \\
&+\nu^4\left(7-12\chi^2\right)\Big)+\nu^4\left(12\chi^2 f(\nu)^2-4\nu^2-7\right)\Big), \qquad \text{(B.35)}
\end{aligned}
$$

$$
\begin{aligned}
N_{P,8} =&\alpha^2 f(\nu)^4\Big(\alpha^4\Big(\nu^2\Big(\left(8-3\nu^2\left(\nu^2+4\right)\right)\chi^4+68\nu^2\\
&+\left(28\nu^4-63\nu^2-104\right)\chi^2+46\Big)-8\Big)\\
&+\alpha^2\nu^2\left(23\nu^4\chi^2\left(\chi^2+2\right)+\nu^2\left(41\chi^4-132\chi^2+116\right)+8\left(\chi^4-14\chi^2+4\right)\right)\\
&+\nu^4\left(12\left(\nu^2+2\right)\chi^4+\left(22\nu^2-39\right)\chi^2+35\right)\Big)\\
&-f(\nu)^3\Big(\alpha^6\Big(\nu^2\Big(36\nu^4+92\nu^2+\left(20\nu^6-115\nu^2-104\right)\chi^2\\
&-\left(4\nu^6+11\nu^4+8\nu^2-8\right)\chi^4+42\Big)-8\Big)+\alpha^4\nu^2\Big(4\left(16\nu^4+33\nu^2+8\right)\\
&+\left(4\nu^6+47\nu^4+45\nu^2+8\right)\chi^4+2\left(18\nu^6-17\nu^4-94\nu^2-56\right)\chi^2\Big)\\
&+\alpha^2\nu^4\left(24\chi^4f(\nu)^2+10\nu^2\left(\left(2\nu^2-1\right)\chi^2+2\right)-39\chi^2+35\right)\\
&+4\nu^6\chi^2(f(\nu)-1)f(\nu)\Big),
\end{aligned}
\tag{B.36}
$$

$$
\begin{aligned}
N_{P,9} =&-\alpha^2\nu f(\nu)^3\Big(\alpha^4\Big(\nu^2\Big(16\nu^4+12\nu^2-3\left(24\nu^4+52\nu^2+19\right)\chi^2\\
&+\left(-4\nu^6+13\nu^4+43\nu^2+32\right)\chi^4-43\Big)+24\left(\chi^2-1\right)\Big)\\
&+\alpha^2\nu^2\Big(4\left(\nu^4+3\nu^2+2\right)\chi^6-2\left(50\nu^4+86\nu^2+21\right)\chi^2+4\left(4\nu^4+3\nu^2-7\right)\\
&+\left(-4\nu^6+33\nu^4+51\nu^2+8\right)\chi^4\Big)\\
&+f(\nu)\Big(\alpha^4\Big(-28\nu^4+31\nu^2+\left(3\nu^4-27\nu^2-32\right)\nu^2\chi^4\\
&+3\left(40\nu^4+23\nu^2-8\right)\chi^2+24\Big)-\alpha^2\nu^2\Big(8\chi^6f(\nu)^2-6\left(26\nu^2+7\right)\chi^2\\
&+28\left(\nu^2-1\right)+\left(\nu^4+47\nu^2+8\right)\chi^4\Big)-\nu^4\left(4\left(\nu^2+2\right)\chi^4-33\chi^2+7\right)\Big)\\
&+\nu^4\left(8\chi^4f(\nu)^2-3\left(8\nu^2+11\right)\chi^2+4\nu^2+7\right)\Big),
\end{aligned}
\tag{B.37}
$$

$$
\begin{aligned}
N_{P,10} =& -\alpha^2\nu^2 f(\nu)^2\Big(\alpha^4\Big(\nu^6\chi^2\left(4\left(8\chi^2-7\right)f(\nu)-53\chi^2+48\right) \\
&+\nu^4\left(\chi^2\left(\chi^2(57f(\nu)-64)-4f(\nu)-25\right)-20f(\nu)+36\right) \\
&+\nu^2\left(\chi^2\left(\chi^2(3f(\nu)+5)+101f(\nu)-129\right)-40f(\nu)+44\right) \\
&-8\left(2\chi^4-7\chi^2+1\right)(f(\nu)-1)\Big) \\
&+\alpha^2\nu^2\Big(2\nu^4\chi^2\left(6\chi^4(f(\nu)-2)+2\chi^2(4f(\nu)-5)-10f(\nu)+17\right) \\
&+\nu^2\left(2\left(18\chi^6+8\chi^4-5\chi^2-4\right)f(\nu)-48\chi^6-11\chi^4+14\right) \\
&+\left(24\chi^6-9\chi^4+34\chi^2-14\right)(f(\nu)-1)\Big) \\
&+\nu^4\chi^2\left(\nu^2(7-4f(\nu))-7f(\nu)+7\right)\Big),
\end{aligned}
\tag{B.38}
$$

$$
\begin{aligned}
N_{P,11} =& -\alpha^4\nu^3 f(\nu)^3\Big(\alpha^2\Big(4\nu^2+\left(3\nu^2+2\right)\left(4\nu^4-3\nu^2-16\right)\chi^4 \\
&+\left(32\nu^4+66\nu^2+19\right)\chi^2+7\Big) \\
&+f(\nu)\Big(-\alpha^2\left(\left(19\nu^2\left(\nu^2-2\right)-32\right)\chi^4+\left(58\nu^2+19\right)\chi^2+7\right) \\
&+\nu^2\chi^6 f(\nu)\left(\alpha^2-\left(\alpha^2+24\right)f(\nu)\right)+\nu^2\chi^2\left(\left(2\nu^2+9\right)\chi^2-14\right)\Big) \\
&+\nu^2\chi^2\left(-3\left(2\nu^2+3\right)\chi^2+8\nu^2+12\left(\nu^4+3\nu^2+2\right)\chi^4+14\right)\Big),
\end{aligned}
\tag{B.39}
$$

$$
\begin{aligned}
N_{P,12} =& \alpha^6\left(-\nu^4\right)\chi^2 f(\nu)^3\Big(f(\nu)\left(-\nu^2\chi^4(f(\nu)-1)f(\nu)+\left(22\nu^2+15\right)\chi^2+7\right) \\
&-4\nu^2-3\left(4\nu^4+10\nu^2+5\right)\chi^2-7\Big)-4\alpha^4\nu^6\chi^6 f(\nu)^5\left(-2f(\nu)+\nu^2+2\right),
\end{aligned}
\tag{B.40}
$$

and

$$
\begin{aligned}
O_P =& (f(\nu)-1)\sqrt{f(\nu)(f(\nu)+1)}\left(f(\nu)-2f(\nu)^2\right)(\nu z+1) \\
&\times\left(\alpha^2\left(z^2\left(\nu\chi^2 z-1\right)+1\right)+1\right)\left(\alpha^2+\alpha^2\chi^2 z^4 f(\nu)^2\right. \\
&\left.-z^2\left(-3\alpha^2 z^2+4\alpha^2\nu z+(\chi+\nu\chi z)^2+2\nu z+3\right)-1\right)^2.
\end{aligned}
\tag{B.41}
$$

B.2 Tensionless limit: Kerr-Newman-AdS

In the tensionless limit $\ell \to \infty$ the acceleration of the C-metric vanishes and the metric limits to the corresponding member of the Kerr-Newman-AdS family of solutions. In the static case, this limit is straightforward and was discussed in [134]. The limit is more subtle in the rotating case and it is the purpose of this appendix to discuss the relevant details.

We have used this limit to make contact between our calculations of the gyromagnetic ratio and the well-established result $g = 2$ for four-dimensional Kerr-Newman-AdS black holes.

We begin with the C-metric and reproduce the metric and its functions here for convenience:

$$\begin{aligned} \mathrm{d}s^2 = \frac{1}{\Omega^2}\Bigg[& -\frac{H(r)}{\Sigma(x,r)}\left(\mathrm{d}t + ax^2\mathrm{d}\phi\right)^2 + \frac{\Sigma(x,r)}{H(r)}\mathrm{d}r^2 \\ & + r^2\left(\frac{\Sigma(x,r)}{G(x)}\mathrm{d}x^2 + \frac{G(x)}{\Sigma(x,r)}\left(\mathrm{d}\phi - \frac{a}{r^2}\mathrm{d}t\right)^2\right)\Bigg] , \end{aligned} \tag{B.42}$$

where

$$\begin{aligned} H(r) &= \frac{a^2}{r^2} + \kappa + \frac{\ell^2 q^2}{r^2} + \frac{r^2}{\ell_3^2} - \frac{\ell\mu}{r} , \quad G(x) = \frac{a^2x^4}{\ell_3^2} - q^2x^4 - \mu x^3 - \kappa x^2 + 1 , \\ \Sigma(x,r) &= 1 + \frac{a^2x^2}{r^2} , \quad \Omega = 1 + \frac{xr}{\ell} , \end{aligned} \tag{B.43}$$

and the gauge field takes the form

$$A_\mu dx^\mu = \frac{2}{\ell_\star}\left(-\frac{\ell q r}{a^2x^2 + r^2} , 0 , 0 , -\frac{a\ell q r x^2}{a^2x^2 + r^2}\right) . \tag{B.44}$$

It is only in the case $\kappa = +1$ the Kerr-Newman-AdS metric will be recovered, and henceforth we make this restriction. We rescale the parameters of the solution in the following way

$$\mu = \frac{2m}{\ell x_1^3} , \quad q = \frac{Q}{\ell x_1^2} , \quad a = \frac{\hat{a}}{x_1^2} \tag{B.45}$$

and transform some of the coordinates,

$$t = x_1\hat{t} - \hat{a}\hat{\phi} , \quad r = \frac{\hat{r}}{x_1} , \quad \phi = \frac{x_1\hat{\phi}}{\Xi} . \tag{B.46}$$

We can then take the limit $\ell \to \infty$ and obtain a finite metric and gauge field. When taking the limit, we keep the four-dimensional parameters ℓ_4, G_4 and g_4 fixed. To express the final result in Boyer-Lindquist form, we define $x = x_1\cos\theta$ in terms of which the metric and gauge field read

$$\mathrm{d}s^2 = -\frac{\Delta_r}{\Sigma}\left[\mathrm{d}\hat{t} - \frac{\hat{a}\sin^2\theta}{\Xi}\mathrm{d}\hat{\phi}\right]^2 + \frac{\Sigma}{\Delta_r}\mathrm{d}\hat{r}^2 + \frac{\Sigma}{\Delta_\theta}\mathrm{d}\theta^2 + \frac{\Delta_\theta\sin^2\theta}{\Sigma}\left[\hat{a}\mathrm{d}\hat{t} - \frac{\hat{r}^2 + \hat{a}^2}{\Xi}\mathrm{d}\hat{\phi}\right]^2 , \tag{B.47}$$

$$A = -\frac{2Q\hat{r}}{\ell_\star \Sigma}\left[\mathrm{d}\hat{t} - \frac{\hat{a}\sin^2\theta}{\Xi}\mathrm{d}\hat{\phi}\right], \tag{B.48}$$

where

$$\Delta_r = (\hat{r}^2 + \hat{a}^2)\left(1 + \frac{\hat{r}^2}{\ell_4^2}\right) - 2m\hat{r} + Q^2\,, \quad \Delta_\theta = 1 - \frac{\hat{a}^2}{\ell_4^2}\cos^2\theta\,, \quad \Sigma = \hat{r}^2 + \hat{a}^2\cos^2\theta\,, \tag{B.49}$$

and

$$\Xi = 1 - \frac{\hat{a}^2}{\ell_4^2}\,, \quad x_1 = \sqrt{1 + \frac{\hat{a}^2}{\ell_4^2}}\,. \tag{B.50}$$

The above parameter rescalings also allow one to recover the Kerr-Newman-AdS thermodynamics from the quantum black hole thermodynamics discussed in this manuscript. The only subtlety is that one must subtract the Casimir energy contribution from the mass,

$$M_{\mathrm{KNAdS}} = \lim_{\ell\to\infty} M - M_{\mathrm{cas}} = \frac{m}{\Xi^2}\,. \tag{B.51}$$

In terms of this Casimir subtracted mass, we find (upon using the above parameter rescalings)

$$\lim_{\ell\to\infty} \frac{J}{M - M_{\mathrm{cas}}} = \hat{a}\,, \tag{B.52}$$

which, as required, matches the ratio of angular momentum to mass of the Kerr-Newman-AdS black hole.

Let us further note the following. If instead of starting from the metric (7.2) we start from the metric written in the 'barred' coordinates of (7.19) then the following differences must be accounted for. The transformation of the (t, ϕ) coordinates of (7.19) result in the Kerr-Newman-AdS metric in a frame which does not rotate at infinity. That is, taking the limit in the barred (t, ϕ)-coordinates yields a metric that is equivalent to (B.47) up to the following coordinate transformation,

$$\hat{t} = \hat{T}\,, \quad \hat{\phi} = \hat{\Phi} - \frac{\hat{a}}{\ell_4^2}\hat{T}\,. \tag{B.53}$$

To understand the implications of the new radial coordinate introduced in (7.19), we must recall that the Kerr-Newman-AdS metric written in the Boyer-Lindquist coordinates (B.47) is not manifestly asymptotically AdS as the metric components do not have the required

fall off properties [205]. Instead, to bring the metric into a manifestly asymptotically AdS form requires performing the following transformations to the Boyer-Lindquist coordinates as appearing in (B.47):

$$\hat{t} = \hat{T}\,, \quad \hat{\phi} = \hat{\Phi} - \frac{\hat{a}}{\ell_4^2}\hat{T}\,, \quad \hat{R}\cos\hat{\Theta} = \hat{r}\cos\theta\,, \tag{B.54}$$

$$\Xi\hat{R}^2 = \hat{r}^2 + \hat{a}^2\sin^2\theta - \frac{\hat{a}^2}{\ell_4^2}\hat{r}^2\cos^2\theta\,, \tag{B.55}$$

where $(\hat{T}, \hat{R}, \hat{\Theta}, \hat{\Phi})$ are the coordinates in the manifestly asymptotically AdS chart. Given this, one recognizes that $\bar{r}$ from (7.19) limits to $\hat{R}$ when restricting to the location of the brane, $\theta = \pi/2$.